

# Active Structural-Acoustic Control of Double Panel Systems

## Including Hierarchical Control Approaches

by

James P. Carneal

Dissertation submitted to the faculty of the

Virginia Polytechnic University and State University

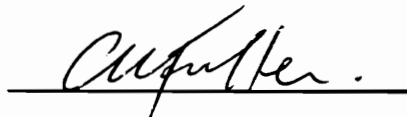
in partial fulfillment of the requirements for the degree of

**Doctor of Philosophy**

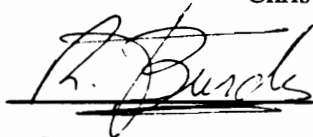
in

**Mechanical Engineering**

APPROVED:



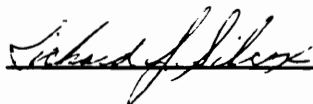
Chris R. Fuller, Chairman



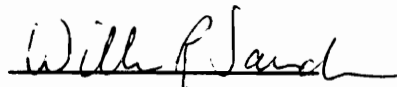
Ricardo A. Burdisso



Harry H. Robertshaw



Richard J. Silcox



William R. Saunders

c.2

LD  
5655  
V856  
1996  
C376  
c.2

# **Active Structural Acoustic Control of Double Panel Systems**

## **Including Hierarchical Control Approaches**

by

James P. Carneal

Chris R. Fuller, Committee Chairman

Department of Mechanical Engineering

### **Abstract**

The general trends and principles of active structural acoustic control when applied to double panel systems are investigated to determine the respective advantages and limitations of this approach. Included is the application of a novel hierarchical control approach which may reduce the controller complexity and the collinearity issue for large order controllers. This research was initiated by an interest in studying the noise transmission path from the noise field generated by an advanced turboprop engine through the aircraft fuselage and the interior trim into the interior acoustic field which can be modeled as a double panel system.

The system studied was a double panel model consisting of two rectangular, uniform, flat plates separated by a sealed air cavity, mounted in a transmission loss test facility and excited by an oblique acoustic plane wave. Piezoelectric control inputs were mounted directly on the double panel system incident or radiating plates. Error sensors were microphones placed in the acoustic free field. The cost function was defined as the total radiated sound power from the double panel system. The investigation was carried out analytically with experimental verification.

Results of active structural acoustic control (ASAC) applied to double panel systems indicated that the best control performance was exhibited by a double panel system controlled by PZT control actuators mounted on a sandwich board radiating plate. The sandwich board radiating plate double panel system exhibits a decreased coupling of the incident and radiating plates and a lower modal density which results in increased uncontrolled and controlled transmission loss. Piezoelectric (PZT) control actuators should be mounted on the radiating plate of a double panel system which can couple into the radiating acoustic field better than actuators mounted on the incident plate. As expected, better control is achieved with more control actuators since a more distributed forcing function can be attained. However, for on-resonance excitation, the increased number of actuators decreases performance due to collinearity of the actuators which results in spillover.

Results of the biologically inspired hierarchical (BIO) control algorithm indicated that significant performance increases over a one output channel controller were attained for all of the BIO methods while performance lagged compared to a full order controller with the same number of control channels. One advantage of the hierarchical control structure was the ability to avoid the collinearity issue when the degrees of freedom excited in the double panel system was less than the number of control channels. In this instance, the hierarchical structure exhibited less spillover than a fully adaptive LQOCT controller.

## *Acknowledgments*

The author wishes to thank his advisor, Chris Fuller, for the opportunity to pursue and complete my Ph.D. Gary Gibbs provided valuable insight and direction to the completion of this project along with invaluable motivation and relaxation as we discussed life over a few beers. Dawn Williams thankfully administrated the funding to allow this work to be completed as well as helped me navigate the administrative jungle. The rest of the VAL personnel were also helpful in completing this project.

I thank my committee members for reading this dissertation and providing insight to my project along the way.

The author gratefully acknowledge the support of this work by The Structural Acoustics Branch at NASA Langley Research Center, Dr. Harold Lester, Technical Monitor.

My family has provided support for what I wanted to do all of my life. I am very lucky to have such a wonderful family. Finally, I want to thank my fiancée, Margaret Geerdes. We were re-acquainted near the end of my first year into this degree and since has provided great spiritual support.

# **Table of contents**

1. Introduction.....	1
1.1. Sound transmission through plates .....	5
1.1.1. Single panel and double panel models .....	5
1.1.2. Mechanisms of sound radiation .....	8
1.1.3. Active control of sound transmission .....	10
1.2. Basic control approach.....	15
1.3. Scope and objectives.....	17
1.4. Organization .....	19
2. Structural and Acoustic Models.....	21
2.1. Structural models.....	21
2.1.1. Single plate.....	21
2.1.2. Double panel system.....	23
2.1.3. Clamped boundary conditions .....	28
2.1.4. Sandwich board stiffness .....	29
2.2. Acoustic models.....	30
2.2.1. Incident pressure field .....	30
2.2.2. Radiated pressure field .....	31
2.2.3. Transmission Loss .....	34
2.2.4. Air cavity resonances.....	34

2.3. Plate forcing functions .....	35
2.3.1. Incident pressure field .....	35
2.3.2. Piezoelectric actuator.....	37
2.4. Total structural response .....	39
2.5. Cost function .....	40
3. Controller development .....	41
3.1. Theory .....	43
3.1.1. Master control input .....	43
3.1.2. Local control approaches.....	45
3.2. Stability analysis.....	54
3.2.1. Master control input .....	55
3.2.2. Local rules.....	56
3.3. Linear quadratic optimal control .....	58
4. Experimental investigation .....	62
4.1. Experimental test rig.....	62
4.1.1. Double panel system.....	62
4.1.2. Cessna experimental aircraft fuselage .....	76
4.2. Controller .....	78
4.2.1. Filtered-X LMS algorithm.....	78
4.2.2. Biologically inspired hierarchical control algorithm .....	81
4.3. Performance criteria.....	84

4.4. Experimental procedure .....	87
5. Analytical results.....	89
5.1. Acoustical cavity resonances.....	89
5.2. Model validation.....	90
5.2.1. Plate and double panel system natural frequencies.....	91
5.2.2. Double panel uncontrolled transmission loss .....	96
5.3. Active control of double panel systems .....	101
5.3.1. Effect of radiating plate stiffness on control performance .....	102
5.3.2. Effect of PZT location on control performance.....	111
5.3.3. Effect of incident acoustic field on control performance .....	120
5.3.4. Effect of the number of control actuators on control performance .....	123
5.3.5. Effect of air cavity mass and stiffness on control performance .....	129
5.3.6. Summary.....	135
5.4. Biologically inspired hierarchical (BIO) control of double panel systems.....	136
5.4.1. BIO control performance.....	137
5.4.2. Effect of number of actuators on control performance .....	157
5.4.3. Effect of master actuator choice on control performance .....	160
5.4.4. Computational effort .....	161



5.4.5. Stability.....	163
6. Experimental Results.....	166
6.1. Active structural acoustic control of double panel systems.....	166
6.1.1. Preliminary results: double panel behavior .....	167
6.1.2. Effect of radiating plate stiffness on control performance .....	170
6.1.3. Effect of PZT location on control performance.....	173
6.1.4. Effect of incident acoustic field on control performance .....	176
6.1.5. Effect of excitation frequency on control performance .....	180
6.1.6. Effect of the number of control actuators on control performance .....	182
6.1.7. Summary .....	183
6.2. BIO control of double panel systems.....	184
6.2.1. BIO control performance.....	185
6.2.2. Stability.....	202
6.3. ASAC of Cessna experimental fuselage double panel system.....	204
6.3.1. Filtered-X LMS algorithm.....	205
6.3.2. TAG LMS and biologically inspired hierarchical (BIO) algorithms .....	208
6.3.3. Summary .....	210
7. Conclusions.....	211
8. Recommendations .....	216

## **List of Figures**

Figure 2-1. Single plate coordinate system .....	23
Figure 2-2. Double panel system coordinate system .....	28
Figure 2-3. Incident pressure field and piezoelectric actuator coordinate system .....	30
Figure 2-4. Radiating pressure field and piezoelectric actuator coordinate system.....	33
Figure 3-1. Biologically inspired control approach .....	42
Figure 3-2. Traditional adaptive feedforward control system schematic .....	44
Figure 3-3. Phase variation control system schematic .....	48
Figure 3-4. Simply supported beam mode two magnitude .....	50
Figure 3-5. Adaptive magnitude and adaptive phase control system schematic .....	51
Figure 3-6. Optimal distribution control system schematic .....	54
Figure 4-1. Transmission loss test facility setup for ASAC tests.....	68
Figure 4-2. Radiating plate PZT and node line locations for ASAC tests .....	68
Figure 4-3. Transmission loss test facility setup for BIO tests .....	74
Figure 4-4. PZT and node line locations for BIO tests .....	74
Figure 4-5. Photograph of radiating chamber anechoic insert, error microphones, and 2D laser traverse for BIO tests.....	75
Figure 4-6. Cessna experimental aircraft fuselage schematic.....	77
Figure 4-7. Cessna microphone locations (top view) .....	77
Figure 4-8. Cessna interior trim cockpit ceiling PZT locations (top view).....	78
Figure 4-9. Filtered-X LMS control system schematic for ASAC tests .....	81
Figure 4-10. Biologically inspired hierarchical (BIO) control system schematic .....	84

Figure 5-1. Uncontrolled aluminum radiating plate double panel system TL. .... 99

Figure 5-2. Third octave uncontrolled aluminum radiating plate double panel system TL..... 100

Figure 5-3. Uncontrolled sandwich board radiating plate double panel system TL..... 100

Figure 5-4. Third octave uncontrolled sandwich board radiating plate double panel system TL..... 101

Figure 5-5. Uncontrolled and controlled transmission loss for double panel system with aluminum radiating plate (oblique incident wave; radiating plate PZT location) ..... 107

Figure 5-6. Uncontrolled and controlled transmission loss for double panel system with sandwich board radiating plate (oblique incident wave; radiating plate PZT location)..... 108

Figure 5-7. Uncontrolled and controlled double panel system modal amplitudes at 500 Hz with sandwich board radiating plate (oblique incident wave; radiating plate PZT location) ..... 108

Figure 5-8. Uncontrolled and controlled double panel system modal amplitudes at 500 Hz with aluminum radiating plate (oblique incident wave; radiating plate PZT location)..... 109

Figure 5-9. Uncontrolled and controlled double panel system modal amplitudes at 100 Hz with aluminum radiating plate (oblique incident wave; radiating plate PZT location)..... 109

Figure 5-10. Uncontrolled and controlled double panel system modal amplitudes at 110 Hz with aluminum radiating plate (oblique incident wave; radiating plate PZT location)..... 110

Figure 5-11. Uncontrolled and controlled double panel system modal amplitudes at 130 Hz with aluminum radiating plate (oblique incident wave; radiating plate PZT location)..... 110

Figure 5-12. Maximum control effort for a double panel system with an aluminum and sandwich board radiating plate (oblique incident wave; PZTs located on radiating plate). 111

Figure 5-12. Uncontrolled and controlled transmission loss for double panel system with PZTs located on incident and radiating plates (oblique incident wave; sandwich board radiating plate) ..... 115

Figure 5-13. Uncontrolled and controlled double panel system modal amplitudes at 360 Hz with PZTs located on incident plate (oblique incident wave; sandwich board radiating plate)..... 116

Figure 5-14. Uncontrolled and controlled double panel system modal amplitudes at 360 Hz with PZTs located on radiating plate (oblique incident wave; sandwich board radiating plate)..... 116

Figure 5-15. Uncontrolled and controlled transmission loss for double panel system with PZTs located on incident and radiating plates (normal incident wave; aluminum radiating plate) ..... 117

Figure 5-16. Uncontrolled and controlled double panel system modal amplitudes at 300 Hz with PZTs located on incident plate (normal incident wave; aluminum radiating plate).... 117

Figure 5-17. Uncontrolled and controlled double panel system modal amplitudes at 300 Hz with PZTs located on radiating plate (normal incident wave; aluminum radiating plate) .. 118

Figure 5-18. Uncontrolled and controlled double panel system modal amplitudes at 390 Hz with PZTs located on incident plate (normal incident wave; aluminum radiating plate).... 118

Figure 5-19. Uncontrolled and controlled double panel system modal amplitudes at 390 Hz with PZTs located on radiating plate (normal incident wave; aluminum radiating plate) .. 119

Figure 5-20. Maximum control effort for PZTs located on incident and radiating plates of a double panel system (normal incident wave; aluminum radiating plate)..... 119

Figure 5-21. Uncontrolled and controlled transmission loss for double panel system excited by normal and oblique incident waves (radiating plate PZT location; aluminum radiating plate) ..... 122

Figure 5-22. Uncontrolled and controlled double panel system modal amplitudes excited by normal incident wave at 200 Hz (radiating plate PZT location; aluminum radiating plate)..... 122

Figure 5-23. Uncontrolled and controlled double panel system modal amplitudes excited by oblique incident wave at 200 Hz (radiating plate PZT location; aluminum radiating plate)..... 123

Figure 5-24. Uncontrolled and controlled transmission loss for double panel system excited by 2 and 4 PZT actuators (normal incident wave; PZT located on aluminum radiating plate)..... 126

Figure 5-25. Uncontrolled and controlled transmission loss for double panel system excited by 2 and 4 PZT actuators (oblique incident wave; PZTs located on sandwich board radiating plate) ..... 127

Figure 5-26. Uncontrolled and controlled double panel system modal amplitudes controlled by 2 PZT actuators at 340 Hz (normal incident wave; PZTs located on aluminum radiating plate) ..... 127

Figure 5-27. Uncontrolled and controlled double panel system modal amplitudes controlled by 4 PZT actuators at 340 Hz (normal incident wave; PZT located on aluminum radiating plate) ..... 128

Figure 5-28. Uncontrolled and controlled double panel system modal amplitudes controlled by 2 PZT actuators at 500 Hz (oblique incident wave; PZT located on sandwich board radiating plate) .....	128
Figure 5-29. Uncontrolled and controlled double panel system modal amplitudes controlled by 4 PZT actuators at 500 Hz (oblique incident wave; PZT located on sandwich board radiating plate) .....	129
Figure 5-30. Uncontrolled and controlled transmission loss for baseline and 200% air cavity mass (normal incident wave; PZTs located on aluminum radiating plate) .....	132
Figure 5-31. Uncontrolled and controlled modal response for baseline mass and stiffness at 250 .....	133
Figure 5-32. Uncontrolled and controlled modal response for 200% air cavity mass at 250 Hz (normal incident wave; PZTs located on aluminum radiating plate) .....	133
Figure 5-33. Uncontrolled and controlled transmission loss for baseline and 200% air cavity stiffness (normal incident wave; PZTs located on aluminum radiating plate) .....	134
Figure 5-34. Uncontrolled and controlled modal response for 200% air cavity stiffness at 250 Hz (normal incident wave; PZTs located on aluminum radiating plate).....	135
Figure 5-35. Uncontrolled and controlled double panel system transmission loss for the master, phase variation and baseline algorithms (normal plane wave; aluminum radiating plate ) .....	142
Figure 5-36. Baseline algorithm relative control voltage magnitude and phase when controlling double panel system transmission loss (normal plane wave; aluminum radiating plate) .....	143

Figure 5-37. Baseline algorithm relative control voltage magnitude and phase when controlling double panel system transmission loss (oblique plane wave; aluminum radiating plate) ..... 143

Figure 5-38. Uncontrolled and controlled double panel system transmission loss for the master, phase variation and baseline algorithms (oblique plane wave; sandwich board radiating plate) ..... 144

Figure 5-39. Uncontrolled and controlled double panel system modal amplitudes for the master algorithm at 500 Hz (oblique incident wave; sandwich board radiating plate) ..... 144

Figure 5-40. Uncontrolled and controlled double panel system transmission loss for the master, adaptive magnitude and baseline algorithms (normal plane wave; aluminum radiating plate ) ..... 148

Figure 5-41. Uncontrolled and controlled double panel system modal amplitudes for the adaptive magnitude method at 500 Hz (normal incident wave; aluminum radiating plate) 148

Figure 5-42. Uncontrolled and controlled double panel system modal amplitudes for the baseline algorithm at 500 Hz (normal incident wave; aluminum radiating plate)..... 149

Figure 5-43. Uncontrolled and controlled double panel system transmission loss for the master, adaptive magnitude and baseline algorithms (oblique plane wave; sandwich board radiating plate )..... 149

Figure 5-44. Uncontrolled and controlled double panel system transmission loss for the master, adaptive phase and baseline algorithms (normal plane wave; aluminum radiating plate )..... 153

Figure 5-45. Uncontrolled and controlled double panel system transmission loss for the master, adaptive phase and baseline algorithms (oblique plane wave; aluminum radiating plate ) .....	153
Figure 5-46. Uncontrolled and controlled double panel system transmission loss for the master, adaptive phase and baseline algorithms (oblique plane wave; sandwich board radiating plate ) .....	155
Figure 5-47. Uncontrolled and controlled double panel system transmission loss for the master, optimal and baseline algorithms (normal plane wave; aluminum radiating plate )	156
Figure 5-48. Uncontrolled and controlled double panel system modal amplitudes for the optimal method at 470 Hz (normal incident wave; aluminum radiating plate) .....	156
Figure 5-49. Uncontrolled and controlled double panel system modal amplitudes for the baseline algorithm at 470 Hz (normal incident wave; aluminum radiating plate).....	157
Figure 5-50. Effect of number of PZT actuators on double panel system transmission loss controlled by BIO adaptive phase method (normal incident wave; aluminum radiating plate).....	159
Figure 5-51. Maximum convergence parameter ( $\mu$ ) for Filtered-X LMS, master, and master with slave actuators using phase variation method (normal incident wave; PZTs located on sandwich board radiating plate ) .....	165
Figure 5-52. Maximum convergence parameter ( $\mu$ ) for Filtered-X LMS, and master with slave actuators using adaptive magnitude method (normal incident wave; PZTs located on sandwich board radiating plate ) .....	165
Figure 6-1. Flexible (G10 fiberglass) and stiff (sandwich board (SB)) double panel system frequency response functions.....	169



Figure 6-2. Flexible (G10 fiberglass) and stiff (sandwich board (SB)) plate coupling .....	170
Figure 6-3. Uncontrolled and controlled flexible radiating plate modal amplitudes at 361 Hz (PZTs located on radiating plate; normal incident wave).....	172
Figure 6-4. Uncontrolled and controlled stiff radiating plate modal amplitudes at 361 Hz (PZTs.....)	173
Figure 6-5. Uncontrolled and controlled radiating plate modal amplitudes at 218 Hz with PZTs located on incident plate (reverberant incident wave; G10 radiating plate).....	175
Figure 6-6. Uncontrolled and controlled radiating plate modal amplitudes at 218 Hz with PZTs located on radiating plate (reverberant incident wave; G10 radiating plate).....	176
Figure 6-7. Uncontrolled flexible radiating plate modal amplitudes off-resonance at 218 Hz (PZTs located on radiating plate).....	179
Figure 6-8. Controlled flexible radiating plate modal amplitudes off-resonance at 218 Hz (PZTs located on radiating plate).....	179
Figure 6-9. Uncontrolled and controlled stiff radiating plate modal amplitudes off-resonance at 361 Hz (PZTs located on radiating plate; normal incident wave).....	181
Figure 6-10. Uncontrolled and controlled stiff radiating plate modal amplitudes on-resonance at 496 Hz (PZTs located on radiating plate; normal incident wave).....	182
Figure 6-11. Uncontrolled and controlled modal response for 5 input 1 output Filtered-X LMS controller at 350 Hz (oblique incident wave; PZT's located on sandwich board radiating plate) .....	191
Figure 6-12. Uncontrolled and controlled modal response for 5 input 1 output TAG LMS controller at 350 Hz (oblique incident wave; PZT's located on sandwich board radiating plate).....	192

Figure 6-13. Uncontrolled and controlled modal response for 5 input 4 output Filtered-X LMS controller at 350 Hz (oblique incident wave; PZT's located on sandwich board radiating plate) .....	192
Figure 6-14. Uncontrolled and controlled modal response for 5 input 4 output TAG LMS controller at 350 Hz (oblique incident wave; PZT's located on sandwich board radiating plate) .....	193
Figure 6-15. Uncontrolled and controlled modal response for 5 input 4 output BIO controller using adaptive magnitude method at 350 Hz (oblique incident wave; PZT's located on sandwich board radiating plate) .....	193
Figure 6-16. Uncontrolled and controlled modal response for 5 input 4 output BIO controller using adaptive phase method at 350 Hz (oblique incident wave; PZT's located on sandwich board radiating plate) .....	194
Figure 6-17. Uncontrolled and controlled modal response for 5 input 4 output BIO controller using optimal method at 350 Hz (oblique incident wave; PZT's located on sandwich board radiating plate).....	194
Figure 6-18. Uncontrolled and controlled modal response for 5 input 1 output Filtered-X LMS controller at 653 Hz (oblique incident wave; PZT's located on sandwich board radiating plate) .....	197
Figure 6-19. Uncontrolled and controlled modal response for 5 input 1 output TAG LMS controller at 653 Hz (oblique incident wave; PZT's located on sandwich board radiating plate) .....	198

Figure 6-20. Uncontrolled and controlled modal response for 5 input 4 output Filtered-X LMS controller at 653 Hz (oblique incident wave; PZT's located on sandwich board radiating plate) ..... 198

Figure 6-21. Uncontrolled and controlled modal response for 5 input 4 output TAG LMS controller at 653 Hz (oblique incident wave; PZT's located on sandwich board radiating plate) ..... 199

Figure 6-22. Uncontrolled and controlled modal response for 5 input 4 output BIO controller using adaptive magnitude method at 653 Hz (oblique incident wave; PZT's located on sandwich board radiating plate) ..... 199

Figure 6-23. Uncontrolled and controlled modal response for 5 input 4 output BIO controller using adaptive phase method at 653 Hz (oblique incident wave; PZT's located on sandwich board radiating plate) ..... 200

Figure 6-24. Uncontrolled and controlled modal response for 5 input 4 output BIO controller using optimal method at 653 Hz (oblique incident wave; PZT's located on sandwich board radiating plate)..... 200

Figure B-1. Incident wave magnitude (dB) and phase (degrees) measured at incident panel..... 225

## List of Tables

Table 4-1. Summary of ASAC test plate properties .....	67
Table 4-2. PZT central locations for ASAC tests (m).....	67
Table 4-3. Summary of BIO test plate properties .....	72
Table 4-4. Microphone positions for BIO tests .....	72
Table 4-5. PZT properties .....	73
Table 4-6. PZT central locations for BIO tests.....	73
Table 5-1. Acoustic cavity resonances.....	90
Table 5-2. Aluminum single plate natural frequencies .....	94
Table 5-3. Double panel system natural frequencies (aluminum radiating plate) .....	95
Table 5-4. Theoretical double panel system natural frequencies (sandwich board radiating plate).....	96
Table 5-5. Effect of radiating plate stiffness on frequency averaged transmission loss .....	107
Table 5-6. Effect of PZT location on frequency averaged transmission loss.....	115
Table 5-7. Effect of incident plane wave on frequency averaged transmission loss .....	121
Table 5-8. Effect of number of control actuators on frequency averaged transmission loss (dB); average computed over 50-800 Hz.....	126
Table 5-9. Effect of number of control actuators on frequency averaged transmission loss (dB); average computed over 300-800 Hz.....	126
Table 5-10. Effect of air cavity mass on frequency averaged transmission loss (dB); average computed from 50-800 Hz.....	132

Table 5-11. Effect of air cavity stiffness on frequency averaged transmission loss (dB); average computed from 50-800 Hz .....	134
Table 5-12. Effect of BIO controller phase variation method on frequency averaged transmission loss; average computed from 50-800 Hz.....	141
Table 5-13. Effect of BIO controller phase variation method on frequency averaged transmission loss; average computed from 300-800 Hz.....	142
Table 5-14. Effect of BIO controller adaptive magnitude method on frequency averaged transmission ; average computed from 50-800 Hz.....	147
Table 5-15. Effect of BIO controller adaptive magnitude method on frequency averaged transmission ; average computed from 300-800 Hz.....	147
Table 5-16. Effect of BIO controller adaptive phase method on frequency averaged transmission loss; average computed from 50-800 Hz.....	152
Table 5-17. Effect of BIO controller adaptive phase method on frequency averaged transmission loss; average computed from 300-800 Hz.....	152
Table 5-18. Effect of BIO controller optimal method on frequency averaged transmission loss; average computed from 50-800 Hz (PZTs located on radiating plate) .....	155
Table 5-19. Effect of number of control actuators on BIO controller phase variation method frequency averaged transmission loss; average computed from 50-800 Hz.....	158
Table 5-20. Effect of number of control actuators on BIO controller adaptive magnitude method frequency averaged transmission loss; average computed from 50-800 Hz .....	158
Table 5-21. Effect of number of control actuators on BIO controller adaptive phase method frequency averaged transmission loss; average computed from 50-800 Hz.....	159

Table 5-22. Effect of master actuator on BIO controller phase variation method frequency averaged transmission loss (normal incident wave; aluminum radiating plate) .....	160
Table 5-23. Effect of master actuator on BIO controller adaptive magnitude method frequency averaged transmission loss (normal incident wave; aluminum radiating plate). 160	
Table 5-24. Effect of master actuator on BIO controller adaptive phase method frequency averaged transmission loss (normal incident wave; aluminum radiating plate) .....	161
Table 5-25. Number of floating point operations (flops) for one update of different control strategies .....	162
Table 5-26. Effect of system order and sample period on number of floating point operations of different control strategies .....	163
Table 6-1. Flexible (G10 fiberglass) vs. stiff (sandwich board (SB)) radiating plate control performance (normal plane wave).....	172
Table 6-2. Effect of PZT location on transmission loss (G10 radiating plate; off-resonance reverberant excitation at 218 Hz) .....	175
Table 6-3. Excitation field control performance (218 Hz; flexible plate).....	178
Table 6-4. Excitation frequency control performance (stiff plate; normal plane wave) .....	181
Table 6-5. Influence of number of control actuators on control performance (normal plane wave; flexible radiating plate; 218 Hz) .....	183
Table 6-6. Double panel system increase in TL with control for Filtered-X LMS and TAG LMS control methodologies .....	188
Table 6-7. Double panel system increase in TL with control for various TAG LMS and BIO control methodologies .....	188

Table 6-8. Maximum convergence parameter for various control methodologies (350 Hz oblique incident wave; PZT's located on sandwich board radiating plate) .....	204
Table 6-9. Reduction in interior noise levels (SPL, dB) in Cessna experimental fuselage for Filtered-X LMS algorithm.....	207
Table 6-10. Sound pressure level at microphones in Cessna experimental fuselage for Filtered- .....	208
Table 6-11. Reduction in interior noise levels (dB) in Cessna experimental fuselage for various BIO control methodologies (710 Hz).....	209
Table A-1. Reverberant chamber characteristics .....	223

## Nomenclature

$\alpha_x, \alpha_y$	$m\pi/l_x$ and $n\pi/y$ , respectively
$\epsilon_{pe}$	PZT constant
$\nu_{pe}$	Poisson's ratio for PZT
$\omega_{mn}$	$mn^{\text{th}}$ natural frequency
$\rho$	density
$\nu$	Poisson's ratio
$\omega$	frequency (rad/s)
$\Theta$	transfer function
$\theta$	polar coordinate
$\phi$	polar coordinate
$\Pi$	acoustic power
$\tau$	transmission coefficient
$\delta$	Dirac delta function
$\eta$	damping coefficient
$\mu$	convergence coefficient
$\nabla$	gradient
$\gamma$	control path complex gain
$\Lambda$	eigenvalue matrix
$\lambda$	eigenvalue
$C$	damping coefficient
$C_o$	PZT constant
$c$	speed of sound in medium
$D$	stiffness of structure
$\mathbf{d}$	disturbance
$d_{31}$	piezoelectric strain constant
$E$	modulus of elasticity
$\mathbf{e}$	error



$F_c$	applied PZT force
$H$	control transfer function
$h$	thickness of structure
$I$	acoustic intensity
$J$	cost function
$j$	square root of (-1)
$K$	air spring coefficient
$k$	acoustic wavenumber
$k_s$	structural wavenumber
$l_x, l_y$	length of structure in x and y directions, respectively
$m$	mass density per unit area of the structure
$m_x, m_y$	moment in the x and y direction, respectively
$P$	acoustic pressure amplitude
$p$	acoustic pressure
$p_{mn}$	modally decomposed pressure
$Q$	coordinate transformation matrix
$r$	radius (polar coordinate)
$TL$	transmission loss
$t$	time
$V$	voltage
$v$	transformed convergence vector
$W$	modal response of structure
$w$	flexural response of structure
$w$	output of fir filter
$x, y$	Cartesian coordinates
$Y$	integration of far field radiation terms

## SUBSCRIPTS

$h$	hermitian transpose
$i$	incident

<i>k</i>	iteration index
<i>m,n</i>	modal indices
<i>opt</i>	optimal
<i>r</i>	radiating
<i>s</i>	air cavity
<i>t</i>	time index
<i>x,y</i>	x and y direction ,respectively

#### SUPERSCRIPTS

<i>c</i>	control
<i>d</i>	disturbance
<i>i</i>	incident
<i>r</i>	radiating

## **1. Introduction**

The environment in which humans spend most of their time has become louder due to the increased mechanization in our society. Unfortunately, these increased noise levels have detrimental physiological and psychological effects on humans. The physiological effects of noise can range from harmless to painful and physically damaging (Kinsler, et. al., 1982). The most common form of physically damaging effect is hearing loss, which became prevalent enough to be included in the Occupational Safety and Health Act (OSHA) of 1970. In OSHA, the permissible noise exposure levels were regulated for industries doing business with the U.S. Federal government. The psychological effects can range from negligible to annoyance and anger to psychologically disruptive. Although no government regulation has been implemented, it has been well documented that humans will experience increased fatigue when exposed to high noise levels. Therefore, by controlling the noise level in the environment, the psychological and physiological effects can be minimized resulting in more productivity in the workplace, a more pleasant experience on a plane flight, etc.

There are two methods of noise control, passive and active. Passive noise control primarily changes the physical properties of a structure to reduce the amount of radiated noise using absorptive materials, vibration dampers, etc. Unfortunately, the effectiveness of passive techniques is limited to relatively high frequency applications where the acoustical wavelength is

relatively small. For low frequency applications, the acoustical wavelength is relatively long (approximately 1 meter at 343 Hz) and passive techniques require large heavy installations. Active noise control (ANC) techniques have shown promise to reduce the radiated noise from vibrating structures by employing a secondary source(s) to cancel the offending vibration and/or noise without the disadvantages of passive techniques such as weight and size. Active noise control has evolved from using acoustic secondary sources to using vibration secondary sources directly mounted on the offending structure, known as Active Structural Acoustic Control (ASAC) (Fuller, 1989). This approach has been extensively verified analytically and experimentally.

The development of ANC and ASAC technology is largely motivated by an interest in reducing the interior noise levels of aircraft. Currently, propeller driven aircraft experience a serious low frequency interior noise problem at the blade passage frequency and its harmonics. Also, recent developments in turbofan technology (ultra high bypass turbofans and unducted fans) will lead to increased low frequency noise fields impinging on the exterior of the aircraft fuselage thereby making the interior noise problem worse (Mixson and Powell, 1984). Since traditional methods of low frequency noise reduction require heavy damping material which will offset the performance gains of the turbofans, ASAC has been extensively investigated for this application.

The application of ASAC technology to control aircraft interior noise has mainly focused on controlling the fuselage of the aircraft. However, the application of control actuators to the fuselage has shown several disadvantages. Studies have shown that ASAC of the interior noise field can produce increased vibrational energy of the fuselage at some locations, which leads to a

concern of structural fatigue (Silcox, et al. 1992) (Thomas, 1992). In addition, implementing control actuators on the fuselage shows other key disadvantages. Installation and repair of sensors and actuators would be extremely difficult since the structure is not removable. Design of a fuselage for dynamics conducive to more effective noise attenuation is limited. Most of these disadvantages are the result of the fuselage doubling as a pressure vessel and is therefore subject to strict FAA regulation.

In addition to the fuselage, exterior noise must also transmit through the interior trim of a modern aircraft. The application of control actuators to the interior trim was seen to have distinct advantages. There is likely to be no increase in fuselage vibrational energy. Panels can be removed allowing facilitated installation and repair of sensors and actuators. Design of the panel can be changed to be more conducive to transmission. In general, advantage can be taken of the double panel behavior.

To test the above hypothesis, Carneal and Fuller (1995c) performed an experimental investigation on a double panel system, which is a simplified model of the aircraft fuselage and interior trim. In particular, the influence of the location of the piezoelectric control actuators (fuselage vs. trim) and radiating panel stiffness on double panel transmission loss was determined. It was found that the application of the control inputs to the radiating panel resulted in greater transmission loss (TL) due to its direct effect on the nature of the structural-acoustic coupling between the radiating panel and the radiated acoustic field. Also, a double panel system with a stiffer radiating panel resulted in increased attenuation due to passive and active effects.

However, there is a disadvantage: control of the interior trim will tend to impart local control of the interior acoustic fields. To impart global, several actuators must be used on a multitude of interior trim panels which will result in a large number of secondary control sources. Since current controller algorithms have shown a number of problems with large number of control channels, the biologically inspired (BIO) controller will be investigated as an alternative approach. This control approach uses a hierarchical control structure that has been shown to alleviate some of the problems traditional control methodologies have with a large number of actuators. The BIO control approach has been analytically and experimentally studied for beam vibration (Fuller and Carneal, 1993) (Carneal and Fuller, 1995a) and sound transmission through plates (Carneal and Fuller, 1995b).

The application of active control to double panel systems will be the main subject of this dissertation. First, an analytical model must be developed for investigating active control of double panel systems using traditional adaptive feedforward control algorithms, which are implemented theoretically by linear quadratic optimal control theory (LQOCT) and experimentally by the Filtered-X LMS algorithm (Widrow and Stearns, 1985). This model will be used to study the influence of double panel system parameters on control performance which will be detailed later in this chapter. The BIO control approach will be applied to the double panel system to determine the influence of different approaches on control system performance including computational complexity and stability considerations.

The following sections will provide a brief introduction and literature review of the disciplines involved: the sound transmission through structures, sound radiation mechanisms, and the basic

control approach.

### **1.1. Sound transmission through plates**

The basic model for the sound transmission studies is a structure which separates two fluids. The fluid on both sides of the plate is assumed to be air which means the structure is lightly fluid loaded, i.e. the radiated pressure due to structural vibration is assumed negligible compared to the *blocked* pressure (twice the incident pressure) exciting the structure (Roussos, 1985). Restating, the radiation impedance is small compared to the structural input impedance. This is an important assumption since it greatly facilitates the solution of the equation of motion for the structure. The structure is excited by an oblique incident acoustic plane wave which impinges on the *incident* side of a structure. The induced structural vibration then radiates an acoustic field from the *radiating* side of the structure. To quantify the amount of sound power that is transmitted by the structure, the transmission coefficient ( $\tau$ ) is defined as the ratio of the power radiated from the structure to the power incident upon the structure. The more recognized quantity is sound transmission loss (TL) which is defined as  $10\log_{10}(1/\tau)$  (Fahy, 1985).

#### **1.1.1. Single panel and double panel models**

The most basic model of sound transmission is a normal incident plane wave impinging on an infinite rigid plate which is supported by a spring and damper system (Fahy, 1985). This model approximates the fundamental mode of a plate and its solution shows the following trends. Below the fundamental frequency of the plate, the TL is determined primarily by the elastic stiffness of the mounting and is insensitive to mass and damping. In this region, TL decreases with frequency by 6 dB per octave. At the fundamental frequency of the plate, the transmission coefficient is approximately unity (without damping) which means all of the incident intensity is transmitted. Above the fundamental frequency of the plate, the TL is determined primarily by the

mass of the structure and is largely independent of the stiffness and damping. The TL increases with frequency at 6 dB per octave and 6 dB per doubling of mass. This is known as the *normal incidence mass law*.

The next model discussed is the transmission of sound by an infinite flexible plate (Fahy, 1985). Unlike the previous model, the plate is now flexible and the incident plane wave is not restricted to be normal to the plate. Since the plate is flexible, there exists a coincidence condition where the acoustic trace wavenumber equals the free flexural wavenumber of the plate. If the acoustic plane wave has normal incidence, the plate behavior follows the normal incidence mass law described previously. However, the following trends are observed if the incident plane wave is oblique. If the excitation frequency is below the coincidence frequency, the TL shows the same trends as the normal incidence mass law, however the magnitude decreases with increasing angle of incidence. Near the coincidence frequency, the TL dips to a minimum due to the coincidence condition and is damping controlled. Above the coincidence frequency, the TL is dominated by the stiffness of the plate and TL increases by 18 dB per doubling of frequency.

The next general model discussed is the behavior of two plates separated by an acoustic cavity which is known as a double panel system. Theoretical analysis of sound transmission behavior is difficult due to the large number of parameters, the inclusion of the acoustical coupling between the plates, etc. (Fahy, 1985). The following analyses are presented to show the general physical mechanisms involved versus accurate quantitative assessments.

The model discussed is the transmission of normally incident plane waves through an unbounded



rigid double panel system (Fahy, 1985). The double panel system consists of two uniform, non-flexible partitions are separated by an air cavity and mounted upon viscously damped, elastic suspensions. Since the two plates are separated by an air cavity which can be viewed as a linear elastic uniformly distributed spring at low frequencies (i.e. below the first acoustical cavity resonance), the double panel system exhibits a mass-air-mass resonance frequency ( $\omega_{om}$ ). Below  $\omega_{om}$ , the double panel system behaves like a single plate (normal incidence mass law) with the mass equal to the sum of the two plates. Near  $\omega_{om}$ , the TL is at a minimum and can be made less severe by using plates of different weight. Unfortunately, maximizing the TL at  $\omega_{om}$  will decrease performance at higher frequencies. Above  $\omega_{om}$ , the TL increases at 18 dB/octave until  $kd \approx 1$  where  $k$  is the acoustic wavenumber ( $k=\omega/c$ ) and  $d$  is the separation distance of the two plates. In this range the second plate acts as a mass driven by a spring excited by the motion of the first plate. When  $kd \gg 1$ , there exist minima and maxima in the TL corresponding to the resonances and anti-resonances of the acoustic cavity, respectively. At resonances, the loading on the first plate is the same as if the second plate were directly attached and a line through the resonances (the minima) would have a slope of 6 dB/octave. At anti-resonances (the maxima), the asymptotic values of TL are approximately equal to the sum of the TL of the individual plates which have a slope of 12 dB/octave.

The addition of an acoustic absorptive material in the air cavity between the two plates provides additional attenuation at high frequencies if the acoustic wavelength is on the order of the separation distance of the plates (cavity depth). However, for low frequency applications the effects of adding sound absorbing materials in the acoustic cavity between the two panels is negligible since the acoustic wavelength is usually much greater the cavity depth (Fahy, 1985)

(Grosveld, 1985).

The generalization of the rigid double panel model to a flexible model shows the same trends as the rigid model with a few exceptions (Fahy, 1985). At high frequencies and oblique incident angles there exists a coincidence condition of the panels. As stated earlier, the analysis becomes too complex to show general trends and must be evaluated on a case by case basis.

Grosveld (1985) developed theoretical formulations for infinite, semi-infinite and finite double panel structures based on a multiple-reflection ray theory. Although this model is good for predictions of transmission loss from an incident reverberant field, it does not lend itself to the traditional structural, deterministic, modal model upon which most active control analytical research is based.

Vaicaitis (1983) developed a theoretical modal model of noise transmission through double panel systems. Agreement between experimental and analytical results was good for one third octave bands from 63 to 1000 Hz. The analytical model was used to perform a parametric analysis to maximize transmission loss through double wall aircraft windows. This model is the primary double panel model used in this dissertation. However, the model did not provide for forcing functions applied to the radiating plate of a double panel system. Therefore, the model was expanded to include radiating plate forcing functions. This model is presented in more detail in Chapter 2.

### **1.1.2. Mechanisms of sound radiation**

Sound transmission includes the topic of sound radiation from a structure. The basic mechanisms

of sound radiation are outlined in this section to give insight on the physics of the problem.

Sound radiation from a planar radiator in an infinite baffle can be viewed from a structural wavenumber approach (Fahy, 1985). There are structural wavenumber components which radiate acoustic energy to the far field and those which create near field acoustic disturbances. The separation between these regions depends on the relationship between the structural wavenumber ( $k_s = \sqrt{k_x^2 + k_y^2}$  where  $k_x = m\pi/l_x$  and  $k_y = n\pi/l_y$  for a rectangular plate) and the acoustic wavenumber ( $k = \omega / c$ ). The region where  $k/k_s > 1$ , is where acoustic energy is radiated and is called the supersonic region. Conversely, the region where  $k/k_s < 1$ , where acoustic energy is not radiated is called the subsonic region. Therefore, to minimize radiated acoustic energy, a structure should be designed to have a structural wavenumber that is primarily in the subsonic region.

Maidanik (1962) first noticed that structures exhibit different types of acoustic radiation termed the surface mode, edge mode and corner mode. It is further explained in Fahy (1985) that surface mode radiation occurs when the acoustic wavenumber is greater than the structural wavenumber ( $k/k_s > 1$ ) (the supersonic region) and the entire surface contributes significantly to the acoustic radiation. Edge mode radiation occurs when the acoustic wavenumber is greater than the x or y structural wavenumber component [either ( $k/k_x > 1$  and  $k/k_y < 1$ ) or ( $k/k_x < 1$  and  $k/k_y > 1$ )] and is less efficient than surface mode radiation since only the edges contribute significantly to the acoustic radiation. The least efficient is corner mode radiation occurs when  $k < k_x$  and  $k < k_y$  when only the corners contribute significantly to the acoustic radiation.

Wallace (1972) defined a radiation efficiency term for each associated mode of plate vibration which can be written as:

$$\sigma_{mn} = \frac{\Pi_{mn}}{\rho c A \langle \dot{w}_{mn}^2 \rangle} \quad (1.1)$$

where  $\Pi_{mn}$  is the radiated acoustic power,  $\rho$  and  $c$  are the density and speed of sound of the acoustic medium, respectively,  $A$  is the surface area of the vibrating structure, and  $\langle \dot{w}_{mn}^2 \rangle$  is the temporal and spatial average of the mean surface velocity of the (m,n) mode. For simply supported structures, Wallace showed that when  $k/k_s < 1$ , the odd-odd modes have a higher radiation efficiency than odd-even (or even-odd) and even-even modes have the lowest radiation efficiency. When  $k/k_s > 1$ , the radiation efficiency is approximately one.

The radiation efficiency is important to the active control of sound transmission/radiation from finite plates. For effective attenuation, only the odd-odd modes must be controlled since they have a radiation efficiency several orders of magnitude greater than the even-even modes. Therefore the dimensionality of the controller is effectively reduced (compared to vibration control where all of the modes are evenly weighted).

### 1.1.3. Active control of sound transmission

The following is a brief literature review of the active control of sound transmission which includes both theoretical and experimental investigations.

When control is applied to the sound transmission/radiation from finite plates, it was found that the controller employed two different mechanisms, *modal suppression* and *modal restructuring* (Fuller , 1989). In modal suppression, the amplitude of each mode that contributes significantly

to the acoustic radiation is reduced therefore the acoustic and vibration response of the dominant mode is attenuated. In modal restructuring, the control force modifies the plate source characteristics. The efficient acoustic modes are attenuated while some inefficient acoustic modes are increased. The net result provides acoustic attenuation but may increase vibrational response.

Fuller and Jones (1987) applied active vibration control using a single shaker to reduce the interior noise field of a cylinder excited by an exterior monopole. While global control was achieved at resonance, off-resonance control exhibited spillover into uncontrolled shell modes, some of which were well coupled into the interior acoustic field resulting in increased noise levels in some areas. Further analysis showed that only the shell modes which couple well into the interior acoustic field need to be controlled for effective reduction of interior noise levels. Also, global attenuation was achieved using only one point source compared to the distributed nature of the disturbance field. These results demonstrated that a low number of vibration control sources could effectively reduce the low frequency interior noise field of a cylinder.

Several experiments have been performed on reverberant noise transmission through clamped single plates. Thomas, et al. (1990) used point force vibration control actuators and achieved 3-17 dB reduction in cost function which was defined as the sum of the squares of the pressure amplitude at 24 control microphones over a frequency range of 80 to 100 Hz. It was noticed that the effect of control position was not significant near the structural resonance, however as frequency increases, the position of a single control force became critical. While significant global reductions in the transmitted noise field were achieved with a single control actuator for on-resonance excitation, off-resonance reductions have been poor due to the increased number of

modes in the plate response even at very low frequencies. An increase in the number of control actuators was seen to improve performance.

Zhou (1992) used one to three piezoceramic control actuators and achieved significant reduction (up to 20 dB) at three error microphones over a frequency range of 350 to 900 Hz. Again, significant global reductions in the transmitted noise field were achieved for on-resonance excitation, while off-resonance reductions have been poor due to the high number of excited modes present in the plate response.

Simpson, et al. (1991) applied vibration control inputs (shakers) to a realistic aircraft fuselage. Using microphones as error sensors, an average of 4-13 dB of attenuation was attained depending on source location, control actuator location and the number of error sensors. However, due to the more complex interior acoustic field of the realistic structure, there was some spillover at one or more of the microphone locations for most of the test cases. This was attributed to the spectrally white excitation provided by point force control sources.

Fuller, et al. (1990) applied piezoelectric actuators to an aluminum cylinder of dimensions 0.508 m diameter, 1.245 m long and 1.63 mm thick modeling an aircraft fuselage. Experiments were performed on the bare cylinder and with a floor installed at a structural resonance and an acoustic resonance covering a frequency range of 260 to 666 Hz. Global attenuations of the interior acoustic field on the order of 10 dB were experimentally demonstrated. At structural resonances, attenuation of the interior acoustic field was achieved using one control actuator. However, at acoustical resonances, two control actuators were required due to the high modal density of the

acoustic cavity. Increased vibration levels of the controlled cylinder was also noticed at the acoustical resonances. The structural resonance exhibited the control mechanism *modal suppression* and the acoustical resonance exhibited the control mechanism *modal restructuring*. It was also noticed that the structural and acoustic response exhibited increased damping with the addition of the floor.

Silcox, et al. (1992) subsequently demonstrated active control of interior noise using PZT actuators mounted on a large-scale composite fuselage model of dimensions 1.68 m diameter, 3.66 m long and 1.7 mm thick stiffened by stringers and ring frames with a plywood floor rigidly mounted the ring frames. Error sensors were distributed within the interior acoustic field. Control actuators were attached to the skin and the ring frame. At 136 Hz where the interior acoustic response is driven by the structural resonant mode, an average of 8 dB reduction in the interior noise field was achieved using skin mounted actuators while shell vibration levels were mostly reduced. The poor acoustic performance was attributed to the coupling of the control system into the residual acoustic modes. At 172 Hz where the structural acoustic response is dominated by the acoustic resonant mode, both skin and ring frame mounted actuators produced 12 dB of attenuation of the interior noise field and increased local vibration levels of the skin. For the skin mounted actuators, the increased vibration levels were attributed to the small size of the actuators and control spillover into higher order modes. Therefore mounting the control actuators on the fuselage leads to a concern of structural fatigue. This was verified in an analytical model by Thomas (1992).

Experiments have also been performed on active control of reverberant sound transmission

through double panel systems. Grosveld, et al. (1991) applied acoustic control inputs to the cavity in between the double panel system. This concept was experimentally verified in a transmission loss test facility where 8.2 dB of global attenuation was achieved. Verification in a realistic aircraft fuselage test facility showed spillover in some areas while good attenuation was achieved near the error microphones. Attenuation became less global when 1) fewer control speakers were used 2) fewer error microphones were used and 3) the excitation frequency increased from 100 Hz to 250 Hz.

Thomas (1992) applied electromagnetic shakers acting between a double panel system consisting of a clamped steel plate and four aluminum honeycomb composite panels mounted in a flexible gasket. This arrangement allowed the composite panels to vibrate in a rigid body mode. Attenuations up to 15 dB in sound pressure difference were attained over a frequency range of 80 to 300 Hz using a single frequency controller. It was noticed that the passive sound pressure isolation of the double panel system was relatively high. With the application of control, it was theorized that the structural flanking path through the separation wall transmission loss test facility started to dominate the noise transmission path thereby resulting in reduced control performance at some frequencies.

Carneal and Fuller (1995c) performed an experimental investigation on the influence of the location of the piezoelectric control actuators (incident vs. radiating panel) and radiating panel stiffness on double panel transmission loss. The incident plate was a thin aluminum plate. Two radiating panels were tested, one relatively flexible made of G10 fiberglass and one relatively stiff made of fiberglass sandwich board. It was found that the application of the control inputs to



the radiating panel resulted in greater transmission loss (TL) due to its direct effect on the nature of the structural-acoustic coupling between the radiating panel and the radiated acoustic field. A double panel system with a stiffer radiating panel resulted in increased controlled TL due to a lower modal density. A radiating plate with this low modal density also has a greater stiffness to weight ratio resulting in increased uncontrolled TL.

In summary, the application of the control actuators to the fuselage skin and/or frame rings may be hindered by the increased vibration levels. As an alternative approach, the application of the control actuators to the interior trim has been investigated. However, global control using double panel systems was seen to decrease with decreasing control system order and increasing excitation frequency. In addition, the inherent damping added to the interior acoustic space with the addition of realistic interiors to an aircraft, it is evident that global control of a realistic aircraft fuselage will require a large number of actuators and sensors. Therefore, the next section will review the basic control approach and present its advantages and limitations.

## **1.2. Basic control approach**

The basic control approach used in the investigation of this thesis is a least mean squares feedforward control algorithm commonly known as the LMS algorithm (Widrow and Stearns, 1985). By introducing a control loop that is adaptive in nature, the error can now be defined as the sum of the open loop (disturbance) and the control loop. Using the assumption that the disturbance and control loops are linear, the error amplitude can be squared to form a quadratic cost function with a unique global minimum. The controller uses gradient information to adapt the control loop so the total response will be minimized. In this dissertation the disturbance is assumed to be a single frequency harmonic signal which is appropriate for propeller noise.

For application to active control of sound, the Filtered-X LMS control algorithm has been demonstrated as a robust and effective algorithm (Elliot, et al., 1987). The gradient is approximated as the product of the error signal and the filtered reference signal. The filtered reference signal is generated by passing the reference signal through a digital filter representing the mechanical system behavior, which is provided by a system identification done on-line prior to the invocation of the algorithm.

Recently, the speed of the digital signal processors (DSP) upon which these algorithms have been implemented has increased to the point that a time averaged gradient (TAG) method can be used effectively. In this method, the gradient is calculated from the finite difference approximation of the time averaged cost function. Therefore no system identification is required to implement this algorithm which is a distinct advantage. However, the speed of adaptation is inherently slower than the Filtered-X LMS algorithm. Both the Filtered-X LMS and the TAG LMS algorithms will be discussed in detail in Chapter 3.

As mentioned in the previous section, global control of complex structures (i.e. aircraft fuselage or interior trim) will require a large number of control actuators and sensors. For the Filtered-X LMS algorithm, the high number of control channels has a number of problems mainly associated with memory requirements and computational time in the hardware systems used to implement the control. In addition, collinearity of transducer transfer functions causes stability problems in systems with a high number of transducers. These problems are mainly the result of the inherent structure of the Filtered-X LMS algorithm where every control channel converges

simultaneously. Using the TAG LMS algorithm solves the above problems, however each control channel is now updated independently, which leads to long convergence times for a large number of control channels.

One possible solution for the problems mentioned above is the use a control system based on a hierarchical control structure. Carneal and Fuller (1993, 1995a) developed the biologically inspired (BIO) control approach which based on the TAG LMS algorithm and used a hierarchical control structure to shorten convergence times. The control approach was inspired by the hierarchy of biological natural systems used to initiate movement in a muscle. This hierarchy will be discussed further in Chapter 3.

### **1.3. Scope and objectives**

The intent of this investigation is to investigate and demonstrate the general trends and principles of active structural acoustic control when applied to double panel systems and determine the advantages and limitations of this approach. This includes the application of a novel hierarchical control approach. This research was initiated by an interest in reducing the interior noise levels that are produced as a result of advanced technology turboprop and turbofan engines by active noise control .

The system to be studied is a double panel model consisting of two rectangular, uniform, flat plates separated by a sealed air cavity. This double panel system model approximates the behavior of an aircraft fuselage and interior trim. The disturbance is an oblique acoustic plane wave that is assumed to be steady state, single frequency and sinusoidal which is an approximation of the exterior acoustic field generated by an advanced turboprop engine. The

double panel system vibration radiates energy into an acoustic free field which approximates a highly damped interior acoustic space of the fuselage. Control inputs are provided by piezoelectric transducers that are mounted directly on the double panel system incident or radiating plates. Error sensors are microphones placed in the acoustic free field. The cost function is defined as the total radiated sound power into an acoustic free field surrounding the radiating plate.

Specifically, the objectives of this investigation are:

1) Study the application of active structural acoustic control to double panel systems:

- Develop a model for investigating active control with structural control inputs and an acoustic cost function of double panel systems. Although most of the component models are presently available, double panel system excitation from the radiating panel must be derived and the models must then be combined.
- Study the influence of double panel system parameters on control performance. Variations of the double panel and active control system are presented including the radiating plate stiffness, the application of PZT actuators to the incident or radiating plates, the oblique angle of incident plane wave, and air cavity mass and stiffness.

2) Apply the biologically inspired (BIO) hierarchical controller to the double panel system.

- Study the influence of the number of control actuators and the master actuator number on the various local rules.
- Compare computational effort and stability aspects of the BIO and Filtered-X LMS

controllers.

This investigation will be carried out analytically with experimental verification. Experiments were performed in the Transmission Loss Test Facility at Virginia Tech which consists of two reverberation chambers separated by a common wall. The experimental investigation will be discussed further in Chapter 4.

Analytically, control was implemented using linear quadratic optimal control theory (LQOCT) for active structural acoustic control to double panel systems (objective 1 above). Due to its structure which will be discussed later, the BIO algorithm was analytically implemented using the least mean squares (LMS) algorithm. Experimentally, control was implemented using the Filtered-X LMS for active structural acoustic control to double panel systems (objective 1 above). Again due to its inherent structure, the BIO algorithm was experimentally implemented using the TAG LMS algorithm.

#### **1.4. Organization**

The study of active control of double panel systems is inter-disciplinary concentrating on the subjects of acoustics, control theory, and structural vibrations. First, the basic mathematical models for structural vibrations of double panel systems and acoustics are presented in Chapter 2. The development of the BIO controller is presented in Chapter 3, which starts with LMS control theory as a basis. The experimental investigation of double panel systems is presented in Chapter 4 including the experimental setup, the performance metrics and the experimental procedure. Results from the analytical investigation are presented in Chapter 5 while results from the experimental investigation are presented in Chapter 6. Conclusions and recommendations are

then presented in Chapter 7.

Some notes on terminology should be mentioned. In acoustics, sound transmits through a *panel* or a *plate*, depending upon the author. In vibrations, a *plate* vibrates. Since these terms are somewhat interchangeable, the following conventions will be used. The *double panel system* consists of an *incident plate* and a *radiating plate*. By this definition the concerns of both the acoustics and vibrations professionals will be addressed.

In this dissertation there are a multitude of figures and tables presented. Therefore all of the figures and tables were positioned at the end of the section in which they were presented. This has been done to avoid fragmenting the text and make the dissertation more readable.

## **2. Structural and Acoustic Models**

Double panel system structural and free field acoustic models used in this investigation are reviewed in this chapter.

### **2.1. Structural models**

Double panel system structural models are presented. The general assumptions are 1) the system has a steady state sinusoidal response 2) the spatial response of all of the governing equations can be represented by an infinite series of eigenfunctions. Therefore, the response can be written as a homogeneous solution of the modal amplitudes and eigenvectors. The modal amplitudes are then determined by the application of a specific forcing function.

#### **2.1.1. Single plate**

The following derivations are based on classic thin-plate theory, which assumes that the rotation of the differential element is much less than the vertical translation and the shear deformation is much less than the bending deformation. These assumptions have been proven valid if the length to thickness ratio of the plate is greater than ten (Meirovitch, 1986). Using these assumptions, the governing equation of motion of an isotropic plate can be written as:

$$m\ddot{w} + C\dot{w} + D\nabla^4 w = 0 \quad (2.1)$$

where  $w$  is the out-of-plane displacement,  $m$  is the mass per unit area of the plate:

$$m = \rho h \quad (2.2)$$

$\rho$  and  $h$  are the density and the thickness of the plate, respectively. The flexural stiffness ( $D$ ) is written:

$$D = \frac{Eh^3}{12(1-\nu^2)} \quad (2.3)$$

where  $E$  is the modulus of elasticity and  $\nu$  is Poisson's ratio of the plate. The damping coefficient ( $C$ ) is a known quantity and  $\nabla^4$  is the square of the Laplacian operator:

$$\nabla^4 = \frac{\partial^4}{\partial x^4} + 2\frac{\partial^4}{\partial x^2\partial y^2} + \frac{\partial^4}{\partial y^4} \quad (2.4)$$

The coordinate system for a single plate is shown in Figure 2-1.

Upon specification of the boundary conditions, the boundary value problem will be complete. For a simply supported plate, the deflection and the bending moment are zero at the boundary, which can be written as:

$$\begin{aligned} w(x, y) = \frac{\partial^2 w(x, y)}{\partial x^2} = 0 & \quad x = 0, l_x \\ w(x, y) = \frac{\partial^2 w(x, y)}{\partial y^2} = 0 & \quad y = 0, l_y \end{aligned} \quad (2.5)$$

The boundary value problem can be solved by the separation of variables technique. A general solution that will satisfy the boundary conditions is assumed and substituted into the equation of motion and the boundary conditions. This yields the characteristic equation which can then be solved for the eigenvalues (natural frequencies). The eigenvalues of a simply supported plate can be written as:



$$\omega_{mn} = \left(\frac{D}{m}\right)^2 (\alpha_m^2 + \alpha_n^2) \quad (2.6)$$

where  $\alpha_m = m\pi/l_x$  and  $\alpha_n = n\pi/l_y$ .

The free vibration flexural response of a lightly damped simply supported plate can then be written as a series of infinite eigenfunctions:

$$w(x, y, t) = \sum_{m=1}^{\infty} \sum_{n=1}^{\infty} W_{mn} \sin(\alpha_m x) \sin(\alpha_n y) e^{j\omega t} \quad (2.7)$$

where the modal amplitudes ( $W_{mn}$ ) are determined by the application of a specific forcing function. It should be noted that an infinite sum is impractical to calculate, therefore the modal summation was limited to a finite number of modes.

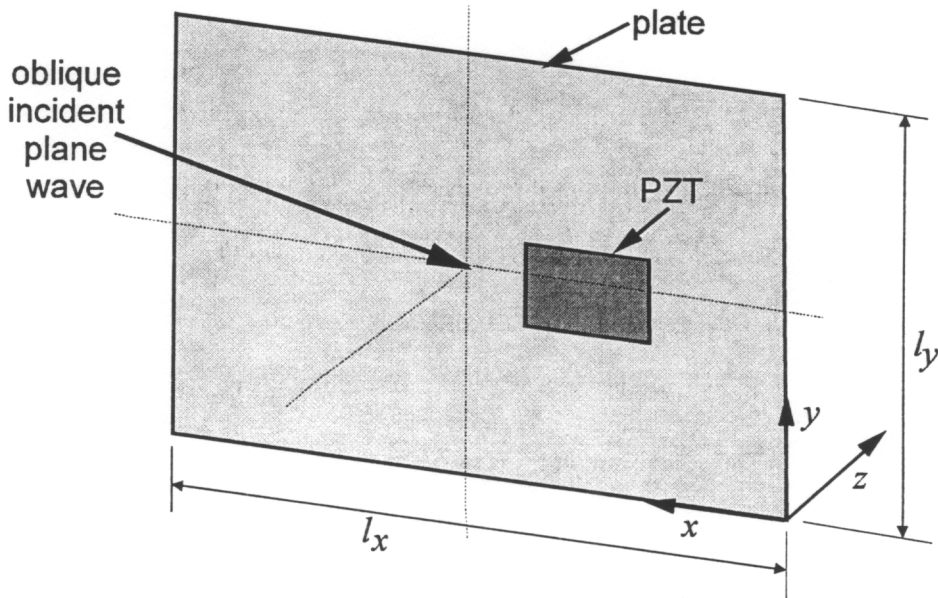


Figure 2-1. Single plate coordinate system

### 2.1.2. Double panel system

The following derivations are based on those originally performed by Vaicaitis (1983) and the reader is referred to this reference for specifics. The double panel system considered in this investigation consists of two single plates separated by an air cavity as seen in Figure 2-2. This configuration approximates the fuselage (incident plate) and internal trim (radiating plate) of modern aircraft. The air cavity between the two plates can be analytically described as a uniformly distributed linear air spring ( $K_s$ ) which acts on the relative displacement of the two plates. This assumption is valid well below the first transverse resonance (in the z-direction in Figure 2-2) of the air cavity. The governing equations of motion for the double panel system can be written as:

$$\begin{aligned} m_i \ddot{w}_i + C_i \dot{w}_i + D_i \nabla^4 w_i + K_s (w_i - w_r) + \left(\frac{1}{3}\right) m_s \ddot{w}_i + \left(\frac{1}{6}\right) m_s \ddot{w}_r &= 0 \\ m_r \ddot{w}_r + C_r \dot{w}_r + D_r \nabla^4 w_r + K_s (w_r - w_i) + \left(\frac{1}{3}\right) m_s \ddot{w}_r + \left(\frac{1}{6}\right) m_s \ddot{w}_i &= 0 \end{aligned} \quad (2.8)$$

where

$$\nabla^4 = \frac{\partial^4}{\partial x^4} + 2 \frac{\partial^4}{\partial x^2 \partial y^2} + \frac{\partial^4}{\partial y^4} \quad (2.9)$$

$$\begin{aligned} m_i &= \rho_i h_i \\ m_r &= \rho_r h_r \\ m_s &= \rho_s h_s \end{aligned} \quad (2.10)$$

$$\begin{aligned} D_i &= \frac{E_i h_i^3}{12(1-\nu_i^2)} \\ D_r &= \frac{E_r h_r^3}{12(1-\nu_r^2)} \end{aligned} \quad (2.11)$$

where  $w_i$  and  $w_r$  are the flexural displacements of the incident and radiating plates, respectively.

Subscripts  $i, r$ , and  $s$  denote the incident plate, the radiating plate and the air space, respectively.

The air spring ( $K_s$ ) is modeled as a linear elastic spring with no damping:

$$K_s = \frac{E_s}{h_s} = \frac{\rho_s c^2}{h_s} \quad (2.12)$$

(where  $c$  is the speed of sound in air) which acts on the relative displacement of the two plates. It was assumed that the inertial force varied linearly across the air space and therefore the air inertia terms ( $m_s/3$  and  $m_s/6$ ) were apportioned to the individual plates. Webster's dictionary (1981) defines apportioned as "to divide and assign in just proportion according to a definite rule." Therefore, the mass of the air cavity was divided and assigned to the individual plates. For further explanation of this concept, the reader is referred to Vaicaitis (1983).

The flexural response of the individual plates can be written as the summation of the product of the modal amplitudes and the eigenvectors which satisfy the simply supported boundary conditions:

$$\begin{aligned} w_i(x, y, t) &= \sum_{m=1}^{\infty} \sum_{n=1}^{\infty} W_{mn}^i \sin(\alpha_m x) \sin(\alpha_n y) e^{j\omega t} \\ w_r(x, y, t) &= \sum_{m=1}^{\infty} \sum_{n=1}^{\infty} W_{mn}^r \sin(\alpha_m x) \sin(\alpha_n y) e^{j\omega t} \end{aligned} \quad (2.13)$$

where  $W_{mn}^i$  and  $W_{mn}^r$  are the modal amplitudes for the incident and radiating plates, respectively.

Substituting Eq. (2.13) into Eq. (2.8) and utilizing the orthogonality principle yields a set of coupled differential equations in  $W_{mn}^i$  and  $W_{mn}^r$ .

After algebraic manipulation, the frequency response functions ( $\Theta_{mn}^{i,r}$  defined as the ratio of the

structural response to the forcing function modal amplitudes) can be written for a forcing function acting on the incident plate as:

$$\Theta_{mn}^i = \frac{X_{mn}^i}{1 - \left( \frac{E_s}{h_s} + \omega^2 b_s \right)^2 \left( \frac{X_{mn}^i}{m_i} \right) \left( \frac{X_{mn}^r}{m_r} \right)} \quad (2.14)$$

$$\Theta_{mn}^r = \Theta_{mn}^i \left( \frac{E_s}{h_s} + \omega^2 b_s \right)^2 \left( \frac{X_{mn}^r}{m_r} \right)$$

and for a forcing function acting on the radiating plate:

$$\Theta_{mn}^r = \frac{X_{mn}^r}{1 - \left( \frac{E_s}{h_s} + \omega^2 b_s \right)^2 \left( \frac{X_{mn}^i}{m_i} \right) \left( \frac{X_{mn}^r}{m_r} \right)} \quad (2.15)$$

$$\Theta_{mn}^i = \Theta_{mn}^r \left( \frac{E_s}{h_s} + \omega^2 b_s \right)^2 \left( \frac{X_{mn}^i}{m_i} \right)$$

where:

$$X_{mn}^i = \left[ (\omega_{mn}^i)^2 - \left( \frac{a_i}{m_i} \right) \omega^2 + 2j\omega_{mn}^i \omega \eta_{mn}^i + \frac{E_s}{h_s m_i} \right]^{-1} \quad (2.16)$$

$$X_{mn}^r = \left[ (\omega_{mn}^r)^2 - \left( \frac{a_r}{m_r} \right) \omega^2 + 2j\omega_{mn}^r \omega \eta_{mn}^r + \frac{E_s}{h_s m_r} \right]^{-1}$$

$$a_i = m_i + \frac{m_s}{3} \quad a_r = m_r + \frac{m_s}{3} \quad b_s = \frac{m_s}{6} \quad (2.17)$$

In the above equations  $\eta$  is the structural damping coefficient,  $\omega$  is the excitation frequency and  $\omega_{mn}^i$ ,  $\omega_{mn}^r$  are the uncoupled natural frequencies of the incident and radiating plates, respectively, defined as:

$$\begin{aligned}\omega_{mn}^i &= \left(\frac{D_i}{m_i}\right)^2 (\alpha_m^2 + \alpha_n^2) \\ \omega_{mn}^r &= \left(\frac{D_r}{m_r}\right)^2 (\alpha_m^2 + \alpha_n^2)\end{aligned}\tag{2.18}$$

The natural frequencies of the double panel system can be determined by setting the damping to zero and maximizing the frequency response functions in Equations (2.14) and (2.15):

$$\omega_{mn} = \sqrt{\frac{B_{mn} \pm \sqrt{B_{mn}^2 - 4AC_{mn}}}{2A}}\tag{2.19}$$

where

$$\begin{aligned}A &= a_i a_r - b_s^2 \\ B_{mn} &= \left(m_i \omega_{mn}^i + \frac{E_s}{h_s}\right) a_r + \left(m_r \omega_{mn}^r + \frac{E_s}{h_s}\right) a_i + 2b_s \frac{E_s}{h_s} \\ C_{mn} &= \left(m_i \omega_{mn}^i + \frac{E_s}{h_s}\right) \left(m_r \omega_{mn}^r + \frac{E_s}{h_s}\right) - \left(\frac{E_s}{h_s}\right)^2\end{aligned}\tag{2.20}$$

These equations give two real eigenvalues for each set of modal indices. The lesser of the two represents the in-phase flexural response and greater of the two represents the out-of-phase dilatation response of the double panel system. Physically, the in-phase flexural response is when the displacement of the two plates comprising the double panel system is in-phase, i.e. both plates travel in the positive z-direction at the same instant. The out-of-phase dilatational response is when the displacement of the two plates is out-of-phase, i.e. one plate travels in the positive z-direction and the other travels in the negative z-direction. This last response was apparently named by Vaicaitis (1983) due to the expansion and contraction of the air cavity as dilatation is defined as “the act of expanding” (Webster’s, 1981). Physically, there is little or no relative

displacement between the individual plates which means that the spring rate of the acoustical cavity has little effect for the in-phase flexural motion. For the out-of-phase dilatational motion, the relative displacement between the plates is significant and the increased stiffness (due to the spring rate of the acoustical cavity) of the system results in an increased natural frequency. This will be discussed further in the analytical results (Chapter 5).

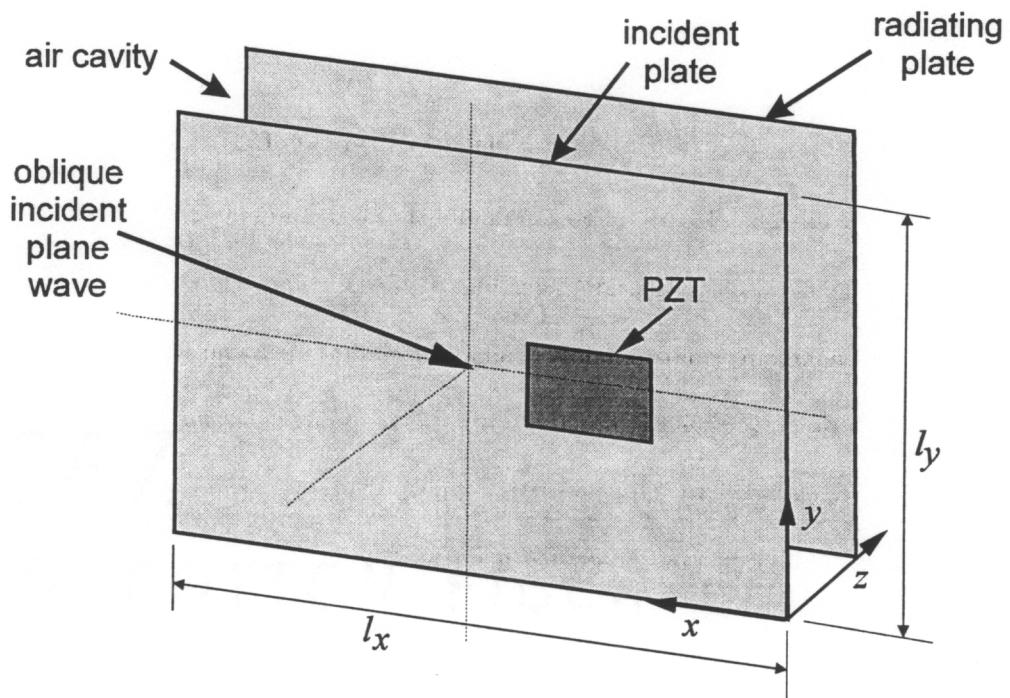


**Figure 2-2. Double panel system coordinate system**

### 2.1.3. Clamped boundary conditions

The above analyses were performed for simply supported boundary conditions. To be able to experimentally verify the models, simply supported boundary conditions are difficult if not impossible to implement for determining transmission loss. The accepted method for experimentally investigating transmission loss includes plates mounted in a frame that

approximates clamped boundary conditions and allows no acoustical transmission path. This method also reduces other factors such as structure-borne flanking transmission paths which can taint the results of the transmission loss experiments. Due to the above conditions, the theoretical models must be modified to approximate clamped boundary conditions.

Although simply supported mode shapes have been shown to be a good approximation of clamped mode shapes (Vaicaitis, 1983) (Leissa, 1993) the associated simply supported natural frequencies are incorrect due to the lack of stiffness inherent to the simply supported boundary conditions compared to the clamped boundary conditions. As an approximation, the stiffness of the simply supported plate can be increased by  $\sqrt{2}$  for each boundary (Vaicaitis 1983) to approximate the clamped boundary conditions and therefore the natural frequencies will more accurately represent clamped boundary conditions. This has been shown to have little effect on the validity of the theoretical model (Vaicaitis 1983) since the associated modal radiation efficiencies of clamped and simply supported plates has been shown to be directly proportional (Berry, et al. ,1990).

#### 2.1.4. Sandwich board stiffness

Since the sandwich board is isotropic but not a homogeneous material with respect to thickness, the sandwich board flexural stiffness can be approximated by (Hexcel, 1986) :

$$D = \frac{Eth^2}{2(1-\nu^2)} \quad (2.21)$$

where  $t$  is the thickness of the sandwich board skin and  $h$  is the thickness of the entire sandwich board. It should be noted that all of the properties are for the sandwich board skin and do not

include the stiffness of the inner core since it is assumed the inner core does not contribute to the flexural stiffness. For further information, the reader is referred to the above reference.

## 2.2. Acoustic models

### 2.2.1. Incident pressure field

The incident pressure field is assumed to be an oblique incident plane wave which impinges on the incident side of the single plate or the incident plate of the double panel system. The mathematical expression for the plane wave can be written as (Roussos, 1985):

$$p_i(x, y, t) = P_i \exp[j(\omega t - kx \sin \theta_i \cos \phi_i - ky \sin \theta_i \sin \phi_i - kz \cos \theta_i)] \quad (2.22)$$

where  $P_i$  is the blocked pressure magnitude and  $\theta_i, \phi_i$  are the incident angles in spherical coordinates shown in Figure 2-3. Further discussion of the incident pressure field as a forcing function is presented in the next section.

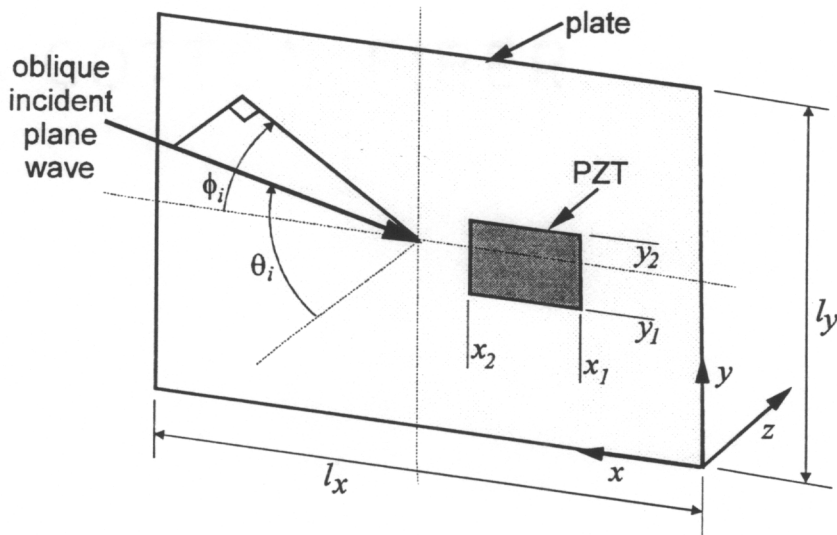


Figure 2-3. Incident pressure field and piezoelectric actuator coordinate system



The incident intensity is the amount of intensity that is normal to the plate:

$$I_i = \frac{P_i^2 \cos \theta_i}{2\rho c} \quad (2.23)$$

The incident acoustic power is the incident intensity times the area of the plate:

$$\Pi_i = \frac{P_i^2 \cos \theta_i l_x l_y}{2\rho c} \quad (2.24)$$

### 2.2.2. Radiated pressure field

The radiated pressure field emits from the radiating side of a single plate or the radiating plate of a double panel system. The equation for the radiated pressure from a plate is derived from the model of the radiated pressure from an elementary volume source mounted in an infinite rigid baffle. From an acoustical viewpoint, the motion of the plate can be seen as a multitude of these elementary volume sources. Therefore, the total radiation from a plate can be found by integrating the radiated pressure from an elementary volume source over the domain of the plate seen in Figure 2-4. The result is the well known Rayleigh integral for a plate which is written as (Roussos, 1985):

$$p_r(r, \theta, \phi) = \int_{x'=-l_x/2}^{l_x/2} \int_{y'=-l_y/2}^{l_y/2} \frac{j\rho_o \omega}{2\pi r'} \frac{\partial w(x', y', t)}{\partial t} \exp\left(\frac{-j\omega r'}{c}\right) dy' dx' \quad (2.25)$$

where  $x' = x - l_x / 2$  and  $y' = y - l_y / 2$ . This formulation is valid if the source dimension is small compared to the wavelength ( $kd \ll 1$ ).

Utilizing the far field approximation

$$\frac{1}{r'} \approx \frac{1}{r} \quad (2.26)$$

and

$$\exp(-jkr') \approx \exp\left[-jkr\left(1 - \frac{\sin\theta \cos\phi}{r}x' - \frac{\sin\theta \sin\phi}{r}y'\right)\right] \quad (2.27)$$

the far field radiated/transmitted pressure can be given by:

$$p_r(r, \theta, \phi) = \frac{j\omega\rho_o}{2\pi r} \int_{x'=-l_x/2}^{l_x/2} \int_{y'=-l_y/2}^{l_y/2} \frac{\partial w(x', y', t)}{\partial t} \exp\left[-jkr\left(1 - \frac{\sin\theta \cos\phi}{r}x' - \frac{\sin\theta \sin\phi}{r}y'\right)\right] dy' dx' \quad (2.28)$$

Since the plate motion is assumed to have the form as described in Eq. (2.13), the velocity can be written as:

$$\frac{\partial w(x, y, t)}{\partial t} = j\omega w(x, y, t) \quad (2.29)$$

therefore a closed form solution for the Rayleigh integral is (Roussos, 1985):

$$p_r(r, \theta, \phi) = -\frac{\omega^2 \rho_o l_x l_y}{2\pi r} \exp\left\{j\omega\left[t - \frac{r}{c} - \frac{\sin\theta}{2c}(l_x \cos\phi + l_y \sin\phi)\right]\right\} \sum_{m=1}^{\infty} \sum_{n=1}^{\infty} W_{mn} Y_m Y_n \quad (2.30)$$

where

$$Y_m = \begin{cases} -\frac{j}{2} \text{sgn}(\sin\theta_r \cos\phi_r) & ((m\pi)^2 = [\sin\theta_r \cos\phi_r (\omega l_x / c)]^2) \\ \frac{m\pi \{1 - (-1)^m \exp[-j \sin\theta_r \cos\phi_r (\omega l_x / c)]\}}{(m\pi)^2 - [\sin\theta_r \cos\phi_r (\omega l_x / c)]^2} & ((m\pi)^2 \neq [\sin\theta_r \cos\phi_r (\omega l_x / c)]^2) \end{cases}$$

$$Y_n = \begin{cases} -\frac{j}{2} \text{sgn}(\sin\theta_r \cos\phi_r) & ((n\pi)^2 = [\sin\theta_r \cos\phi_r (\omega l_y / c)]^2) \\ \frac{n\pi \{1 - (-1)^n \exp[-j \sin\theta_r \cos\phi_r (\omega l_y / c)]\}}{(n\pi)^2 - [\sin\theta_r \cos\phi_r (\omega l_y / c)]^2} & ((n\pi)^2 \neq [\sin\theta_r \cos\phi_r (\omega l_y / c)]^2) \end{cases}$$

(2.31)

As a result of the far field assumption, the pressure wave can be locally approximated by a plane wave. Therefore the far field intensity at a point can be written as:

$$I_r = \frac{|p_r(r, \theta, \phi)|^2}{2\rho c} \quad (2.32)$$

The total radiated power is defined as the integral of the far field intensity over a hemisphere enclosing and centered on the baffled plate which can be written as:

$$\Pi_r = \int_{\phi=0}^{2\pi} \int_{\theta=0}^{\pi/2} I_r r^2 \sin\theta d\theta d\phi \quad (2.33)$$

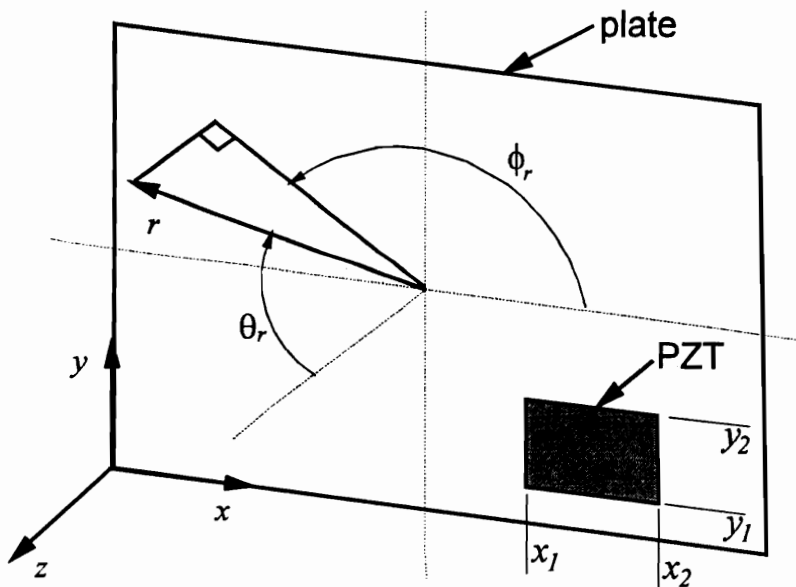


Figure 2-4. Radiating pressure field and piezoelectric actuator coordinate system

### 2.2.3. Transmission Loss

The plate transmission loss is defined as (Fahy, 1985):

$$TL(dB) = 10 \log_{10} \left( \frac{1}{\tau} \right) = 10 \log_{10} \left( \frac{\Pi_i}{\Pi_r} \right) \quad (2.34)$$

where  $\tau$  is defined as the transmission coefficient which is defined as  $\Pi_r/\Pi_i$ .

For engineering design, it is useful to have a single acoustic performance index that can be compared. Therefore, the transmission loss will be averaged over a frequency range. This index is more applicable than the total power reduction since the disturbance is tonal in nature. The frequency averaged transmission loss is defined as:

$$TL_{avg}(dB) = 10 \log_{10} \left( \frac{\Pi_{i,avg}}{\Pi_{r,avg}} \right). \quad (2.35)$$

where the frequency averaged acoustic power is defined as:

$$\Pi_{avg} = \frac{1}{N} \sum_{n=1}^N \Pi_n \quad (2.36)$$

where  $N$  is the number of frequency bins. Note that this assumes the transmission loss data is discrete over the frequency range. The frequency averaged acoustic power is a linear average of the auto-spectrum which denotes the average power over a frequency range. Note that the analytical results in Chapter 5 are presented in terms of frequency averaged transmission loss.

### 2.2.4. Air cavity resonances

The air cavity separating the incident and radiating plates of the double panel system has acoustical resonances that are not accounted for in the double panel system model above since

the air mass was apportioned to the incident and radiating plates as explained previously in Section 0. Determining these resonances may help explain some of the double panel system behavior. The air cavity resonances for a rigid wall box of the same dimensions can be written as (Kinsler, et al, 1982):

$$\omega_{mnk} \text{ (Hz)} = \frac{c}{2\pi} \sqrt{\left(\frac{m\pi}{l_x}\right)^2 + \left(\frac{n\pi}{l_y}\right)^2 + \left(\frac{k\pi}{l_z}\right)^2}. \quad (2.37)$$

## 2.3. Plate forcing functions

### 2.3.1. Incident pressure field

When the incident pressure field impinges on the plate, there are two traveling waves on the negative z side of the plate (see Figure 2-3), the incident pressure and the reflected pressure. Conversely, on the positive z side of the plate, there is one traveling wave, the radiated pressure. In previous analyses, it was found that the incident and reflected pressure wave magnitudes can be assumed equal since the impedance of the plate approximates a rigid boundary for air loading (Fahy, 1985). Therefore, the pressure exciting the plate is assumed to be the *blocked* pressure which is twice the magnitude of the incident wave. The inclusion of the radiated pressure into the solution of the non-homogeneous solution of the plate motion produces a very complicated equation known as the *fluid loaded* plate equation. However when the fluid is air, it was found that the transmitted pressure was negligible compared to the blocked pressure (Roussos, 1985). Without the radiated pressure term, the equation of motion of the plate can readily be solved for the *in-vacuo* (which is sometimes called *light fluid loaded*) case.

As stated earlier, the forcing function can be decomposed into an infinite series of

eigenfunctions. Using the coordinate system in Figure 2-3 , the blocked pressure ( $p_b$ ) can be represented as:

$$p_b = 2p_i(x, y, t) = P_i \exp[j(kx \sin \theta_i \cos \phi_i - kys \sin \theta_i \sin \phi_i)] = \sum_{m=1}^{\infty} \sum_{n=1}^{\infty} p_{mn}^d \sin(\alpha_m x) \sin(\alpha_n y) \quad (2.38)$$

where  $p_{mn}$  is given by:

$$p_{mn}^d = \frac{8P_i}{l_x l_y} \int_{x=0}^{l_x} \int_{y=0}^{l_y} \exp[j(kx \sin \theta_i \cos \phi_i - ky \sin \theta_i \sin \phi_i)] \sin(\alpha_m x) \sin(\alpha_n y) dy dx \quad (2.39)$$

This integration has a closed form solution:

$$p_{mn}^d = 8P_i Y_m Y_n \quad (2.40)$$

where  $Y_m$  and  $Y_n$  were defined as:

$$Y_m = \begin{cases} -\frac{j}{2} \text{sgn}(\sin \theta_i \cos \phi_i) & ((m\pi)^2 = [\sin \theta_i \cos \phi_i (\omega l_x / c)]^2) \\ \frac{m\pi \{1 - (-1)^m \exp[-j \sin \theta_i \cos \phi_i (\omega l_x / c)]\}}{(m\pi)^2 - [\sin \theta_i \cos \phi_i (\omega l_x / c)]^2} & ((m\pi)^2 \neq [\sin \theta_i \cos \phi_i (\omega l_x / c)]^2) \end{cases}$$

$$Y_n = \begin{cases} -\frac{j}{2} \text{sgn}(\sin \theta_i \cos \phi_i) & ((n\pi)^2 = [\sin \theta_i \cos \phi_i (\omega l_y / c)]^2) \\ \frac{n\pi \{1 - (-1)^n \exp[-j \sin \theta_i \cos \phi_i (\omega l_y / c)]\}}{(n\pi)^2 - [\sin \theta_i \cos \phi_i (\omega l_y / c)]^2} & ((n\pi)^2 \neq [\sin \theta_i \cos \phi_i (\omega l_y / c)]^2) \end{cases} \quad (2.41)$$

Note that the above expression is the same as defined in Eq. (2.31) except for those angles are radiating coordinates where Eq. (2.41) uses incident coordinates.

The modal amplitudes can now be written for a double panel system by multiplying the modally

decomposed disturbance (Eq. (2.40)) by the frequency response function for a forcing function acting on the incident plate (Eq. (2.14)):

$$\begin{aligned} W_{mn}^{d,i} &= p_{mn}^d \Theta_{mn}^i \\ W_{mn}^{d,r} &= p_{mn}^d \Theta_{mn}^r \end{aligned} \quad (2.42)$$

### 2.3.2. Piezoelectric actuator

Piezoelectric plate actuators generally consist of a lead zirconate titanate (PZT) actuator co-located pair (on each side of the plate) wired out of phase to produce pure bending in the structure. Their forcing function can be modeled as line moments applied at the PZT element boundary (Dimitriadis, et al. 1989). The resulting forcing function when applied to a simply supported plate can be written:

$$F_c(x, y, t, V) = \frac{\partial^2 m_x}{\partial x^2} + \frac{\partial^2 m_y}{\partial y^2} \quad (2.43)$$

where:

$$\begin{aligned} \frac{\partial^2 m_x}{\partial x^2} &= C_o \varepsilon_{pe} [\delta'(x - x_1) - \delta'(x - x_2)][h(y - y_1) - h(y - y_2)] \\ \frac{\partial^2 m_y}{\partial y^2} &= C_o \varepsilon_{pe} [h(x - x_1) - h(x - x_2)][\delta'(y - y_1) - \delta'(y - y_2)] \end{aligned} \quad (2.44)$$

and  $m_x$  and  $m_y$  are the moments in the  $x$  and  $y$  direction, respectively,  $C_o$  is the piezoelectric strain-plate moment coupling term,  $\varepsilon_{pe}$  is the piezoelectric strain,  $\delta'$  is the first derivative of the delta function and  $h$  is the unit step function. The coordinates for the piezoelectric actuator are presented in Figure 2-3 and Figure 2-4 for an actuator mounted on the incident and radiating plates of a double panel system, respectively.

Following the solution for the incident pressure field, the PZT forcing function can be decomposed into an infinite series of eigenfunctions. In this case, the PZT actuator can be represented as:

$$F_c(x, y, t, V) = \frac{\partial^2 m_x}{\partial x^2} + \frac{\partial^2 m_y}{\partial y^2} = \sum_{m=1}^{\infty} \sum_{n=1}^{\infty} p_{mn}^c \sin(\alpha_m x) \sin(\alpha_n y) \quad (2.45)$$

Using mode orthogonality, the modally decomposed forcing function can be written:

$$p_{mn}^c = 4C_o \varepsilon_{pe} \left( -\frac{\alpha_x^2 + \alpha_y^2}{\alpha_x \alpha_y} \right) [\cos(\alpha_x x_1) - \cos(\alpha_x x_2)] [\cos(\alpha_y y_1) - \cos(\alpha_y y_2)] \quad (2.46)$$

where

$$\varepsilon_{pe} = \frac{d_{31} V}{t} \quad (2.47)$$

$$C_o = -E \frac{(1+\nu_{pe})}{(1-\nu)} \frac{P}{1+\nu - (1+\nu_{pe})P} \frac{2h^2}{3} \quad (2.48)$$

$$P = -\frac{E_{pe} (1-\nu^2)}{E (1-\nu_{pe}^2)} K \quad (2.49)$$

$$K = \frac{3th(2h+t)}{2(h^3 + t^3) + 3ht^2} \quad (2.50)$$

and  $t$  is the thickness of the piezoelectric element. Most importantly,  $V$  is the voltage applied to the actuator. As can be seen in Eq. (2.47) the actuator in-plane strain is linearly related to the control voltage.

The modal amplitudes can now be written for a PZT actuator located on the incident plate of a double panel system by multiplying the modally decomposed disturbance (Eq. (2.46)) by the frequency response function for a forcing function acting on the incident plate (Eq. (2.14)):



$$W_{mn}^{c,i} = p_{mn}^c \Theta_{mn}^i = p_{mn}^c \frac{X_{mn}^i}{1 - \left( \frac{E_s}{h_s} + \omega^2 b_s \right)^2 \left( \frac{X_{mn}^i}{m_i} \right) \left( \frac{X_{mn}^r}{m_r} \right)} \quad (2.51)$$

$$W_{mn}^{c,r} = p_{mn}^c \Theta_{mn}^r = p_{mn}^c \Theta_{mn}^i \left( \frac{E_s}{h_s} + \omega^2 b_s \right)^2 \left( \frac{X_{mn}^r}{m_r} \right)$$

Likewise, the modal amplitudes can be written for a PZT actuator located on the radiating plate of a double panel system by multiplying the modally decomposed disturbance (Eq. (2.46)) by the frequency response function for a forcing function acting on the radiating plate (Eq. (2.15)):

$$W_{mn}^{c,r} = p_{mn}^c \Theta_{mn}^r = p_{mn}^c \frac{X_{mn}^r}{1 - \left( \frac{E_s}{h_s} + \omega^2 b_s \right)^2 \left( \frac{X_{mn}^i}{m_i} \right) \left( \frac{X_{mn}^r}{m_r} \right)} \quad (2.52)$$

$$W_{mn}^{c,i} = p_{mn}^c \Theta_{mn}^i = p_{mn}^c \Theta_{mn}^r \left( \frac{E_s}{h_s} + \omega^2 b_s \right)^2 \left( \frac{X_{mn}^i}{m_i} \right)$$

## 2.4. Total structural response

The total structural response of the system can be determined by the superposition of the system response to the disturbance (the incident pressure field in this dissertation) and the control field defined as the sum of each piezoelectric actuator response. The total modal response of the system can be written:

$$\begin{aligned} W_{mn}^{t,i} &= W_{mn}^{d,i} + \sum_{j=1}^C W_{mn}^{c_j,i} \\ W_{mn}^{t,r} &= W_{mn}^{d,r} + \sum_{j=1}^C W_{mn}^{c_j,r} \end{aligned} \quad (2.53)$$

where  $C$  is the total number of piezoelectric actuators.

## 2.5. Cost function

The stated objective is the reduction of the transmission loss of a double panel system. This is accomplished by reducing the radiated sound power from the radiating plate of a double panel system, which can be written for a baffled plate as:

$$\Pi_r = \frac{1}{\rho c} \int_0^{2\pi} \int_0^{\pi/2} |p_r(r, \theta, \phi)|^2 r^2 \sin \theta d\theta d\phi \quad (2.54)$$

where  $p_r$  is the far field pressure given in Eq. (2.28). Writing Eq. (2.54) in terms of the total modal response of the radiating plate and rearranging:

$$\Pi_r = \sum_{m=1}^{\infty} \sum_{n=1}^{\infty} \sum_{k=1}^{\infty} \sum_{l=1}^{\infty} \Delta_{mnkl} W_{mn}^{t,r} W_{kl}^{t,r*} \quad (2.55)$$

where (Song, 1995):

$$\Delta_{mnkl} = \frac{1}{\rho c} \int_0^{2\pi} \int_0^{\pi/2} A A^* Y_m Y_n Y_k^* Y_l^* r^2 \sin \theta d\theta d\phi \quad (2.56)$$

where  $Y_m$  was previously defined in Eq. (2.31) and:

$$A = -\frac{\omega^2 \rho_o l_x l_y}{2\pi r} \exp \left\{ j\omega \left[ t - \frac{r}{c} - \frac{\sin \theta}{2c} (l_x \cos \phi + l_y \sin \phi) \right] \right\}. \quad (2.57)$$

### **3. Controller development**

As stated in Section 1.2, one possible solution for the problems associated with global control of complex structures is the use of a control system based on a hierarchical control structure. Carneal and Fuller (1993, 1995a) developed the biologically inspired (BIO) hierarchical control approach which is based on the LMS algorithm and used a hierarchical control structure to shorten convergence times. The control approach was inspired by the hierarchy of biological natural systems when initiating movement. A simplified biological model can be stated as follows (Landau, 1976): A movement signal originates in a single motor neuron in the motor cortex of the brain. This signal is transmitted along an axon to diverging neuronal circuits in the spinal cord which thereby excites multiple anterior motor neurons. The signal from each of the anterior motor neurons stimulates more diverging neuronal circuits which are connected to multiple muscle fibers. In concept, a signal for movement is generated in the motor cortex of the brain and is distributed by external diverging neuronal circuits to multiple muscle fibers.

As an extreme simplification of the biological hierarchical structure, the BIO control approach uses a centralized processor to generate a control signal (analogous to the motor cortex of the brain) which is distributed by local simple learning rules (analogous to diverging neuronal

circuits) to multiple control actuators (analogous to muscle fibers). As seen in Figure 3-1, the BIO control approach has one control input chosen as the "master" which is under direction of the centralized controller. The other "slave" inputs derive their control laws by localized, simple learning rules related to the behavior of their neighbor actuators and are proportional to the centralized controller direct signal. This control structure has been successfully applied to beam vibration (Fuller and Carneal, 1993) (Carneal and Fuller, 1995a) and sound transmission through single panel structures (Carneal and Fuller, 1995b).

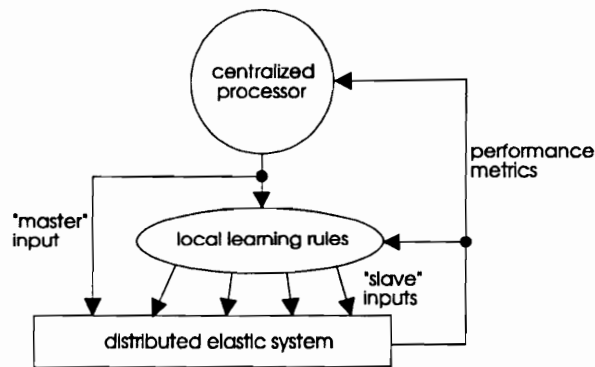


**Figure 3-1. Biologically inspired control approach**

This type of control system is a subclass of the hierarchical control approach, which is summarized as follows (Singh, 1980): The main objective of the hierarchical control system is shared by all levels. Decentralized decision making units exist at all levels due to the complexity of the main control objective, and limited information handling capabilities of each unit. Also, several of these units can operate in parallel. One can see the similarities in a hierarchical control system and a biologically inspired control system. However, there is one significant difference. In what is strictly defined as a hierarchical control approach, the time horizon of interest increases as one goes up the hierarchy, i.e. the lower levels of the hierarchy are concerned with short term goals whereas the top level of the hierarchy is concerned with long term goals.

Conversely, the time horizon of interest for the biologically inspired control system is the same for all levels (the centralized control processor and the local learning rules), while the *complexity* of the controller changes at each level. Therefore, to distinguish the approach from formal hierarchical control the approach was named "a biologically inspired" controller (Fuller and Carneal, 1993). However, the "biologically inspired" controller can be seen to be hierarchical in that the controller has different levels of operating complexity.

In this Chapter, the control system theory is developed for the biologically inspired controller, followed by a stability analysis. Linear quadratic optimal control is then discussed.

### **3.1. Theory**

The control system theory is developed for the biologically inspired controller, with an emphasis on the effects of driving multiple actuators with one main control channel. To gain insight on multiple actuator-single channel control system performance, a frequency domain LMS algorithm was used to derive the control theory since it incorporates the control path transfer functions into the update equation. The physical implementation of the LMS algorithm, commonly referred to as the Filtered-X LMS, is discussed in Section 4.2.1. First, the master control input is analyzed, followed by local rules studied in this thesis; the phase variation, adaptive magnitude, adaptive phase and optimal methods which are discussed later.

#### **3.1.1. Master control input**

The control system analysis for the master actuator is a frequency domain analysis for a single output adaptive feedforward LMS control system, following Widrow and Stearns (1985) and Boucher, et al. (1990). As seen in Figure 3-2, the complex error ( $\mathbf{e}$ ) can be described as the sum

of the primary disturbance ( $\mathbf{d}$ ) and the secondary control sources:

$$\mathbf{e}(\omega_o) = \mathbf{d}(\omega_o) + \mathbf{H}(\omega_o)\mathbf{w}(\omega_o) \quad (3.1)$$

where  $\mathbf{H}$  denotes the control loop transfer function,  $\mathbf{w}$  is the complex adaptive filter transfer function, and  $\omega_o$  is the excitation frequency. The system is assumed to be steady state and the disturbance is assumed to be single frequency harmonic, therefore the dependence of the variables on  $\omega_o$  will be dropped for convenience.

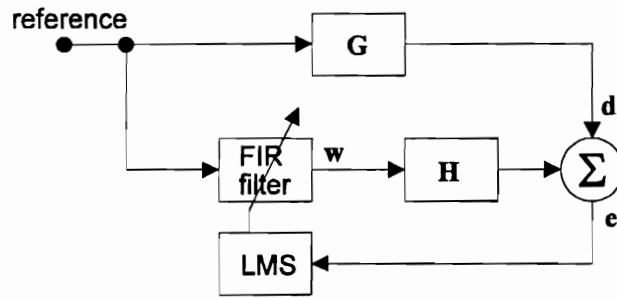


**Figure 3-2. Traditional adaptive feedforward control system schematic**

By defining the cost function as the square of the error:

$$J = \mathbf{e}^h \mathbf{e} = \mathbf{d}^h \mathbf{d} + \mathbf{d}^h \mathbf{H} \mathbf{w} + \mathbf{w}^h \mathbf{H}^h \mathbf{d} + \mathbf{w}^h \mathbf{H}^h \mathbf{H} \mathbf{w} \quad (3.2)$$

(where the superscript  $h$  denotes the Hermitian transpose), a quadratic function of the adaptive filter output is formed with a unique global minimum. Taking the derivative of the cost function with respect to the adaptive filter:

$$\frac{\partial J}{\partial \mathbf{w}} = 2\mathbf{H}^h \mathbf{d} + 2\mathbf{H}^h \mathbf{H} \mathbf{w} = 2\mathbf{H}^h \mathbf{e} \quad (3.3)$$

the optimal adaptive filter can be found by:

$$\mathbf{w}_{opt} = -\frac{\mathbf{H}^h \mathbf{d}}{\mathbf{H}^h \mathbf{H}}. \quad (3.4)$$

From the standard gradient descent technique, the update equation for the adaptive filter at

iteration  $k$  is written as:

$$\mathbf{w}_{k+1} = \mathbf{w}_k + \mu(-\nabla_k) \quad (3.5)$$

where  $\mu$  is the convergence coefficient and  $\nabla_k$  is the gradient of the mean square error performance surface. However, the gradient can be defined as:

$$\nabla_k = \frac{\partial J}{\partial \mathbf{w}} = 2\mathbf{H}^h \mathbf{e}_k \quad (3.6)$$

therefore, the update equation becomes:

$$\mathbf{w}_{k+1} = \mathbf{w}_k - 2\mu\mathbf{H}^h \mathbf{e}_k. \quad (3.7)$$

In traditional multiple input multiple output (MIMO) adaptive feedforward control, the adaptive filter would be represented by the complex vector  $\mathbf{w}$ , having a number of rows equal to the number of control channels.

In the biologically inspired controller, the adaptive filter output for the master control channel remains a single output complex vector, with the additional degrees of freedom implemented downstream of the update equation through the use of local control approaches. Note that we have not discussed a procedure for choosing the particular actuator to which the master signal is to be applied. The choice of the master actuator is one area to be investigated and the influence of this choice on control performance will be addressed in Chapter 5.

### 3.1.2. Local control approaches

The control inputs to the slave channels are derived using local learning rules. Four local learning rules are developed and analyzed, the *phase variation*, *adaptive magnitude*, *adaptive phase*, and the *optimal* methods. The phase variation method varies the phase of the slave control path

relative to the master control input, while holding the magnitude constant. The adaptive magnitude method uses a reduced order adaptive filter where only the magnitude is adapted relative to the master input. The adaptive phase method uses a reduced order adaptive filter where only the phase is adapted relative to the master input. The optimal method allows both the magnitude and phase of the master control input to be varied in application to the slave control paths. This method determines the slave actuator control inputs *a priori* and makes use of the hierarchical structure to construct a distributed actuator from multiple slave inputs.

Mathematically, the local control approach can be expressed as adaptive filters ( $\gamma$ ) applied to the output of the master control channel to determine the control inputs applied to the slave control paths. Note that the method of determining the slave filters is not limited to the above methods, but could also include experimental, neural network, and genetic algorithm methods. For example, an experimental approach might determine the transfer functions from the control actuators to the error sensors and determine the optimal slave filters that need to be applied. This is similar to the optimal method discussed above and could be done using the system identification routine that is done on-line prior to the invocation of the Filtered-X LMS control algorithm.

### ***Phase variation method***

The following approach for a local learning rule is based on the observation that, for a distributed elastic system with little damping, the phase between two arbitrary points on the structure will be close to 0 (in-phase) or  $\pi$  (180° out-of-phase). Thus the local learning approach is to take the



master control input and apply it to a slave control path while varying the phase. This can be accomplished by multiplying the master control input by -1 or 1. A detailed explanation of the algorithm is given in the following paragraph but first the schematic of the phase variation algorithm is presented in Figure 3-3. Using the traditional adaptive feedforward control system schematic (seen in Figure 3-2) as a baseline, note that  $\mathbf{H}_1$  is now defined as the master control path. Also, note the addition of the slave control paths,  $\mathbf{H}_2$  to  $\mathbf{H}_C$ , along with slave filters  $\gamma_2$  to  $\gamma_C$ , where  $C$  is the total number of control paths.

The phase variation algorithm is defined as follows. With the master control input locked at its optimal value, the slave control input is tried in-phase ( $\gamma=+1$ ), out-of-phase ( $\gamma=-1$ ) or turned off ( $\gamma=0$ ) while the cost function is observed for each change. The condition that results in the lowest cost function is kept and the process is then applied to the next slave control path until all slave control paths are progressively tested. The master control channel is then unlocked and continues to adapt to changes in the system. Note that the sequence of activating the slave paths can be varied. By this method, a distributed actuator with a generalized function that drives a response similar to the uncontrolled vibration distribution with low control spillover is constructed. Note that the previous process is sub-optimal as are many biological systems. However, it is believed that good control performance will still be obtained.

Since the master control channel is allowed to converge to an optimal value before the application of the phase variation algorithm, the update for the adaptive filter remains the same as the single output case:

$$\mathbf{w}_{k+1} = \mathbf{w}_k - 2\mu\mathbf{H}_1^h \mathbf{e}_k \quad (3.8)$$

where  $\mathbf{H}_1$  denotes the master control channel transfer function.

During the phase variation adaptation, the error can be written for the  $j$ th control input as follows:

$$\mathbf{e}_k = \mathbf{d}_k + (\mathbf{H}_1 + \sum_{i=2}^j \gamma_i \mathbf{H}_i) \mathbf{w}_k \quad (3.9)$$

Since this method uses a trial and error approach based on bounded filters, there is no calculated gradient and therefore no update equation for the slave filters.

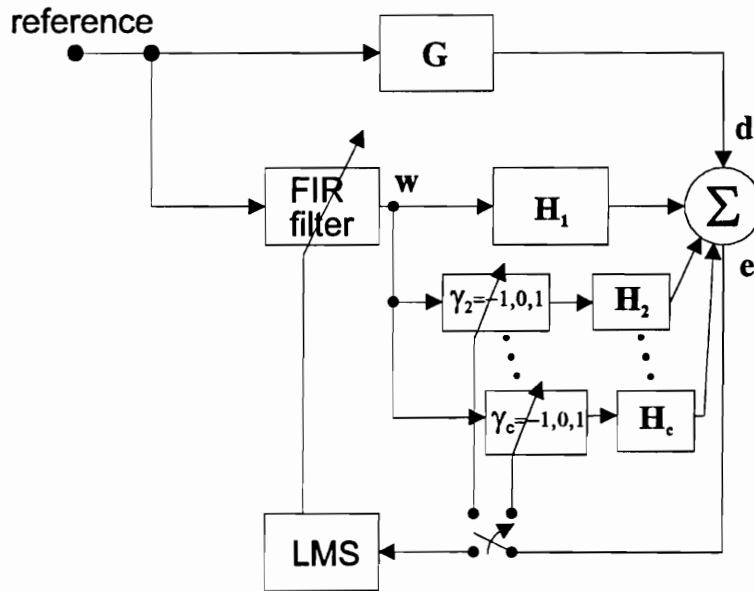


**Figure 3-3. Phase variation control system schematic**

However, after the phase variation adaptation, the error must be rewritten to include the slave inputs:

$$\mathbf{e}_k = \mathbf{d}_k + (\mathbf{H}_1 + \sum_{i=2}^c \gamma_i \mathbf{H}_i) \mathbf{w}_k \quad (3.10)$$

which leads to a new update equation for the master filter:

$$\mathbf{w}_{k+1} = \mathbf{w}_k - 2\mu(\mathbf{H}_1 + \sum_{i=2}^C \gamma_i \mathbf{H}_i)^h \mathbf{e}_k. \quad (3.11)$$

It is evident from the above equation that the update equation for the master control input is now dependent upon the additional slave control paths. This will have important considerations in the stability analysis section below.

### ***Adaptive magnitude method***

The adaptive magnitude local rule was based on the observation that the spatial variation of a lightly damped structural mode varies continuously in magnitude while the phase is bounded to be near 0 or  $\pi$  as detailed in the previous section. To illustrate the concept, Figure 3-4 shows an instant in time of a simply supported beam vibrating at the second mode resonance frequency. The magnitude of this mode varies as a sine function along the beam having positive and negative real values. The phase of the left half of the beam is 180° out-of-phase with the right half of the beam. Therefore, the local rule is to allow the slave actuator filter to adapt relative to the master actuator in magnitude only which should allow the actuators to match the uncontrolled vibration distribution of a lightly damped structure. This effectively reduces the order of the slave filter to be on the real interval  $\{-\infty:\infty\}$ , which includes in-phase and out-of-phase values. Referring to the schematic for this local rule in Figure 3-5, the adaptive magnitude algorithm is now discussed followed by the update equations for the master and slave filters.

The adaptive magnitude algorithm proceeds as follows:

- 1) the master channel is invoked and allowed to reach an optimal value.

2) the slave channels are then updated one by one in magnitude only (relative to the master channel) using the LMS algorithm (see following paragraph).

3) the master control channel is updated (which now updates the slave actuator outputs).

Repeat steps 2) and 3) continually until a converged solution is reached.

Since the master control channel is allowed to converge to an optimal value before the application of the adaptive magnitude method, the update for the master filter remains the same as the single output case as defined in Eq. (3.8). When the slave channels are being adapted, the error must include the slave control paths. The error can be written:

$$\mathbf{e} = \mathbf{d} + (\mathbf{H}_1 + \sum_{i=2}^c \gamma_i \mathbf{H}_i) \mathbf{w}. \quad (3.12)$$

This leads to a new update equation for the slave filter for the  $j$ th slave actuator:

$$\gamma_{j,k+1} = \gamma_{j,k} - 2\mu(\mathbf{H}_j \mathbf{w})^h \mathbf{e}. \quad (3.13)$$

Note that the slave filter is restricted to be real on the interval  $\{-\infty:\infty\}$ . After the slave input adaptation, the update equation for the master filter is the same as the update equation for the phase variation method seen in Eq. (3.11).

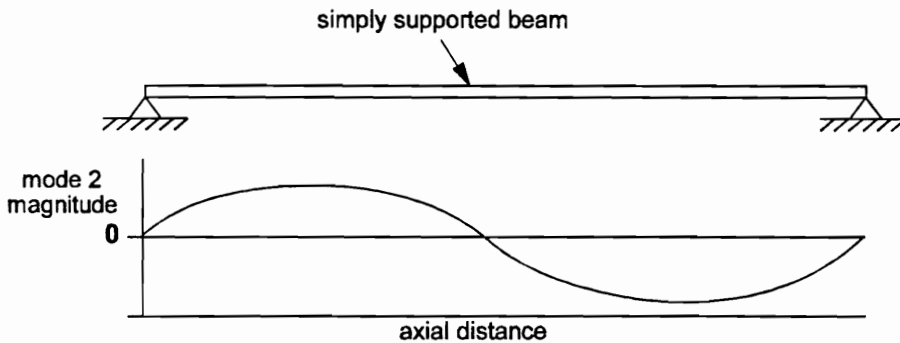


**Figure 3-4. Simply supported beam mode two magnitude**

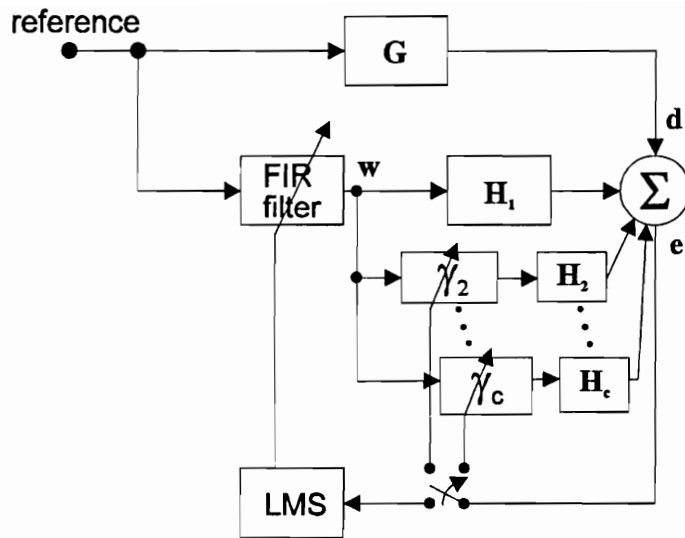


**Figure 3-5. Adaptive magnitude and adaptive phase control system schematic**

***Adaptive phase method***

The adaptive phase local rule was based on the knowledge that matching the phase in an adaptive system is the most critical to successful control. This method also allows for *modal restructuring* (Fuller, 1989) where the adaptive magnitude method does not. Therefore, the local rule is to allow the slave filter to adapt relative to the master actuator in phase only, i.e. the magnitude of the slave filter is held constant at one. Although the slave filter must still use the number of coefficients as for a fully adaptive system (i.e. 2 coefficients for a single frequency), the order of the adaptivity is reduced leading to significant decreases in computational complexity as will be presented in Chapter 5. The schematic for this local rule is the same as the schematic for the adaptive magnitude method which was presented in Figure 3-5. Unlike the previous two rules, the slave filters are initialized to be in phase and a magnitude of one relative to the master channel.

The adaptive phase algorithm proceeds as follows:

- 1) the master channel is invoked and allowed to reach an optimal value; (the adaptation includes the slave filters which were initialized as 1).
- 2) the phase of the slave channels are then adapted one by one (relative to the master channel) using the LMS algorithm (the magnitude is kept constant).
- 3) the master control channel is updated (which now updates the slave actuator outputs).

Repeat steps 2) and 3) continually until a converged solution is reached.

Since the master control channel converges with the slave channels activated, the update for the master filter is the same as the master and slave update equation as defined in Eq. (3.11).

When the slave channels are being adapted, the error must include the slave control paths. For the  $j$ th slave actuator, the error can be written as for the adaptive magnitude method in Eq. (3.12) leading to a new update equation for the slave filter:

$$\gamma_{j,k+1} = \gamma_{j,k} - 2\mu(\mathbf{H}_j \mathbf{w})^h \mathbf{e}. \quad (3.14)$$

Note that the slave filter is restricted to have a magnitude of one.

After the slave input adaptation, the update equation for the master filter is the same as the update equation for the phase variation seen in Eq. (3.11).

### ***Optimal method***

The optimal method was developed from MIMO linear quadratic optimal control theory

(LQOCT; which will be discussed in Section 3.3) and is solved off-line and prior to the algorithm invocation. Essentially the measured or calculated control path transfer functions between the actuators and sensors are used to calculate the theoretical optimal slave filters. The slave filters are then scaled relative to the master actuator which calibrates the slave filters relative to the master actuator. The weights of the master filter can then be adapted to minimize the cost function and simultaneously the slave control signals will be derived by proportion. Written in terms of the slave filters applied to the slave actuators ( $\gamma$ ) and the master control channel adaptive filter ( $\mathbf{w}$ ), this forms a system of linear equations:

$$\begin{Bmatrix} -\mathbf{H}_1^h \mathbf{d} \\ \vdots \\ -\mathbf{H}_p^h \mathbf{d} \end{Bmatrix} = \begin{bmatrix} \mathbf{H}_1^h \mathbf{H}_1 & \cdots & \mathbf{H}_1^h \mathbf{H}_p \\ \vdots & \ddots & \vdots \\ \mathbf{H}_p^h \mathbf{H}_1 & \cdots & \mathbf{H}_p^h \mathbf{H}_p \end{bmatrix} \begin{Bmatrix} \gamma_1 \\ \vdots \\ \gamma_p \end{Bmatrix} \mathbf{w} \quad (3.15)$$

where  $\mathbf{d}$ , and  $\mathbf{H}_i$  are defined in the preceding section. The solution to this linear system of equations provides a least squares solution of the optimal slave filters. The slave filters are then scaled so that the gain of the master control channel ( $\gamma_1$ ) is 1. Although this method is not a local “learning” algorithm, it uses a hierarchical control structure to construct a distributed actuator made up of the master and slave actuators. This has been done to show the advantages of a hierarchical control structure. The disadvantage of this method is that it requires prior knowledge of the system which can be obtained analytically or experimentally. Carneal and Fuller (1994, 1995a, 1995b) have used both analytical and experimental means to implement the optimal method and it is obvious that simple systems can be modeled analytically where complex systems must use experimental data to provide the required system identification.

The implementation of the optimal distribution into the control system is shown in Figure 3-6.

The control signal fed to the master control input ( $\mathbf{w}$ ) is operated on by the optimal slave filters ( $\gamma_2 \dots \gamma_p$ ) and fed to the slave transfer functions ( $\mathbf{H}_2 \dots \mathbf{H}_p$ ). With the addition of the slave control paths, the error can now be written:

$$\mathbf{e}_k = \mathbf{d}_k + (\mathbf{H}_1 + \sum_{i=2}^C \gamma_i \mathbf{H}_i) \mathbf{w}_k \quad (3.16)$$

therefore leading to a new update equation for the master adaptive filter:

$$\mathbf{w}_{k+1} = \mathbf{w}_k - 2\mu(\mathbf{H}_1 + \sum_{i=2}^C \gamma_i \mathbf{H}_i)^h \mathbf{e}. \quad (3.17)$$

It is evident from the above equation that the update equation for the master control input is now dependent upon the additional slave control paths.

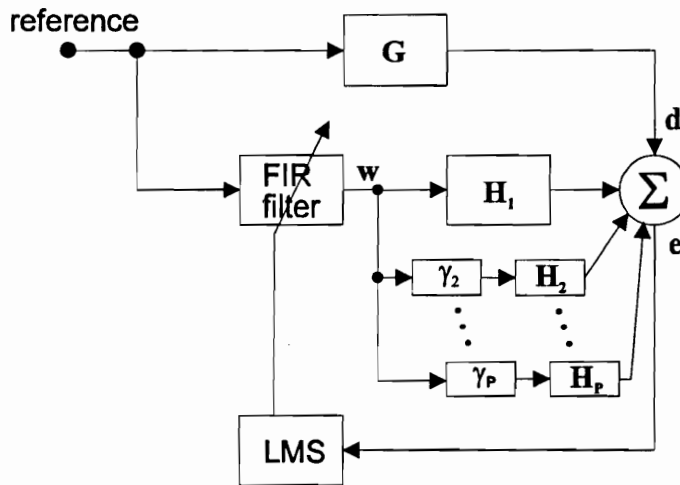


Figure 3-6. Optimal distribution control system schematic

### 3.2. Stability analysis

A stability analysis of the master control input and the various local learning rules is presented. The analysis starts with square of the estimated control loop transfer function ( $\mathbf{H}^h \mathbf{H}$ ) which



defines the coordinates of the performance surface. The performance surface coordinates can be translated into principle coordinates using standard matrix theory which gives a matrix of eigenvectors and eigenvalues. The upper bound on the convergence parameter is then defined by the maximum eigenvalue. For further information on this subject, the reader is referred to Widrow and Stearns (1985) and Boucher, et al. (1990).

### 3.2.1. Master control input

Following the frequency domain analysis of Widrow and Stearns (1985) and Boucher, et al. (1990), the coordinates of the error surface can be translated into principle coordinates defined by the eigenvalues of the physical system (i.e. the control loop transfer functions) by expanding the expected value of the matrix  $\mathbf{H}^h\mathbf{H}$  into  $\mathbf{Q}\Lambda\mathbf{Q}^h$  where  $\mathbf{Q}$  is a matrix of eigenvectors and  $\Lambda$  is a diagonal matrix of eigenvalues. The rotated and translated set of coordinates can be defined by:

$$\mathbf{v} = \mathbf{Q}^h(\mathbf{w} - \mathbf{w}_{opt}). \quad (3.18)$$

The update equation can now be written in terms of the principle coordinates of the error surface:

$$\mathbf{v}_k = [\mathbf{I} - 2\mu\Lambda]^k \mathbf{v}_0, \quad (3.19)$$

where by definition the eigenvalue matrix ( $\Lambda$ ) is diagonal. This leads to an independent set of converging eigenvalues so that:

$$v_{m,k} = (1 - 2\mu\lambda_m)^k v_{m,0}, \quad (3.20)$$

where  $v_m$  is the coordinate of the  $m$ th eigenvector corresponding to the  $m$ th eigenvalue ( $\lambda_m$ ). For stability, the update of  $v_m$  should be bounded, or:

$$\lim_{k \rightarrow \infty} (1 - 2\mu\lambda_m)^k = 0 \quad \forall m \quad (3.21)$$

leading to the inequality:

$$|1 - 2\mu\lambda_m| < 1 \quad \forall m \quad (3.22)$$

or:

$$0 < \mu < \frac{1}{\lambda_m} \quad \forall m. \quad (3.23)$$

Therefore, upper bound of the convergence parameter ( $\mu$ ) is limited by the maximum eigenvalue ( $\lambda_{max}$ ).

### 3.2.2. Local rules

As described above, the local rules share common structures. The phase variation and adaptive magnitude rules allow the master actuator to converge before the local rules are activated. While the master control input is converging, stability bounds are determined by the above analysis for the master control adaptive filter ( $\mathbf{w}$ ) which is continuous and has no bound. Since the slave filters ( $\gamma$ ) and slave control inputs have no influence on the master control input, the convergence parameter ( $\mu$ ) is limited by the maximum eigenvalue ( $\lambda_{max}$ ), which is derived from the master control input transfer function ( $\mathbf{H}_1$ ). Once the phase variation method is invoked, the master filter is locked at its optimal value.

The phase variation method then applies the optimal filter from the master channel to the slave channels operated on by a discrete and bounded slave filter ( $\gamma$ ) which must have the value -1, 0, or +1. By definition, bounded filters must be stable, therefore the phase variation method is stable.

However, the adaptive magnitude method uses a continuous unbounded filter. Since the slave filters ( $\gamma$ ) (and corresponding slave inputs) are invoked one by one and the master input is locked, the above stability analysis shows that the matrix  $\mathbf{H}^h\mathbf{H}$  must be written for the adapting

slave control path only. For the  $j$ th actuator, this matrix is written  $\mathbf{H}_j^h \mathbf{H}_j$ . As in the analysis for the master control input, this matrix can be expanded into  $\mathbf{Q}\Lambda\mathbf{Q}^h$ , similar to the above analysis, and likewise, the upper bound of the convergence parameter ( $\mu$ ) is limited by the maximum eigenvalue ( $\lambda_{max}$ ). Since the slave filters are limited to be real, it is evident that the corresponding maximum eigenvalue will always be less than or equal to the maximum eigenvalue for a complex slave filter. Therefore, the convergence parameter will be greater than or equal to the convergence parameter for a complex slave filter. This applies to the slave channel adaptation for the adaptive phase method as well.

After the slave input adaptation, the phase variation and adaptive magnitude methods unlock the master input to further adapt to changes in the system. At this point, the slave channels are activated and directly proportional to the master channel due to the hierarchical structure. This also occurs for the adaptive phase method before and after the slave channel adaptation and for the optimal method where the slave inputs were determined *a priori*. During this adaptation sequence, the update equation for all three methods include the slave channel filters ( $\gamma$ ) and transfer functions ( $\mathbf{H}_i$ ) as seen in Eqs. (3.11) and (3.17). Therefore, that the matrix  $\mathbf{H}^h \mathbf{H}$  must also include the slave input filters and transfer functions ( $\mathbf{H}_i$ ):

$$\mathbf{H}^h \mathbf{H} = \left( \mathbf{H}_1 + \sum_{i=2}^C \gamma_i \mathbf{H}_i \right)^h \left( \mathbf{H}_1 + \sum_{i=2}^C \gamma_i \mathbf{H}_i \right) \quad (3.24)$$

This matrix can be expanded into  $\mathbf{Q}\Lambda\mathbf{Q}^h$ , similar to the above analysis, and likewise, the upper bound of the convergence parameter ( $\mu$ ) is limited by the maximum eigenvalue ( $\lambda_{max}$ ).

By definition, the matrix,  $\mathbf{Q}\Lambda\mathbf{Q}^h$ , is symmetric and has a orthonormal set of eigenvectors. Also, the matrix must have positive eigenvalues since it is a physical system. From these facts, it is evident that the addition of other control inputs will increase the largest eigenvector in the matrix, therefore decreasing the upper bound on the convergence parameter ( $\mu$ ). It is apparent that the determination of the convergence parameter for the optimal distribution is case specific and depends on the values of the slave filters ( $\gamma$ ) and the master and slave control paths ( $\mathbf{H}_1$  through  $\mathbf{H}_p$ ). Analytical results of this analysis are presented in Chapter 5.

### 3.3. Linear quadratic optimal control

For the analytical results, linear quadratic optimal control theory (LQOCT) is used to determine the optimal control inputs for the application of active structural acoustic control (ASAC) to double panel systems as well as the biologically inspired hierarchical (BIO) master and optimal methods. However, the above control analysis assumed the optimal control inputs are achieved by LMS and Filtered-X LMS methods. In theory, LQOCT and the adaptive algorithms will reach the same optimal solution, however the technique used to arrive at this solution is extremely different. In this section, the specifics for applying LQOCT to the reduction of transmission loss of a double panel system are presented.

The reduction of the transmission loss of a double panel system is accomplished in practice by reducing the radiated sound power from the radiating panel of a double panel system, which can be written as:

$$\Pi_t = \sum_{m=1}^{\infty} \sum_{n=1}^{\infty} \sum_{k=1}^{\infty} \sum_{l=1}^{\infty} \Delta_{mnl} W_{mn}^{r,l} W_{kl}^{r,l*} \quad (3.25)$$

where  $\Delta_{mnl}$  was previously defined in Chapter 2. Using superposition, the total modal response of the radiating panel can be written as a function of the applied piezoelectric force, which is a function of applied voltage ( $V$ ):

$$W_{mn}^{r,l} = W_{mn}^{r,d} + \sum_{i=1}^C W_{mn}^{r,c_i} V_i \quad (3.26)$$

It is evident from the substitution of Eq. (3.26) into Eq. (3.25) that the radiated sound power is a quadratic function of the applied piezoelectric voltage. Taking the derivative of radiated power with respect to the piezoelectric voltage (the control signal to each actuator) and setting the result equal to zero will give the equation for the optimal applied piezoelectric voltage:

$$\begin{Bmatrix} V_1 \\ \vdots \\ V_C \end{Bmatrix} = \begin{bmatrix} \beta W_{mn}^{r,c_1} W_{kl}^{r,c_1*} & \dots & \beta W_{mn}^{r,c_1} W_{kl}^{r,c_C*} \\ \vdots & \ddots & \vdots \\ \beta W_{mn}^{r,c_C} W_{kl}^{r,c_1*} & \dots & \beta W_{mn}^{r,c_C} W_{kl}^{r,c_C*} \end{bmatrix}^{-1} \begin{Bmatrix} -\beta W_{mn}^{r,d} W_{kl}^{r,c_1*} \\ \vdots \\ -\beta W_{mn}^{r,d} W_{kl}^{r,c_C*} \end{Bmatrix} \quad (3.27)$$

where

$$\beta = \sum_{m=1}^{\infty} \sum_{n=1}^{\infty} \sum_{k=1}^{\infty} \sum_{l=1}^{\infty} \Delta_{mnl} \quad (3.28)$$

The above results apply for the MIMO LMS control algorithm as well as the determination of the slave filters for the optimal solution.

For the master channel update where all of the slave filters are set to zero, Eq. (3.27) reduces to a single complex quantity:

$$\{-\beta W_{mn}^d W_{kl}^{c,1*}\} = [\beta W_{mn}^{c,1} W_{kl}^{c,1*}] \{V_1\} \quad (3.29)$$

When the slave filters are not equal to zero, the master channel update remains a single complex quantity, however the control modal amplitudes in the above equation must include the slave

channels which can be written as:

$$\left\{ -\beta W_{mn}^{r,d} \left( W_{kl}^{r,c_1} + \sum_{i=2}^C \gamma_i W_{kl}^{r,c_i} \right)^* \right\} = \left[ \beta \left( W_{mn}^{r,c_1} + \sum_{i=2}^C \gamma_i W_{mn}^{r,c_i} \right) \left( W_{kl}^{r,c_1} + \sum_{i=2}^C \gamma_i W_{kl}^{r,c_i} \right)^* \right] \{V_1\} \quad (3.30)$$

Using LQOCT for the determination of the optimal adaptation for the adaptive phase and magnitude methods presented problems of limiting the slave filters to be real or to have a magnitude of one, respectively. Specifically, solving Eq. (3.27) gives complex numbers for all of the control inputs ( $V$ ). Taking the signed magnitude of the slave inputs (for the adaptive magnitude method) or limiting the magnitude to 1 (for the adaptive phase method) did not produce the correct optimal control inputs. In some cases this resulted in increased radiated power when the slave control inputs were applied. Therefore, the analytical solution for the adaptive phase and adaptive magnitude methods was achieved using the LMS algorithm. This algorithm perturbs the slave filter to determine the gradient then steps in the direction of the negative gradient until the cost function increases which is an indication that a minima has been reached. The update for the slave filter can be written as:

$$\gamma_{j,k+1} = \gamma_{j,k} + \mu(-\nabla_k) \quad (3.31)$$

where

$$\nabla_k = \frac{\Delta J}{\Delta \gamma} = \left( \frac{J_k - J_{k-1}}{\gamma_k - \gamma_{k-1}} \right) \quad (3.32)$$

and the cost function is defined as the radiated acoustic power given in Eq. (3.25) with the total modal response written as:

$$W_{mn}^{r,t} = W_{mn}^{r,d} + \left( W_{mn}^{r,c_i} + \sum_{i=2}^C \gamma_i W_{mn}^{r,c_i} \right) V_1 \quad (3.33)$$

Note that the slave filter ( $\gamma_i$ ) is the perturbed value in the above equation not  $V_j$ . It is assumed the reader is familiar with the LMS algorithm and is referred to Widrow and Stearns (1985) for further information.

## **4. Experimental investigation**

The details of the experimental investigation are presented in this chapter. First, the experimental test rigs are discussed, followed by experimental controller implementation. The controller performance criteria is then presented, followed by a discussion of the experimental procedure which concludes this chapter.

### **4.1. Experimental test rig**

The Filtered-X LMS and biologically inspired hierarchical (BIO) control algorithms were applied to two different double panel system test rigs. The first test rig was a double panel system which consisted of a flexible incident plate and either a flexible or a stiff radiating plate mounted in a transmission loss test facility. The second was a realistic double panel system in a Cessna Citation III aircraft. The double panel system consisted of the aircraft fuselage and the interior trim panel above the cockpit.

#### **4.1.1. Double panel system**

There were two different double panel systems tested in this experimental investigation. The first set of tests were performed to experimentally determine the effect of double panel system parameters such as radiating plate stiffness, PZT location, and the number of control actuators, etc. on active structural acoustic control (ASAC) performance. The second set of tests were



performed to verify the biologically inspired (BIO) hierarchical control concept. Both sets of tests were performed in the transmission loss test facility, however the experimental setup of each test was different enough that the tests must be described separately.

#### ***Active structural acoustic control tests***

The double panel system, consisting of two plates separated by an air cavity, was mounted in the common wall between two reverberation chambers of a transmission loss test facility. The arrangement of the test chamber, the double panel system, and the location of the three test positions of the acoustical source are shown in Figure 4-1. The characteristics of the transmission loss test facility are presented in Appendix A. The incident plate was made of aluminum and had dimensions 0.381 m long x 0.305 m wide x 1.6 mm thick. Two radiating plates of different materials were tested, one made of G10 fiberglass (which is relatively flexible) and one made of sandwich board construction (which is relatively stiff). Both radiating plates had dimensions of 0.381 m long x 0.305 m wide, and thickness' of 1.6 mm and 10.2 mm for the flexible and stiff plates, respectively. A summary of plate properties are presented in Table 4-1. The plates were mounted in a heavy steel frame which approximates clamped boundary conditions, allowing very little displacement or rotation of the plate edges. The air cavity, which separated the plates with a 48 mm gap, also had dimensions of 0.381 m long x 0.305 m wide. Harmonic excitation for the incident plate was produced by a large speaker placed in the source chamber. The structureborne flanking sound transmission path from the source to the receiving chamber was assumed negligible.

The controller configuration in the experiments was varied between controlling the incident plate to controlling the radiating plate. Two different types of radiating plates with different stiffness'

were tested to determine the influence of radiating plate stiffness on performance. The flexible and stiff plates were excited on-resonance and off-resonance to determine the influence of excitation frequency. As determined by the double panel system frequency response function, the on-resonance frequency was chosen where both plates were close to a resonance, conversely the off-resonance frequency was chosen where neither plate exhibited a nearby resonant frequency. The choice of test frequencies is detailed later in Chapter 6. To determine the influence of the incident acoustic field, three different types of acoustic excitation, normal plane wave, oblique plane wave, and reverberant, were tested as shown in Figure 4-1. The normal plane wave excitation was produced by a speaker placed 0.260 m from the incident plate, at an angle of zero degrees from the plate normal, producing a uniform pressure wave at the incident plate with no phase variation over the plate. The oblique plane wave excitation was placed the same distance from the incident plate, but at an angle of 45 degrees from the normal, producing a uniform pressure wave at the incident plate with variations in phase. Placing a speaker in the far corner of the room produces a pressure wave at the incident plate with random phase, indicative of reverberant excitation. Verification of the different excitation types is presented in Appendix B.

Traversing microphones in the source and receiving chambers were calibrated allowing direct measurements of acoustic pressure. Acoustic pressure measurements for the incident field were taken from a microphone mounted directly in front of the incident plate for the normal and oblique plane wave excitations. For the reverberant case, a microphone was traversed across the chamber, and sound pressure was sampled at 10 discrete locations. The source acoustic power level in the chamber was determined from an average of these measurements. For all excitation cases, radiated field acoustic power level was determined from an average of 10 pressure

measurements taken across a traverse of the receiving chamber as seen in Figure 4-1. Note all acoustic measurements are in dB referenced to 20  $\mu\text{Pa}$ . Analysis of the acoustic data was performed using a Bruel and Kjaer Type 2032 dual channel signal analyzer.

From the above acoustical measurements, the power in a reverberant environment can be calculated by (Kinsler, et al., 1982):

$$\Pi = \frac{13.9P_r^2V}{\rho c^2T} \quad (4.1)$$

where  $V$  is the reverberant chamber volume ( $\text{m}^3$ ),  $T$  is the reverberation time (s),  $P_r$  is the spatially averaged effective pressure amplitude of the reverberant sound field,  $\rho$  is the density of the acoustic medium and  $c$  is the speed of sound in the acoustic medium. Values of the reverberant chamber volume and the reverberation time for this transmission loss test facility can be found in Appendix A. From the above equation, the *increase in transmission loss with control* can be calculated as:

$$\Delta TL(\text{dB}) = 10 \log_{10} \left( \frac{\Pi_{\text{uncontrolled}}}{\Pi_{\text{controlled}}} \right). \quad (4.2)$$

where  $\Pi_{\text{uncontrolled}}$  is defined as the uncontrolled radiated sound power and  $\Pi_{\text{controlled}}$  is defined as the controlled radiated sound power. The experimental data in Chapter 6 as well as the analytical data in Chapter 5 are presented in these terms. The incident acoustic power for a plane wave and oblique plane wave excitation can be calculated from:

$$\Pi_i = \frac{P_b^2}{\rho c} A \quad (4.3)$$

where  $P_b$  is the blocked pressure and  $A$  is the area of the incident panel.

The active control system used was a multi-channel Filtered-X LMS algorithm implemented on a TMS320C25 DSP mounted in an AT computer (Clark, et al., 1991). The system is capable of reading up to six error signals plus one reference signal, and generating up to six control signals (i.e. voltages applied to the piezoelectric actuators). The signal generator in a Bruel and Kjaer Type 2032 dual channel signal analyzer provided the harmonic excitation signal for the double panel system. The reference signal for the controller was taken directly from the signal generator. Note that the controller convergence parameter, which determines the rate of convergence, and the sampling frequency were varied to provide a stable system. The Filtered-X LMS algorithm is discussed in detail in Section 4.2.1.

Three microphones placed in the receiving chamber provided error signals for the controller. The signals from the error microphones were adjusted to provide uniform weighting of the error signals to the controller. The control inputs were implemented by three PZT actuators. Incident plate PZT locations were chosen by Clark (1992) to allow coupling with odd modes in the x- and y-directions. These PZT's were then mounted by Zhou (1992). Radiating plate PZT locations, shown in Figure 4-2, were chosen as follows: PZT #1 was located over the node lines for the higher order odd modes, and therefore unable to couple into these modes. PZT #2 was positioned orthogonal to higher order even modes, while PZT #3 was located to couple into both higher order odd and even modes.

To perform a detailed vibrational analysis of the radiating plates, a scanning laser vibrometer was used to measure the out-of-plane vibration velocity of the plate over a grid containing 32 points

along the x-axis and 20 points along the y-axis. A calibrated accelerometer was positioned at one of the scan points on the plate, which was used as the reference signal for the modal analysis. This arrangement allows the calibration of the vibration measurements in engineering units ( $m/s^2$ ). These detailed vibrational measurements were also used to perform a modal decomposition (Fuller, et al., 1989) of the radiating plate response in order to determine the effects of active control on the various double panel system configurations.

**Table 4-1. Summary of ASAC test plate properties**

properties	incident plate	flexible plate	stiff plate
material	aluminum	G10 fiberglass	sandwich board
dimensions (m)	.381 x .305 x .00159	.381 x .305 x .00159	.381 x .305 x .01022
density( $kg/m^3$ )	2700	179.8	2.51
modulus of elasticity (GPa)	64	18.6	39.3

**Table 4-2. PZT central locations for ASAC tests (m)**

PZT #	incident plate	radiating plate
1	0.305, 0.144	0.127, 0.200
2	0.076, 0.056	0.190, 0.150
3	0.191, 0.240	0.082, 0.060

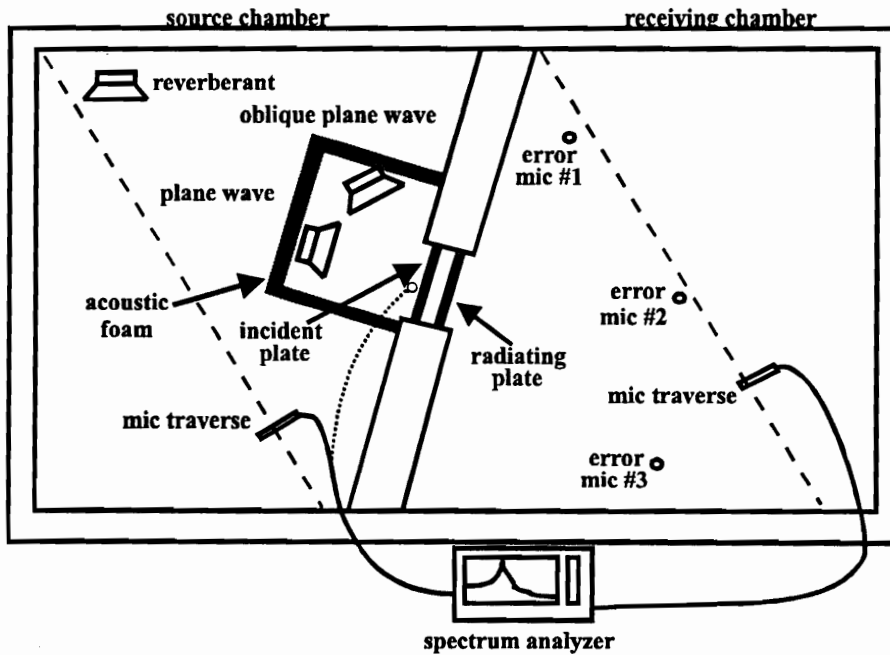


Figure 4-1. Transmission loss test facility setup for ASAC tests

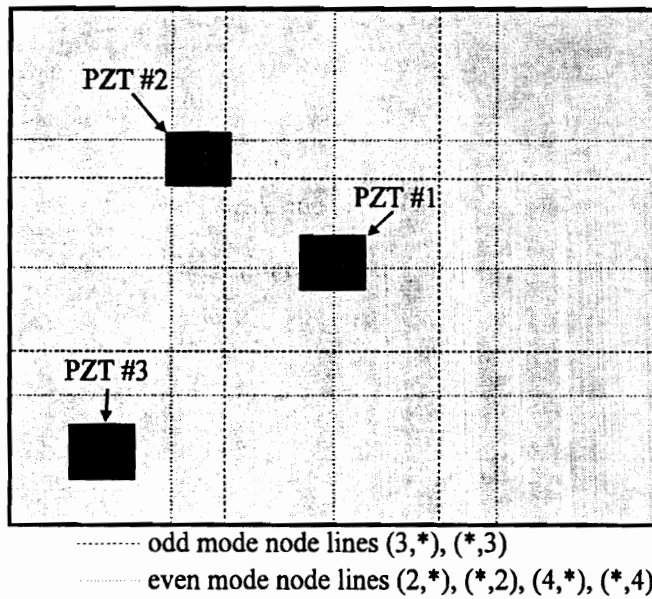


Figure 4-2. Radiating plate PZT and node line locations for ASAC tests

### ***Biologically inspired hierarchical (BIO) control tests***

The double panel system studied in these investigations consisted of two plates of various materials of dimensions length 0.381 m, width 0.305 m and various thickness, the properties of which are given in Table 4-3. For all of the tests, the incident plate was a thin aluminum plate which approximates the fuselage skin of an aircraft. Two different radiating plates were tested: one relatively flexible made of thin aluminum (the same as the incident panel) and one relatively stiff made of sandwich board (similar to a trim panel). The plates were mounted in a common wall between a reverberant chamber and an anechoic chamber as shown in Figure 4-3. The mounting apparatus clamped the plates at the boundaries which allowed negligible rotation of the boundary and negligible transverse displacement in order to approximate clamped boundary conditions. Harmonic, narrow band excitation was provided by an approximation of a oblique plane wave from a speaker in the source (reverberant) chamber placed at 0 and 45 degrees from the plate normal. The speaker was placed at 0.250 m from the plate and the acoustic path from the speaker to the incident plate of the double panel system was surrounded by acoustic foam so that the direct radiated field dominated the disturbance. When transmission loss data was required, a microphone was positioned at the center of the incident plate to record the incident pressure. The incident power was calculated as previously presented in Eq. (4.3).

Error signals were provided by the output of five microphones mounted in a hemispherical configuration in the receiving (anechoic) chamber, which was experimentally determined to approximate acoustic free field conditions above approximately 300 Hz (i.e. the cutoff frequency of the anechoic chamber was approximately 300 Hz). The microphones were placed according to

equal area calculations of a hemisphere, and their positions are presented in Table 4-4. From the microphone measurements, an approximation of radiated sound power can be calculated as:

$$\Pi = \sum_{i=1}^M |V_i|^2 \quad (4.4)$$

where  $V_i$  is the microphone voltage, subscript  $i$  indicates the microphone number index, and  $M$  is the total number of microphones. Note that the above equation assumes the microphones are placed according to equal area calculations. If this were not the case, each microphone voltage would be weighted by the area the measurement represents.

Control of the double panel system was provided by four ceramic piezoelectric (PZT) patches each having dimensions 0.038 m long x 0.032 m wide x 2.59E-04 m thick, the properties of which are presented in Table 4-5. The PZT patches were directly bonded to the plate at evenly spaced central locations forming a 2 by 2 grid on the plate, the locations of which are shown in Table 4-6. This configuration was selected from several candidate PZT locations based on the theoretically predicted overall attenuation of controlled transmission loss. As can be seen in Figure 4-4, the PZTs are able to couple into any mode of order (4,4) or less since none of the node lines passes through the center of the PZT.

Wiring a PZT pair into a bimorph pair proved difficult for a double panel system since the double panel system air cavity did not have any available wiring. Another option was to drill holes in the incident and radiating plates of the double panel system which later proved difficult to seal. This was the method used for the active structural acoustic control (ASAC) tests. To avoid this added difficulty in this experimental setup, the PZT actuators were bonded to one side



of the plate only, instead of the usual PZT pair. This was expected to have little effect on performance since previous experiments have determined that the one-sided PZT actuators were as effective as the two-sided actuators for exciting transverse motion in a beam (Gibbs and Fuller, 1992). However, it should be noted that the control effort required for a one-sided PZT is approximately twice that of a two-sided PZT. In addition, the associated axial (in-plane) excitation inherent in using one sided PZTs is negligible since the excitation frequencies of this investigation are well below the first axial mode.

For a more detailed analysis of the response of the double panel system, a laser vibrometer was used to determine the out-of-plane velocity for the uncontrolled and controlled cases. Transverse vibrational measurements were taken at 25 evenly spaced locations which formed a 5 by 5 point grid on the radiating plate of the double panel system. The laser vibrometer provides a voltage signal proportional to the radiating plate velocity and can be used for broadband velocity measurements. In this experimental investigation, only narrowband data was used by analyzing the laser vibrometer signal with a B&K 2032 digital signal analyzer and downloading the data at the frequency of interest. The laser vibrometer was mounted in a 2D traverse which positioned the laser vibrometer head at the points described above. This traverse is controlled using in-house software and 2 stepper motors. The radiating plate velocity data was then decomposed into a series of assumed orthogonal mode shapes using a modal decomposition technique (Fuller, et al., 1989) to gain further insight on controller behavior. A photograph of the radiating chamber setup showing the anechoic insert, error sensors, and 2D laser traverse is shown in Figure 4-5.

**Table 4-3. Summary of BIO test plate properties**

properties	incident panel	"flexible" panel	"stiff" panel
material	aluminum	aluminum	sandwich board
dimensions (m)	.381 x .305 x .0016	.381 x .305 x .0016	.381 x .305 x .0102
density(kg/m <sup>3</sup> )	2700	2700	1690*
E (GPa)	64	64	39.3*
phase speed, Cp (m/s)	5104	5104	4871*
coincidence freq. (Hz)	1274	1274	994

\*These properties are for the composite panel skin and do not include the core properties.

**Table 4-4. Microphone positions for BIO tests**

microphone #	position (r,θ,φ) (m,rad,rad)
1	1.3,0,0
2	1.3,0.3π,0.25π
3	1.3,0.3π,0.75π
4	1.3,0.3π,1.25π
5	1.3,0.3π,1.75π

**Table 4-5. PZT properties**

properties	
material	lead zirconate titanate
density(kg/m <sup>3</sup> )	7600
strain coefficient (m/volt)	166E-12
elastic modulus (N/m <sup>2</sup> )	63E+9

**Table 4-6. PZT central locations for BIO tests**

PZT #	Position (x,y) (m)
1	.111,.212
2	.269,.212
3	.111,.087
4	.269,.087

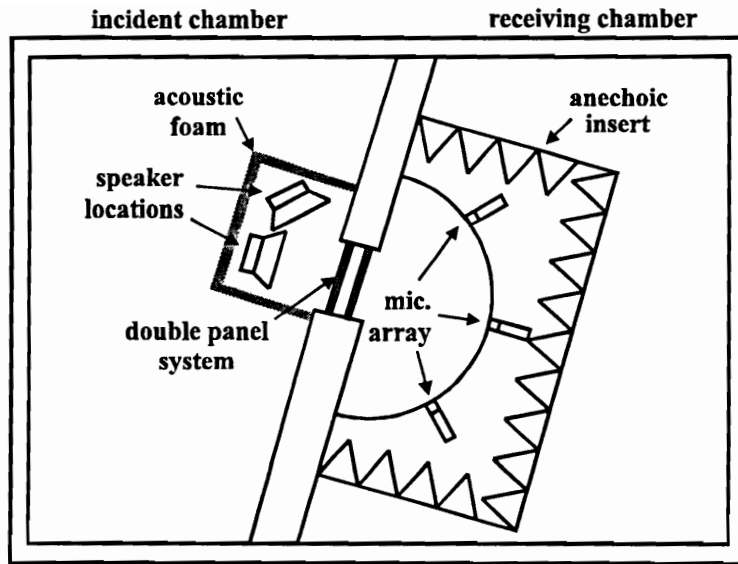


Figure 4-3. Transmission loss test facility setup for BIO tests

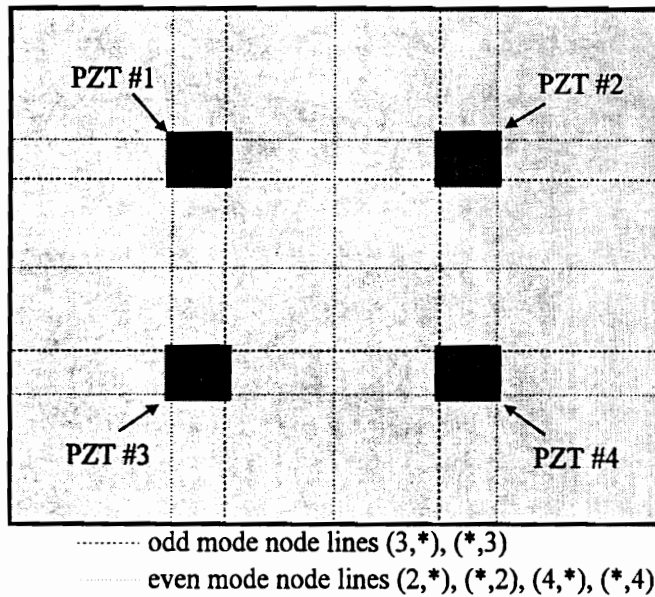


Figure 4-4. PZT and node line locations for BIO tests

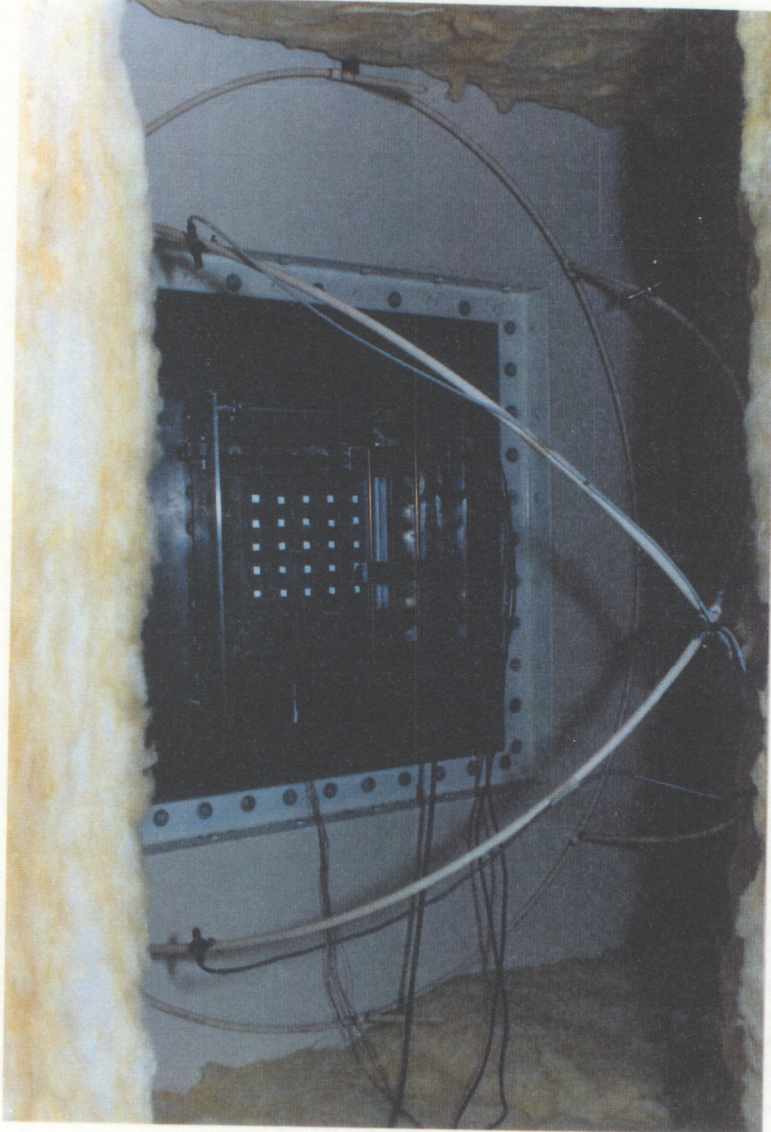


Figure 4-5. Photograph of radiating chamber anechoic insert, error microphones, and 2D laser traverse for BIO tests

#### 4.1.2. Cessna experimental aircraft fuselage

The Filtered-X LMS and biologically inspired hierarchical (BIO) control systems were implemented to control the sound transmission through a realistic structure: a Cessna experimental aircraft fuselage at Virginia Tech. The system to be controlled was the noise transmission path from the exterior of the fuselage through the fuselage skin and the interior trim panel (called a “crown” trim panel) above the cockpit into a “green” interior, i.e. a bare interior that has no acoustic treatment such as foam, interior trim panels or carpet, etc. A schematic of the experimental fuselage is presented in Figure 4-6. Single frequency harmonic excitation was provided by 3 speakers wired in-phase with each other and mounted above the cockpit. The speakers were enclosed in a cabinet to minimize the radiation into the Cessna laboratory outside the fuselage.

There were several observation microphones placed in the fuselage as shown in Figure 4-7. Error signals were provided by 4 microphones placed randomly in cockpit. Additional microphone measurements were taken from 12 microphones placed randomly in the cockpit and main body of the fuselage to determine the effect of control on the global sound field. There were several PZT locations mounted on the interior trim panel as seen in Figure 4-8. In these experiments, either one, four or eight PZT control actuators were used for control. The actuators locations were chosen from a variety of candidate locations (Mahnken, 1995) to provide the best interior trim response at the frequencies of interest. Each of the actuators had the dimensions 0.064 m long x 0.038 m wide x 0.159 mm thick, the properties of which are shown in Table 4-5. The PZT actuators attached to a metal shim and mounted with beeswax as to allow easy removability of the actuators (McCray, 1994). In the provided reference, it has been shown that the removable

PZT actuators have little performance degradation compared to permanent mounted ones.

Reductions in the interior sound field were obtained at the error microphones and the additional microphones in the fuselage. To approximate the sound power of the interior acoustic field, a sum of the microphone mean square voltages was calculated as described in Eq. (4.4). The increase in transmission loss (TL) with control was then calculated as described in Eq. (4.2).

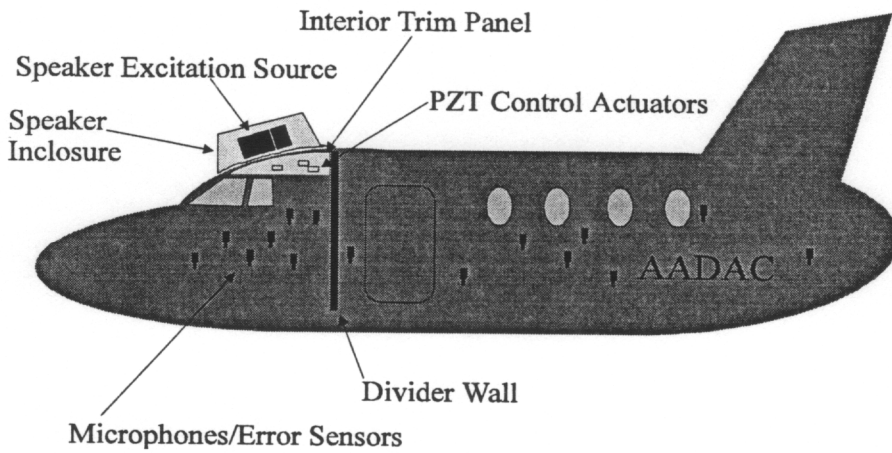


Figure 4-6. Cessna experimental aircraft fuselage schematic

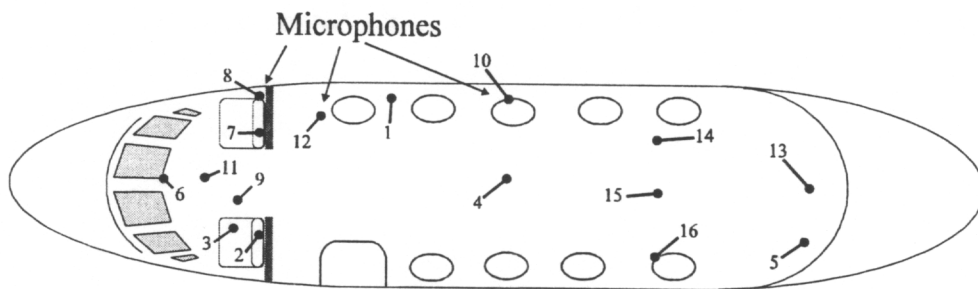
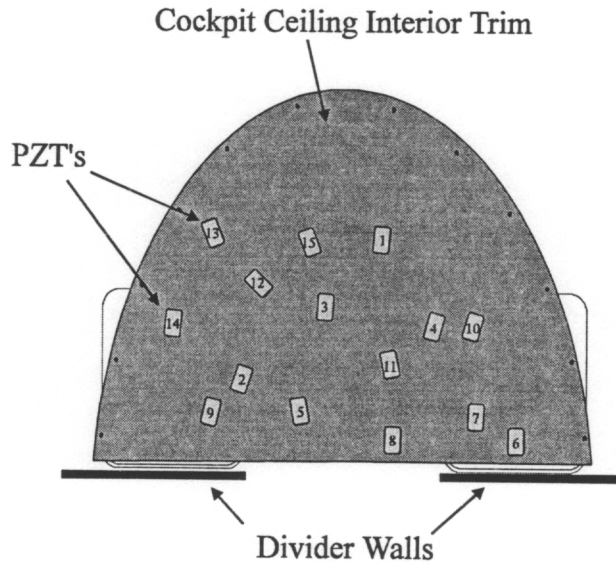


Figure 4-7. Cessna microphone locations (top view)



**Figure 4-8. Cessna interior trim cockpit ceiling PZT locations (top view)**

## **4.2. Controller**

Two different control algorithms were experimentally implemented on the test rigs mentioned above: the Filtered-X LMS and the biologically inspired hierarchical (BIO) controller. Details of the experimental implementation of these algorithms are presented.

### **4.2.1. Filtered-X LMS algorithm**

A multi-channel version of the Filtered-X LMS control algorithm, described in detail by Elliot, et al. (1987), and implemented on a TMS320C30 DSP mounted in an AT computer was used to control transmission loss through the double panel system. The system is capable of acquiring up to six error signals plus one reference signal, and generating up to six control signals. A schematic of the control system utilizing three error sensors and three control channels is presented in Figure 4-9.

The sampled error ( $e$ ) of the  $l$ th sensor at the  $n$ th time step can be stated as the sum of the error



due to the primary source ( $d_l$ ) and the error due to each of the actuators:

$$e_l(n) = d_l(n) + \sum_{m=1}^M \sum_{j=0}^{N-1} P_{lmj} \sum_{i=0}^{N-1} w_{mi}(n-j)x(n-i-j) \quad (4.5)$$

where  $P_{lmj}$  is the  $j$ th coefficient of the transfer function between the output of the  $m$ th adaptive filter and the  $l$ th error sensor,  $w_{mi}$  are the coefficients of the FIR filters, and  $x(n)$  is the sampled reference signal. The number of control actuators and filter coefficients are designated by  $M$  and  $N$ , respectively.

The total mean square error can be written as the sum of all the error signals:

$$J = E \left[ \sum_{l=1}^L e_l^2(n) \right] \quad (4.6)$$

From linear system theory, squaring the error constructs a quadratic cost function with only one minimum solution. It follows that the cost function ( $J$ ) can be minimized by adapting the FIR filter coefficients ( $w_{mi}$ ).

Using a modified form of the LMS algorithm, the FIR coefficients are updated by an estimate of the gradient of the cost function:

$$w_{mi}(n+1) = w_{mi}(n) - \mu \sum_{l=1}^L e_l(n) r_{lm}(n-i) \quad (4.7)$$

where  $\mu$  is the convergence coefficient and  $r_{lm}$  is defined as:

$$r_{lm}(n-i) = \sum_{j=0}^{N-1} \hat{P}_{lmj} x(n-i-j) \quad (4.8)$$

The filtered reference signal ( $r_{lm}$ ) utilizes digital filters ( $\hat{P}_{lmj}$ ) as estimates of the actual transfer

functions from the control inputs to the error signals. These transfer functions include the inherent physical system time delay from the control inputs to the error signals. Since the LMS algorithm assumes that the error  $e_{\ell}(n)$  is an instantaneous result of the control input, a more accurate gradient estimate is obtained using the filtered reference signal  $r_{lm}(n)$  versus  $x(n)$ . The inclusion of compensating filters ( $\hat{P}_{lmj}$ ) necessitates the measurement of the transfer functions from the control inputs to the error signals prior to the invocation of the Filtered-X LMS algorithm.

Since single frequency harmonic excitation was used, two coefficients are required for the adaptive FIR filter. Both the sampling frequency and convergence parameter, which determines the rate of convergence, were varied to provide a stable system. As a rule of thumb, the sampling frequency should be 4 to 10 times the highest frequency to be controlled. The maximum convergence parameter could be determined from the measured transfer functions as described in Chapter 3, however in practice, the initial convergence parameter is on the order of  $1 \times 10^{-5}$  to  $1 \times 10^{-4}$ . This number can then be increased to yield faster convergence times. However, the control system will go unstable if too large a convergence parameter is used.

Since the cost function was not directly accessible for the Filtered-X LMS algorithm, the uncontrolled and controlled cost function ( $J$ ) was determined by measuring the voltages ( $v$ ) of the microphones (error sensors) and summing the square of these voltages:

$$J_t = \sum_{i=1}^M |V_i|^2 \quad (4.9)$$

where  $M$  is the number of error sensors. Note that this process is similar to the determination of

cost function for the BIO controller as seen in Eq. (4.13) in the next section.

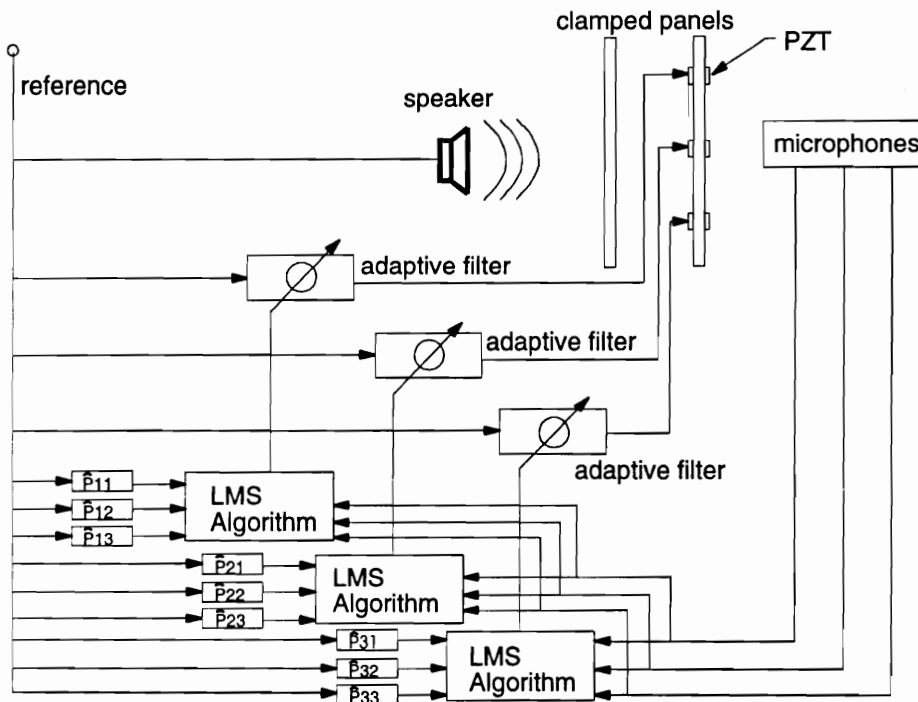


Figure 4-9. Filtered-X LMS control system schematic for ASAC tests

#### 4.2.2. Biologically inspired hierarchical control algorithm

In the theoretical analysis for the biologically inspired hierarchical (BIO) controller (Chapter 3), a frequency domain analysis was used which included the control path transfer function ( $H$ ) to determine the effect of the addition slave control paths on the update equation. Physical implementation of a frequency domain controller requires that the error signal be transformed from the time domain to the frequency domain which is extremely inefficient computationally. However, it is well known that the frequency domain magnitude of a single frequency harmonic signal can be approximated by the sum of the squares of the time domain signal. The implementation of this approximation has much less computational complexity than a frequency

domain transformation. The approximation has been implemented to estimate the gradient of a LMS controller which is referred to as the time averaged gradient (TAG) LMS algorithm and has been shown to be suitable for averaging out noisy error signals. For the above reasons, the TAG LMS algorithm was chosen for the physical implementation of the biologically inspired control algorithm. The implications of using the TAG LMS versus the frequency domain algorithm are discussed in the following paragraph.

The update equation used for the time averaged LMS control algorithm was defined in Eq. (3.5). For the TAG LMS algorithm, the gradient ( $\nabla$ ) at iteration  $k$  is defined as the finite difference approximation of the change in the time averaged cost function ( $J$ ) with respect to the vector of FIR filter coefficients ( $w$ ), written as:

$$\nabla_k = \frac{\Delta J}{\Delta w} = \left( \frac{J_k - J_{k-1}}{w_k - w_{k-1}} \right). \quad (4.10)$$

where the time averaged cost function at time step  $t$  is defined as:

$$J_k = \frac{1}{N} \sum_{t=1}^N J_t \quad (4.11)$$

and  $N$  is the total number of time sample points. By combining the update equation (Eq. (3.5)) with Eq. (4.10), the TAG LMS update equation can now be written:

$$w_{k+1} = w_k + \mu(-\nabla_k) = w_k - \mu \frac{\Delta J}{\Delta w} = w_k - \mu \left( \frac{J_k - J_{k-1}}{w_k - w_{k-1}} \right) \quad (4.12)$$

Note that the use of the time averaged LMS algorithm does not directly include the control path transfer function ( $H$ ) in the gradient or the adaptive filter update equation. However, it can be shown that the finite difference approximation of the gradient in Eq. (3.6) is equivalent to the

gradient defined in Eq. (4.10) as  $\Delta w \rightarrow 0$ . Therefore, when applied to a physical system, the frequency domain controller and the time averaged LMS controller will converge to the same optimal adaptive filter ( $w_{opt}$ ) and stability bounds are comparable.

An effective cost function for active noise control is radiated sound power. An approximation of radiated sound power has already been defined in Eq. (4.4) as the sum of the microphone mean square voltage. Therefore a cost function which approximates radiated sound power at a time step  $t$  can be defined as:

$$J_t = \sum_{i=1}^M |V_i|^2 \quad (4.13)$$

where  $V_i$  is the microphone voltage, subscript  $i$  indicates the microphone number index, and  $M$  is the total number of microphones.

The biologically inspired hierarchical control algorithm (BIO) was programmed on a TMS320C30 digital signal processor (DSP) mounted in a 80386 33 MHz Personal Computer (PC). To increase the maximum sampling rate, the number of operations performed by the DSP was minimized. Therefore, the I/O functions, the cost function and the FIR filter calculations were performed on the DSP, while the controller logic was performed on the PC and communicated to the DSP. The sample rate for the controller was set at approximately ten times the excitation frequency with each error signal consisting of 250 time sample points, leading to an update for the FIR filter approximately every 0.05 seconds at a sampling frequency of 5000 Hz. Figure 4-10 shows the experimental schematic of the BIO controller for the double panel experiments.

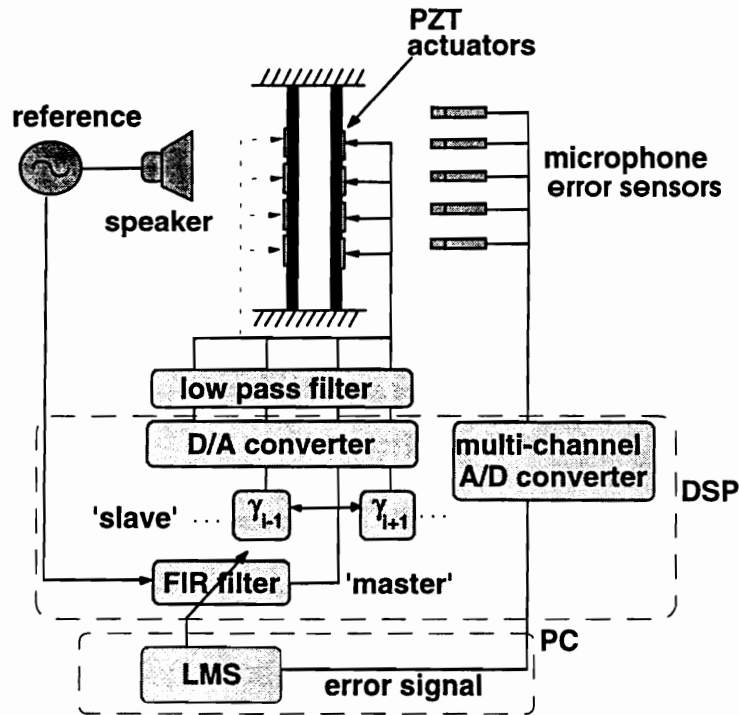


Figure 4-10. Biologically inspired hierarchical (BIO) control system schematic

### 4.3. Performance criteria

Controller performance was evaluated in terms of reduction in cost function, which is defined as the reduction in transmission loss (TL). A comparison of stable system convergence parameters is determined to show that stability bounds are predictable for the novel control approach. Finally, controller performance for the BIO controller was compared to those of a conventional MIMO Filtered-X LMS controller for a benchmark comparison.

#### *Controller performance*

Performance of the control algorithm is most logically defined as the reduction in the cost function as:

$$reduction(dB) = 10 \log_{10} \left( \frac{J_{uncontrolled}}{J_{controlled}} \right) \quad (4.14)$$

where  $J_{uncontrolled}$  is the uncontrolled cost function and  $J_{controlled}$  is the controlled cost function as defined in Section 4.2. However, the preceding discussion in this chapter and specifically the definitions of Eqs. (4.2), (4.4), and (4.13) show that the reduction in cost function is directly an approximation of the *increase in transmission loss with control*. Since this is the fundamental measure of double panel system acoustic performance, the analytical data in Chapter 5 as well as the experimental data in Chapter 6 are presented in these terms.

### ***Controller convergence***

It was predicted in Section 3.2 and Carneal and Fuller (1995a) that the maximum convergence parameter ( $\mu_{max}$ ) for stability would be less for a BIO controller compared to the maximum convergence parameter for a single output system. Experiments were performed to verify this trend.

To determine the maximum convergence parameter, the control program was run with the convergence parameter set at different values. The program was allowed to continue until it was determined to be unstable, marginally stable or stable as explained in the following paragraph. The maximum convergence parameter was defined as the largest value that resulted in a stable system.

To determine the stability of the system, the variation in cost function was determined, which was defined as difference in the maximum and minimum cost functions over several hundred

iterations of the update equation. This was done using a time trace of the cost function. The stability of the system was divided into three categories: unstable, marginally stable and stable. A stable system was defined as having the variation in cost function being less than 5% of the uncontrolled cost function. A marginally stable algorithm was defined as having the variation in cost function being greater than 5% of the uncontrolled cost function, but the maximum cost function did not increase with time. An unstable system was defined as the maximum cost function increasing with time.

### ***MIMO Filtered-X LMS comparison***

To provide a benchmark comparison with existing control algorithms used, the BIO controller performance was compared to MIMO Filtered-X LMS controller performance when applied to the double panel system test rig described in Sections 4.1.1 and 4.1.2. For the controller comparison, the test conditions were kept the same and only the control methodologies were changed. For example, the same number of error microphones and control actuators were used and the double panel system configuration was kept the same (i.e. the same incident plane wave angle, the same PZT location, the same radiating plate stiffness, etc.). As stated previously in Section 4.2.1, the cost function was not directly accessible for the Filtered-X LMS and the uncontrolled and controlled cost function ( $J$ ) was determined by measuring the voltages of the microphones (error sensors) and summing the square of these voltages. Again, note that this process is similar to the determination of cost function for the BIO controller as seen in Eq. (4.13).



#### 4.4. Experimental procedure

Several different active structural acoustic control (ASAC) test cases were performed on the double panel system test rig and the Cessna experimental aircraft fuselage described in Section 4.1 including off-resonance and on-resonance frequency excitation. As explained previously, two different control algorithms were tested: the Filtered-X LMS and biologically inspired hierarchical (BIO) controllers. For all these tests, the experimental procedure was the same and is detailed by the controller performance criteria as described in Section 4.3.

##### *Controller performance*

The experimental procedure for the BIO controller master, phase variation, adaptive magnitude, and adaptive phase methods proceeded as follows: First, the disturbance was turned on. The uncontrolled double panel system radiating plate out-of-plane vibrational velocity was then measured using the laser vibrometer, and the uncontrolled cost function was measured. Next, the control program was initialized: the convergence parameter ( $\mu$ ) was set at approximately .01, the master control channel was set to the desired value, and the sampling frequency was set at ten times the excitation frequency. After the invocation of the control algorithm, the master control channel was allowed to converge, then the cost function and the double panel system radiating plate vibration were measured for the *master* case. The local algorithm (phase variation, adaptive magnitude, or adaptive phase) was invoked, and after completion, the cost function and the elastic system vibration was measured for the *local rule* case. The controller was then turned off.

For the optimal method, the disturbance was set at approximately the same level. Uncontrolled double panel system radiating plate vibration and cost function were then measured. The control

programs were initialized: the convergence parameter ( $\mu$ ) was set at approximately .01, the master control channel was set to the desired value, the sampling frequency was set at ten times the excitation frequency, and the local gains were loaded into the algorithm. After the controller was started and allowed to converge, the double panel system radiating plate vibration and cost function were measured for the controlled case.

### ***Controller convergence***

The experimental procedure for the controller convergence test for the BIO controller was as follows: The program was initialized: the step size, the master actuator, and the sampling frequency were set to desired values. The uncontrolled cost function was recorded, then the control algorithm was invoked. While recording the cost functions at each iteration, the algorithm was allowed to continue until it was determined to be unstable, marginally stable or stable. This process was repeated for various values of the convergence parameter.

### ***MIMO Filtered-X LMS controller***

A MIMO Filtered-X LMS controller was applied to control radiated sound power using the experimental rig for the plate described above. The program was initialized: the convergence parameter and the sampling frequency were set. A system identification was then performed to determine the transfer functions between the control inputs and the sensors for use in the Filtered-X algorithm. The disturbance was turned on and set at an appropriate level, then the uncontrolled error sensor voltages were recorded and the control algorithm was invoked. After the controller had converged, the controlled error sensor voltages were recorded.

## **5. Analytical results**

Analytical results calculated from the double panel system, acoustic, and controller models developed in Chapters 2 and 3 are presented in this chapter. First, the acoustical cavity resonances are discussed. Next, the analytical double panel system model is validated through a comparison of the theoretical and experimental system eigenvalues and uncontrolled transmission loss. The analytical model is then applied to the active control of double panel systems and a parametric analysis including the location of control actuators, the radiating plate stiffness, the incident wave oblique angle, the number of control actuators, and the air cavity parameters. Finally, the BIO control algorithm and its various local rules are applied for the case of multiple actuators including computational effort and convergence considerations.

### **5.1. Acoustical cavity resonances**

The acoustical cavity resonances are presented in the light that they may give insight to certain double panel system behavior at or near the resonances. The acoustical cavity resonances were calculated from the Eq. (2.37) using the properties of air and cavity dimensions of 0.381 m long x 0.305 m wide x 0.048 m deep. Note that these dimensions are the same length and width as the incident and radiating plates which were previously presented in Table 4-3. As can be seen in Table 5-1, there are three acoustic cavity resonances in the frequency range of interest (<800 Hz).

These resonances occur at 457 Hz for the (1,0,0) mode, at 581 Hz for the (0,1,0) mode and at 739 Hz for the (1,1,0) mode. Note that the acoustical resonances occur in the x and y directions in this frequency range. The first acoustical resonance in the z-direction (mode (0,0,1)) is at 3572 Hz due to the small cavity depth. This transverse resonance is well above the test frequencies considered in this direction.

**Table 5-1. Acoustic cavity resonances**

mode(m,n,q)	$f_{mnq}$ (Hz)
(1,0,0)	457
(0,1,0)	581
(1,1,0)	739
(2,0,0)	914

## 5.2. Model validation

The analytical double panel system model is validated through a comparison of the theoretical and experimental system eigenvalues and uncontrolled transmission loss. To compare the system eigenvalues, a system identification was performed on the double panel system consisting of aluminum incident and radiating plates. This case represents the more difficult modeling case since a double panel system with an aluminum radiating plate has a higher modal density than a sandwich board radiating plate double panel system as will be discussed. Uncontrolled transmission loss of the theoretical model is then compared to experimental uncontrolled transmission loss data for an aluminum and sandwich board radiating plate double panel system.

### **5.2.1. Plate and double panel system natural frequencies**

A system identification was performed on the double panel system consisting of aluminum incident and radiating plates. There were several tests performed on the individual single plates mounted in the test rig and the total response of the double panel system. For all cases, the system identification was performed using a shaker excited with broadband noise from 0 to 800 Hz. The disturbance signal was obtained from a force transducer between the shaker and the excited plate while the plate flexural motion was determined by using a laser vibrometer mounted on a 2D traverse. Plate flexural velocity was measured at 320 points on a 20 by 16 grid which covered the entire surface of the plate. The signals were input to a B&K model 2032 dual channel signal analyzer where the auto-correlation and cross-correlation of the force transducer and the laser vibrometer were computed. This information was downloaded to a PC compatible computer and analyzed on LMS CADA-PC system identification software which yielded the natural frequencies and mode shapes of the tested system.

A theoretical versus experimental comparison of the single plate natural frequencies is shown in Table 5-2. The theoretical values were calculated using Eq. (2.6) with the plate characteristics given in Table 4-3. The comparison of natural frequencies for the incident plate shows that most values are within 2%. The radiating plate shows a slightly higher variation, but most values are within 4%. The differences in the theoretical and experimental natural frequencies are due to an imperfect modeling of the clamping apparatus of the experimental test rig. Slight variations in the clamped boundary conditions as well as the size of the plates will produce variations in the natural frequencies. Since the theoretical model assumes perfect clamped boundary conditions, variations are expected. Overall, these results indicate good agreement between the analytical

models and the physical system eigenvalues.

The comparison of double panel system natural frequencies is a little more involved. A theoretical versus experimental comparison of the double panel system natural frequencies is presented in Table 5-3. The theoretical values were calculated using Eq. (2.19) with the values given in Table 4-3. As seen in Table 5-3, the double panel system exhibits an in-phase flexural and out-of-phase dilatational motion indicated by two corresponding natural frequencies for each mode. For the in-phase flexural motion, there is little or no relative displacement between the individual plates which means that the spring rate of the acoustical cavity has little effect. For the out-of-phase dilatational motion, the relative displacement between the plates is significant and the increased stiffness (due to the spring rate of the acoustical cavity) of the system results in an increased natural frequency. For a further discussion of the double panel system motion please refer to Section 0.

Again referring to Table 5-3, the comparison of natural frequencies for the in-phase motion shows that most of the values are within 4%. The out-of-phase motion shows slightly higher variation at low frequencies, but most are within 4%. The differences in the theoretical and experimental natural frequencies can be attributed to the clamping apparatus of the experimental test rig as explained previously as well as error propagation from the single plate model into the double panel system model. As with most theoretical models, certain parameters were perturbed to achieve the desired results. It is possible to obtain better estimates of the lower natural frequencies at the cost of poorer estimates of the higher ones. Since the lower frequency limit of the experiments is approximately 300 Hz (due to the anechoic chamber properties), a better

estimate was obtained at the higher frequency range while sacrificing accuracy at the lower range. Overall, both of these results indicate good agreement between the theoretical model and the physical double panel system eigenvalues.

Table 5-4 shows the theoretical natural frequencies for a sandwich board radiating plate double panel system. As compared to the double panel system (aluminum radiating plate) natural frequencies in Table 5-3, the double panel system with a sandwich board radiating plate has a significantly lower modal density due to the elevated natural frequencies of the out-of-phase dilatational motion. This is due to the sandwich board radiating plate which has one natural frequency in the range considered at 497 Hz as determined by the theoretical model of a single sandwich board plate.

For brevity, a system identification is not presented in this dissertation for the sandwich board double panel system. Since the aluminum double panel system represents a more complex case due to the increased modal density, further validation of this sort is repetitive. However, it should be noted that the experimental sandwich board double panel system in-phase and out-of-phase natural frequencies were within 4 % of the theoretical ones presented in Table 5-3. Also, the comparison of theoretical and experimental transmission loss presented in the next section further validates the sandwich board radiating plate radiating plate double panel system model.

**Table 5-2. Aluminum single plate natural frequencies**

plate	incident- theo.	incident - exp.		radiating- theo.	radiating- exp.	
mode	$f_{mn}$ (Hz)	$f_{mn}$ (Hz)	variation (%)	$f_{mn}$ (Hz)	$f_{mn}$ (Hz)	variation (%)
1,1	114	114	0.0	118	113	4.4
2,1	199	197	1.0	205	205	0.0
1,2	263	260	1.2	271	261	3.8
2,2	337	332	1.5	348	341	2.1
3,1	341	342	0.2	351	352	0.2
3,2	472	458	3.1	487	467	4.3
1,3	488	494	1.2	504	490	2.9
4,1	525	534	1.7	542	543	0.2
2,3	564	558	1.1	583	563	3.6
4,2	656	646	1.5	676	643	5.1
3,3	690	697	1.0	712	700	1.7
5,1	761	787	3.3	785	782	0.4



**Table 5-3. Double panel system natural frequencies (aluminum radiating plate)**

mode (m,n)	in-phase $f_{mn}$ (Hz)			out-of-phase $f_{mn}$ (Hz)		
	theo.	exp.	variation (%)	theo.	exp.	variation (%)
1,1	114	119.5	4.6	156	170.7	8.6
2,1	200	196.4	1.8	228	208.5	9.4
1,2	263	260.8	0.8	287	268.8	6.8
2,2	338	335.9	0.6	359	348.5	3.0
3,1	341	348.1	2.1	362	359.1	0.8
3,2	472	463.2	1.9	493	490.3	0.6
1,3	488	500.2	2.4	509	501.3	1.5
4,1	524	543.9	3.7	546	562.4	2.9
2,3	563	560.5	0.4	586	584.5	0.3
4,2	654	642.8	1.7	678	680.1	0.3
3,3	688	698.4	1.5	713	719.5	0.9
5,1	758	-		785	-	

**Table 5-4. Theoretical double panel system natural frequencies (sandwich board radiating plate)**

mode (m,n)	$f_{mn}$ (Hz)	
	in-phase	out-of-phase
1,1	135	500
2,1	211	863
1,2	271	1136
2,2	343	1458
3,1	347	1474
3,2	475	2039
1,3	491	-
4,1	527	-
2,3	566	-
4,2	656	-
3,3	690	-
5,1	760	-

### 5.2.2. Double panel uncontrolled transmission loss

To further validate the double panel system model, experimental and theoretical uncontrolled transmission losses are compared. Theoretical results are calculated from analytical models detailed in Chapter 2 using the properties defined in Table 4-3. The system is described as follows: A normal acoustic plane wave excites the incident plate of a double panel system. The induced incident plate motion excites the acoustic cavity thereby inducing motion in the radiating

plate. The radiating plate then emits acoustic power into an acoustic free field. For experimental implementation, the incident acoustic field was provided by a speaker positioned adjacent to the incident plate of the double panel system as described in Chapter 4. A broadband signal of 0 to 800 Hz was input to the speaker providing excitation of the double panel system. Incident pressure measurements were taken by a single microphone positioned near the center of the incident plate. Radiated pressure measurements were taken by a microphone positioned at several points on a hemisphere in the anechoic insert of the transmission loss test facility. The hemisphere was divided into equal areas and one microphone was placed at the center of each area. The locations of the microphones were given in Table 4-4. From the microphone measurements, an approximation of radiated acoustic power can then be calculated as in Eq. (4.4). All pressure measurements were processed by a B&K model 2032 dual channel signal analyzer where the auto-correlation and cross-correlation of the disturbance signal and the pressure measurements were computed. This information was downloaded to an PC compatible computer and analyzed using a MATLAB code which yielded the transmission loss data as per calculations detailed in Chapter 2. The data was then averaged using the one third octave band technique.

A comparison of the theoretical and experimental uncontrolled transmission loss of the aluminum radiating plate double panel system is shown in Figure 5-1. Note that the transmission loss minima correspond to the natural frequencies of the system with the most prominent occurring at the in-phase and out-of-phase (1,1) (~120-170 Hz), (3,1) (~350-360 Hz), and (1,3) (~490-500 Hz) modes. This agrees with the theoretical model for an normal plane wave which indicates that a uniform excitation field can only excite the symmetric modes, i.e. modes that

have an odd-odd index. However, the experimental results show minima at other natural frequencies of the double panel system, namely the (1,2) (~260-280 Hz) and (4,1) (~520-560 Hz) modes. The excitation of these modes could be attributed to a number of things including an imperfect normal acoustic plane wave and/or the structural flanking path.

The one third octave band results are presented in Figure 5-2 where it can be seen that the theoretical and experimental uncontrolled transmission loss trends compare very well. The differences in magnitude are due to the discrepancies in off-resonance transmission loss. Sources of this discrepancy can be attributed to the radiated acoustic pressure model as well as the off-resonance excitation levels of the double panel system. As stated earlier, the intent is to provide a model to investigate the trends involved with active control of double panel systems, not to predict exact magnitudes. As can be seen in Figure 5-1 and Figure 5-2, this goal has been attained.

A comparison of the theoretical and experimental uncontrolled transmission loss of the sandwich board radiating plate double panel system is shown in Figure 5-3. In this plot, the prominent transmission loss minima occur at the in-phase (1,1) mode (~135 Hz), the in-phase (3,1) mode (~350 Hz) and the out-of-phase (1,1) mode (~500 Hz). Notice there are less minima compared to the aluminum radiating plate double panel system (Figure 5-1) due to the lower modal density of the sandwich board radiating plate. As seen in Figure 5-4, the theoretical and experimental one third octave band levels show good agreement. It should be noted that the transmission loss level are significantly higher (as compared to Figure 5-2) in the low frequency range of 100-200 Hz due to the absence of an efficient acoustic radiating mode resonance. These results agree with

Carneal and Fuller (1995c) who found that a stiff radiating plate exhibited increased uncontrolled transmission loss over a more flexible radiating plate.

In summary, the theoretical and experimental results show good agreement in the double panel system natural frequencies and the trends in uncontrolled transmission loss. Further improvements in modeling of the incident acoustic field and/or the double panel system boundary conditions could possibly minimize the discrepancies seen in transmission loss magnitudes.

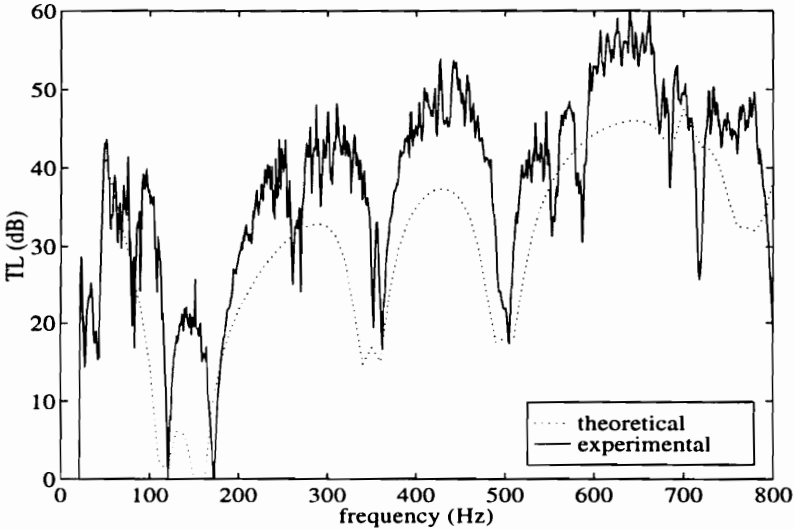


**Figure 5-1. Uncontrolled aluminum radiating plate double panel system TL.**

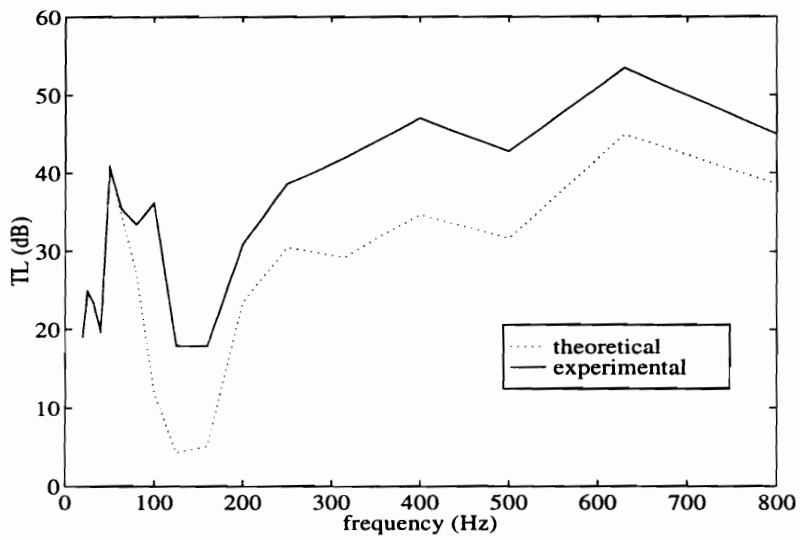


**Figure 5-2. Third octave uncontrolled aluminum radiating plate double panel system TL.**

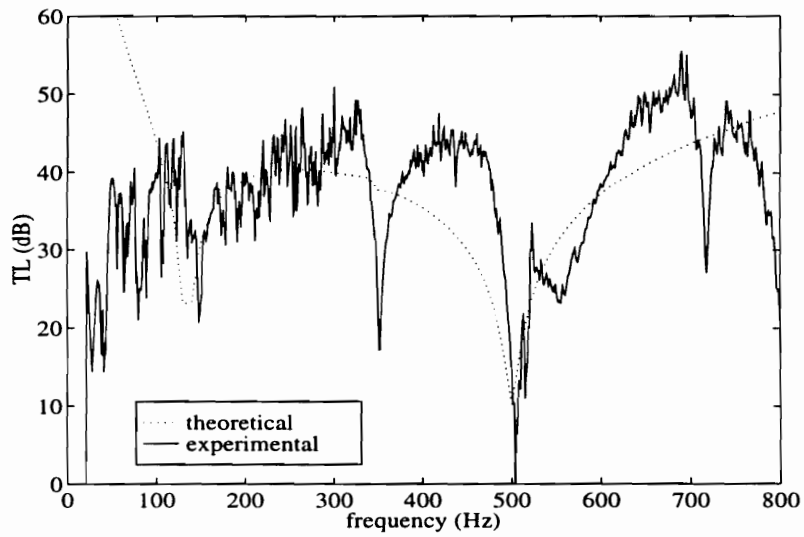


**Figure 5-3. Uncontrolled sandwich board radiating plate double panel system TL.**

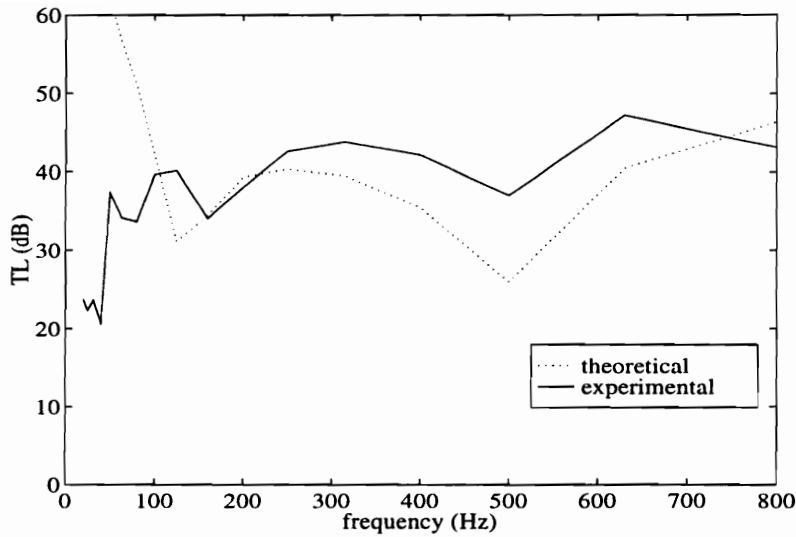


**Figure 5-4. Third octave uncontrolled sandwich board radiating plate double panel system TL.**

### 5.3. Active control of double panel systems

This section theoretically investigates the active control of double panel systems. The theoretical investigation uses the models previously defined in Chapter 2 with the properties presented in Table 4-3. The basic double panel system model can be stated as follows: An oblique acoustic plane wave excites an aluminum incident plate of a double panel system. The induced incident plate motion excites the acoustic cavity thereby inducing motion in the radiating plate. The radiating plate then emits acoustic power into an acoustic free field. In this investigation, the cost function is defined as the radiated acoustic power from the radiating plate. This was calculated using a Simpson's rule approximation of the radiated power formulation defined in Eq. (2.54). Control is provided by four piezoelectric (PZT) actuators at the locations given in Table 4-6. Note that the analytical model PZT actuator locations were positioned to match the experimental PZT locations. Control inputs are generated by linear quadratic optimal control theory (LQOCT)

as previously described in Section 3.3. The results are presented in several subsections that provide insight to the active control of double panel systems by perturbing the basic double panel system parameters. Specifically, the influence of the following double panel system parameters on control performance are studied: the radiating plate stiffness (aluminum or sandwich board), PZT actuator location (incident or radiating plate), the incident pressure field (normal or oblique incident wave), the number of PZT actuators, and air cavity parameters (mass and stiffness). Note that the incident plate of the double panel system is always aluminum which is an approximation of the fuselage skin of an aircraft.

In this and the following chapters, the compound adjectives associated with a full system description can become excessive. For instance, for the PZT location parameter, the full description of the double panel system would be *a sandwich board radiating plate double panel system with incident plate PZT locations*. In this dissertation, this full description will be stated only once for brevity. Once the full description has been stated, an abbreviated description using the word *case* will be used. For example, the above description will be shortened to the *incident PZT case*.

It should also be noted that the same data is presented in Table 5-5, Table 5-6, and Table 5-7 although the table format has been restructured. This has been done to allow an easier comparison of the values presented.

### **5.3.1. Effect of radiating plate stiffness on control performance**

The first perturbed parameter is the radiating plate stiffness where an aluminum radiating plate is used for a relatively flexible case and a sandwich board is used for a relatively stiff case. The



effect of radiating plate stiffness on the increase in frequency averaged transmission loss ( $TL_{avg}$ , as defined in Eq. (2.35)) with control is presented in Table 5-5 for the perturbed double panel system parameters of incident plane wave and PZT location. The increase in  $TL_{avg}$  is presented for two distinct averages, one from 50-800 Hz and 300-800 Hz. This has been done to provide results that can be compared with the experimental results in Chapter 6. (Recall in Chapter 4 that the lower frequency limit of the radiating chamber anechoic insert of the transmission loss test facility was 300 Hz). Note that the double panel system parameters for all of the figures in this section are for a double panel system excited by an oblique incident plane wave and controlled by PZTs located on the radiating plate.

As can be seen in Table 5-5, better control is achieved for a double panel system with a sandwich board radiating plate over an aluminum radiating plate by approximately 11-30 dB depending on the system parameters. The explanation for this behavior is due to the modal density of the double panel system. Figure 5-5 shows the uncontrolled and controlled transmission loss for a double panel system excited by an oblique incident wave with the PZTs located on an aluminum radiating plate. As compared to the same test parameters with a sandwich board radiating plate in Figure 5-6, the aluminum case exhibits several more TL minima compared to the sandwich board case, which indicates the aluminum case has a higher modal density. Since the amount of control is directly related to the number of control channels with respect to the number of excited modes (and the controllability of those modes), a double panel system with a higher modal density will attain less control than one with a low modal density for a given number of control actuators.

This is verified in the uncontrolled and controlled modal response of the aforementioned double

panel systems at 500 Hz with a sandwich board radiating plate and an aluminum radiating plate seen in Figure 5-7 and Figure 5-8, respectively. The uncontrolled radiating plate response for the sandwich board case shows one mode is excited (the fundamental mode) where three modes are excited (the (3,2), (1,3), and (4,1) modes) for the aluminum case. From these results, it is evident that the aluminum case has a higher number of excited modes than the sandwich board case. Control of the sandwich board case results in no significant spillover where the aluminum case shows spillover for both the incident and radiating plates.

Double panel systems exhibit interesting behavior which can be seen by comparing of Figure 5-9, Figure 5-10, and Figure 5-11 where the uncontrolled and controlled double panel system modal amplitudes for the aluminum case are presented for an excitation frequency of 100, 120, and 130 Hz, respectively. These three frequencies are slightly below the in-phase fundamental (114 Hz), slightly above the in-phase fundamental, and half way in between the in-phase and out-of-phase fundamental frequencies, respectively. As seen in Figure 5-9, control is achieved by reducing the (1,1) mode of the radiating plate with some spillover into the higher order modes. This also produces a reduction in the fundamental of the incident plate as well, however the effect of the radiating plate on the incident plate is small. As the excitation frequency crosses the in-phase fundamental, a reduction in TL is achieved by the same method, however the radiating plate spillover has increased as seen in Figure 5-10. The reduction of the incident plate response is more significant indicating that the plates are more coupled than at the previous frequency. As the excitation frequency increases to 130 Hz (Figure 5-11), the uncontrolled response of the radiating plate is greater than the incident plate and control of the radiating plate actually increases the fundamental mode of the incident plate. This behavior is mirrored as the frequency

increases and passes the out-of-phase fundamental. The uncontrolled response of the incident plate becomes greater than the radiating plate response, the influence of the radiating plate control on the incident plate decreases, and the incident and radiating plate spillover decreases. This behavior was also noticed near the (3,1) in-phase and out-of-phase resonances. From this behavior, it is evident that the coupling of the acoustic cavity is greatest near and in between the in-phase and out-of-phase resonances for a double panel system with an aluminum radiating plate.

However, the coupling of the incident and radiating plate is much less for the sandwich board case. As seen in Figure 5-7, the modal response of a double panel system with a sandwich board radiating plate excited at the out-of-phase fundamental resonance shows that control of the radiating plate has little effect on the incident plate. This type of behavior is typical for the sandwich board case and is independent of excitation frequency. This is a result of the low modal density of the radiating plate. Control is achieved by modal reduction which reduces the response of the radiating plate. Since the incident and radiating plate are not well coupled, the influence of the control actuators on the incident plate is minimal.

Maximum control effort for a double panel system excited by an oblique incident wave and with PZTs mounted on the radiating plate is shown in Figure 5-12. The maximum control effort is defined as the sum of the absolute value of the control voltages calculated in Eq. (3.27). As can be seen in this figure, a double panel system with an aluminum radiating plate requires more control effort (voltage) than one with a sandwich board radiating plate. At first this seems to be an erroneous result since the sandwich board radiating plate is much stiffer than the aluminum

radiating plate. However, the sandwich board radiating plate is also thicker than the aluminum radiating plate. The end result is that the sandwich board radiating plate PZT forcing function ( $p_{mn}^c$  in Eq. (2.46) with a unit applied PZT voltage (V)) is an order of magnitude greater than the one for an aluminum radiating plate.

For an explanation of this behavior, the response of the radiating plate must be examined. First, the total radiating plate response ( $W_{mn}^{t,r}$  in Eq. (3.26)) is the superposition of the response of the radiating plate to the disturbance ( $W_{mn}^{d,r}$ ) and each PZT actuator ( $W_{mn}^{c,r}$ ). The radiating plate response to a disturbance ( $W_{mn}^{d,r}$  in Eq.(2.42)) can further be reduced to the product of the radiating plate frequency response function ( $\Theta_{mn}^r$ ) and the disturbance forcing function ( $p_{mn}^d$ ). Likewise, the radiating plate response to the PZT actuators (Eq. (2.52)) can be reduced to the product of the radiating plate frequency response function ( $\Theta_{mn}^r$ ) and the PZT actuator forcing function ( $p_{mn}^c$ ). Now, the effect of the increased stiffness of the sandwich board radiating plate actually decreases the double panel system frequency response function ( $\Theta_{mn}^r$ ) which decreases both the disturbance ( $W_{mn}^{d,r}$ ) and the PZT ( $W_{mn}^{c,r}$ ) modal amplitudes. However, the increased thickness of the sandwich board radiating plate also increases the radiating plate PZT forcing function ( $p_{mn}^c$  in Eq. (2.46) with a unit applied PZT voltage (V)). Therefore, the applied voltage to the PZT for control will be less for the thicker sandwich board radiating plate than the aluminum one although the disturbance ( $W_{mn}^{d,r}$ ) and the PZT ( $W_{mn}^{c,r}$ ) modal amplitudes have decreased.

In summary, control of a double panel system with a stiff radiating plate exhibits better increase in transmission loss with control due to a lower modal density of the system and reduced coupling between the incident and radiating plates. When the PZTs are mounted on the sandwich board radiating plate, control effort is seen to decrease compared to an aluminum radiating plate due to its increased thickness leading to better impedance matching.

**Table 5-5. Effect of radiating plate stiffness on frequency averaged transmission loss**

		radiating plate			
		aluminum	sandwich board	aluminum	sandwich board
PZT location	incident wave	increase in $TL_{avg}$ (dB) 50-800 Hz		increase in $TL_{avg}$ (dB) 300-800 Hz	
incident	normal	30.0	49.1	11.4	22.6
	oblique	30.3	48.8	11.0	22.9
radiating	normal	23.8	53.6	12.3	39.9
	oblique	24.2	53.4	10.8	38.3

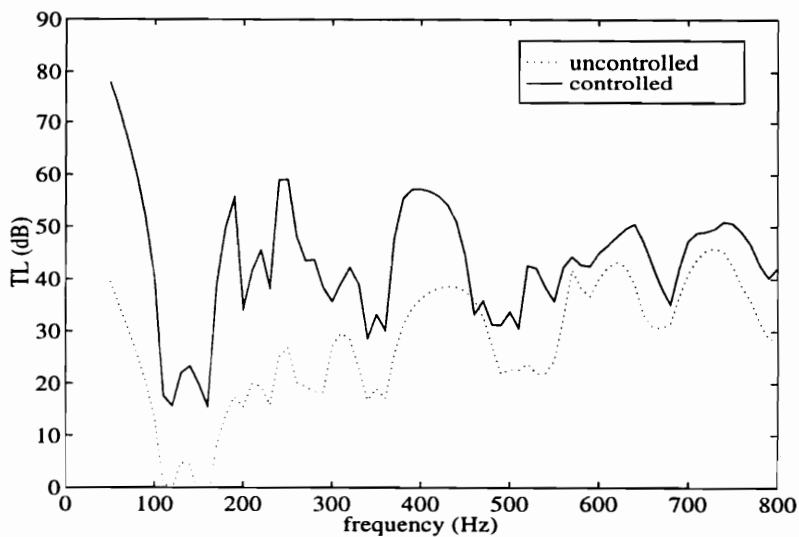


**Figure 5-5. Uncontrolled and controlled transmission loss for double panel system with aluminum radiating plate (oblique incident wave; radiating plate PZT location)**

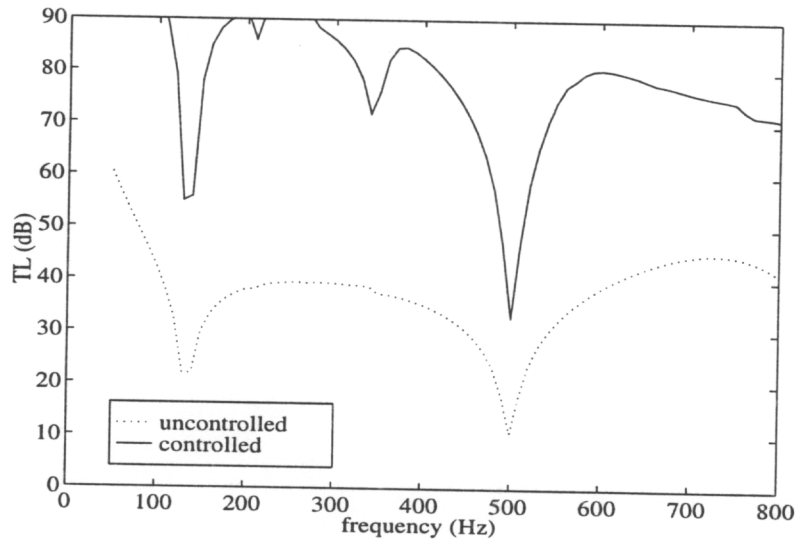


**Figure 5-6. Uncontrolled and controlled transmission loss for double panel system with sandwich board radiating plate (oblique incident wave; radiating plate PZT location)**

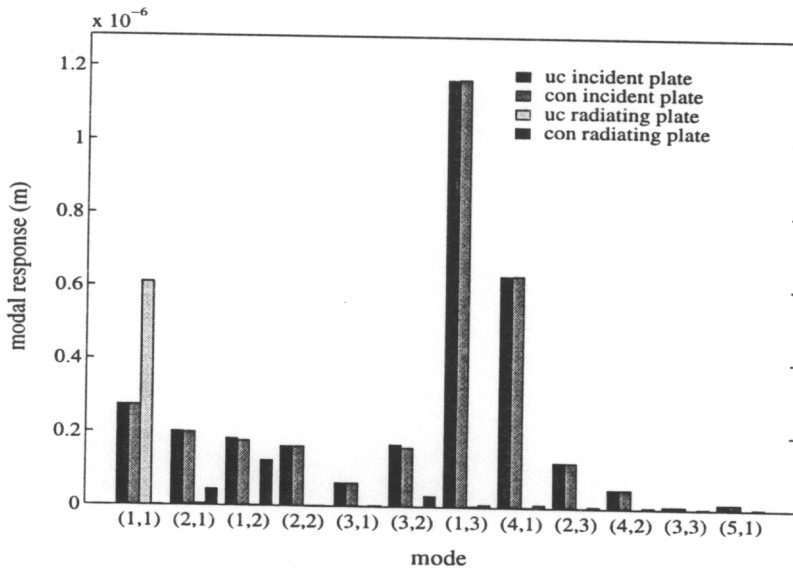


**Figure 5-7. Uncontrolled and controlled double panel system modal amplitudes at 500 Hz with sandwich board radiating plate (oblique incident wave; radiating plate PZT location)**

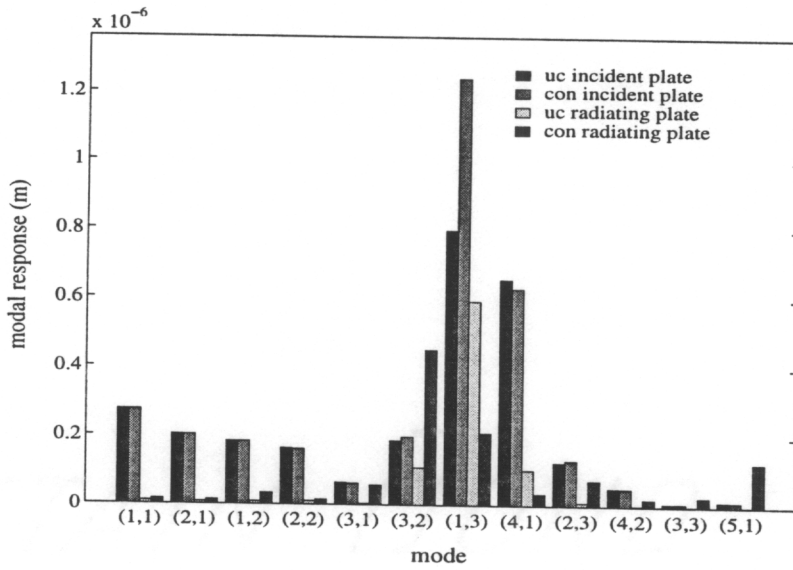


**Figure 5-8. Uncontrolled and controlled double panel system modal amplitudes at 500 Hz with aluminum radiating plate (oblique incident wave; radiating plate PZT location)**

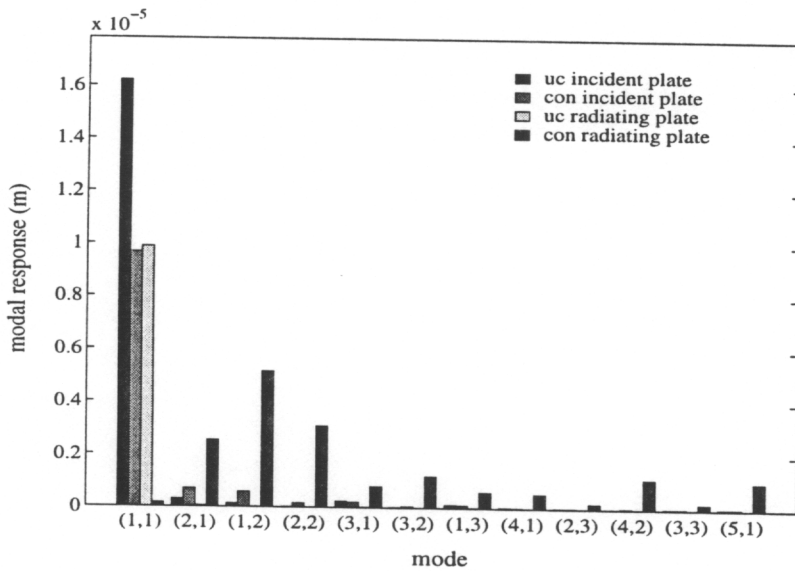


**Figure 5-9. Uncontrolled and controlled double panel system modal amplitudes at 100 Hz with aluminum radiating plate (oblique incident wave; radiating plate PZT location)**

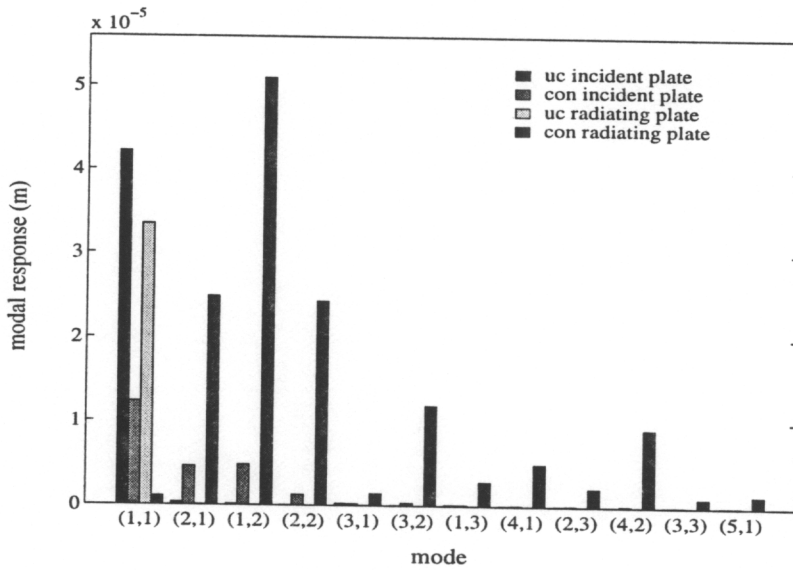


Figure 5-10. Uncontrolled and controlled double panel system modal amplitudes at 120 Hz with aluminum radiating plate (oblique incident wave; radiating plate PZT location)

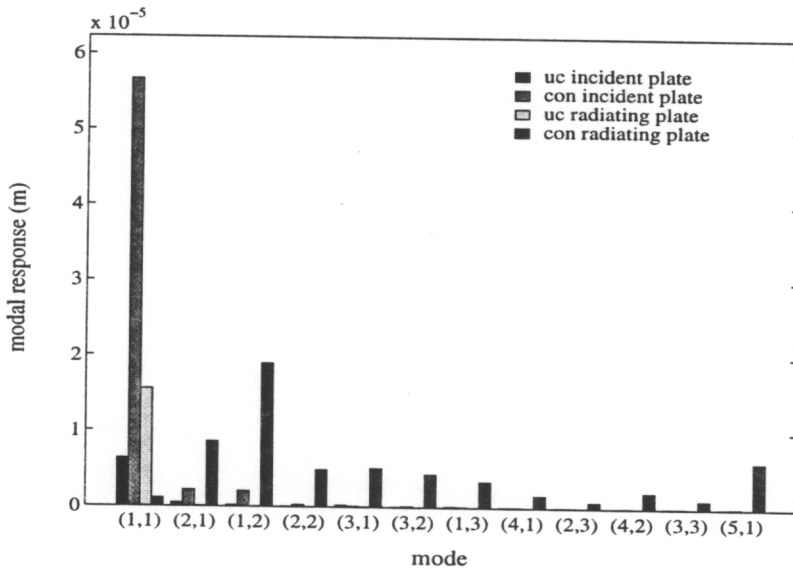
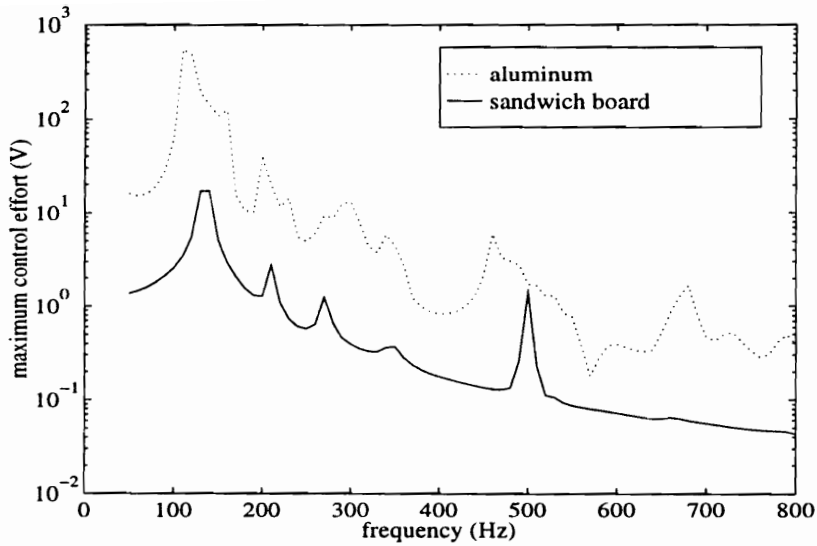


Figure 5-11. Uncontrolled and controlled double panel system modal amplitudes at 130 Hz with aluminum radiating plate (oblique incident wave; radiating plate PZT location)





**Figure 5-12. Maximum control effort for a double panel system with an aluminum and sandwich board radiating plate (oblique incident wave; PZTs located on radiating plate)**

### 5.3.2. Effect of PZT location on control performance

In this section, the effect of the control actuator location on double panel system control performance is presented. The control actuators (piezoelectric actuators or PZTs) can be positioned either on the incident or radiating plate of the double panel system and will be referred to as the *incident PZT case* and the *radiating PZT case*. As can be seen in Table 5-6, the effect of PZT location on frequency averaged transmission loss ( $TL_{avg}$ ) depends on the choice of radiating plate stiffness and the range over which the transmission loss was averaged. For an aluminum radiating plate with control performance averaged from 50-800 Hz, the incident PZT case attained approximately 6 dB more  $TL_{avg}$  than the radiating PZT case. Looking at the performance numbers for the 300-800 Hz averaged transmission loss, the incident PZT case indicates no advantage for the aluminum radiating plate double panel system. However, for the sandwich board radiating plate double panel system, the radiating PZT case performs better than the incident PZT case regardless of the transmission loss averaging range.

The uncontrolled and controlled transmission loss for a double panel system with a sandwich board radiating plate and excited by an oblique plane wave is shown in Figure 5-13. Control of the system with PZTs mounted on the radiating plate is more effective by approximately 20 dB at frequencies above 300 Hz. This behavior can be explained by the coupling of the control actuators into the radiating acoustic field. As seen in the modal response of the incident PZT case at 360 Hz (Figure 5-14), control of the double panel system results in significant spillover of the incident plate into several higher order modes. As stated in the previous section, the motion of the incident plate is not significantly coupled into the motion of the sandwich board radiating plate and therefore is not coupled significantly into the radiated acoustic field. Compared to the radiating PZT case with the same parameters (Figure 5-15), there is no spillover for the incident or radiating plates. The PZTs are directly coupled into the radiated acoustic field and therefore better control is achieved.

The results for a aluminum radiating plate double panel system are not as definite. Figure 5-16 shows the uncontrolled and controlled transmission loss for an aluminum radiating plate double panel system excited by a normal incident plane wave. As can be seen, the effect of the PZT location on control performance varies with frequency. Again, the amount of coupling between the PZT actuators and the radiated acoustic field is the issue. For an excitation frequency of 300 Hz, the incident PZT case shows reduction of the incident plate (1,1) mode with spillover into the (3,1) and (1,3) modes and reduction of the radiating plate (1,1) mode as seen in Figure 5-17. The incident plate PZT's achieved modal reduction (Fuller, 1989) of the radiating plate (1,1) mode with some spillover. Conversely, the modal response of the radiating PZT case seen in

Figure 5-18 shows significant spillover into all the radiating plate efficient acoustic radiators (modes (1,1), (3,1) and (1,3)) with little change in the incident plate response. It is evident that the main control mechanism of the radiating PZT case is modal restructuring (Fuller, 1989) of the radiating plate. Since modal restructuring is a less efficient mechanism of reducing sound power than modal reduction, the incident PZT case resulted in better reduction in the radiated sound power which results in increased transmission loss.

At an excitation frequency of 390 Hz, the radiating PZT case shows better control performance than the incident PZT case as seen in Figure 5-16. The modal response of the incident PZT case (Figure 5-19) shows reduction of the incident plate (1,1) and (3,1) modes with significant spillover of the (2,1) (4,1) (2,3) and (5,1) modes. The radiating plate response shows a reduction of the (1,1) and (3,1) modes with spillover into the rest of the modes. Conversely, the modal response of the radiating PZT case (Figure 5-20) shows little change in the incident plate response and good reduction of the radiating plate (1,1) and (3,1) modes. Both the incident and radiating PZT case exhibit modal reduction (Fuller, 1989) of the radiating plate with spillover. However, it is evident that the radiating PZT case can couple more effectively into the double panel system response and achieve more effective modal reduction of the radiating plate than the incident PZT case. The result is better reduction in the radiated sound power and increased transmission loss.

An explanation for the behavior of the aluminum radiating plate double panel system is not as apparent as the above example. As can be seen in Figure 5-16, the effect of the PZT location on control performance varies with frequency. Note that there are several crossover frequencies

where the PZT location resulting in greater controlled TL switches between the incident and the radiating PZT case. The first crossover frequency is near the out-of-phase (3,1) resonance (~360 Hz). The second crossover frequency occurs near the first acoustic cavity resonance (~440 Hz) and the third crossover frequency occurs near the second acoustic cavity resonance (~580 Hz). Due to occurrence of the crossovers at these frequencies, it can be speculated that the complex modal behavior of the incident and radiating plates coupled by an acoustic cavity changes the amount of influence that a control actuator will have on the response of a double panel system with an aluminum radiating plate. For some frequencies, the influence is greater for the incident PZT case and for others the influence is greater for the radiating PZT case. As was discussed previously, the sandwich board radiating plate double panel system did not exhibit such behavior.

It should be noted that the above analysis did not take the PZT control effort into account. This quantity is defined as the sum of the absolute value of the control voltages calculated in Eq. (3.27). As can be seen in Figure 5-21, the maximum control effort for the incident PZT case is significantly higher than the radiating PZT case. This again demonstrates that a direct coupling of the control actuators into the radiated acoustic field (i.e. PZT's located on the radiating plate) is beneficial. Taking the very large amount of increased control effort for the incident PZT case and the relatively small increase in frequency averaged transmission loss into account, placement of the PZT actuators on the incident plate would be a poor choice.

In summary, better reduction in transmission loss is attained with a double panel system having PZT actuators placed on a sandwich board radiating plate. For an aluminum radiating plate

double panel system, the increased control effort and inconsistent performance of the incident plate PZT location over the frequency range makes the radiating plate PZT location the better choice.

**Table 5-6. Effect of PZT location on frequency averaged transmission loss**

		PZT location			
		incident	radiating	incident	radiating
radiating plate	incident wave	increase in $TL_{avg}$ (dB) 50-800 Hz		increase in $TL_{avg}$ (dB) 300-800 Hz	
		aluminum	normal	30.0	23.8
	oblique	30.3	24.2	11.0	10.8
sandwich board	normal	49.1	53.6	22.6	39.9
	oblique	48.8	53.4	22.9	38.3

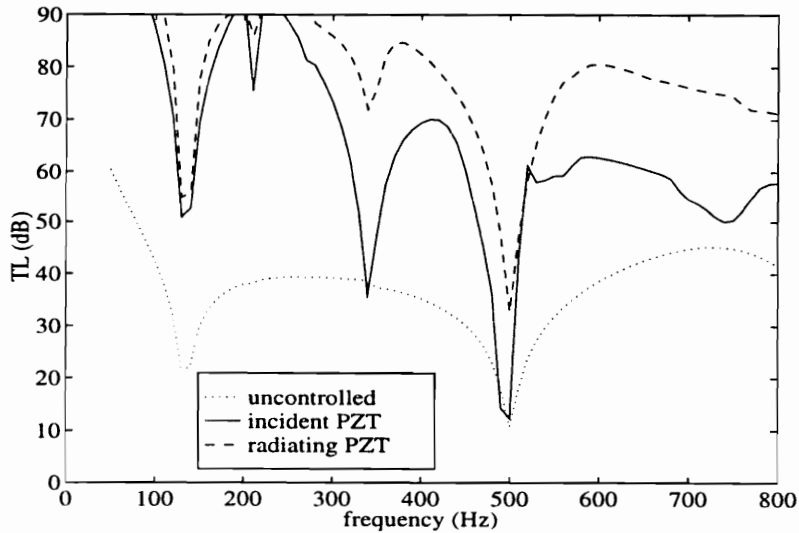


**Figure 5-13. Uncontrolled and controlled transmission loss for double panel system with PZTs located on incident and radiating plates (oblique incident wave; sandwich board radiating plate)**

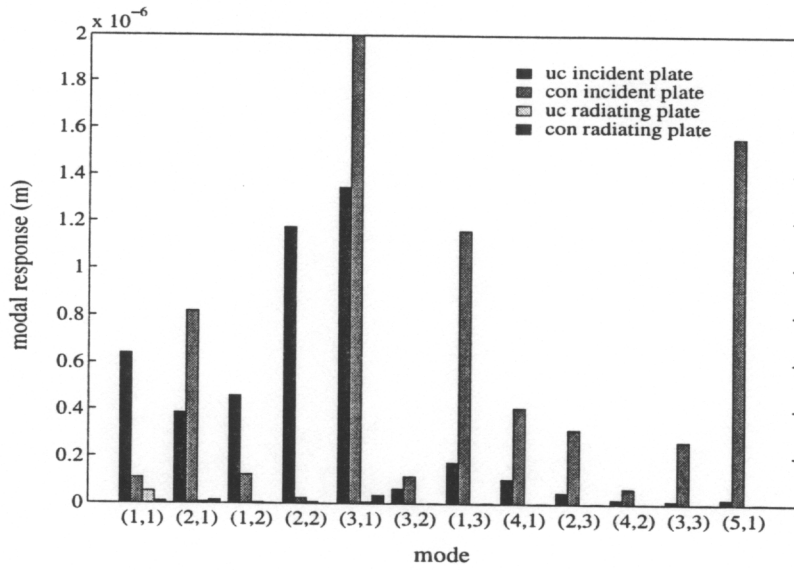


Figure 5-14. Uncontrolled and controlled double panel system modal amplitudes at 360 Hz with PZTs located on incident plate (oblique incident wave; sandwich board radiating plate)

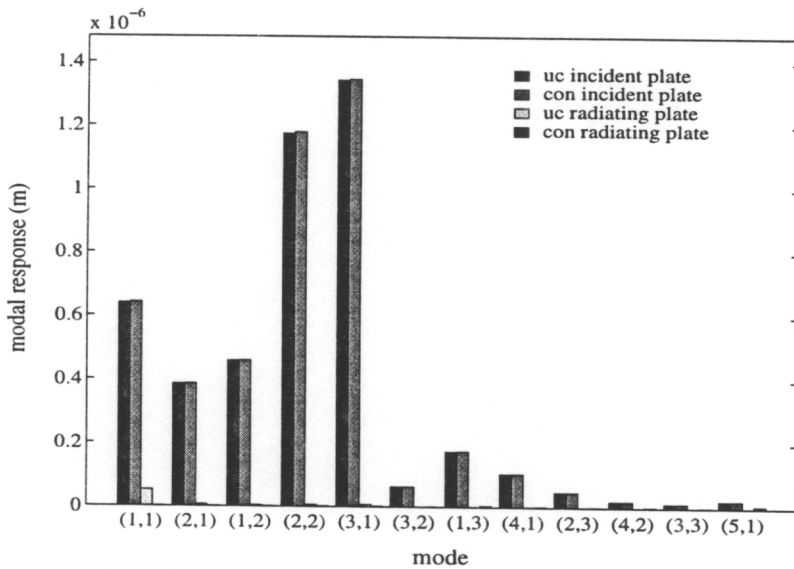
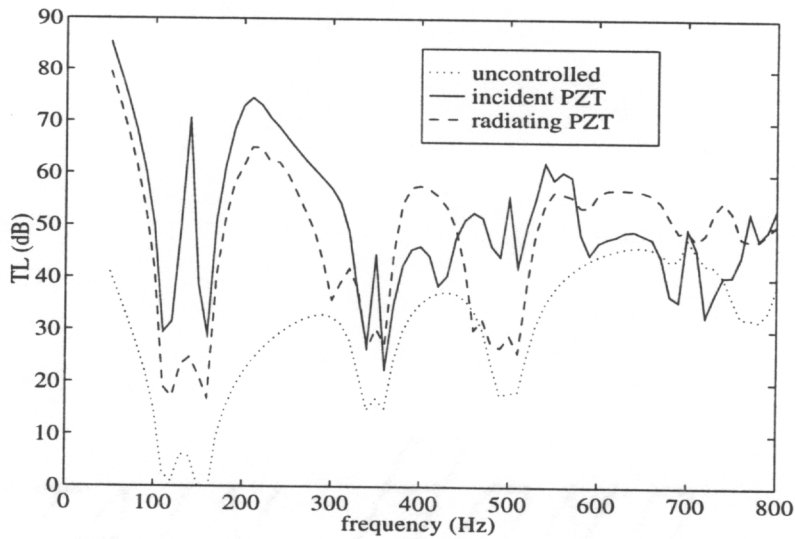
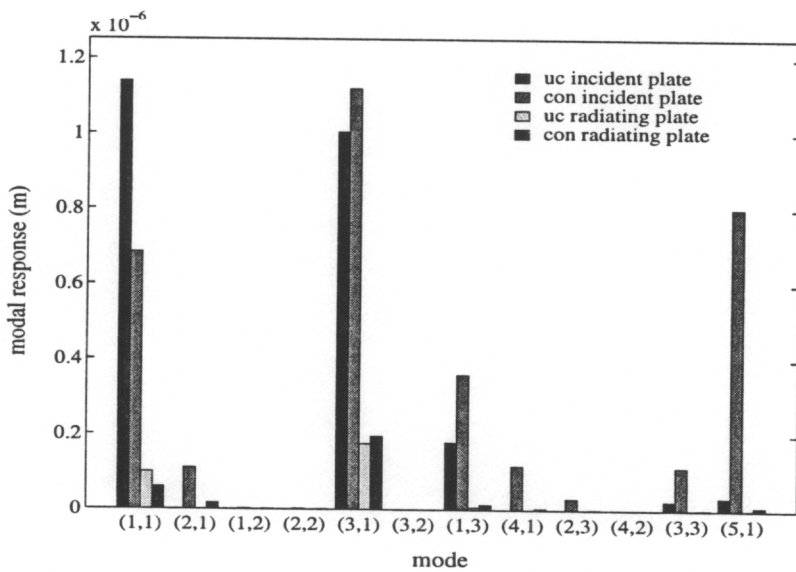


Figure 5-15. Uncontrolled and controlled double panel system modal amplitudes at 360 Hz with PZTs located on radiating plate (oblique incident wave; sandwich board radiating plate)



**Figure 5-16. Uncontrolled and controlled transmission loss for double panel system with PZTs located on incident and radiating plates (normal incident wave; aluminum radiating plate)**



**Figure 5-17. Uncontrolled and controlled double panel system modal amplitudes at 300 Hz with PZTs located on incident plate (normal incident wave; aluminum radiating plate)**

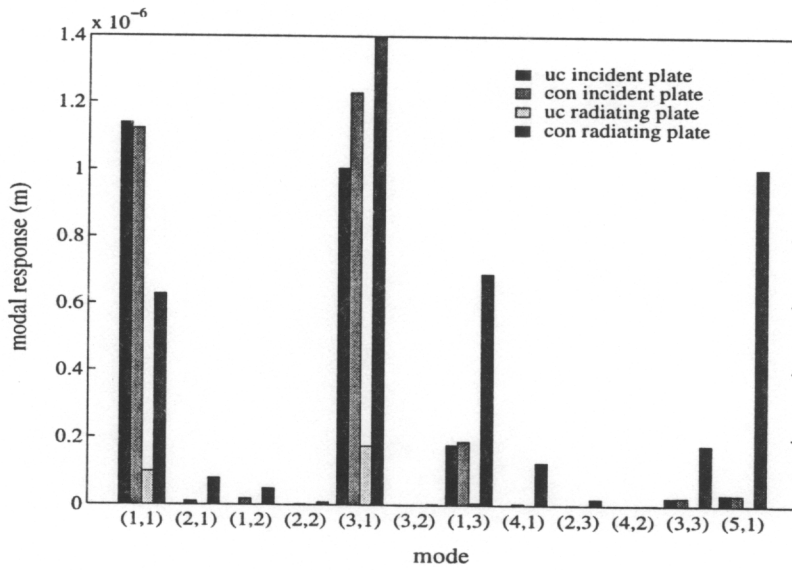


**Figure 5-18. Uncontrolled and controlled double panel system modal amplitudes at 300 Hz with PZTs located on radiating plate (normal incident wave; aluminum radiating plate)**

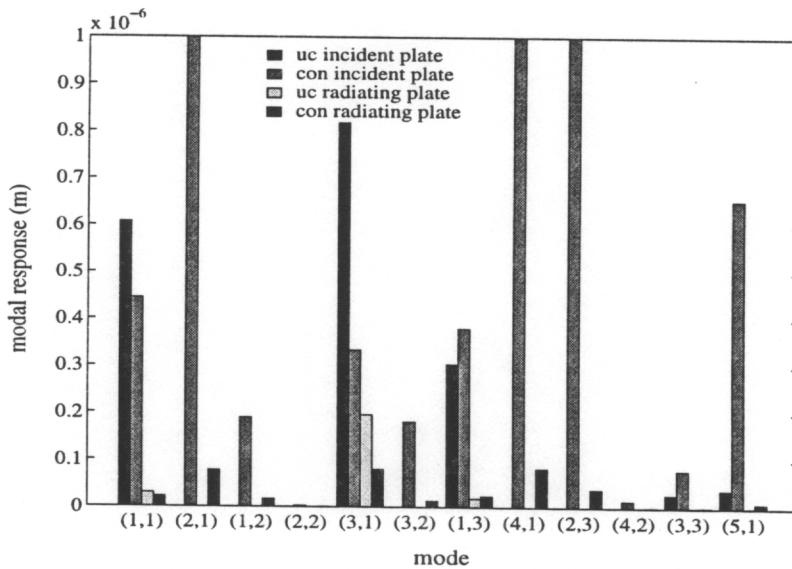


**Figure 5-19. Uncontrolled and controlled double panel system modal amplitudes at 390 Hz with PZTs located on incident plate (normal incident wave; aluminum radiating plate)**



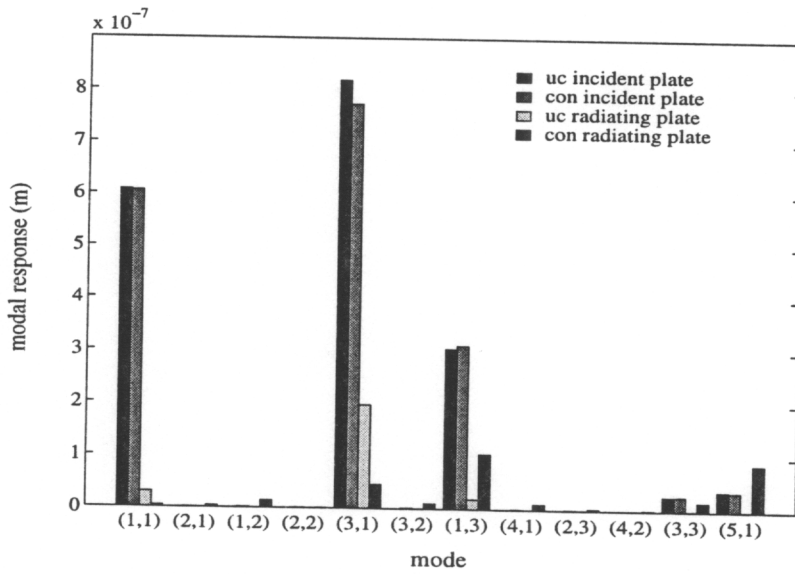


Figure 5-20. Uncontrolled and controlled double panel system modal amplitudes at 390 Hz with PZTs located on radiating plate (normal incident wave; aluminum radiating plate)

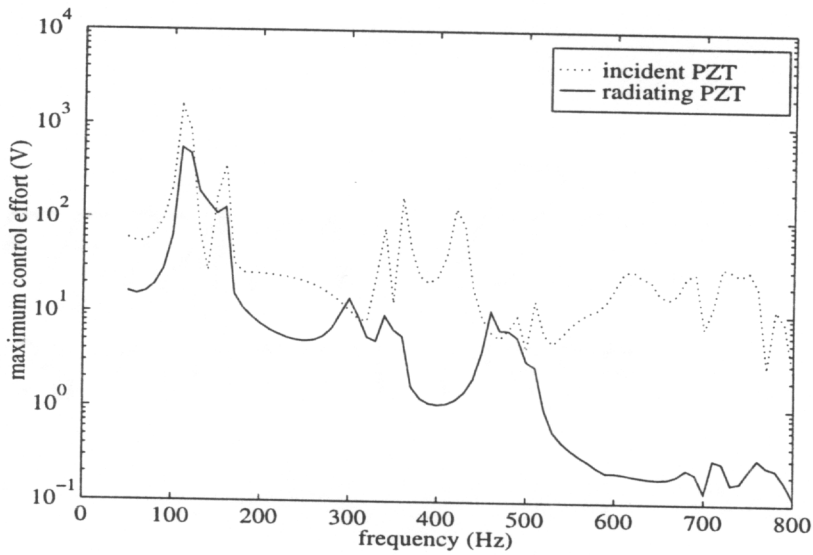


Figure 5-21. Maximum control effort for PZTs located on incident and radiating plates of a double panel system (normal incident wave; aluminum radiating plate)

### 5.3.3. Effect of incident acoustic field on control performance

In this section, the effect of the incident acoustic field on control performance is studied. The response of the double panel system was calculated using a normal and oblique (45 degrees from normal) incident wave angles. The effect of incident wave angle on the increase in frequency average transmission loss ( $TL_{avg}$ ) with control is presented in Table 5-7 for the perturbed double panel system parameters of radiating plate stiffness and PZT location. For most of the cases, better control of a double panel system is attained for a normal incident wave, although the effect is not very significant.

As can be seen in Figure 5-22, better transmission loss is achieved by an aluminum radiating plate double panel system excited by a normal acoustic plane wave than one excited by an oblique plane wave. This is due to the uniform forcing function of the normal plane wave compared to the non-uniform forcing function of the oblique plane wave. Theoretically, the normal incident wave can only excite the symmetric modes (i.e. the odd-odd modes) of the plate, while an oblique plane wave can excite symmetric and anti-symmetric modes leading to a system with a higher number of excited modes.

This is precisely the type of behavior that is shown in Figure 5-23 and Figure 5-24, which exhibits the modal response of the uncontrolled and controlled double panel system at 200 Hz with PZT's located on an aluminum radiating plate for the normal and oblique plane wave cases, respectively. The normal plane wave can only excite the symmetric modes (i.e. the (1,1), (3,1), and (1,3), etc. modes) of the plate. Control is achieved by reducing the radiating plate (1,1) mode

with slight spillover into the (3,1) and (1,3) modes. However, the oblique plane wave is able to excite more modes than the normal plane wave as indicated by the uncontrolled modal response in Figure 5-24. Control is attained by reduction of the radiating plate (1,1) and (2,1) modes with significant spillover into the (2,2) mode.

Since the amount of control is directly related to the number of excited system modes relative to the number of observable control channels, more effective control will be obtained for a system with a lower number of excited modes which is the normal plane wave case (assuming the number of observable control channels is constant).

**Table 5-7. Effect of incident plane wave on frequency averaged transmission loss**

		incident wave			
		normal	oblique	normal	oblique
radiating plate	PZT location	increase in $TL_{avg}$ (dB) 50-800 Hz		increase in $TL_{avg}$ (dB) 300-800 Hz	
		aluminum	incident	30.0	30.3
radiating	23.8		24.2	12.3	10.8
sandwich board	incident	49.1	48.8	22.6	22.9
	radiating	53.6	53.4	39.9	38.3

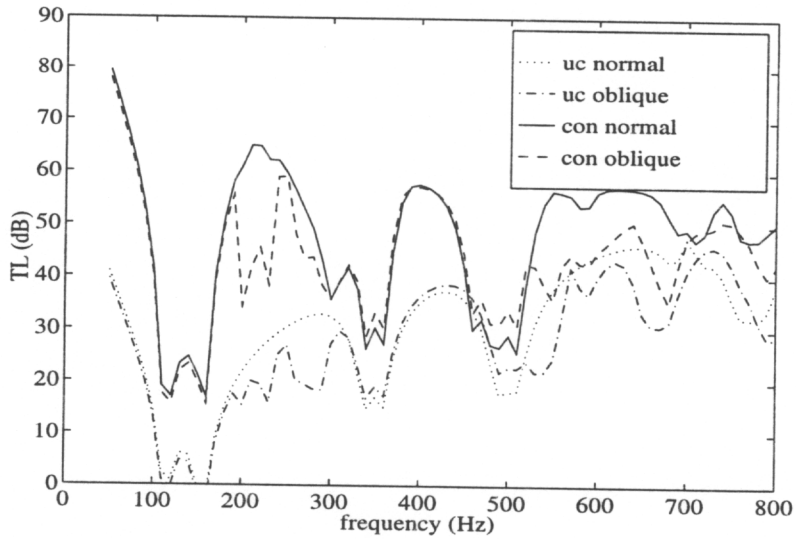


Figure 5-22. Uncontrolled and controlled transmission loss for double panel system excited by normal and oblique incident waves (radiating plate PZT location; aluminum radiating plate)

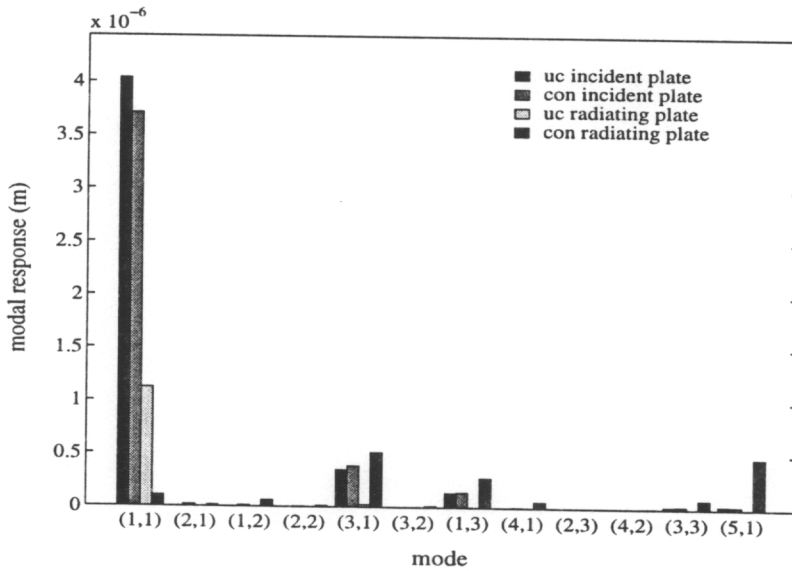
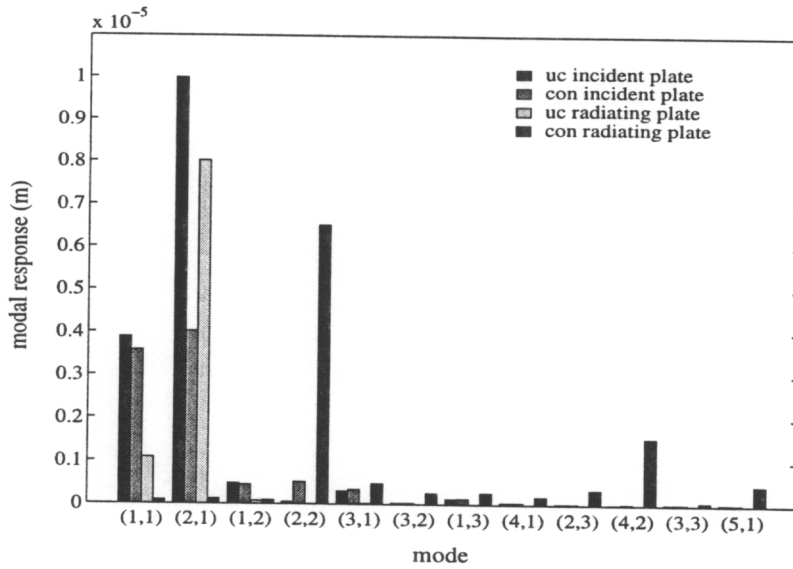


Figure 5-23. Uncontrolled and controlled double panel system modal amplitudes excited by normal incident wave at 200 Hz (radiating plate PZT location; aluminum radiating plate)



**Figure 5-24. Uncontrolled and controlled double panel system modal amplitudes excited by oblique incident wave at 200 Hz (radiating plate PZT location; aluminum radiating plate)**

### 5.3.4. Effect of the number of control actuators on control performance

In this section, the effect of the number of control actuators on control performance is studied. The response of the double panel system was calculated using two and four PZT actuators. For the two actuator case, PZT'2 #1 and #4 were used as shown in Figure 4-4. The effect of the number of actuators on the increase in frequency average transmission loss ( $TL_{avg}$ ) with control is presented in Table 5-8 for  $TL_{avg}$  from 50-800 Hz and Table 5-9 for  $TL_{avg}$  from 300-800 Hz. As expected, better control is achieved for an increased number of control actuators when the system has a high modal density ( $TL_{avg}$  from 300-800 Hz). When the modal density is not high, an increase in the number of actuators actually decreases control performance ( $TL_{avg}$  from 50-800 Hz). The exception is the sandwich board double panel system with radiating plate PZT locations where the performance difference is less than 2 dB. Further explanation of this behavior is presented in the following paragraphs. It should be noted that all of the above trends presented in

the previous sections are independent of the number of control actuators (the reader is reminded that four control actuators were used in the previous sections).

The effect of the number of control actuators is plotted versus frequency in Figure 5-25 for an aluminum radiating plate double panel system excited by a normal incident wave and controlled by incident plate PZTs. Figure 5-26 shows the effect of the number of control actuators for a sandwich board radiating plate double panel system excited by an the oblique incident wave and controlled by radiating plate PZT's. As can be seen in these figures, control performance is better with 4 PZT actuators compared to 2 PZT actuators over most of the frequency range. The exception is at the double panel system resonances, e.g. below ~190 Hz in Figure 5-25 and ~120 and ~500 Hz in Figure 5-26.

Note that the increase in transmission loss (TL) from the increased number of control actuators from Figure 5-26 does not seem to correspond to the increase in frequency averaged transmission loss (50-800 Hz) in Table 5-8. This is due to the computational process associated with calculating the frequency averaged transmission loss as seen in Eqs. (2.35) and (2.36). First note that the incident acoustic power is a constant over the frequency range and therefore the transmission loss is directly proportional to the radiated acoustic power. An extremely high radiated acoustic power over a small single frequency range can have a significant effect on the average value. This is the case indicated in Table 5-8 and Figure 5-26. Although the 4 PZT case performs approximately 20 dB better than the 2 PZT case for most of the frequency range, the asymptotic response of the radiated acoustic power (and therefore the transmission loss) at low frequencies dominate the average radiated acoustic power. This is precisely why the frequency

averaged transmission loss is presented for the 300-800 Hz range throughout this chapter and in Table 5-9.

The modal response of the double panel system excited by a normal plane wave at 340 Hz with PZT actuators located on an aluminum radiating plate is shown in Figure 5-27 and Figure 5-28 for the case of 2 and 4 PZT actuators, respectively. This is between the (2,2) in-phase and out-of-phase double panel system resonance. It is evident from these figures that the configuration with more PZT actuators can construct a more distributed forcing function which can control the plate response effectively without spillover. This results in better control. With a fewer number of actuators, control is attained by slight reduction in the acoustically efficient radiating plate mode (3,1) with significant spillover into the (2,2) mode.

The modal response of the double panel system excited by an oblique incident wave at 500 Hz with PZT actuators located on an sandwich board radiating plate is shown in Figure 5-29 and Figure 5-30 for the case of 2 and 4 PZT actuators, respectively. This case corresponds to the out-of-phase fundamental frequency of the sandwich board double panel system. At resonant frequencies, the majority of the modal response can theoretically be controlled with one actuator (Meirovitch and Norris, 1984). When more actuators are implemented, the actuators become redundant which leads to increased spillover. This is seen in Figure 5-30 where the controlled radiating plate response shows an increase in modes (2,1) and (1,2). It should be noted that these results give rise to the collinearity issue discussed in the introduction.

**Table 5-8. Effect of number of control actuators on frequency averaged transmission loss (dB); average computed over 50-800 Hz**

radiating plate	aluminum				sandwich board			
PZT location	incident		radiating		incident		radiating	
incident wave	normal	oblique	normal	oblique	normal	oblique	normal	oblique
2 PZTs; increase in $TL_{avg}$	42.5	43.2	37.6	38.4	61.2	60.5	52.1	51.8
4 PZTs; increase in $TL_{avg}$	30.0	30.3	23.8	24.2	49.1	48.8	53.6	53.4

**Table 5-9. Effect of number of control actuators on frequency averaged transmission loss (dB); average computed over 300-800 Hz**

radiating plate	aluminum				sandwich board			
PZT location	incident		radiating		incident		radiating	
incident wave	normal	oblique	normal	oblique	normal	oblique	normal	oblique
2 PZTs; increase in $TL_{avg}$	7.3	7.5	4.9	3.2	9.5	10.3	21.7	19.2
4 PZTs; increase in $TL_{avg}$	11.4	11.0	12.3	10.8	22.6	22.9	39.9	38.3

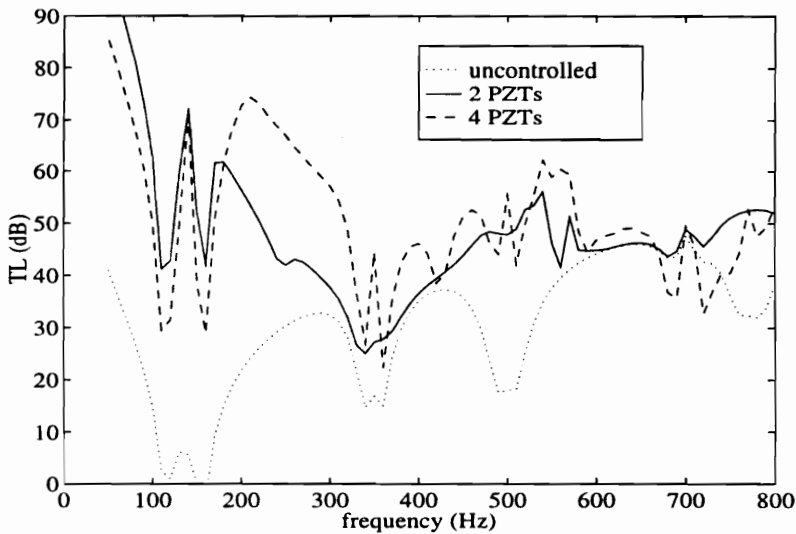


**Figure 5-25. Uncontrolled and controlled transmission loss for double panel system excited by 2 and 4 PZT actuators (normal incident wave; PZT located on aluminum radiating plate)**



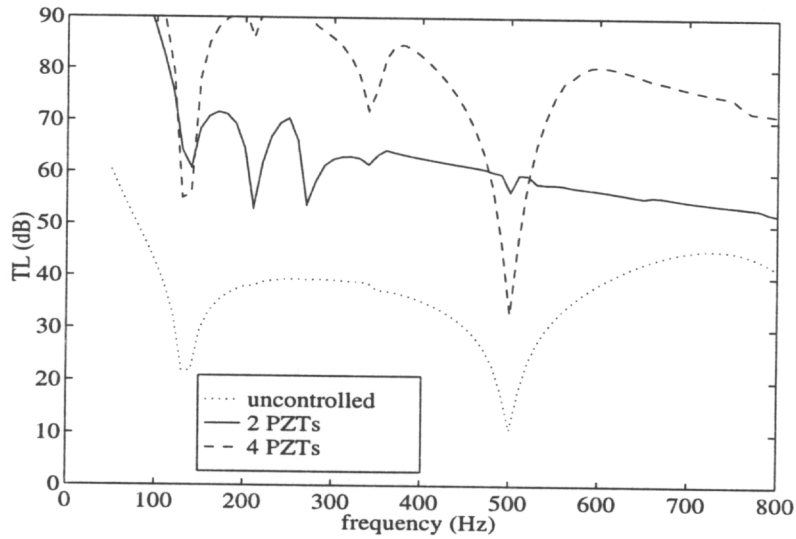


**Figure 5-26. Uncontrolled and controlled transmission loss for double panel system excited by 2 and 4 PZT actuators (oblique incident wave; PZTs located on sandwich board radiating plate)**

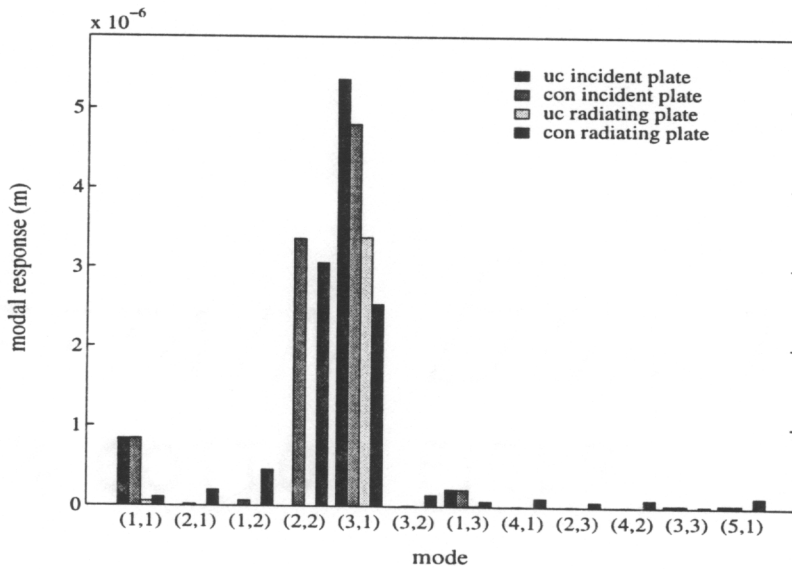


**Figure 5-27. Uncontrolled and controlled double panel system modal amplitudes controlled by 2 PZT actuators at 340 Hz (normal incident wave; PZTs located on aluminum radiating plate)**

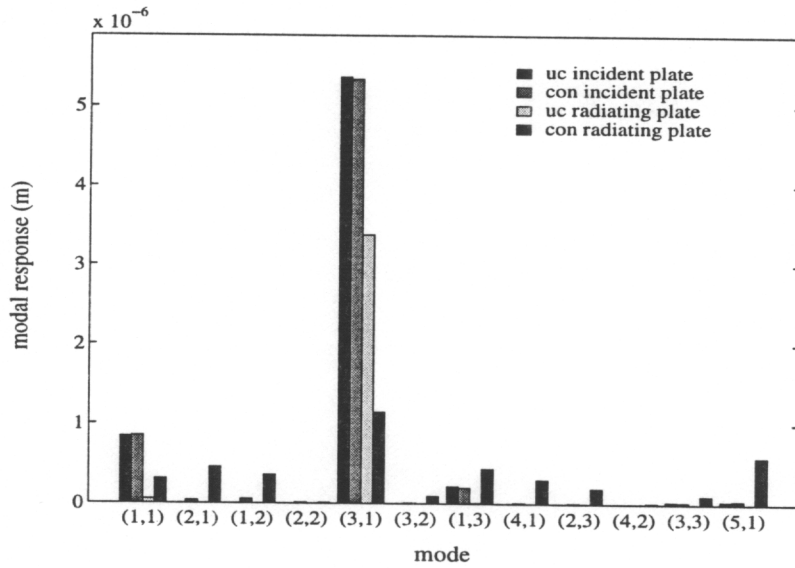


Figure 5-28. Uncontrolled and controlled double panel system modal amplitudes controlled by 4 PZT actuators at 340 Hz (normal incident wave; PZT located on aluminum radiating plate)

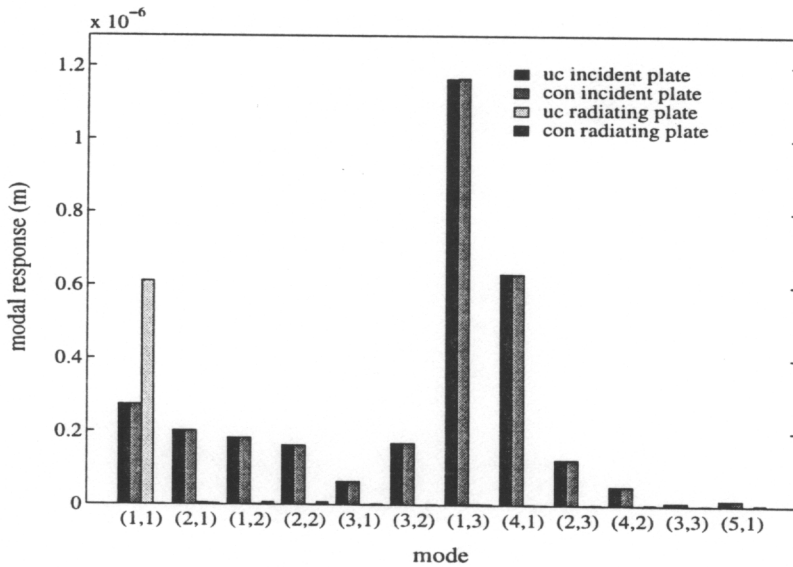
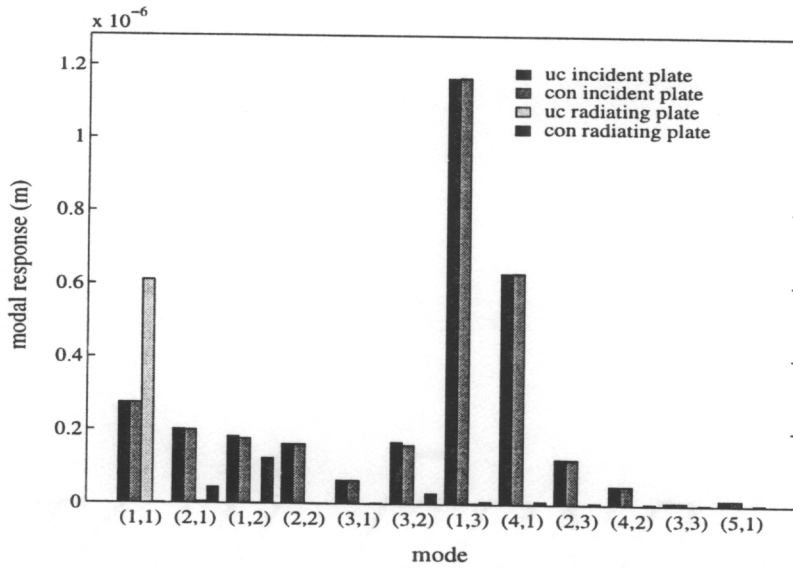


Figure 5-29. Uncontrolled and controlled double panel system modal amplitudes controlled by 2 PZT actuators at 500 Hz (oblique incident wave; PZT located on sandwich board radiating plate)



**Figure 5-30. Uncontrolled and controlled double panel system modal amplitudes controlled by 4 PZT actuators at 500 Hz (oblique incident wave; PZT located on sandwich board radiating plate)**

### 5.3.5. Effect of air cavity mass and stiffness on control performance

In this section, the influence of air cavity mass and stiffness on control performance is studied. The effect of doubling the air cavity mass on frequency averaged transmission loss ( $TL_{avg}$ ) is presented in Table 5-10 for the frequency averaging range of 50-800 Hz. For time and space considerations, the results of averaged transmission loss over the frequency range of 300-800 Hz are not reported. The effect of the doubled mass is seen to have the small effect on control performance of increasing  $TL_{avg}$  by approximately 0.3 to 2.1 dB depending on the double panel system parameters.

The uncontrolled and controlled transmission loss for a baseline and 200% air cavity mass double panel system is shown in Figure 5-31. The double panel system was excited by a normal

incident wave with PZT actuators located on an aluminum radiating plate. As can be seen, the additional mass of the air cavity has a small effect on control performance and the additional mass decreases the uncontrolled and controlled transmission loss. This effect also increases with frequency. This can be seen in the coupling terms of the double panel system equations in Eq. (2.14) where the mass term is multiplied by the square of the frequency. The modal response of the baseline and 200% mass case at 250 Hz shown in Figure 5-32 and Figure 5-33, respectively, shows no significant differences in modal structure.

The effect of doubling the air cavity stiffness on frequency averaged transmission loss ( $TL_{avg}$ ) is presented in Table 5-11. Doubling the air cavity stiffness has the effect of increasing the control performance for PZTs located on the incident plate and decreasing the control performance for PZTs located on the sandwich board radiating plate. In either case, the maximum effect on control performance is approximately 2.7 dB.

The uncontrolled and controlled transmission loss for a baseline and 200% air cavity stiffness double panel system is shown in Figure 5-34. The double panel system was excited by a normal incident wave with PZT actuators located on an aluminum radiating plate. As can be seen, the additional stiffness of the air cavity has little effect on control performance, however the additional stiffness decreases uncontrolled and controlled transmission loss by approximately 6 dB. Note that the increased stiffness has little effect at the in-phase natural frequency (110 and 340 Hz). At these frequencies, the incident and radiating plates are vibrating in-phase with little relative motion between the plates and therefore the increased air cavity stiffness has little or no effect. This can be seen in the double panel system equations in Eq. (2.8) where the air cavity

stiffness is written as a function of the difference of the incident and radiating plate flexural motion. However, the increased stiffness has the effect of increasing the out-of-phase resonant frequencies. For example, the out-of-phase fundamental is increased from 156 Hz to approximately 190 Hz as seen in Figure 5-34.

The modal response of the baseline and 200% stiffness case at 250 Hz shown in Figure 5-32 and Figure 5-35, respectively, shows increased coupling between the incident and radiating plates for the 200% stiffness case. Looking at the uncontrolled response in Figure 5-35, this is exhibited by the increased modal response of the radiating plate (1,1) mode. For the controlled response, the incident plate exhibits increased attenuation of the (1,1) mode and increased spillover of the (3,1) mode compared to the baseline.

The increased coupling between the two plates explains the behavior seen in Table 5-11. With the PZTs located on the incident plate, the increased plate coupling achieves better control since the incident PZT can better affect the radiating plate. Conversely, with the PZTs located on the sandwich board radiating plate, the increased plate coupling achieves worse control since the increased coupling results in a more complex double panel system modal structure.

In summary, it has been seen that increased mass and stiffness of the air cavity decreased uncontrolled and control transmission loss while slight increases in control performance were achieved.

**Table 5-10. Effect of air cavity mass on frequency averaged transmission loss (dB); average computed from 50-800 Hz**

radiating plate	aluminum				sandwich board			
PZT location	incident		radiating		incident		radiating	
incident wave	normal	oblique	normal	oblique	normal	oblique	normal	oblique
air; increase in $TL_{avg}$	30.0	30.3	23.8	24.2	49.1	48.8	53.6	53.4
double air mass; increase in $TL_{avg}$	31.7	32.3	25.4	26.3	49.4	49.2	53.9	53.8

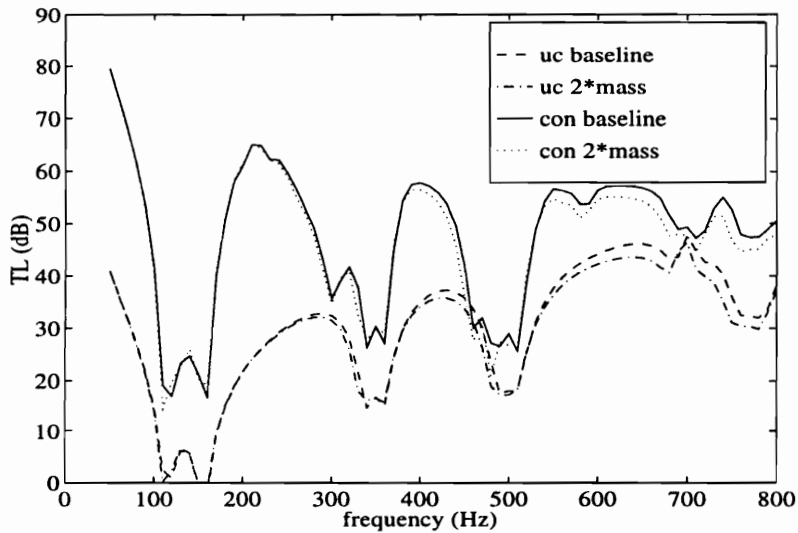


**Figure 5-31. Uncontrolled and controlled transmission loss for baseline and 200% air cavity mass (normal incident wave; PZTs located on aluminum radiating plate)**

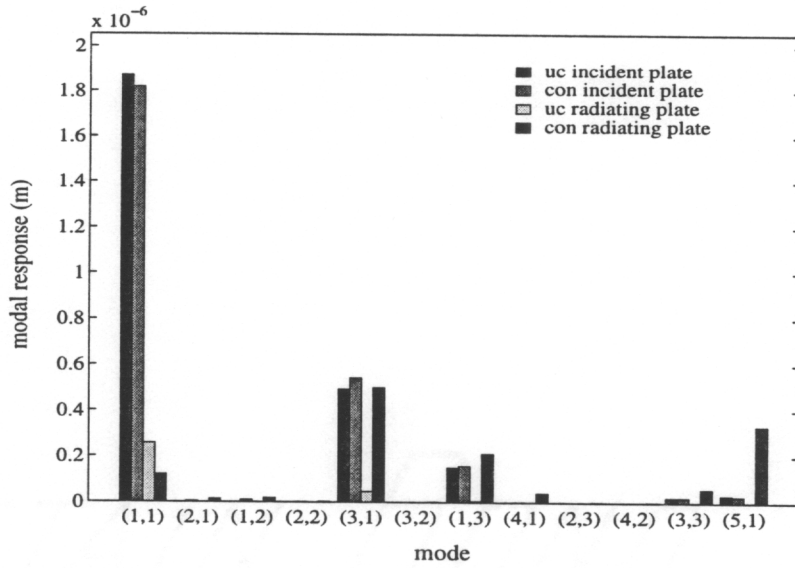


**Figure 5-32. Uncontrolled and controlled modal response for baseline mass and stiffness at 250 Hz (normal incident wave; PZTs located on aluminum radiating plate)**

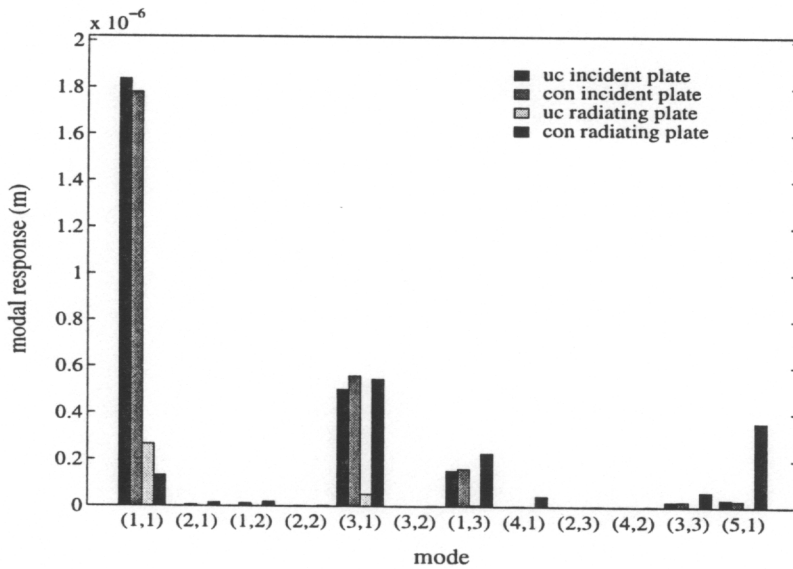


**Figure 5-33. Uncontrolled and controlled modal response for 200% air cavity mass at 250 Hz (normal incident wave; PZTs located on aluminum radiating plate)**

**Table 5-11. Effect of air cavity stiffness on frequency averaged transmission loss (dB); average computed from 50-800 Hz**

radiating plate	aluminum				sandwich board			
PZT location	incident		radiating		incident		radiating	
incident wave	normal	oblique	normal	oblique	normal	oblique	normal	oblique
air; increase in $TL_{avg}$	30.0	30.3	23.8	24.2	49.1	48.8	53.6	53.4
double air stiffness; increase in $TL_{avg}$	31.4	32.9	24.2	25.6	51.6	51.5	53.1	52.9

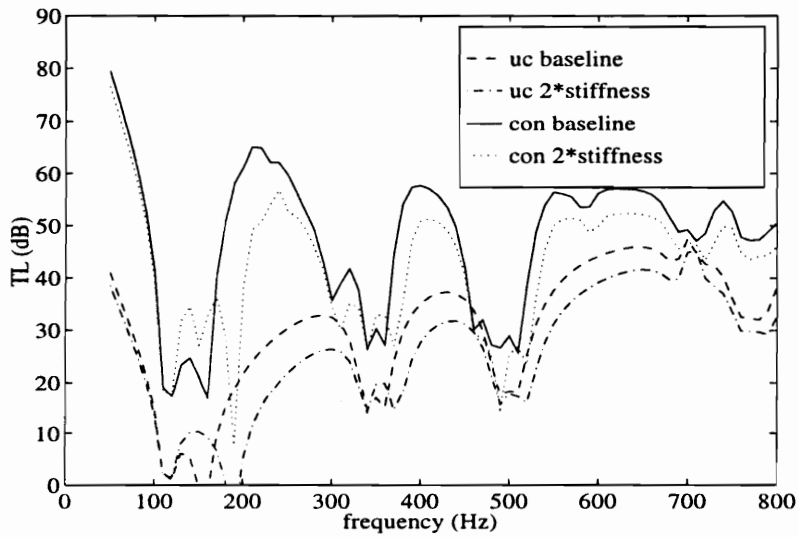


**Figure 5-34. Uncontrolled and controlled transmission loss for baseline and 200% air cavity stiffness (normal incident wave; PZTs located on aluminum radiating plate)**



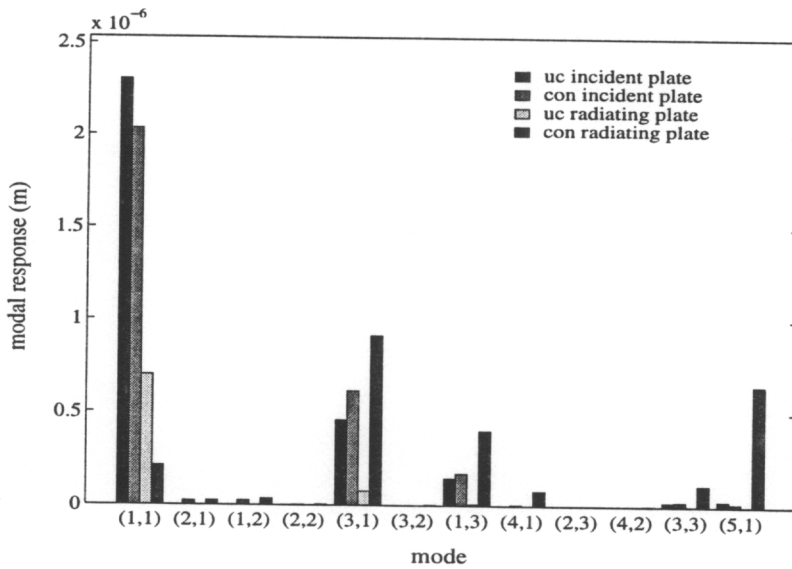


**Figure 5-35. Uncontrolled and controlled modal response for 200% air cavity stiffness at 250 Hz (normal incident wave; PZTs located on aluminum radiating plate)**

### 5.3.6. Summary

From the parametric study, the best control performance was exhibited by a double panel system excited by a normal plane wave and controlled by PZT control actuators mounted on a sandwich board radiating plate. The sandwich board radiating plate double panel system exhibits a decreased coupling of the incident and radiating plates and a lower modal density which results in increased uncontrolled and controlled transmission loss. A sandwich board radiating plate was also seen to decrease the control effort required due to better impedance matching between the PZT and the radiating plate. Taking the control effort into account, piezoelectric (PZT) control actuators should be mounted on the radiating plate of a double panel system which can couple into the radiating acoustic field better than actuators mounted on the incident plate. A double panel system excited by a normal incident wave exhibits better control performance than one

excited by an oblique incident wave due to more uniform forcing function which again results in a double panel system response with a lower modal density. As expected, better control is achieved with more control actuators since a more distributed forcing function can be attained. However, for on-resonance excitation, the increased number of actuators decreases performance due to collinearity of the actuators which results in spillover. Doubling the air cavity mass has little effect on control performance, however uncontrolled TL is slightly reduced at higher frequencies (>400 Hz). Doubling the air cavity stiffness increases the coupling between the incident and radiating plates resulting in decreased uncontrolled TL and slightly better control performance for PZT's mounted on the incident plate.

For brevity, the parameter of control actuator location (i.e. mounted on the incident versus radiating plate) will be dropped from the parameters discussed in the next section which focuses on the use of different control paradigms. The perturbations will include aluminum versus sandwich board radiating plates and normal versus oblique incident waves to judge the performance of the control paradigms over a range of double panel system modal densities and incident-radiating plate coupling.

#### **5.4. Biologically inspired hierarchical (BIO) control of double panel systems**

This section investigates the influence of different hierarchical control strategies on double panel system control behavior. The analytical investigation uses the models previously defined in Chapters 2 and 3 with the properties presented in Table 4-3. The basic double panel system model is the same as the previous section and can be stated as follows: An oblique acoustic plane

wave excites an aluminum incident plate of a double panel system. The induced incident plate motion excites the acoustic cavity thereby inducing motion in the radiating plate. The radiating plate then emits acoustic power into an acoustic free field. The cost function is defined as the radiated acoustic power from the radiating plate. Control is provided by piezoelectric (PZT) actuators located on the radiating plate of the double panel system, the positions of which are given in Table 4-6. Specifics of the investigation include analytical control performance comparisons of the linear quadratic optimal control theory (LQOCT) with the biologically inspired (BIO) control strategy. Computational effort and stability of different physical implementations of the Filtered-X least mean squares (FXLMS), time averaged gradient (TAG) LMS, and BIO TAG LMS algorithms will then be presented. For the BIO algorithm, four different local rules will be studied, the phase variation, adaptive magnitude, adaptive phase, and optimal methods.

#### **5.4.1. BIO control performance**

A comparison of biologically inspired hierarchical (BIO) control performance relative to standard linear quadratic optimal control theory (LQOCT) is presented. To determine the influence of only the control algorithm, the BIO control strategy was implemented using LQOCT for the master control channel. However, LQOCT is not directly applicable to the local control approaches which is evident from the discussion of the algorithms previously presented in Section 3.1.2. Therefore, the local control algorithms were implemented in the following way. Control inputs for the phase variation method used a simple trial and error method once the master actuator had converged. The adaptive magnitude and adaptive phase local rules used a LMS technique to converge the individual slave actuators since using the magnitude or phase of the LQOCT

solution provided incorrect results. The control inputs for the optimal method were derived from the LQOCT solution. The slave control inputs were then scaled relative to the master actuator as described in Chapter 3.

In the following sections, the BIO control performance is compared to a four input, one output (4I1O) LQOCT controller and a four input, four output (4I4O) LQOCT controller since the BIO algorithm control complexity is somewhere between these two configurations. Note that the 1 output LQOCT method will be referred to as the master algorithm, and the 4 output LQOCT method will be referred to as the baseline algorithm. Note that in some tables and figures in this section, the terms phase variation is shortened to PV, adaptive magnitude is shortened to AM, and adaptive phase is shortened to AP.

### ***Phase variation method***

In this section, the influence of the BIO phase variation method on control performance is studied. The effect of this control strategy on frequency averaged transmission loss ( $TL_{avg}$ ) is presented in Table 5-12 for a frequency range of 50-800 Hz and Table 5-13 for a frequency range of 300-800 Hz. In general, the phase variation method attained less control than the baseline algorithm and equal or greater control than the master algorithm. Specifically, the phase variation method applied to an aluminum radiating plate double panel system excited by a normal plane wave showed a 3.6 dB improvement in control performance over the master algorithm for the frequency averaged range of 50-800 Hz. Over a frequency averaged range of 300-800 Hz, the control performance increase was 11.5 dB. From both tables it is evident that the phase variation method performs better than the master algorithm for double panel systems with normal incident wave excitation at frequencies in the range of 300-800 Hz. The poorest increase in control

achieved by the phase variation method over the master algorithm in both tables was a sandwich board radiating plate double panel system excited by an oblique incident wave.

Figure 5-36 shows the uncontrolled and controlled master, phase variation, and baseline algorithm transmission loss for an aluminum radiating plate double panel system excited by a normal plane wave. As can be seen in this figure, the phase variation method did not increase control performance over the master algorithm below 180 Hz. In this range, the fundamental mode dominates the response of the double panel system and good control can be achieved with one control actuator. Therefore the increase in  $TL_{avg}$  over a frequency range of 50-800 Hz (Table 5-12) was poor. However, above 180 Hz the phase variation method attains much better transmission loss with control compared to the master algorithm and performs comparably to the baseline algorithm as can be seen in Figure 5-36. This is indicated in Table 5-13 where the transmission loss is averaged over a frequency range of 300-800 Hz.

It is evident that the phase variation method works better for normal plane wave excitation as seen in Table 5-13. Figure 5-37 shows the relative control voltage magnitude and phase for the baseline algorithm transmission loss for an aluminum radiating plate double panel system excited by a normal incident wave. In this figure, the control voltage magnitude and phase of the four control actuators was normalized relative to the master actuator. Therefore the master actuator magnitude is unity and phase is zero. The other three lines denote the other three actuators relative magnitude and phase. The important aspect of the figure is the relative control actuator magnitude and phase and not which one is which. As can be seen in this figure, the relative phase of the control actuators is close to 0(or 360) degrees, while the magnitudes are close to one for

most of the frequency range. Since the phase variation method bounds the magnitude of the slave actuators to one and the phase to be 0 or 180 degrees, additional control actuators can be implemented by the phase variation algorithm thereby creating a distributed actuator that is better able to couple into the uncontrolled system response. The result is additional control performance over the master algorithm with little increase in control system complexity. Note that the relative control voltage phase is not close to zero or 180 degrees for the frequency range of less than 180 Hz. Since the phase variation method is not capable of continuously adapting the phase of the slave control actuators, additional control performance over the master algorithm is poor in this region.

This type of behavior is apparent over more of the frequency range for the oblique incident wave excitation. Figure 5-38 shows the relative control voltage magnitude and phase for baseline algorithm transmission loss for an aluminum radiating plate double panel system excited by an oblique incident wave. As can be seen in this figure, the relative phase of the PZT actuators is not close to zero (360) or 180. Again, the phase variation method is not able to adapt the phase of the slave actuators as needed to attain the maximum control and therefore results in poor additional control performance over the master algorithm.

The application of the phase variation method to the sandwich board radiating plate double panel system excited by a normal incident wave shows little improvement over the master algorithm as seen in Table 5-12 and Figure 5-39. Good control is achieved from the master algorithm due to the low modal density of the sandwich board radiating plate double panel system. The phase variation method does not contribute any further reduction until the master algorithm exhibits

poor control in the range of 600-700 Hz. This is where the modal density of the response of the double panel system is greater than one and more than one control actuator is needed. At a frequency of 500 Hz (the out-of-phase fundamental of the sandwich board radiating plate double panel system), the master algorithm actually performs better than the baseline algorithm with four control actuators. Figure 5-40 shows the uncontrolled and controlled modal amplitudes for the master algorithm at 500 Hz for a sandwich board radiating plate double panel system excited by an oblique incident wave. Comparing the modal amplitudes in this figure with the baseline algorithm (Figure 5-7), the master algorithm exhibits less control spillover into the higher modes resulting in better control performance. This is another example of the collinearity issue mentioned in the introduction. The primary mode can be controlled by one actuator (Meirovitch and Norris, 1984). When more actuators are used to control this mode, increased spillover is noticed due to collinearity of the actuators. This can be seen in the calculation of the optimal control filter in Eq. (3.4) where the collinearity of the  $\mathbf{H}^t\mathbf{H}$  matrix will make the matrix rank deficient and therefore presents difficulties with the matrix inversion.

**Table 5-12. Effect of BIO controller phase variation method on frequency averaged transmission loss; average computed from 50-800 Hz**

radiating plate incident wave	aluminum		sandwich board	
	normal	oblique	normal	oblique
master algorithm; increase in $TL_{avg}$ (dB)	12.1	12.9	25.4	25.2
BIO phase variation; increase in $TL_{avg}$ (dB)	15.7	13.2	25.9	25.2
baseline algorithm; increase in $TL_{avg}$ (dB)	23.8	24.2	53.6	53.4

**Table 5-13. Effect of BIO controller phase variation method on frequency averaged transmission loss; average computed from 300-800 Hz**

radiating plate	aluminum		sandwich board	
incident wave	normal	oblique	normal	oblique
master algorithm; increase in $TL_{avg}$ (dB)	1.9	1.4	8.2	8.8
BIO phase variation; increase in $TL_{avg}$ (dB)	13.4	3.9	23.8	9.3
baseline algorithm; increase in $TL_{avg}$ (dB)	12.3	10.8	39.9	38.3

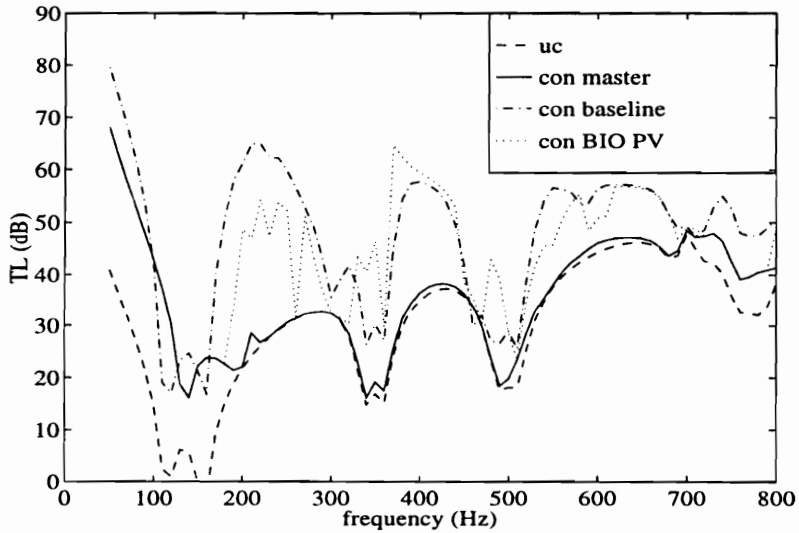


**Figure 5-36. Uncontrolled and controlled double panel system transmission loss for the master, phase variation and baseline algorithms (normal plane wave; aluminum radiating plate )**



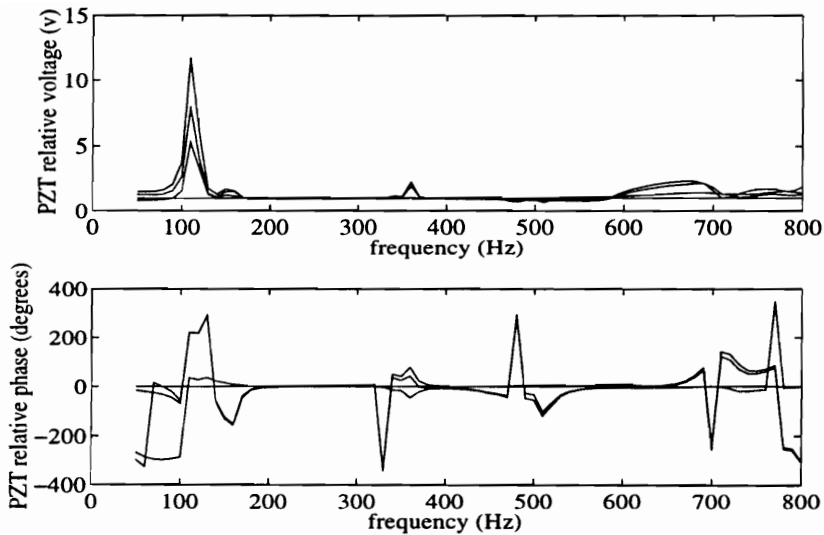


**Figure 5-37. Baseline algorithm relative control voltage magnitude and phase when controlling double panel system transmission loss (normal plane wave; aluminum radiating plate)**

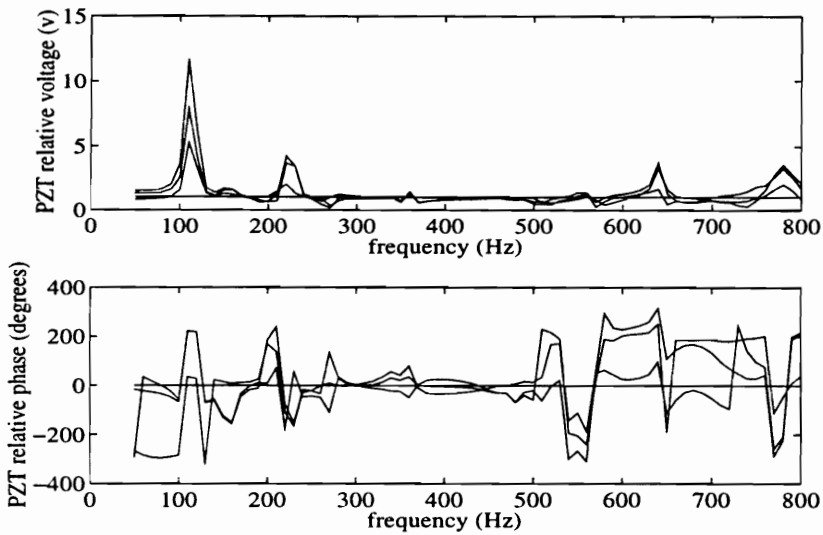


**Figure 5-38. Baseline algorithm relative control voltage magnitude and phase when controlling double panel system transmission loss (oblique plane wave; aluminum radiating plate)**

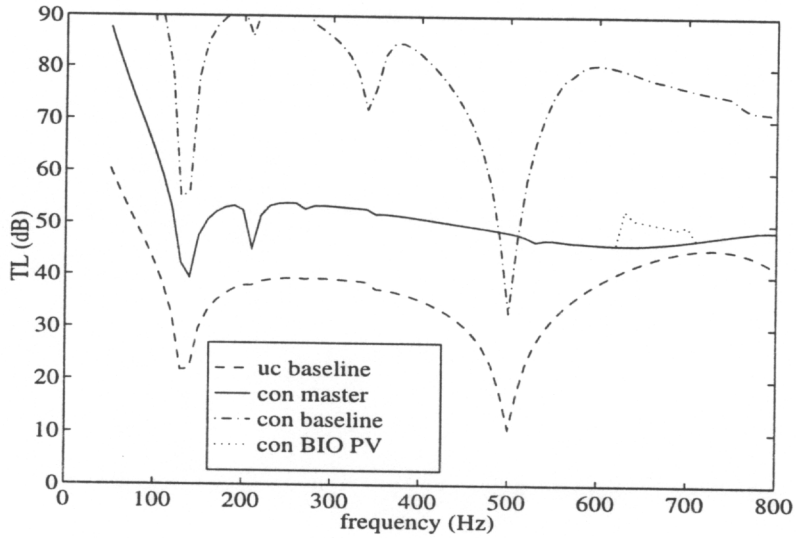


Figure 5-39. Uncontrolled and controlled double panel system transmission loss for the master, phase variation and baseline algorithms (oblique plane wave; sandwich board radiating plate)

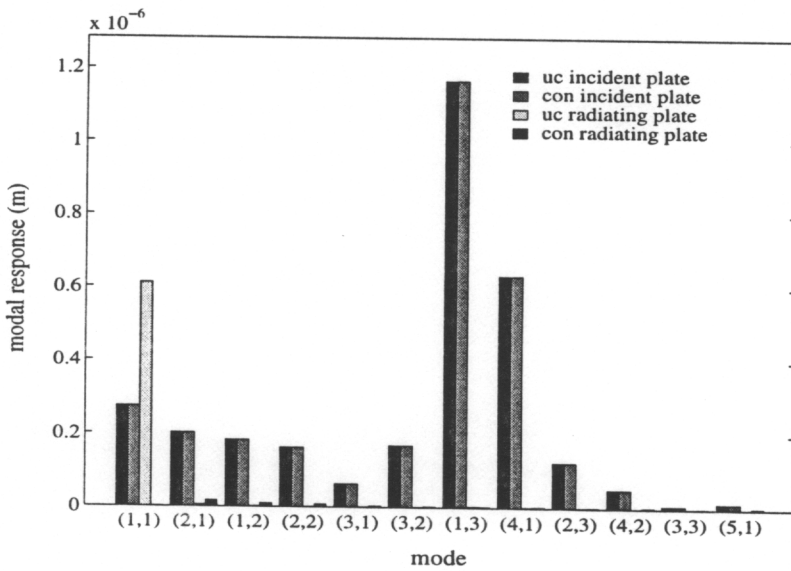


Figure 5-40. Uncontrolled and controlled double panel system modal amplitudes for the master algorithm at 500 Hz (oblique incident wave; sandwich board radiating plate)

### *Adaptive magnitude method*

In this section, the influence of the adaptive magnitude BIO control method on control performance is studied. The effect of this control strategy on frequency averaged transmission loss ( $TL_{avg}$ ) is presented in Table 5-14 for a frequency averaging range of 50-800 Hz and Table 5-15 for a frequency averaging range of 300-800 Hz. As can be seen in Table 5-15, the adaptive magnitude method performance is better than the baseline algorithm. This is unusual since the baseline algorithm is a least mean squares solution to minimize the cost function as discussed in Section 3.3. For an aluminum radiating plate double panel system excited by a normal incident wave, the increase in  $TL_{avg}$  was 3.7 dB for the adaptive magnitude method compared to baseline algorithm. Conversely, the method did not perform as well for the other cases as seen in Table 5-14 and Table 5-15. However, compared to the master algorithm, significant increases were seen from 0.3 up to 24.7 dB depending on the frequency averaging range and the double panel system parameters.

A plot of master, adaptive magnitude and baseline transmission loss is presented in Figure 5-41 for an aluminum radiating plate double panel system excited by a normal incident wave. As can be seen, the adaptive magnitude method attains much better transmission loss with control compared to the master algorithm and performs slightly better than the baseline algorithm over certain frequency ranges. As with the phase variation method, this can be explained by the relative phase of the control actuators. As can be seen in the plot of relative control voltages for the baseline algorithm in Figure 5-37, the relative phase of the control actuators is close to 0 (or 360) degrees, while the magnitudes vary slightly for most of the frequency range. The adaptive magnitude method allows the magnitude to be adapted to account for these magnitude variations,

while control system complexity has been reduced. As seen in the modal response at 500 Hz in Figure 5-42, the adaptive magnitude method attains effective control by reducing the (1,3) mode of the radiating plate, while spillover into the (1,2) and (3,2) radiating plate modes is less compared to the modal response of the baseline algorithm seen in Figure 5-43. The differences in control performance are directly a result of this spillover.

Similar to the phase variation method, oblique plane wave excitation decreases control performance of the adaptive magnitude method as seen in Table 5-14. Also, the adaptive magnitude method does not perform as well as the baseline method as shown in Figure 5-44, where the relative performance of the control algorithms applied to a sandwich board radiating plate double panel system excited by an oblique incident wave is displayed. Note that there is an exception at the fundamental resonances where the adaptive magnitude method performs better than the baseline algorithm. At these fundamental resonances, better control than the baseline algorithm is a result of the collinearity issue raised previously.

In summary, the above behavior is expected since the hierarchical structure of the adaptive magnitude method that can construct a more distributed actuator (from the individual actuators as discussed in Section 3.1.2) than the master algorithm (which has but one actuator). However, the adaptation of these individual elements is less adaptive than the baseline algorithm. It should be noted that the algorithm shows potential to eliminate the collinearity problem of multiple PZT actuators controlling a system at resonance.

**Table 5-14. Effect of BIO controller adaptive magnitude method on frequency averaged transmission ; average computed from 50-800 Hz**

radiating plate incident wave	aluminum		sandwich board	
	normal	oblique	normal	oblique
master algorithm; increase in $TL_{avg}$ (dB)	12.1	12.9	25.4	25.2
BIO adaptive magnitude; increase in $TL_{avg}$ (dB)	17.3	13.5	28.9	25.5
baseline algorithm; increase in $TL_{avg}$ (dB)	23.8	24.2	53.6	53.4

**Table 5-15. Effect of BIO controller adaptive magnitude method on frequency averaged transmission ; average computed from 300-800 Hz**

radiating plate incident wave	aluminum		sandwich board	
	normal	oblique	normal	oblique
master algorithm; increase in $TL_{avg}$ (dB)	1.9	1.4	8.2	8.8
BIO adaptive magnitude; increase in $TL_{avg}$ (dB)	15.0	5.5	33.0	15.3
baseline algorithm; increase in $TL_{avg}$ (dB)	12.3	10.8	39.9	38.3

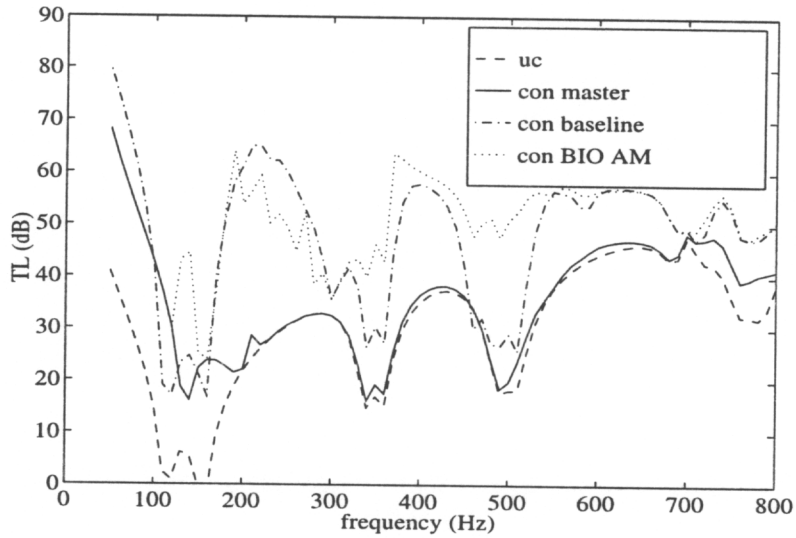


Figure 5-41. Uncontrolled and controlled double panel system transmission loss for the master, adaptive magnitude and baseline algorithms (normal plane wave; aluminum radiating plate)

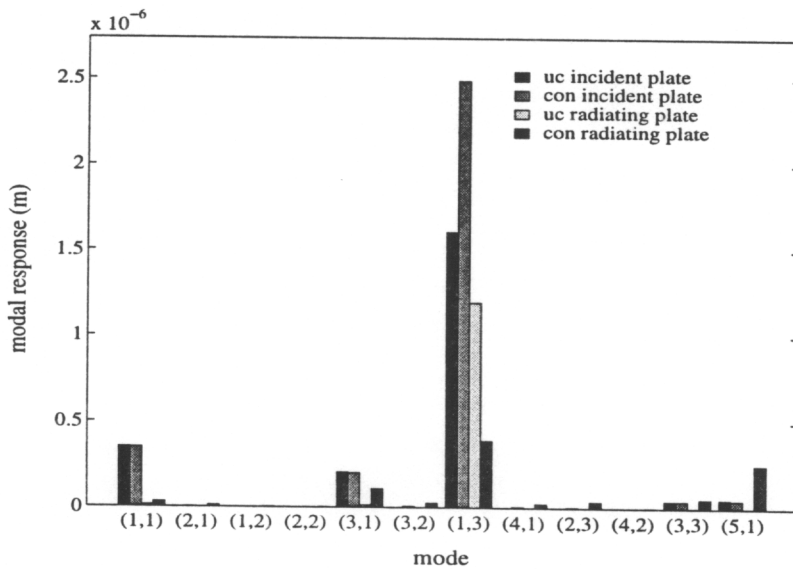


Figure 5-42. Uncontrolled and controlled double panel system modal amplitudes for the adaptive magnitude method at 500 Hz (normal incident wave; aluminum radiating plate)

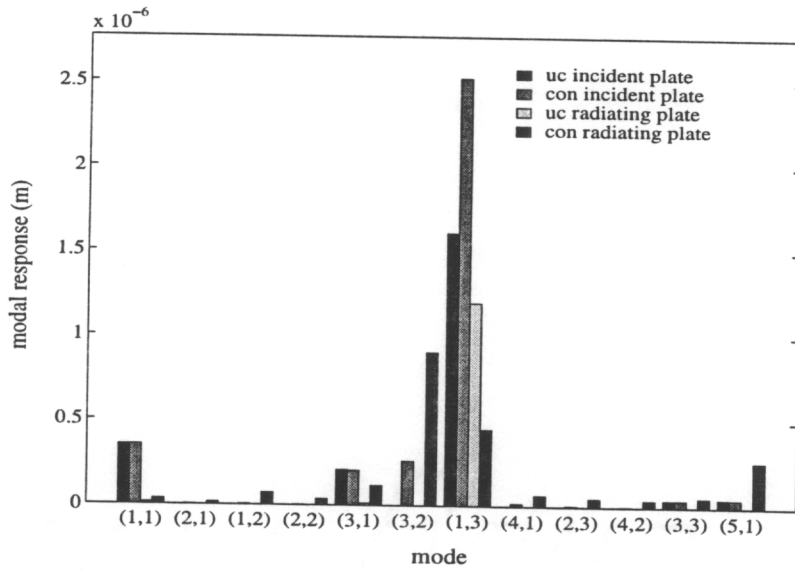


Figure 5-43. Uncontrolled and controlled double panel system modal amplitudes for the baseline algorithm at 500 Hz (normal incident wave; aluminum radiating plate)

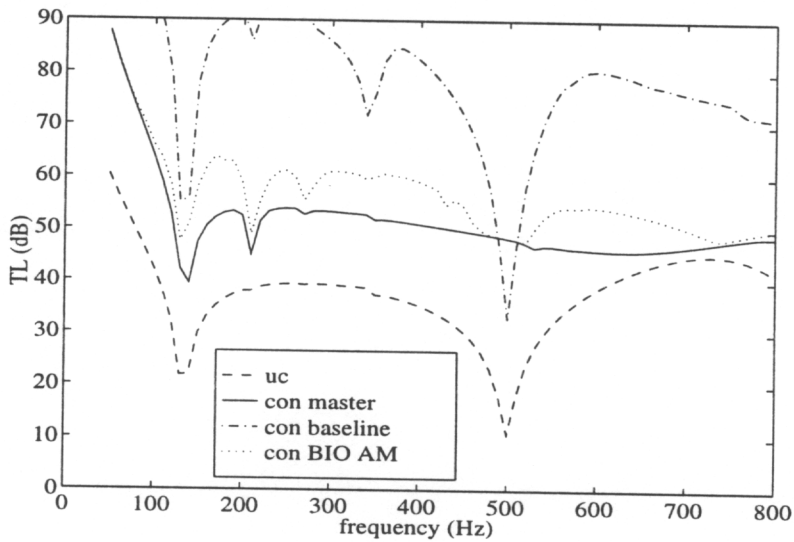


Figure 5-44. Uncontrolled and controlled double panel system transmission loss for the master, adaptive magnitude and baseline algorithms (oblique plane wave; sandwich board radiating plate )

### *Adaptive phase method*

In this section, the influence of the adaptive phase BIO control method on control performance is studied. The effect of the alternative control strategy on frequency averaged transmission loss ( $TL_{avg}$ ) is presented in Table 5-16 for a frequency averaging range of 50-800 Hz and Table 5-17 for a frequency averaging range of 300-800 Hz. As seen in Table 5-16, the adaptive phase algorithm performance is better than the baseline algorithm. As discussed in the previous section, this is unusual except in low modal density situations where the collinearity of the control actuators can impair the baseline algorithm. For a double panel system with an aluminum radiating plate, the increase in  $TL_{avg}$  was ~18 dB for the normal and oblique incident waves. For a double panel system with a sandwich board radiating plate, the method performed 2.0 dB better than baseline for a normal incident wave while performance was 1.6 dB higher for an oblique incident wave.

As can be seen in Figure 5-45, the BIO adaptive phase method performs better than the baseline algorithm over most of the frequency range for an aluminum radiating plate double panel system excited by a normal incident wave. Again, the relative phase of the actuators is the important aspect. As seen in Figure 5-37, the baseline algorithm for this case reveals the relative magnitudes of the control actuators are approximately the same and the relative phase is mostly zero. Since the adaptive phase method is initialized as a distributed actuator with a relative magnitude of one and a relative phase of zero, the method can couple well into disturbance field resulting in good performance.

However, once the disturbance field becomes more complex, the adaptive phase method is able



to change the relative phase of the actuators which allows greater adaptivity over the other local rules (recall from Chapter 3 that matching the phase is most important). Figure 5-46 displays a plot of transmission loss versus frequency for an aluminum radiating plate double panel system excited by an oblique incident wave. As can be seen, the adaptive phase method performs almost as well as the baseline algorithm above 180 Hz and better than baseline below that frequency. As seen in Figure 5-38, the plot of baseline control voltages for this system reveals that the relative magnitude is somewhat constant while the relative phase varies. Since this BIO method has the ability to adapt the relative phase of the actuators, the method can adapt to the disturbed vibrational field resulting in good performance. Since the number of degrees of freedom is restricted, the adaptive phase method performs better than the baseline algorithm when there is a problem with actuator collinearity (low frequencies or near resonances).

Note that the adaptive phase method performs extremely well at and below the in-phase and out-of-phase fundamental frequency of the aluminum radiating plate double panel system. In this region, the (1,1) mode dominates the double panel system response. Since the adaptive phase method is initialized with all of the slave control actuators having a magnitude of one and in-phase with the master actuator, the method forms a distributed actuator that can reduce the (1,1) of the double panel system without spillover into any higher order modes.

For a sandwich board radiating plate double panel system excited by an oblique incident wave, the increase in  $TL_{avg}$  with control was less for the adaptive phase method than the baseline algorithm (Table 5-16). As seen in Figure 5-47, the adaptive phase method performance is good for most of the frequency range except in the frequency range of 190 to 300 Hz compared to the

baseline algorithm. In this frequency range, it is evident that the adaptive phase method is unable to fully adapt to the disturbance field since the relative magnitude of the actuators is restricted to be one. However, performance is still exemplary compared to the master algorithm.

**Table 5-16. Effect of BIO controller adaptive phase method on frequency averaged transmission loss; average computed from 50-800 Hz**

radiating plate incident wave	aluminum		sandwich board	
	normal	oblique	normal	oblique
master algorithm; increase in $TL_{avg}$ (dB)	12.1	12.9	25.4	25.2
BIO adaptive phase; increase in $TL_{avg}$ (dB)	41.8	42.3	55.6	55.0
baseline algorithm; increase in $TL_{avg}$ (dB)	23.8	24.2	53.6	53.4

**Table 5-17. Effect of BIO controller adaptive phase method on frequency averaged transmission loss; average computed from 300-800 Hz**

radiating plate incident wave	aluminum		sandwich board	
	normal	oblique	normal	oblique
master algorithm; increase in $TL_{avg}$ (dB)	1.9	1.4	8.2	8.8
BIO adaptive phase; increase in $TL_{avg}$ (dB)	14.5	9.8	37.5	31.5
baseline algorithm; increase in $TL_{avg}$ (dB)	12.3	10.8	39.9	38.3

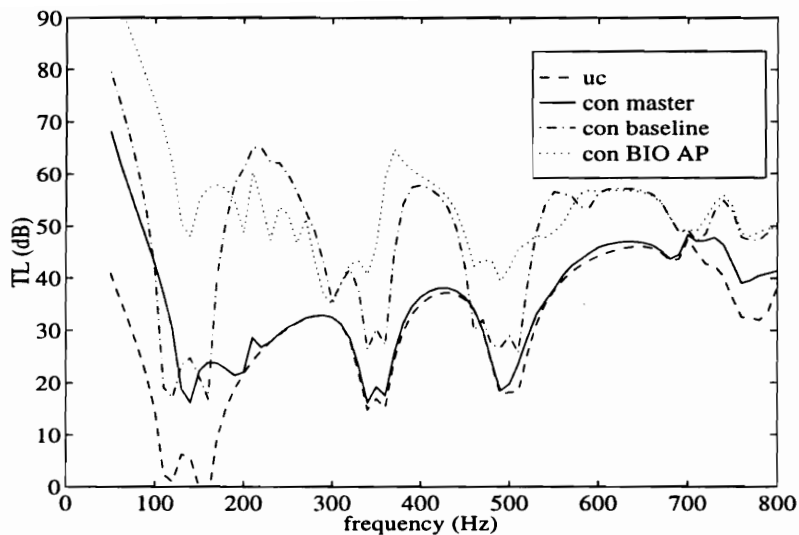


**Figure 5-45. Uncontrolled and controlled double panel system transmission loss for the master, adaptive phase and baseline algorithms (normal plane wave; aluminum radiating plate )**

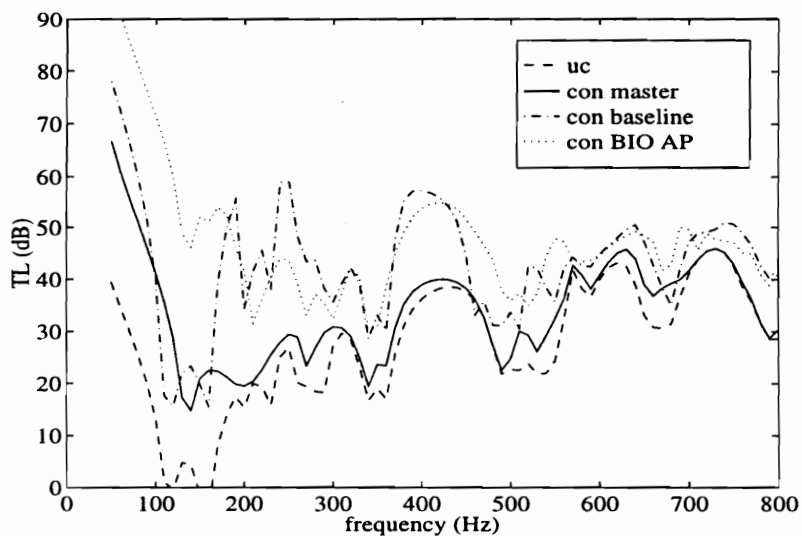


**Figure 5-46. Uncontrolled and controlled double panel system transmission loss for the master, adaptive phase and baseline algorithms (oblique plane wave; aluminum radiating plate )**

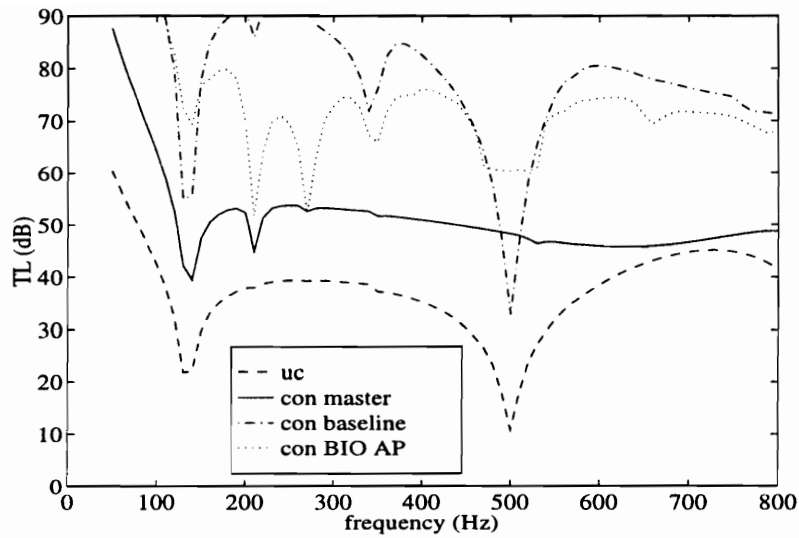


**Figure 5-47. Uncontrolled and controlled double panel system transmission loss for the master, adaptive phase and baseline algorithms (oblique plane wave; sandwich board radiating plate )**

***Optimal method***

In this section, the influence of the optimal BIO control method on control performance is studied. The effect of this control strategy on the frequency averaged transmission loss ( $TL_{avg}$ ) is presented in Table 5-18. Note that only the transmission loss averaged over 50-800 Hz is presented in this and the following sections. This has been done for time and space considerations as the averaging of transmission loss from 300-800 Hz only provided extraneous information in the aforementioned sections. As expected, the optimal method performs the same as the baseline algorithm. However, compared to the master algorithm, significant increases were seen from ~11 to ~28 dB.

A plot of transmission loss for the master, optimal and baseline algorithms for an aluminum radiating plate double panel system excited by a normal incident wave is presented in Figure 5-

48. As can be seen, the optimal method follows the baseline algorithm except in certain regions where the optimal method performs slightly better. A comparison of the uncontrolled and controlled modal amplitudes at 470 Hz for the optimal and baseline algorithm is presented in Figure 5-49 and Figure 5-50, respectively. For both of these plots, modal restructuring is the main mechanism of control, however the optimal method is able to restructure the modes without increasing the amplitudes as much as the baseline algorithm. This is a result of the hierarchical structure inherent in the optimal method where one control actuator is updating versus four for the baseline algorithm.

**Table 5-18. Effect of BIO controller optimal method on frequency averaged transmission loss; average computed from 50-800 Hz (PZTs located on radiating plate)**

radiating plate	aluminum		sandwich board	
incident wave	normal	oblique	normal	oblique
master algorithm; increase in $TL_{avg}$ (dB)	12.1	12.9	25.4	25.2
BIO optimal; increase in $TL_{avg}$ (dB)	23.8	24.2	53.6	53.4
baseline algorithm; increase in $TL_{avg}$ (dB)	23.8	24.2	53.6	53.4

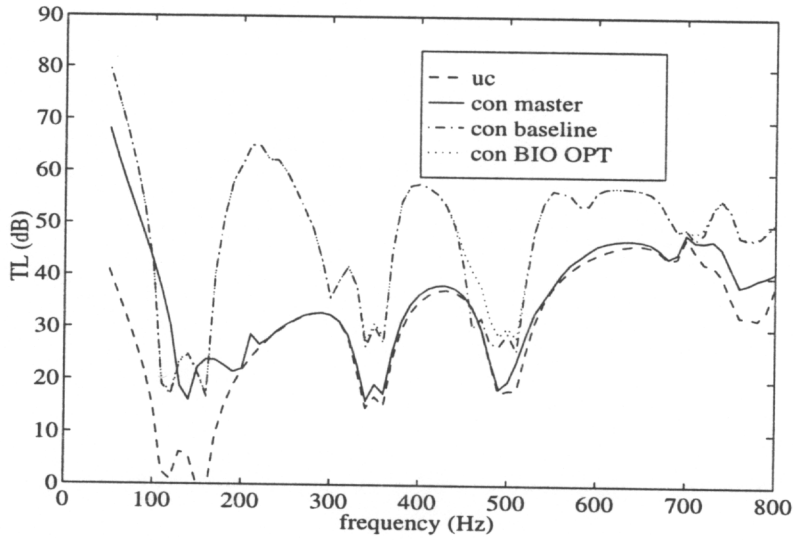


Figure 5-48. Uncontrolled and controlled double panel system transmission loss for the master, optimal and baseline algorithms (normal plane wave; aluminum radiating plate )

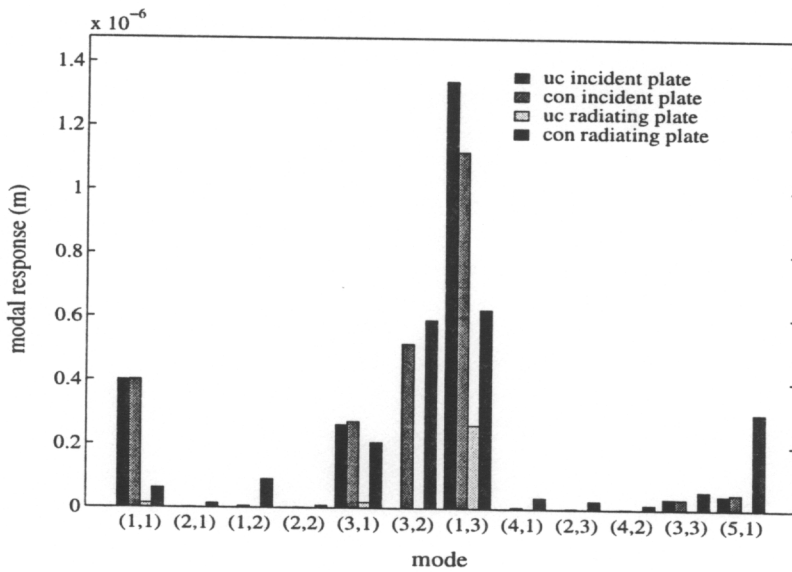
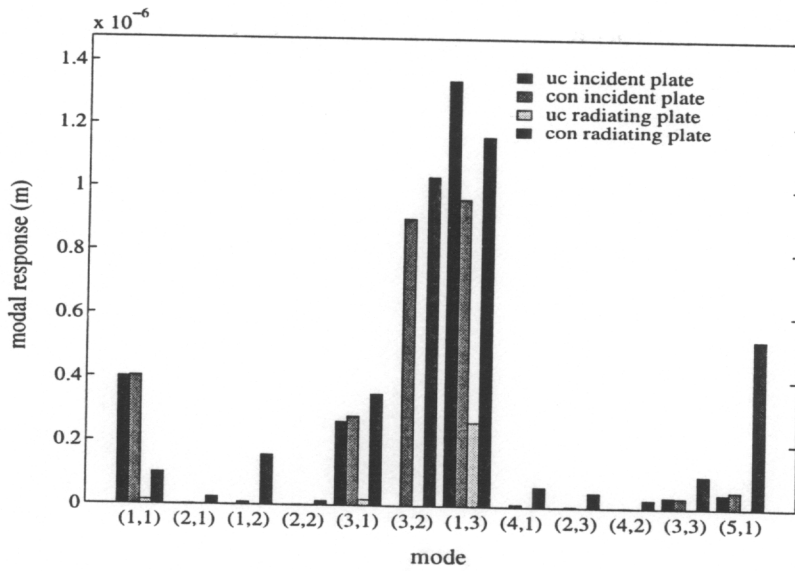


Figure 5-49. Uncontrolled and controlled double panel system modal amplitudes for the optimal method at 470 Hz (normal incident wave; aluminum radiating plate)



**Figure 5-50. Uncontrolled and controlled double panel system modal amplitudes for the baseline algorithm at 470 Hz (normal incident wave; aluminum radiating plate)**

#### 5.4.2. Effect of number of actuators on control performance

The effect of the number of actuators on BIO control performance is presented in Table 5-19, Table 5-20, and Table 5-21 for the phase variation, adaptive magnitude, and adaptive phase methods, respectively. As can be seen in these tables, an increase in the number of control actuators exhibits an increase in the frequency averaged transmission loss.

The above result is the expected result. However, this is only true if the number of degrees of freedom of the system excited by the disturbance is greater than the number of degrees of freedom that the control system can effectively couple into. Conversely, when the control system can couple into more degrees of freedom than exists in the disturbed system, spillover occurs and control performance decreases.

This is precisely the type of behavior that can be seen in Figure 5-51 in the low frequency region (< 280 Hz) for an aluminum radiating plate double panel system excited by a normal incident wave. The adaptive phase method exhibits mixed results where an increase in performance is obtained for an increase from two to four PZT actuators and a decrease in performance is seen at some frequencies for an increase from four to eight PZT actuators. However, above 280 Hz where the system complexity is greater, there is an overall increase in transmission loss for a greater number of actuators.

**Table 5-19. Effect of number of control actuators on BIO controller phase variation method frequency averaged transmission loss; average computed from 50-800 Hz**

radiating plate incident wave	aluminum		sandwich board	
	normal	oblique	normal	oblique
BIO phase variation - 2 PZTs; increase in $TL_{avg}$ (dB)	12.4	13.0	25.4	25.2
BIO phase variation - 4 PZTs; increase in $TL_{avg}$ (dB)	15.7	13.2	25.9	25.2
BIO phase variation - 8 PZTs; increase in $TL_{avg}$ (dB)	15.9	13.3	26.0	25.2

**Table 5-20. Effect of number of control actuators on BIO controller adaptive magnitude method frequency averaged transmission loss; average computed from 50-800 Hz**

radiating plate incident wave	aluminum		sandwich board	
	normal	oblique	normal	oblique
BIO adaptive magnitude - 2 PZTs; increase in $TL_{avg}$ (dB)	12.3	13.1	25.4	25.2
BIO adaptive magnitude - 4 PZTs; increase in $TL_{avg}$ (dB)	17.3	13.5	28.9	25.5
BIO adaptive magnitude - 8 PZTs; increase in $TL_{avg}$ (dB)	19.0	13.7	31.0	25.6



**Table 5-21. Effect of number of control actuators on BIO controller adaptive phase method frequency averaged transmission loss; average computed from 50-800 Hz**

radiating plate incident wave	aluminum		sandwich board	
	normal	oblique	normal	oblique
BIO adaptive phase - 2 PZTs; increase in $TL_{avg}$ (dB)	38.1	38.8	51.8	51.4
BIO adaptive phase - 4 PZTs; increase in $TL_{avg}$ (dB)	41.8	42.3	55.6	55.0
BIO adaptive phase - 8 PZTs; increase in $TL_{avg}$ (dB)	44.5	44.8	58.3	57.4

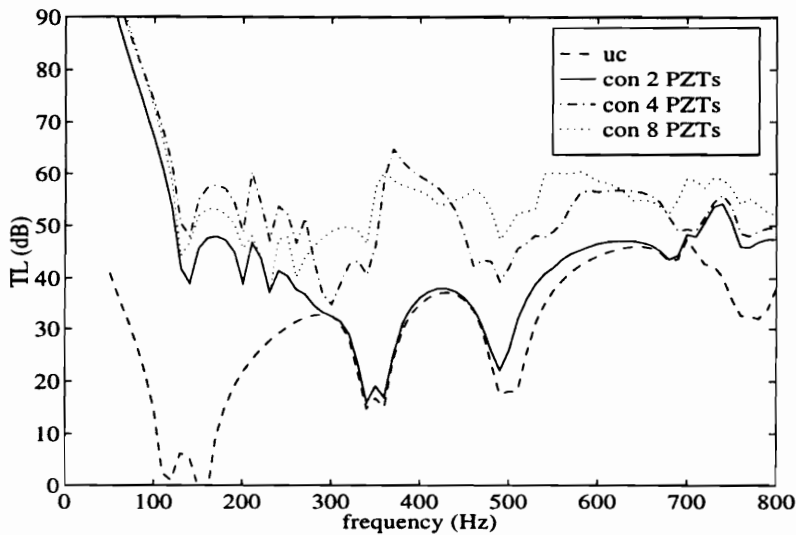


**Figure 5-51. Effect of number of PZT actuators on double panel system transmission loss controlled by BIO adaptive phase method (normal incident wave; aluminum radiating plate)**

### 5.4.3. Effect of master actuator choice on control performance

The effect of the master actuator selection on BIO control performance is presented in Table 5-22, Table 5-23, and Table 5-24 for the phase variation, adaptive magnitude, and adaptive phase methods, respectively. The phase variation and adaptive magnitude methods exhibit a dependence on the choice of master actuators where the adaptive phase method does not. It is evident that the bounded phase of the phase variation method makes choice of master actuator a factor, although the differences in performance is minimal at 2.4 dB.

**Table 5-22. Effect of master actuator on BIO controller phase variation method frequency averaged transmission loss (normal incident wave; aluminum radiating plate)**

Master actuator #	increase in $TL_{avg}$ (dB) 50-800 Hz
1	15.7
2	16.0
3	13.6
4	15.9

**Table 5-23. Effect of master actuator on BIO controller adaptive magnitude method frequency averaged transmission loss (normal incident wave; aluminum radiating plate)**

Master actuator #	increase in $TL_{avg}$ (dB) 50-800 Hz
1	12.3
2	13.6
3	13.7
4	13.4

**Table 5-24. Effect of master actuator on BIO controller adaptive phase method frequency averaged transmission loss (normal incident wave; aluminum radiating plate)**

Master actuator #	increase in $TL_{avg}$ (dB) 50-800 Hz
1	41.8
2	41.8
3	41.8
4	41.8

#### 5.4.4. Computational effort

In this section, the computational effort for a complete update of all control channels is presented. The computational effort was determined by the update equations themselves (see Chapter 3) for the Filtered-X LMS, time averaged gradient (TAG) LMS, and the BIO algorithm and its various local rules. A comparison of the computational effort for the above mentioned algorithms is presented in Table 5-25, where the number of floating point operations (flops) is presented as a function of the number of control channels (C), the number of error sensors (E), and the number of averages for the TAG LMS (N). For the TAG LMS and all of the BIO methods, a good estimate of the cost function requires the period of averaging of the error signals to be at least one wavelength of the disturbance. The theoretical minimum for the implementation of a FIR filter requires the sampling frequency to be 4 times the disturbance frequency (i.e.  $N=4$ ). In standard practice, the sampling frequency is approximately 10 times the disturbance frequency and therefore the number of averages would equal 10 (i.e.  $N=10$ ). However, implementation of the TAG LMS has shown that more averages provide better gradient estimates due to the noise inherent to the system. A more feasible number of averages is approximately 5 wavelengths or the number of averages equals 20 ( $N=20$ ). For this comparison, the theoretical minimum (i.e.

N=4) and a more realistic number of averages (i.e. N=20) will be used in calculating the computational effort.

As seen in Table 5-25, all of the algorithms except the BIO master and BIO optimal method exhibit a dependence on the product of the number of control channels (C) and the error sensors (M). A comparison of the various control algorithms as a function of system order and period length for the TAG is presented in Table 5-26. For a low order system (5 input 4 output), the BIO phase variation, adaptive magnitude and adaptive phase methods do not show much of an improvement over the Filtered-X LMS or TAG LMS algorithms. However, as the system order increases, computational effort of these BIO methods is approximately half of the LMS algorithms. The greatest savings of computational effort is seen in the BIO optimal method where the update of the master actuator also updates the slave actuators. Compared to the LMS algorithms, the BIO optimal method requires an order of magnitude less computational effort. However, the BIO optimal method relies on pre-determined slave actuator filters which is the main disadvantage of the method.

**Table 5-25. Number of floating point operations (flops) for one update of different control strategies**

Controller	# of flops
Filtered-X LMS	$2C(3M+1)$
TAG LMS	$4C(M+3)+2CN$
BIO master	$4M+2N+9$
BIO PV	$C(2M+3)+CN+2M+N+4$
BIO AM	$C(2M+8)+CN+2M+N+10$
BIO AP	$C(2M+8)+CN+2M+N+10$
BIO optimal	$4M+2C+2N+10$

**Table 5-26. Effect of system order and sample period on number of floating point operations of different control strategies**

System order	5 input 4 output (M=5;C=4)		10 input 8 output (M=10;C=8)		40 input 32 output (M=40;C=32)	
	N=4	N=20	N=4	N=20	N=4	N=20
Controller						
Filtered-X LMS	128	-	496	-	7744	-
TAG LMS	160	288	480	736	5760	6784
BIO master	37	69	57	89	177	209
BIO phase variation	91	171	249	393	2877	3405
BIO adaptive magnitude	106	186	284	428	3032	3560
BIO adaptive phase	106	186	284	428	3032	3560
BIO optimal	46	78	74	106	242	274

#### 5.4.5. Stability

In this section, the stability of the Filtered-X LMS, and the BIO algorithm and its various local rules is presented by comparing the maximum convergence parameter ( $\mu$ ). The maximum convergence parameter was calculated using the equations presented in Section 3.2. The double panel system theoretical model described in Chapter 2 was used to determine the transfer functions from four control actuator voltages to the pressure at five far field locations. These locations are the same as the microphone locations described in the experimental setup in Chapter 4. In addition to the PZT model and the radiated acoustic field model, additional factors must be taken into account to determine the maximum convergence parameter. These include the PZT transformer ratio, amplifier gains for the PZT voltage and the microphone error signal, and other considerations such as z-domain mapping of the control actuator magnitude and phase and the ratio of the maximum input voltage to the maximum output voltage of the digital signal

processor. For this section, the double panel system parameters are: normal incident wave and PZT actuators are located on a sandwich board radiating plate.

Physically, the maximum convergence parameter determines the maximum amount of perturbation in the control actuator input that will result in a stable system, i.e. that the converged LMS solution will approach the Weiner solution (Nelson and Elliot, 1992). This is basically a function of the magnitude of the transfer function between the D/A converter and the A/D converter of the DSP. When the magnitude of the transfer function is larger, the convergence parameter is smaller. If it is assumed that the magnitude of the aforementioned transfer functions is the same, a control system with one output will have a greater maximum convergence parameter than a control system with multiple outputs. This is precisely the type of behavior that is seen in Figure 5-52 where the maximum convergence parameter ( $\mu$ ) for the master algorithm (one output channel) is greater than the one for the four output Filtered-X LMS algorithm. Conversely, after the phase variation method has executed, the maximum convergence parameter for the biologically inspired hierarchical (BIO) algorithm decreases by an order of magnitude due to the additional slave control inputs influenced by the perturbations of the master channel. This behavior is also seen in Figure 5-53 where the master and slave actuators (converged with the adaptive magnitude method) have a maximum convergence parameter less than that of the Filtered-X LMS algorithm.

Note that the minimum in Figure 5-52 corresponds to the out-of-phase fundamental for the sandwich board radiating plate double panel system. Near this region, a small amount of control effort will achieve a large amount of vibration in the double panel system and the maximum

convergence parameter will decrease.

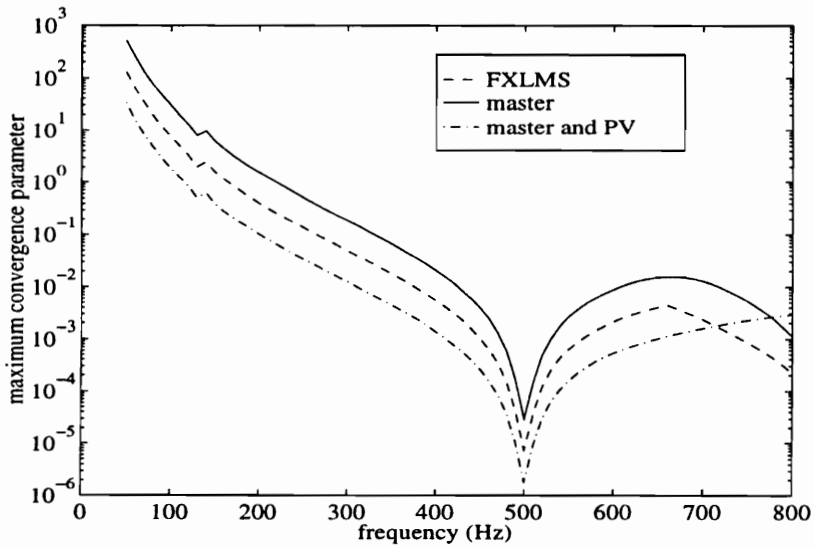


**Figure 5-52. Maximum convergence parameter ( $\mu$ ) for Filtered-X LMS, master, and master with slave actuators using phase variation method (normal incident wave; PZTs located on sandwich board radiating plate )**

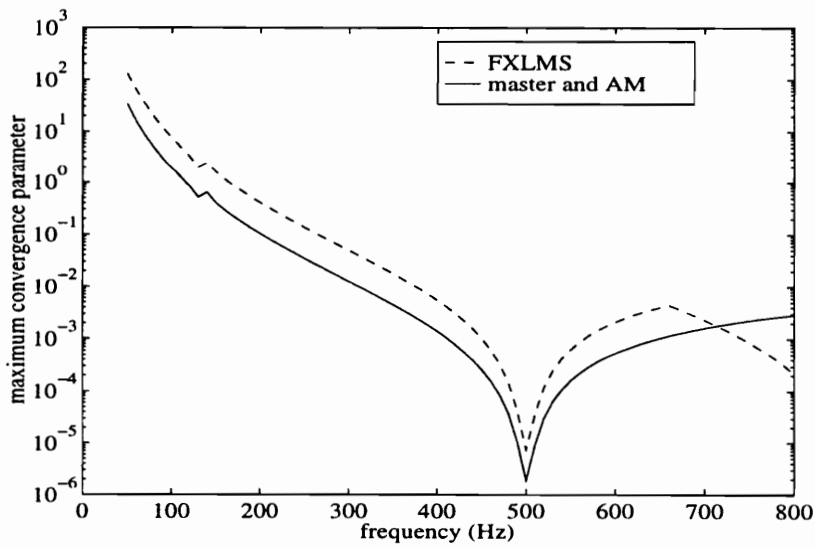


**Figure 5-53. Maximum convergence parameter ( $\mu$ ) for Filtered-X LMS, and master with slave actuators using adaptive magnitude method (normal incident wave; PZTs located on sandwich board radiating plate )**

## **6. Experimental Results**

An experimental investigation of active structural acoustic control of double panel systems was performed to verify the analytical trends presented in Chapter 5. The results from the experimental investigation are presented in this chapter, which is divided into three sections. First, the results of the active structural acoustic control of double panel systems using the Filtered-X LMS algorithm is presented. The biologically inspired hierarchical (BIO) control algorithm is then applied to double panel systems. Finally, the control performance of a real double panel system is investigated on a Cessna experimental aircraft fuselage.

### **6.1. Active structural acoustic control of double panel systems**

The experimental results of active structural acoustic control (ASAC) applied to double panel systems using the Filtered-X LMS algorithm are shown in this section. The arrangement for these experiments was previously discussed in Section 4.1.1. While a wide variety of test cases were experimentally performed, only illustrative results will be presented due to the extensive amount of information collected. First, a system identification of the incident and radiating plates as well as the double panel system are presented to give insight into double panel system behavior. Then the influence of various double panel system parameters on control performance is presented including the influence of radiating plate stiffness, PZT location, excitation



frequency, incident plane wave and number of control actuators. In these sets of experiments, the flexible radiating plate is made of G10 fiberglass and is referred to as the *G10 radiating plate* while the stiff radiating plate is constructed of sandwich board and is referred to as the *sandwich board radiating plate*. Note that all of the results presented in this section are for single frequency excitation only.

### **6.1.1. Preliminary results: double panel behavior**

Preliminary frequency response testing of the individual plates and the double panel system was performed to determine the double panel system resonant frequencies. Tests were performed on the plates clamped in the steel frame of the transmission loss test facility. The spectrally white (in terms of frequency and wavenumber) excitation of each plate was approximated by a point force impulse applied with a modal hammer. The plate and double panel system response was measured with an accelerometer, while the signals were processed by a Bruel and Kjaer Type 2032 dual channel signal analyzer. Frequency response functions were taken for two double panel systems, consisting of the incident plate (aluminum plate), and either the flexible radiating plate (G10 fiberglass) or the stiff radiating plate (sandwich board), and are shown in Figure 6-1. Frequency response functions were also taken for a single plate, consisting of the flexible plate (G10 fiberglass), or the stiff plate (sandwich board). Comparisons of the coupled and uncoupled radiating plates are presented in Figure 6-2. A summary of plate properties was previously presented in Table 4-1.

The choice of a suitable on-resonance and off-resonance excitation frequency for the active structural acoustic control (ASAC) experiments presented in the following sections is now

discussed. These frequencies were determined by the double panel system frequency response function shown in Figure 6-1. The G10 radiating plate double panel system on-resonance frequency was chosen to be 361 Hz, corresponding to a region where both the incident plate and the radiating plate show resonance behavior. Off-resonance excitation was chosen to be 218 Hz, which does not correspond to a resonance for both plates. Due to the high stiffness of the sandwich board radiating plate, both on-resonance and off-resonance conditions were chosen below the fundamental frequency of the radiating plate. The on-resonance case, 496 Hz, is close to the fundamental frequency of the sandwich board radiating plate, and is at a resonance of the incident plate. Off-resonance excitation was chosen to be 361 Hz, which is well below the fundamental of the radiating plate, and off a resonance peak for the incident plate as well.

Another issue was the amount of plate-cavity-plate coupling the individual plates exhibited when placed in a double panel test configuration. Figure 6-2 shows a plot of the uncoupled (individual plate) and coupled (plate-cavity-plate double panel system) G10 fiberglass and sandwich board frequency response functions. As can be seen, there is a significant difference in the individual plate response and the coupled double panel system response of the G10 radiating plate. Below 300 Hz, the plate FRF exhibits a shift in resonance frequencies. In particular, the fundamental resonance frequency was shifted from 85 Hz to 102 Hz. Although not shown in the figure, the incident plate experiences the same type of frequency shift for the fundamental resonance, decreasing from 118 Hz to 102 Hz. From this behavior, it is evident that the incident plate and the flexible plate are highly coupled by the air in the cavity between the incident and radiating plates. The response for the sandwich board radiating plate, also shown in Figure 6-2, does not display a shift in frequency as seen for the G10 radiating plate, but displays a difference in the

sharpness of the fundamental resonance peak. The uncoupled sandwich board radiating plate response displays a significant amount of structural damping, evident from the flatness of the uncoupled response. With the addition of the incident plate, the sandwich board radiating plate response exhibits a decrease in the system damping. Overall, the incident plate has little effect on the sandwich board radiating plate.

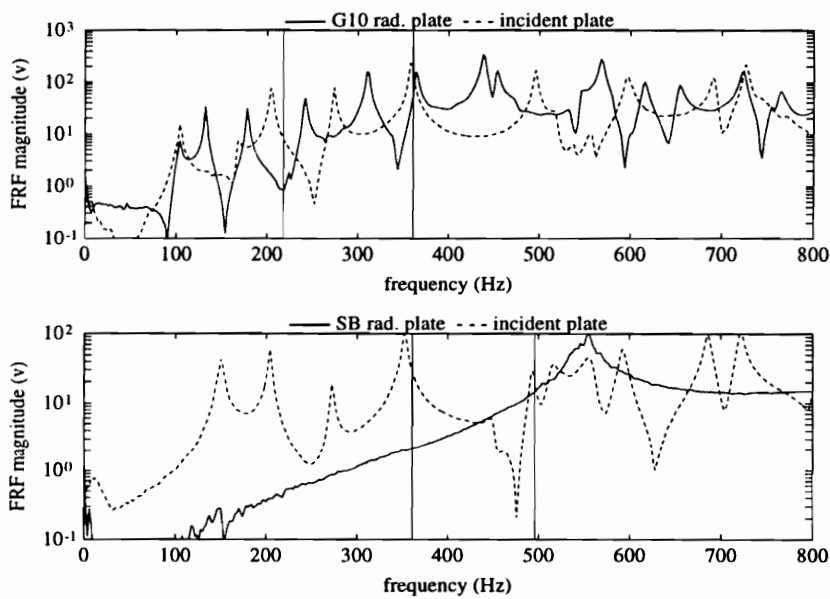


**Figure 6-1. Flexible (G10 fiberglass) and stiff (sandwich board (SB)) double panel system frequency response functions**

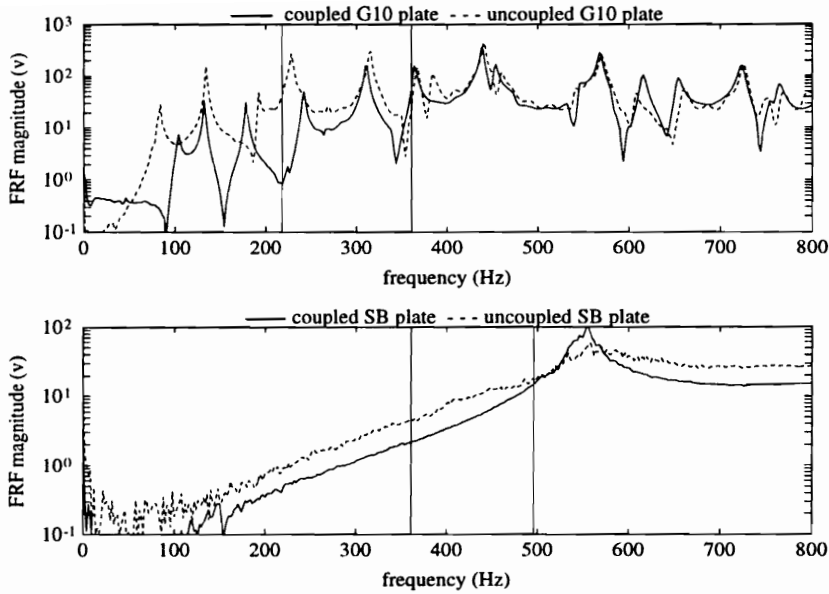


**Figure 6-2. Flexible (G10 fiberglass) and stiff (sandwich board (SB)) plate coupling**

### 6.1.2. Effect of radiating plate stiffness on control performance

To study the influence of radiating plate stiffness, the double panel system was tested with a flexible radiating plate constructed of G10 fiberglass and a stiff radiating plate constructed of sandwich board material. Other test parameters were held constant: The double panel system with the control inputs applied to the radiating plate was excited by a normal plane wave acoustic field. A three input, three output (3I3O) Filtered-X LMS control algorithm was used. Both radiating plates were tested at double panel system resonance and off-resonance frequencies. Acoustical results indicating the increase in transmission loss with control for the G10 and sandwich board radiating plates are presented in Table 6-1. Modal decompositions of the G10 and sandwich board radiating plates excited at a frequency of 361 Hz are presented in Figure 6-3 and Figure 6-4, respectively.

Figure 6-3 shows the uncontrolled and controlled G10 radiating plate modal amplitudes at 361 Hz. This figure indicates that the G10 radiating plate double panel system has a high modal density, which is indicated by several modes contributing to the uncontrolled radiating plate response, specifically the (1,3), (1,1), and the (3,1) modes. Conversely, Figure 6-4 demonstrates that the uncontrolled response of the sandwich board radiating plate has one significant mode at this frequency (the (1,1)) which indicates a double panel system with a low modal density.

A double panel system of low modal density has a fewer number of significant degrees of freedom (in terms of response) and therefore better acoustic attenuation is attained with only three channels of control. This is indicated in Table 6-1, which shows that control of a sandwich board versus a G10 radiating plate double panel system excited on-resonance (361 and 496 Hz for the flexible and stiff radiating plates, respectively) results in an increased transmission loss (TL) with control. In this test case, increase in TL with control was 9.3 dB.

Also, a radiating plate with a low modal density also has a greater stiffness to weight ratio than one with a high modal density, which increases uncontrolled transmission loss (TL). As shown in Table 6-1, a comparison of G10 and sandwich board cases excited off-resonance (218 and 361 Hz for the flexible and stiff radiating plates, respectively) reveals that uncontrolled TL for the sandwich board case is 12.8 dB higher than the G10 case. The increased stiffness also reduces the effect the control actuators have on the radiating plate response and therefore the increase in transmission loss due to active control is reduced. However, the overall transmission loss of the sandwich board case is greater than the G10 case by 7.3 dB.

In summary, a double panel system with a sandwich board radiating plate shows greater overall transmission loss (TL) compared to one with a G10 radiating plate.

**Table 6-1. Flexible (G10 fiberglass) vs. stiff (sandwich board (SB)) radiating plate control performance (normal plane wave)**

Panel	flexible	flexible	stiff	stiff
Frequency (Hz)	218	361	361	496
Resonance ?	no	yes	no	yes
Dominant mode	(3,1)	(1,3)	(1,1)	(1,1)
Uncontrolled TL (dB)	30.8	30.5	43.6	32.1
Controller increase in TL (dB)	10.1	11.1	4.6	20.4
Overall TL (dB)	40.9	41.6	48.2	52.5

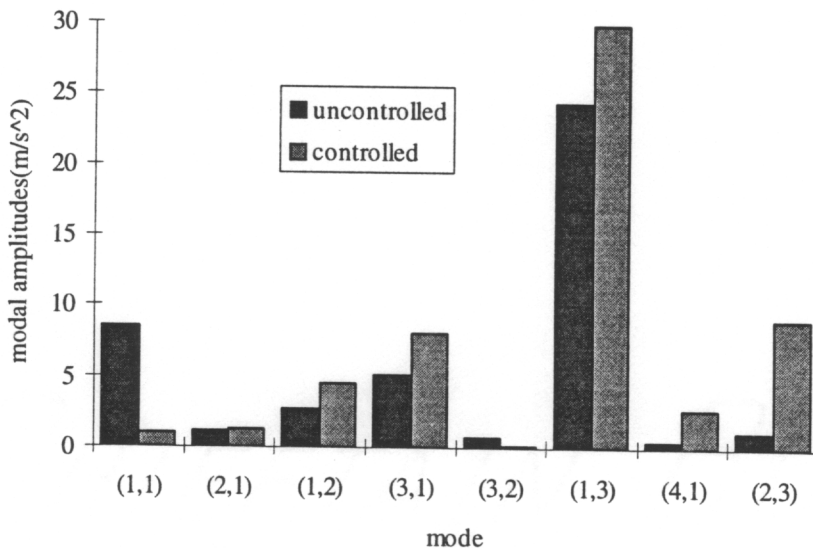


**Figure 6-3. Uncontrolled and controlled flexible radiating plate modal amplitudes at 361 Hz (PZTs located on radiating plate; normal incident wave)**

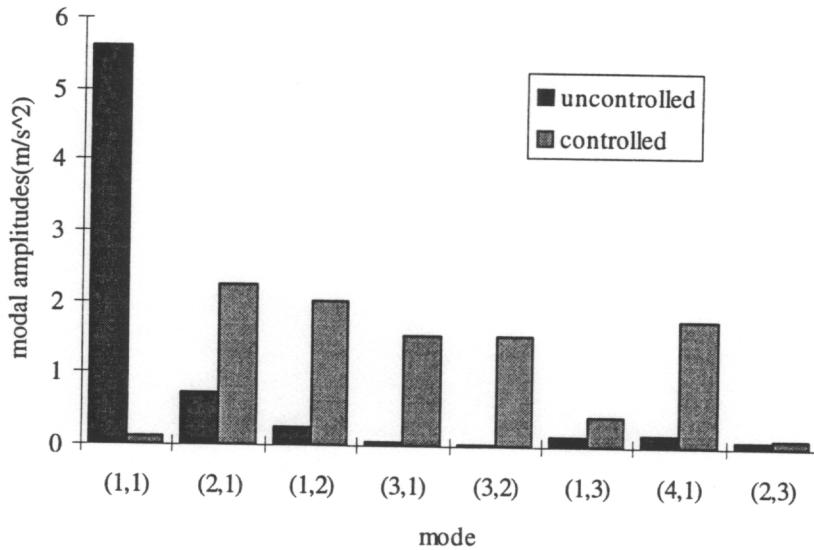


**Figure 6-4. Uncontrolled and controlled stiff radiating plate modal amplitudes at 361 Hz (PZTs located on radiating plate; normal incident wave)**

### 6.1.3. Effect of PZT location on control performance

To study the effect of the PZT location on control performance, the control inputs were applied to the incident plate and then the radiating plate, while holding all other parameters constant: The double panel system with the G10 radiating plate was excited off-resonance at 218 Hz by a reverberant acoustic field. A three input, three output (3I3O) Filtered-X LMS control algorithm was used. The increase in transmission loss (TL) due to the implementation of control are presented in Table 6-2. Modal decompositions of the radiating plate response for the control inputs applied to the incident plate and the radiating plate are presented in Figure 6-5 and Figure 6-6, respectively.

Control of the radiating plate exhibits better overall increase in transmission loss by 5 dB over

control of the incident plate, shown in Table 6-2. Figure 6-5 indicates that when the control inputs are applied to the incident plate, the radiating plate response shows a reduction in the amplitude of the efficient acoustic radiating modes ( (1,1) and (3,1) ), as well as most of the other modes. The mechanism of control is modal suppression (Fuller, 1989). In effect the controlled incident plate is decreasing the source strength transmitted across the air cavity to the radiating plate.

Figure 6-6 shows that when control inputs are applied to the radiating plate, the reduction of the (1,1) and (3,1) modes ( the most efficient acoustic radiators ) is more extreme and there is a sharp increase in the level of the (3,2) mode, which has a lower acoustic radiation efficiency than the (1,1) and (3,1) modes. The mechanism of control is modal restructuring (Fuller, 1989), where the controller restructures the plate modal response into less efficient acoustic radiating modes.

The differences in acoustic performance stem from the ability of the control system to affect the structural-acoustic coupling between the radiating plate and the receiving chamber. Control inputs that can directly affect the structural acoustic coupling (i.e., applied to the radiating plate) can directly control the efficient acoustic radiators whereas control inputs that cannot directly affect the structural acoustic coupling (i.e. applied to the incident plate) must control all of the excited modes. Therefore, for a control system with a finite number of control channels, control inputs applied to the radiating plate are more efficient at reducing sound transmission than control inputs applied to the incident plate. This is due to the relatively lower number of system modes that require control. Note that these results agree with the analytical results presented in Section 5.3.2.



**Table 6-2. Effect of PZT location on transmission loss (G10 radiating plate; off-resonance reverberant excitation at 218 Hz)**

Controlled plate	Incident	Radiating
Increase in TL (dB)	0.3	5.4

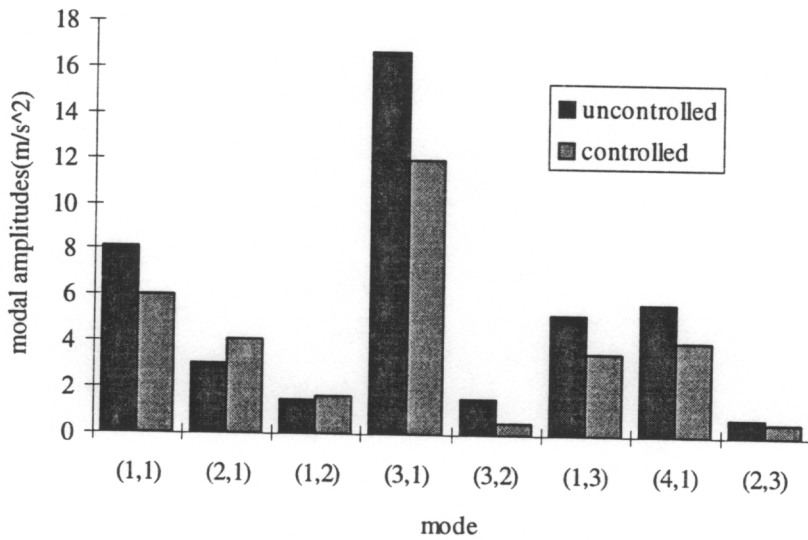


**Figure 6-5. Uncontrolled and controlled radiating plate modal amplitudes at 218 Hz with PZTs located on incident plate (reverberant incident wave; G10 radiating plate)**

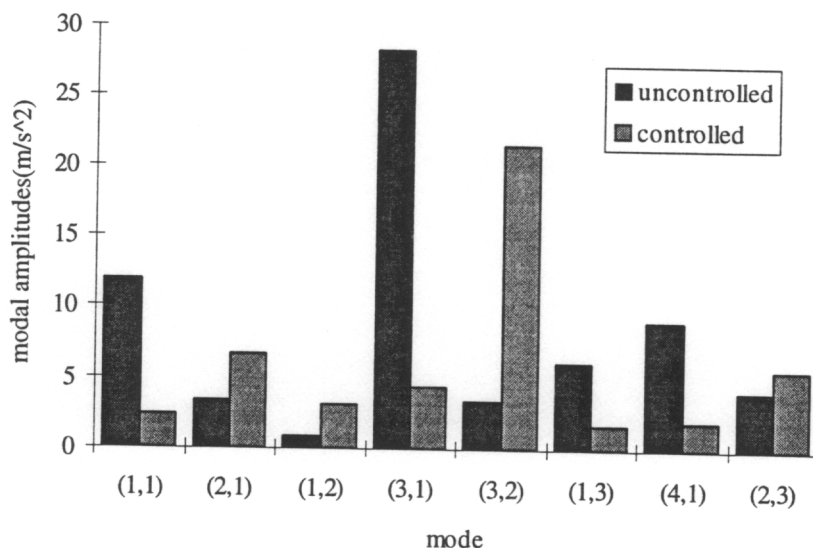


**Figure 6-6. Uncontrolled and controlled radiating plate modal amplitudes at 218 Hz with PZTs located on radiating plate (reverberant incident wave; G10 radiating plate)**

#### 6.1.4. Effect of incident acoustic field on control performance

To study the influence of the incident acoustic field on control performance, the speaker was placed in three different locations indicative of normal plane wave, oblique plane wave, and reverberant excitation, while holding all other parameters constant. The double panel system with the control inputs applied to the G10 radiating plate was excited off-resonance at 218 Hz. A three input, three output (3I3O) Filtered-X LMS control algorithm was used. Acoustical results indicating the increase in transmission loss (TL) due to the implementation of control are presented in Table 6-3. Modal decompositions of the uncontrolled and controlled G10 radiating plate response are presented in Figure 6-7 and Figure 6-8, respectively.

Control performance for a double panel system excited by a plane wave acoustic field is better by 2.2 dB over an oblique plane wave acoustic field and 5.0 dB over a reverberant acoustic field, as

seen in Table 6-3.

As seen in Figure 6-7, all three acoustic excitation fields, normal plane wave, oblique plane wave, and reverberant exhibit similar uncontrolled radiating plate modal response, accounting for variations in source strength. Note that the (1,1) and (3,1) modes were primarily excited. However, the controlled radiating plate modal response for the various excitation fields shows significant differences, as seen in Figure 6-8. Reductions in the (1,1) mode for normal plane wave and oblique plane wave incident fields are similar, while reductions in the (1,1) mode for reverberant incident field was less. Reduction in the (3,1) mode for the plane wave incident field was larger than the reduction in the (3,1) mode for the oblique plane wave and reverberant incident fields. It is evident that the good control performance of the double panel system excited by a normal plane wave acoustic field is due to the ability of the control system to reduce the two most efficient acoustic radiators, the (1,1) and (3,1) modes. The oblique plane wave acoustic field control performance was slightly less due to the poor reduction of the (3,1) mode. The reverberant acoustic field control performance was less due to the poor reduction of the (1,1) and (3,1) modes compared to the normal plane wave case.

Comparing these experimental results to the analytical results in Section 5.3.3, it can be seen that the analytical uncontrolled double panel system modal response for a normal plane wave is significantly different from the oblique plane wave case as seen in Figure 5-23 and Figure 5-24, respectively. The aluminum radiating plate response (comparable to the G10 radiating plate) has a higher number of excited modes for the oblique plane wave versus the normal plane wave. The experimental results did not show this difference. Possible causes for this discrepancy could be

due to the structureborne flanking path. To create acoustic levels in the receiving chamber that were several orders of magnitude above the background noise, the speaker in the source chamber has to create sound levels of approximately 120 dB at the incident plate. These high acoustic excitation levels produced significant vibration of the common wall of the transmission loss test facility. It is possible that this vibration also excited the double panel system and resulted in the uniformity of the uncontrolled experimental modal response.

However, the experimental controlled modal response showed significant variations between the different acoustic excitations. Therefore, it can be reasoned that the incident field had an influence on the double panel system controlled behavior. Control of the double panel system excited by the oblique and reverberant incident waves is more difficult since the incident forcing functions are more complex and couple into more modes of the double panel system.

**Table 6-3. Excitation field control performance (218 Hz; flexible plate)**

Excitation	Normal	Oblique	Reverberant
Increase in TL with control (dB)	10.4	8.2	5.4

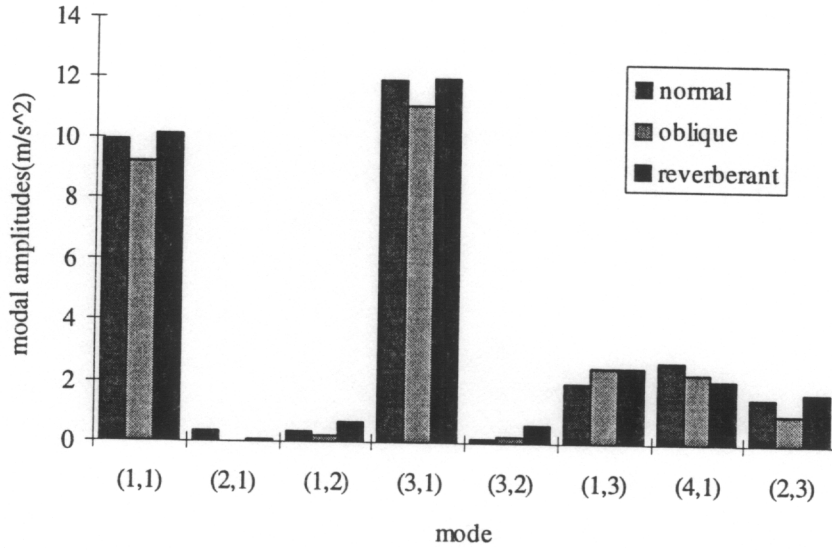


**Figure 6-7. Uncontrolled flexible radiating plate modal amplitudes off-resonance at 218 Hz (PZTs located on radiating plate)**

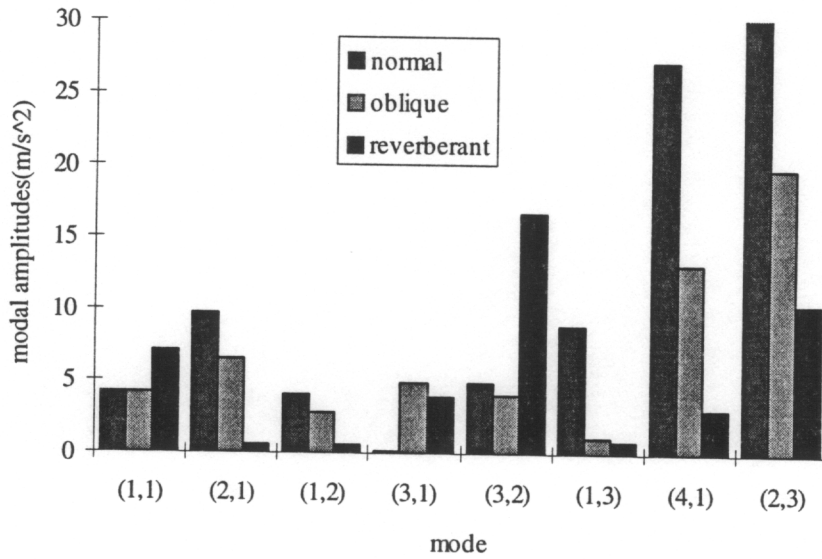


**Figure 6-8. Controlled flexible radiating plate modal amplitudes off-resonance at 218 Hz (PZTs located on radiating plate)**

### 6.1.5. Effect of excitation frequency on control performance

A comparison of the controlled double panel system response excited off-resonance and on-resonance is presented. For this test, the double panel system with a sandwich board radiating plate was excited by a plane wave acoustic field at 361 Hz (off-resonance) and 496 Hz (resonance). A three input, three output (3I3O) Filtered-X LMS control algorithm was used. Acoustical results indicating the increase in transmission loss (TL) due to the implementation of control are presented in Table 6-4. Modal decompositions of the sandwich board radiating plate response excited off-resonance and on-resonance are presented in Figure 6-9 and Figure 6-10, respectively.

Control of the double panel system excited on-resonance was more effective than one excited off-resonance by 15.8 dB, as seen in Table 6-4. The modal decomposition of the sandwich board radiating plate indicates that the uncontrolled response of the (1,1) mode is significantly higher when excited on-resonance (Figure 6-10) compared to off-resonance (Figure 6-9). This is definitive of resonance behavior.

Controlled radiating plate response of the double panel system excited off-resonance, shown in Figure 6-9, shows a significant reduction in the (1,1) mode along with significant increases in most of the other modes. However, the controlled radiating plate response of the system excited at resonance, shown in Figure 6-10, shows little or no increase in the other modes with a significant reduction in the (1,1) mode. Again, this is expected behavior of systems excited at a resonance.

**Table 6-4. Excitation frequency control performance (stiff plate; normal plane wave)**

Frequency (Hz)	361	496
Resonance ?	no	yes
Increase in TL with control (dB)	4.6	20.4

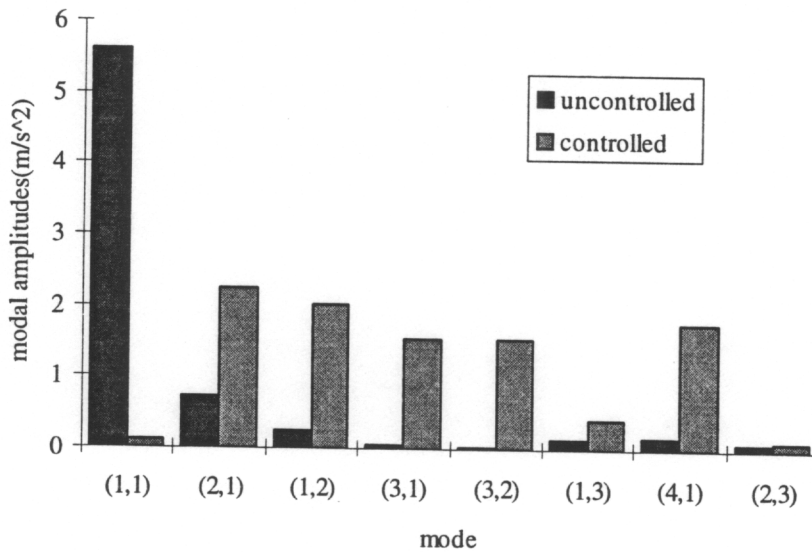


**Figure 6-9. Uncontrolled and controlled stiff radiating plate modal amplitudes off-resonance at 361 Hz (PZTs located on radiating plate; normal incident wave)**

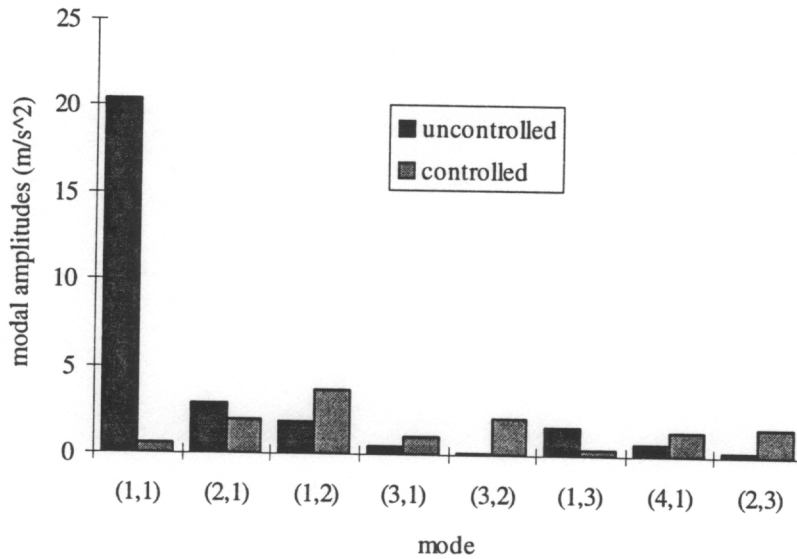


**Figure 6-10. Uncontrolled and controlled stiff radiating plate modal amplitudes on-resonance at 496 Hz (PZTs located on radiating plate; normal incident wave)**

### 6.1.6. Effect of the number of control actuators on control performance

The influence of the number of control actuators on controlled transmission loss is presented for a double panel system by a normal plane wave and controlled by 2 or 3 control actuators mounted to the flexible radiating plate. A three input, three output (3I3O) Filtered-X LMS control algorithm was used. Acoustical results indicating the increase in transmission loss (TL) due to the implementation of control are presented in Table 6-5.

As expected, an increasing number of control actuators increases the amount of control as seen in Table 6-5. For a double panel system excited off-resonance at 218 Hz, increasing the number of control actuators from 2 to 3 increased the TL of the double panel system by 6 dB. This agrees with the analytical results presented in Section 5.3.4.



**Table 6-5. Influence of number of control actuators on control performance (normal plane wave; flexible radiating plate; 218 Hz)**

Number of control actuators	2	3
Increase in TL with control (dB)	5.5	11.5

### 6.1.7. Summary

In Section 6.1, the influence of various double panel system parameters on control performance was experimentally investigated. In all cases, a three input, three output (3I3O) Filtered-X LMS control algorithm was used. The results presented can be summarized as follows. The frequency response functions of the double panel system showed that the plate-cavity-plate coupling was less for a sandwich board radiating plate than the G10 radiating plate in the frequency range examined. This was a result of the increased stiffness of the sandwich board radiating plate. A double panel system with a sandwich board radiating plate was shown to increase the overall transmission loss (TL) due to added stiffness and a lower modal density of the double panel system. The application of the control actuators to the radiating plate of the double panel system proved more effective than controlling the incident plate since the actuators could directly affect the structural-acoustic (or radiation) coupling when applied to the radiating plate. Control of a double panel system excited by a normal plane wave was more effective due to the lower modal density of the system. As expected, more control was achieved for a double panel system excited at resonance than one excited off-resonance. Also, an increase in the number of control actuators increased control performance.

The experimental results presented in this section show the same trends as the analytical model results presented in Chapter 5 and therefore provides validation of the double panel system analytical model. This is important to the design of double panel systems so that they can be optimized to take advantage of active structural acoustic control. It is also important that a double panel systems model exists to investigate different control strategies as is being done in this dissertation.

## **6.2. BIO control of double panel systems**

The experimental results of the biologically inspired hierarchical (BIO) control algorithm applied to double panel systems are detailed in this section. The experimental arrangement for these experiments was previously discussed in Section 4.1.1. The basic double panel system model is the same as the analytical double panel system configuration presented in Chapter 5 and a brief review is presented: An oblique acoustic plane wave excites an aluminum incident plate of a double panel system. The induced incident plate motion excites the acoustic cavity thereby inducing motion of the radiating plate. The radiating plate then emits acoustic power into an acoustic free field. In these sets of experiments, the flexible radiating plate is made of aluminum while the stiff radiating plate is constructed of sandwich board. The cost function is defined as the radiated acoustic power from the radiating plate. Control is provided by piezoelectric (PZT) actuators mounted on the incident or radiating plates. The positions of the PZT's were previously presented in Table 4-6. Note that all of the results presented in this section are for single frequency excitation only.

In the following sections, experimental control performance of the various local rules of the

biologically inspired (BIO) control algorithm is compared to the control performance of the Filtered-X least mean squares (FXLMS) and time averaged gradient (TAG) LMS algorithms, including stability considerations.

### **6.2.1. BIO control performance**

To compare the various control methodologies, the double panel system parameters were set to various configurations and then the various control methodologies were implemented. As can be seen in Table 6-7, there were two double panel system configurations which were both tested on and off-resonance. Both configurations had PZT control actuators mounted on the radiating plate of the double panel system. The first configuration was an aluminum radiating plate double panel system excited by a normal incident wave. The other was a sandwich board radiating plate double panel system excited by an oblique incident wave. The on-resonance excitation frequencies were 355 and 350 Hz for the aluminum and sandwich board radiating plates, respectively and the off-resonance excitation frequencies were 525 and 653 Hz for the aluminum and sandwich board radiating plates, respectively. The control system had either one or four control channels and five error sensors.

The first comparison that was made contrasted the Filtered-X LMS and the TAG LMS algorithms. As can be seen in Table 6-6, the performance of these two algorithms was comparable for the sandwich board radiating plate double panel system configuration and number of output channels. For the aluminum radiating plate double panel system excited at 355 Hz, the increase in transmission loss (TL) with the 5I4O TAG LMS algorithm is 7 dB less than that obtained with the Filtered-X LMS algorithm. This is most likely due to the high transmission

loss (TL) levels with control. The acoustical field in the anechoic insert before control was 25.0 dB above the noise floor of the transmission loss test facility and reductions in the error signals (microphone voltages) greater than 25 dB were therefore difficult. However, the performance difference in the two algorithms was less than 3 dB for 7 out of the 8 cases and therefore the performance of the Filtered-X LMS and the TAG LMS algorithms is comparable. Since the BIO algorithm is directly comparable to the TAG LMS algorithm, the TAG LMS performance numbers will be used as a baseline.

As can be seen in Table 6-7, the BIO phase variation method did not activate any slave actuators as indicated by the control string. In this string, the circle and plus symbol indicates the master control channel is actuator #1. The zeros indicate that the slave actuator output was 0. A plus or a minus would indicate that the slave control actuators are either in-phase or out-of-phase with the master actuator. Therefore, it is expected that the BIO control algorithm using the phase variation method exhibited similar control performance as the 5I1O Filtered-X LMS and TAG LMS algorithms. The poor performance of the phase variation method is due to the discrete slave filters of this method. Since on-resonance control of the master actuator is good, any additional actuators will tend to decrease performance. In off-resonance situations, the main method of control is modal restructuring (Fuller, 1989) where the phase of the actuators restructures the system vibration. Since the phase variation method does not allow this type of adaptation, no additional control inputs are added and no increase in performance is seen compared to the 5I1O TAG LMS algorithm.

Performance for the BIO adaptive magnitude method ranges from a 3 dB increase to a 5.4 dB

decrease compared to the 5I4O TAG LMS as seen in Table 6-7. For on resonance excitation, there was an increase in performance, but there was a decrease in performance off resonance. On resonance the slave actuators will all need to be in-phase or out-of-phase with the master actuator to achieve modal reduction. The adaptive magnitude method allows this type of adaptation. However, off resonance the phase of the actuators must achieve modal restructuring which requires the phasing of the slave actuators not necessarily near 0 (in-phase) or 180 degrees (out-of-phase) compared to the master actuator. Since the adaptive magnitude method does not allow this type of adaptation, performance at off resonance conditions suffers with this approach.

The BIO adaptive phase method compensates for the shortcomings of the adaptive magnitude method. As can be seen in Table 6-7, the performance of the adaptive phase method is within 2 dB of the 5I4O TAG LMS algorithm. The ability of the method to adapt the phase of the actuators allows modal restructuring in off-resonance situations and modal suppression in on-resonance situations.

As expected, the BIO optimal method performance was within 1 dB of the 5I4O TAG LMS performance.

In the following sections, a detailed look at the BIO control performance is presented at on-resonance and off-resonance conditions. A summary of the results is then presented.

**Table 6-6. Double panel system increase in TL with control for Filtered-X LMS and TAG LMS control methodologies**

Controller	Increase in TL with control (dB)			
	Normal incident wave; PZT's on alum. rad. plate		Oblique incident wave; PZT's on SB rad. plate	
	355 Hz on-res.	525 Hz off-res.	350 Hz on-res.	653 Hz off-res.
5I1O Filtered-X LMS	16.5	5.0	15.6	1.5
5I1O TAG LMS	18.9	4.2	15.8	2.0
5I4O Filtered-X LMS	35.5	9.3	17.7	11.5
5I4O TAG LMS	27.5	7.3	17.7	11.0

**Table 6-7. Double panel system increase in TL with control for various TAG LMS and BIO control methodologies**

Controller	Increase in TL with control (dB)			
	Normal incident wave; PZT's on alum. rad. plate		Oblique incident wave; PZT's on SB rad. plate	
	355 Hz on-res.	525 Hz off-res.	350 Hz on-res.	653 Hz off-res.
5I1O TAG LMS	18.9	4.2	15.8	2.0
5I4O BIO phase variation control string	18.9 ⊕000	4.2 ⊕000	15.8 ⊕000	2.0 ⊕000
5I4O TAG LMS	27.5	7.3	17.7	11.0
5I4O BIO adaptive magnitude	30.6	4.5	17.9	5.6
5I4O BIO adaptive phase	28.1	5.0	15.0	11.2
5I4O BIO optimal	28.5	7.5	17.7	11.0

### *On resonance excitation (350 Hz)*

A detailed performance comparison of the various control methodologies is presented in this section. The test parameters are as follows: a double panel system is excited by an oblique plane wave and control is implemented by PZT actuators attached to a sandwich board (SB) radiating plate. The increase in TL with control was previously presented in Table 6-6 and Table 6-7. Modal decompositions of various control methodologies are presented in Figure 6-11 through Figure 6-17.

First, the 5I1O Filtered-X LMS and the 5I1O TAG LMS modal response is compared. As can be seen in Figure 6-11 and Figure 6-12, the uncontrolled and controlled radiating plate modal response of the two control algorithms is nearly identical taking into account the magnitude differences. This together with the performance numbers in Table 6-6, show that the algorithms are equivalent performers and therefore only the Filtered-X LMS case modal response will be discussed.

As seen in Figure 6-11, the uncontrolled radiating plate modal response of the sandwich board radiating plate indicates that the plate response is dominated by the (1,1) mode. By examining the sandwich board radiating plate double panel system natural frequencies in Table 5-4, it is evident that the response of the double panel system is at the in-phase mode (3,1) resonance. Control of the double panel system can effectively be implemented using one control actuator. This is verified in Table 6-6 where the increase in the number of control actuators from one to four increases the amount of control only by approximately 2 dB. Control performance is significant at 15.6 dB and is achieved by modal reduction of the (1,1) mode with spillover

primarily into the (2,1), (2,2) and (3,2) modes.

Control using the 5I4O Filtered-X LMS algorithm shows modal reduction of the (1,1) mode but the additional control actuators push the spillover into the (3,2) radiating plate mode as seen in Figure 6-13. With the additional three control actuators, performance increases by 2 dB to 17.7 dB. It is interesting to see the different spillover characteristics of the 5I4O TAG LMS algorithm in Figure 6-14. Control performance is the same as the 5I4O Filtered-X LMS however this performance is achieved with less reduction of the (1,1) mode and less spillover into the higher order modes. This difference in controlled modal response must be due to the structure of the TAG LMS algorithm where the control channels are updated one at a time. This is in contrast to the Filtered-X LMS algorithm where all of the control channels are updated simultaneously.

The BIO phase variation method did not activate any of the slave control actuators as explained earlier in this section and therefore the modal response is a repeat of the 5I1O TAG LMS algorithm and is not shown. The BIO adaptive phase and adaptive magnitude methods seen in Figure 6-15 and Figure 6-16, respectively, show the same type of controlled modal response as the 5I1O Filtered-X and TAG LMS algorithms. This is obviously a result of the hierarchical control architecture of the adaptive magnitude and adaptive phase methods. When the master channel updates, the effective number of output channels is one. Therefore similar controlled response for one output channel would be expected for the various algorithms in a situation where the additional channels of control are not really needed (i.e. on-resonance).

The BIO optimal method exhibits the same controlled modal response as the 5I4O TAG LMS as



seen in Figure 6-17. This is expected since the BIO optimal method pre-determined slave actuator gains were determined from the 5I4O TAG LMS converged adaptive filters. The method of determining the slave actuator gains using experimental methods is well established by the figure and the same control performance of 17.7 dB as seen in Table 6-5.

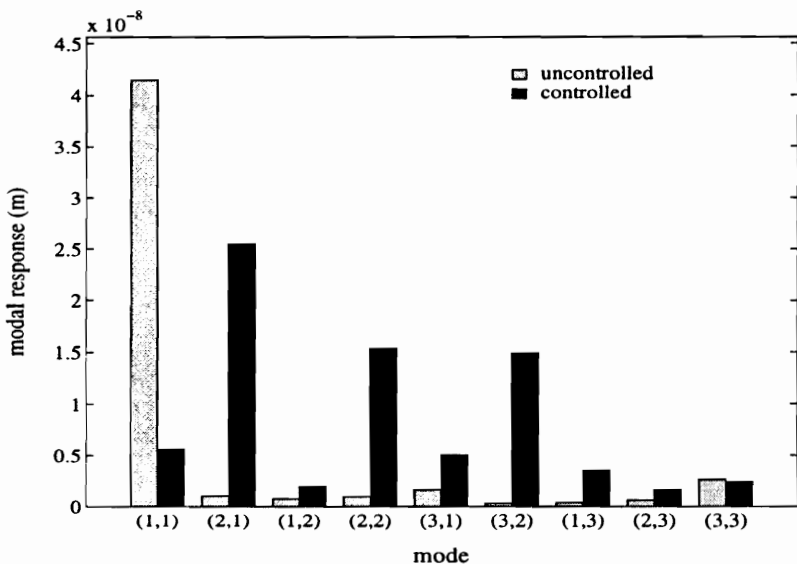


**Figure 6-11. Uncontrolled and controlled modal response for 5 input 1 output Filtered-X LMS controller at 350 Hz (oblique incident wave; PZT's located on sandwich board radiating plate)**

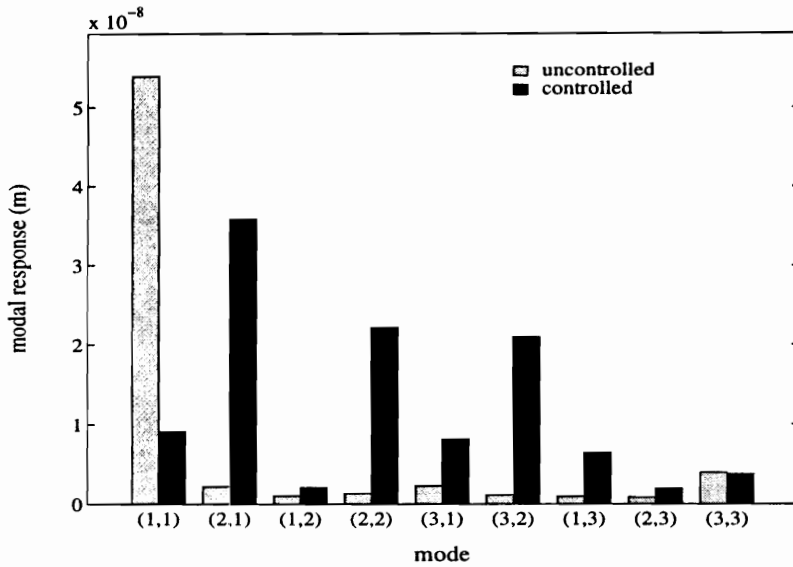


**Figure 6-12. Uncontrolled and controlled modal response for 5 input 1 output TAG LMS controller at 350 Hz (oblique incident wave; PZT's located on sandwich board radiating plate)**

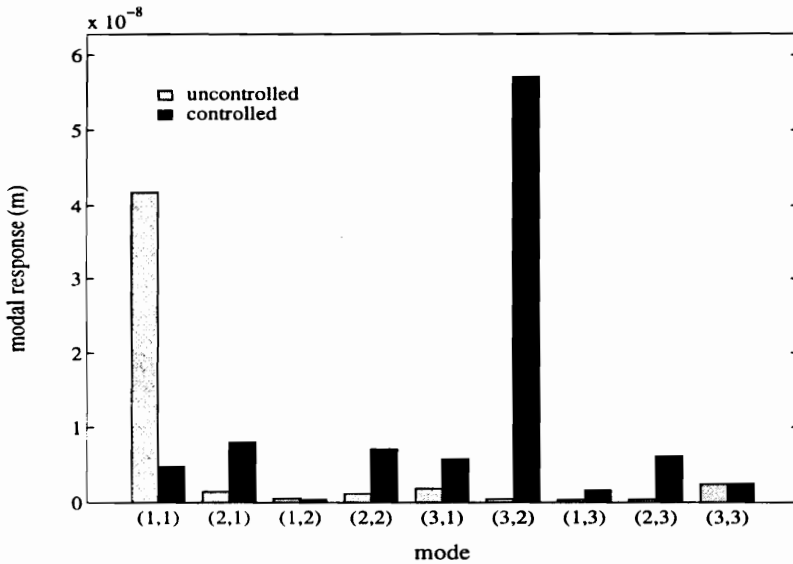


**Figure 6-13. Uncontrolled and controlled modal response for 5 input 4 output Filtered-X LMS controller at 350 Hz (oblique incident wave; PZT's located on sandwich board radiating plate)**

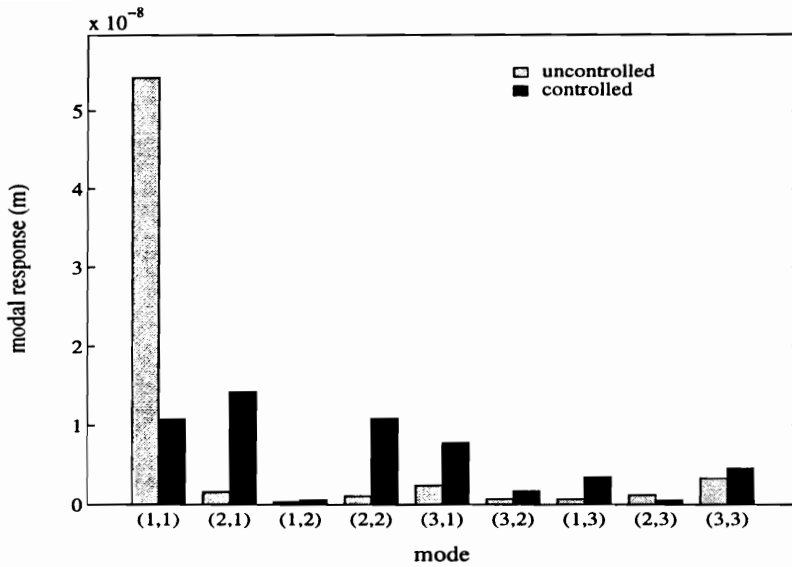


**Figure 6-14. Uncontrolled and controlled modal response for 5 input 4 output TAG LMS controller at 350 Hz (oblique incident wave; PZT's located on sandwich board radiating plate)**

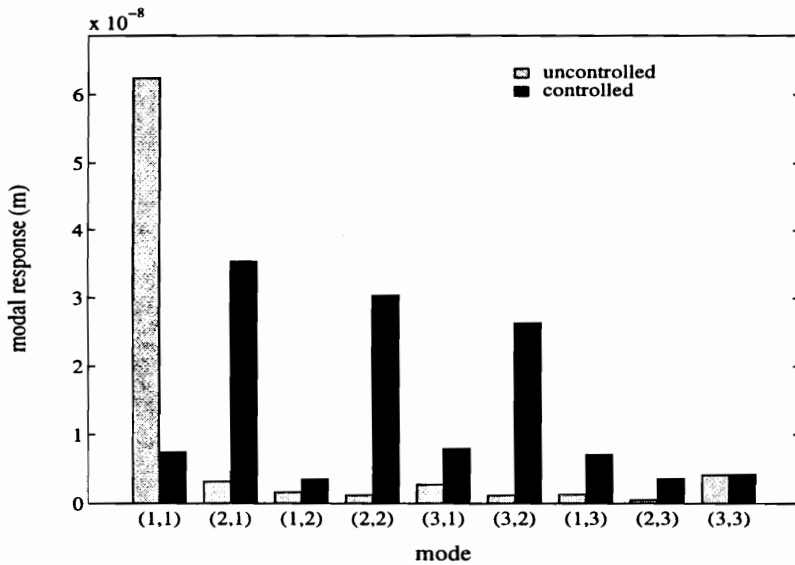


**Figure 6-15. Uncontrolled and controlled modal response for 5 input 4 output BIO controller using adaptive magnitude method at 350 Hz (oblique incident wave; PZT's located on sandwich board radiating plate)**

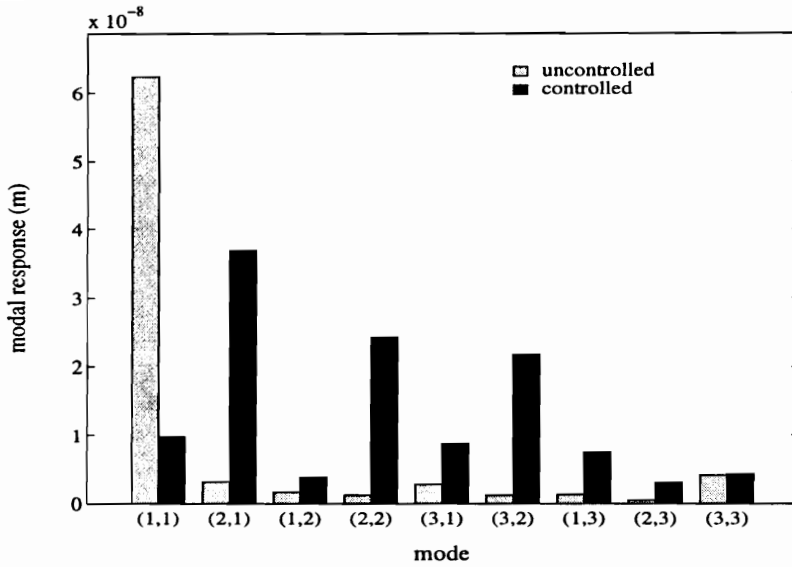


**Figure 6-16. Uncontrolled and controlled modal response for 5 input 4 output BIO controller using adaptive phase method at 350 Hz (oblique incident wave; PZT's located on sandwich board radiating plate)**

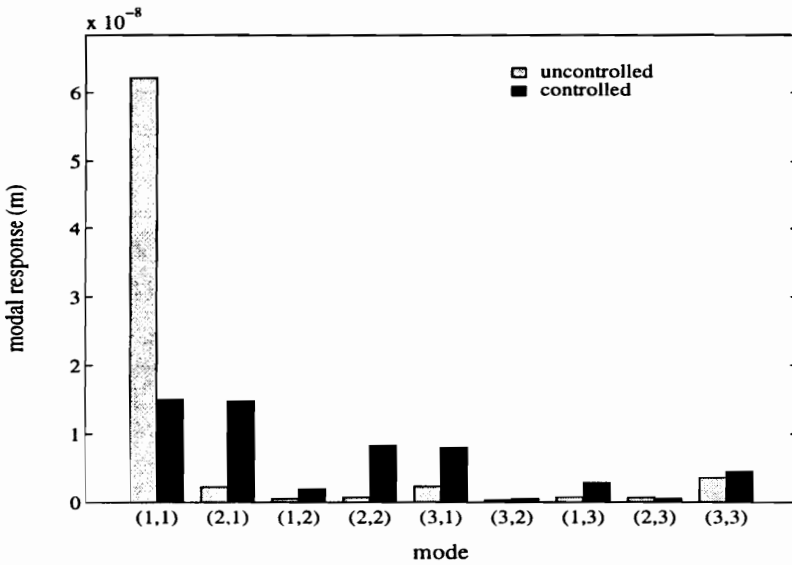


**Figure 6-17. Uncontrolled and controlled modal response for 5 input 4 output BIO controller using optimal method at 350 Hz (oblique incident wave; PZT's located on sandwich board radiating plate)**

### *Off resonance excitation (653 Hz)*

In this section, the performance of the various control algorithms is compared for a double panel system excited off resonance. The test parameters are the same as the preceding section and are repeated: a double panel system is excited by an oblique plane wave and control is implemented by PZT actuators attached to a sandwich board radiating plate. The increase in TL with control was previously presented in Table 6-6 and Table 6-7. Modal decompositions of various control methodologies are presented in Figure 6-18 through Figure 6-24.

First, the 5I1O Filtered-X LMS and the 5I1O TAG LMS modal response is compared. As can be seen in Figure 6-18 and Figure 6-19, the uncontrolled and controlled modal response of the two control algorithms is nearly identical taking into account the magnitude differences. This together with the performance numbers in Table 6-6, show that the algorithms are equivalent performers and therefore only one modal response will be discussed.

As seen in Figure 6-18, the uncontrolled modal response of the sandwich board radiating plate shows that the plate response is dominated by the (1,1) and (2,1) modes, which indicates that the double panel system is not at resonance. Effective control of the double panel system cannot be achieved by using only one control actuator. This is verified in Table 6-6 where the increase in the number of control actuators significantly increases the amount of control from 2.0 dB for the single actuator case to 11.5 dB for the 4 actuator case. For the single actuator case, the main mechanism of control is modal restructuring (Fuller, 1989) where the response of the (2,1), (2,2), and (3,2) modes is increased and properly phased to yield a less efficient radiation pattern.

Control using the 5I4O Filtered-X LMS algorithm shows basically the same modal restructuring however the (2,1) and (3,2) modes show a sharp increase in modal response as seen in Figure 6-20. The additional actuators provide more distributed control and therefore result in better performance of 11.5 dB as seen in Table 6-6. Again, it is interesting to see the different modal restructuring characteristics of the 5I4O TAG LMS algorithm in Figure 6-21. Control performance is comparable to the 5I4O Filtered-X LMS at 11.0 dB, however this performance is achieved with less spillover into the (2,1) and (3,2) modes.

The BIO phase variation method did not activate any of the slave control actuators as explained earlier in this section and therefore the modal response is a repeat of the 5I1O TAG LMS algorithm and is not shown. The BIO adaptive magnitude method, seen in Figure 6-22 shows the same type of controlled modal response as the 5I4O Filtered-X LMS algorithm, except there is a reduction in the (1,1) modal response. Performance of the method was poor compared to the other algorithms at 5.6 dB as seen in Table 6-7. This is consistent with the concept that adapting phase is most important to achieve modal restructuring.

Therefore, the good performance of the adaptive phase method of 11.2 dB as seen in Table 6-7 is expected. The modal response of the method shown in Figure 6-23 exhibits reductions in the (1,1), (2,1), and (3,1) modes and increases in the (1,2), (2,2), and (3,2) modes. It is evident that restricting the adaptation of the slave actuators to phase only has allowed the reduction of all the efficient acoustic radiators with restructuring to the inefficient acoustic radiators. The good performance is a direct result of this restructuring.

As expected, the BIO optimal method exhibits similar controlled modal response as the 5I4O TAG LMS as seen in Figure 6-21. However locking the slave actuators outputs with the predetermined gains (from the 5I4O TAG LMS) allows the same performance of 11.0 dB (as seen in Table 6-7) while reducing the (1,1) mode response.

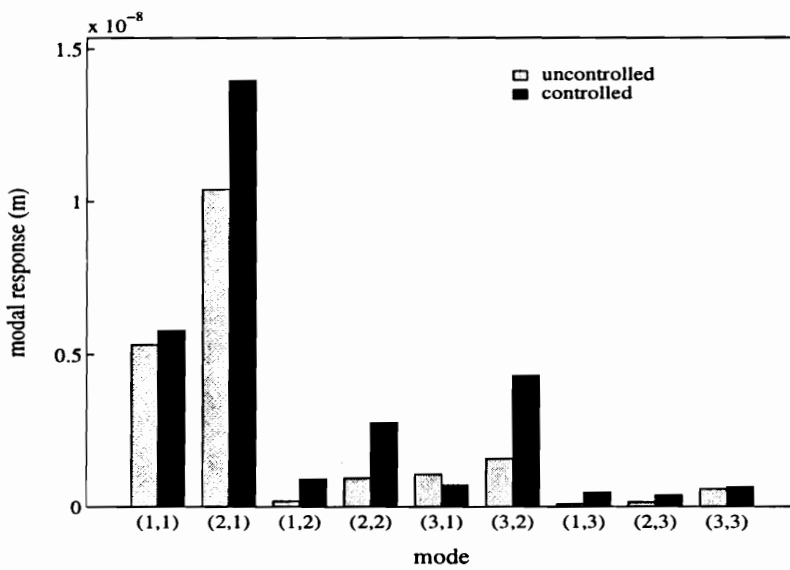


**Figure 6-18. Uncontrolled and controlled modal response for 5 input 1 output Filtered-X LMS controller at 653 Hz (oblique incident wave; PZT's located on sandwich board radiating plate)**

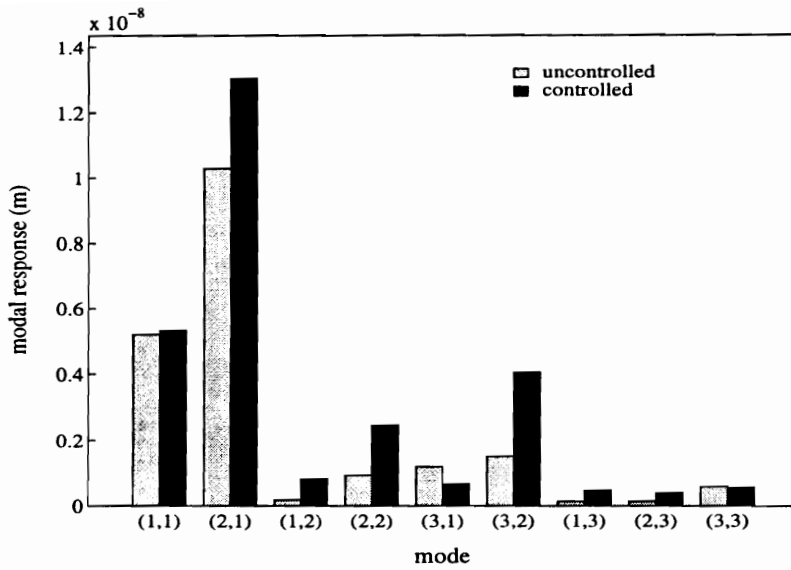


**Figure 6-19. Uncontrolled and controlled modal response for 5 input 1 output TAG LMS controller at 653 Hz (oblique incident wave; PZT's located on sandwich board radiating plate)**

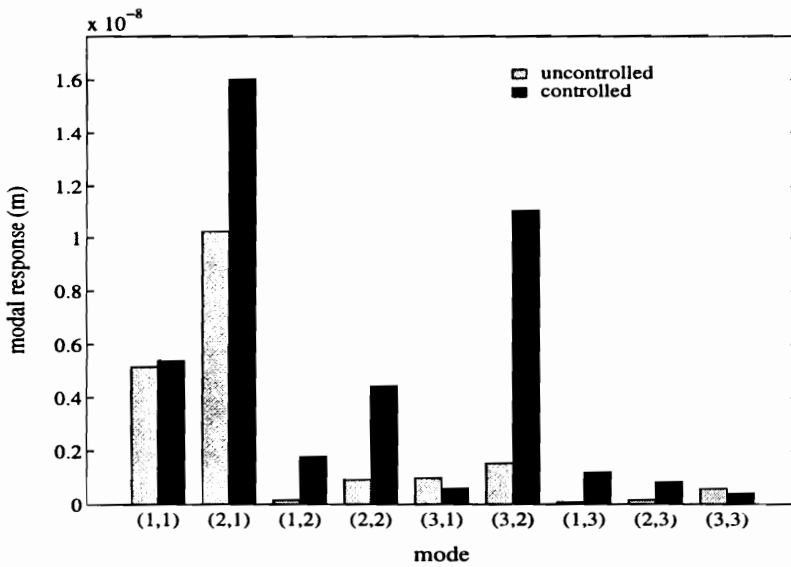


**Figure 6-20. Uncontrolled and controlled modal response for 5 input 4 output Filtered-X LMS controller at 653 Hz (oblique incident wave; PZT's located on sandwich board radiating plate)**



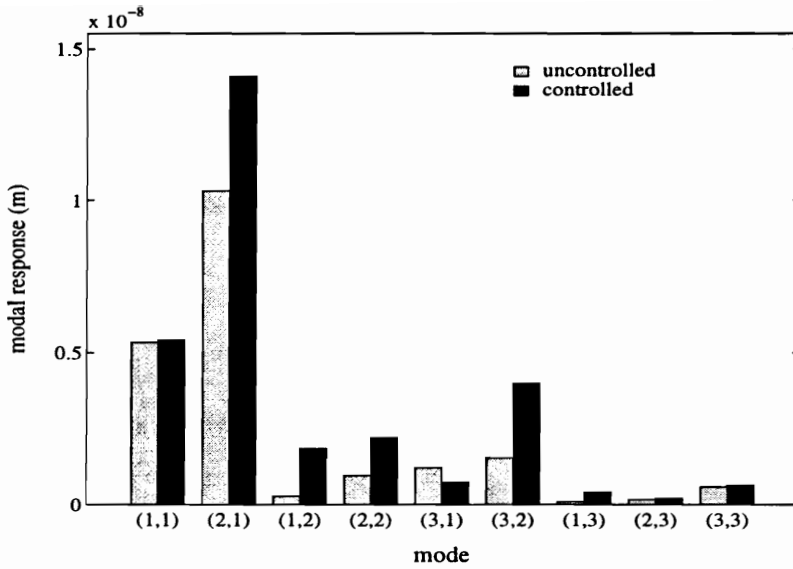


**Figure 6-21. Uncontrolled and controlled modal response for 5 input 4 output TAG LMS controller at 653 Hz (oblique incident wave; PZT's located on sandwich board radiating plate)**

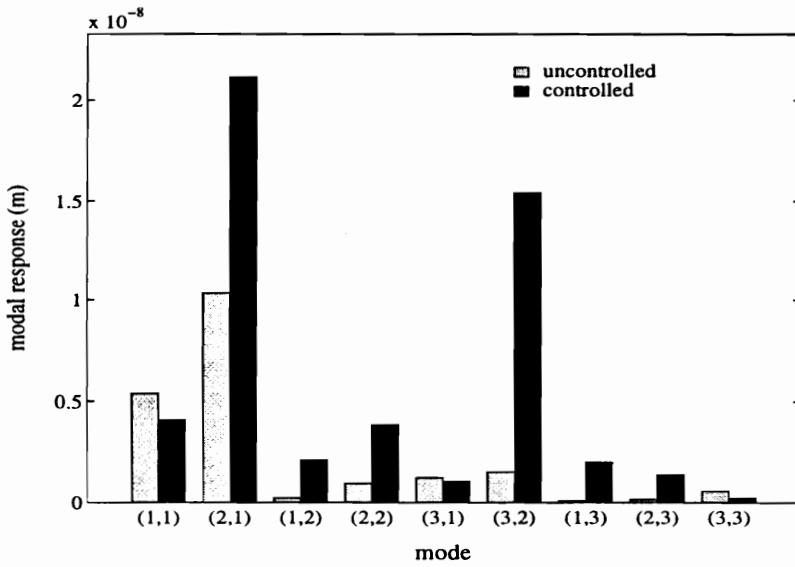


**Figure 6-22. Uncontrolled and controlled modal response for 5 input 4 output BIO controller using adaptive magnitude method at 653 Hz (oblique incident wave; PZT's located on sandwich board radiating plate)**

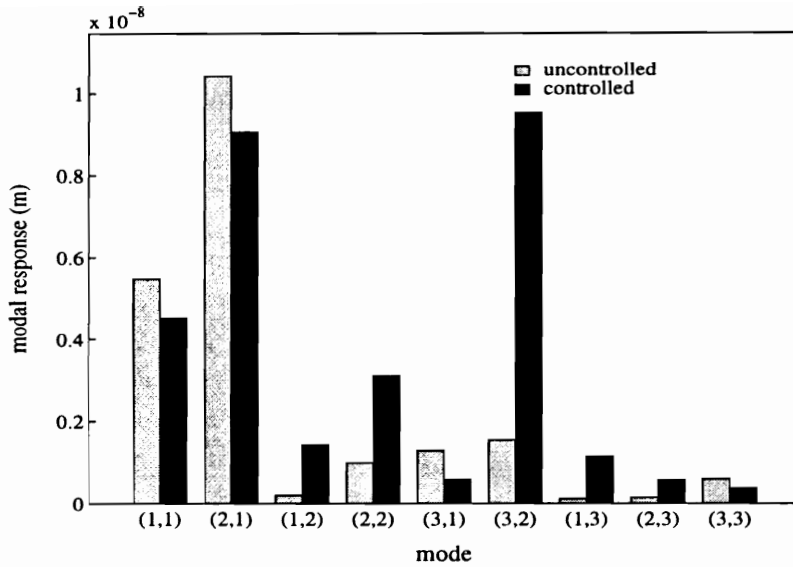


**Figure 6-23. Uncontrolled and controlled modal response for 5 input 4 output BIO controller using adaptive phase method at 653 Hz (oblique incident wave; PZT's located on sandwich board radiating plate)**

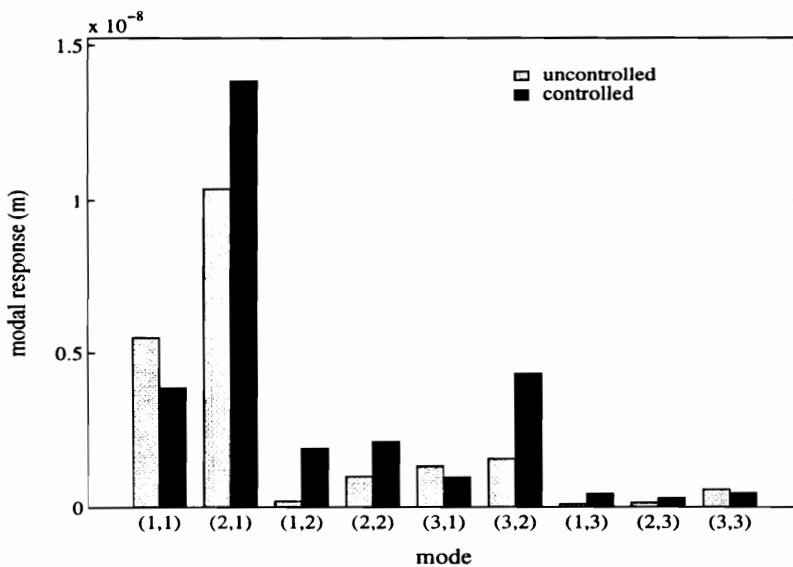


**Figure 6-24. Uncontrolled and controlled modal response for 5 input 4 output BIO controller using optimal method at 653 Hz (oblique incident wave; PZT's located on sandwich board radiating plate)**

### *Summary*

In general, the performance of the biologically inspired hierarchical (BIO) methods was on par to the equivalent TAG LMS system while a reduction in the controller complexity was realized. The maximum performance penalty was 6 dB for the adaptive magnitude method for the 653 Hz case. All of the other cases and methods are within 3 dB.

The BIO phase variation method had poor performance due to the restricted adaptation of this method. The adaptive magnitude method was able to adapt in magnitude only and performance at on-resonance excitation was good. At off-resonance, the main mechanism of control was modal restructuring which required the ability to adapt the phase of the slave filters and poor performance was the result with the adaptive magnitude method. The adaptive phase method performed within 2 dB of the TAG LMS controller regardless of whether the double panel system was excited on-resonance or off-resonance. It is evident that the adaptive phase method will still provide good adaptive control over a range of double panel system conditions while controller complexity can be reduced. As expected, the BIO optimal method showed good performance, however the requirement of prior information to determine the relative slave filters remains a disadvantage.

Compared to the analytical predictions in Chapter 5, the BIO controller experimental results show the same trends. For a system of low modal density which includes on-resonance single frequency excitation, the BIO control methods perform equal or better than a multiple input, multiple output control system due to the ability of the BIO control system to handle the actuator collinearity. For a system of high modal density which includes off-resonance single frequency

excitation, The BIO control methods perform better than a multiple input, single output control system, but worse than a multiple input, multiple output control system of the same order.

### **6.2.2. Stability**

In this section, the stability of the various control methodologies is compared. The theory developed in Section 3.2 predicted that an increased number of control actuators would require a lower maximum convergence parameter. The experimentally determined convergence parameter for a sandwich board radiating plate double panel system excited at 350 Hz is presented in Table 6-8 for the various control methodologies.

First, notice that the 5I1O Filtered-X LMS algorithm has a maximum convergence parameter eight times that of the 5I4O Filtered-X LMS algorithm. The additional control actuators increase the maximum eigenvalue in the update equation (as explained in Sections 3.2 and 5.4.5) and therefore decrease the maximum convergence parameter for a stable system.

The 5I1O TAG LMS, 5I4O TAG LMS, and the 5I4O BIO phase variation method exhibit the same maximum convergence parameter. All of these algorithms adapt the actuators one at a time as explained in Section 3.1.2 and therefore have the same maximum convergence parameter. Note that the phase variation method did not activate any slave actuators as seen in Table 6-7.

The 5I4O BIO adaptive magnitude (master before AM and adaptive magnitude method) method exhibits the same maximum convergence parameter as the above controllers. The first two parts of this method adapts the actuators one at a time as explained in Section 3.1.2 and therefore have

the same maximum convergence parameter. However, the master with slave actuators adaptation has a reduced maximum convergence parameter as seen in Table 6-8. Again, the additional control actuators increase the maximum eigenvalue in the update equation (as explained in Sections 3.2 and 5.4.5) and therefore decrease the maximum convergence parameter for a stable system

The BIO adaptive phase method starts with the slave actuators activated and therefore has a lower maximum convergence parameter than the rest of the BIO algorithms. However, the adaptation of the adaptive phase method has a large maximum convergence parameter of 0.3. It is evident that the adaptive phase update equation has a small maximum eigenvalue.

The BIO optimal method has a small maximum convergence parameter of 0.01 which is expected since the method starts with the slave actuators activated.

In summary, the experimentally determined maximum convergence parameters indicate the same trends predicted in the analytical results and stability bounds are predictable. The addition of control actuators decreases the maximum convergence parameter due to a larger maximum eigenvalue in the update equation.

**Table 6-8. Maximum convergence parameter for various control methodologies (350 Hz oblique incident wave; PZT's located on sandwich board radiating plate)**

Controller	Maximum convergence parameter
5I1O Filtered-X LMS	0.008
5I4O Filtered-X LMS	0.001
5I1O TAG LMS	0.1
5I4O TAG LMS	0.1
5I4O BIO phase variation	0.1
5I4O BIO adaptive magnitude	
master before AM	0.1
adaptive magnitude method	0.1
master w/ slave actuators	.05
5I4O BIO adaptive phase	
master w/ slave actuators	.05
adaptive phase method	.3
5I4O BIO optimal	.01

### **6.3. ASAC of Cessna experimental fuselage double panel system**

The experimental investigations presented in the previous sections were performed on laboratory test structures. These structures are usually simple well defined structures so that the physics of the sound transmission can be usually well understood and perturbations of the basic system properties and controller algorithms can be shown to have a direct effect on the transmission loss. However, there is a need to determine the potential for active structural acoustic control of double panel systems on a realistic structure. Therefore, limited testing of the active structural acoustic control of double panel systems and the BIO hierarchical control strategies was

performed on the Cessna experimental aircraft fuselage that was previously detailed in Section 4.1.2.

The various control methodologies and systems discussed previously were applied to control the interior noise of a Cessna experimental fuselage. The disturbance was a speaker outside and above the cockpit windshield as shown in Figure 4-6. Control was achieved using one, four, or eight PZT actuators mounted to the interior trim *ceiling* of the cockpit called the crown trim panel. Error sensors consisting of four microphones were located at various points in the cockpit and fuselage interior. Another twelve microphones were dispersed throughout the cockpit and fuselage interior to provide additional acoustic measurements to observe the acoustic field before and after control. Further detail of the experimental setup was presented in Section 4.1.2. Tests were run at three frequencies which were determined by Mahnken (1995): a fuselage structural resonance (509 Hz), an fuselage interior acoustical resonance (710 Hz), and a structural and acoustical off resonance (910 Hz). Results are presented for the Filtered-X LMS and TAG LMS algorithms followed by the BIO control methods.

### **6.3.1. Filtered-X LMS algorithm**

In this section, the controller used four error sensors and four control actuators. A comparison of the control performance for the Filtered-X LMS algorithm is presented in Table 6-9. In this Table, the reduction in averaged sound pressure level (SPL, dB) at the error microphones and at all the microphones (referred to as total) is displayed. As can be seen, the Filtered-X LMS controller achieves excellent reduction in sound pressure level at the error sensors while the total reduction in sound pressure level is poor. At the structural resonance (509 Hz), the total reduction

in SPL is only 0.5 dB, however the total reduction at an acoustic resonance is approximately 3.3 dB.

Table 6-10 shows the sound pressure levels at the microphones before control and the  $\Delta$ SPL (dB) with control (i.e. positive numbers indicate a decrease in the SPL) at the acoustical resonance excitation frequency (710 Hz) using the Filtered-X LMS algorithm. As can be seen, significant reduction of the sound pressure field is achieved at the error microphones. Spillover is seen at microphone #2 which is in the vicinity of error microphone #3 (see Figure 4-7) which has good reduction in SPL. Spillover is also seen at microphone #15 while a good reduction in SPL was observed at microphone #16.

For an explanation to this behavior, one must consider the relative excitation levels of the acoustic and structural modes and how these modes interact. At the acoustical resonance, a few control actuators can effectively control the dominant acoustic mode. Control of the interior trim can effectively couple into this mode to reduce the primary global noise field. Spillover is a result of increased excitation of other acoustic modes due to the controlled interior trim (and fuselage) vibration. However, at the structural resonance, there are a multitude of acoustic modes present with no single dominant mode. Also, it has been shown (Gibbs, et al. 1995) that the modal density of the fuselage at higher frequencies (i.e. above 500 Hz) is extremely high (i.e. the individual modes cannot be discerned). Control of the interior trim (and fuselage) structural resonance can result in spillover into other structural modes which couple better into the acoustic field. The result is poor total control of the interior SPL.



These results show the local nature of control which are typical in this frequency range. In this 500-1000 Hz range, the acoustic wavelength is on the order of 0.7 to 0.3 meters, respectively. With shorter wavelengths, active control becomes less global and more local to the vicinity of the error microphones. To achieve global control at these higher frequencies, a multitude of error sensors and actuators must be used.

**Table 6-9. Reduction in interior noise levels (SPL, dB) in Cessna experimental fuselage for Filtered-X LMS algorithm**

Controller	Frequency					
	509 Hz		710 Hz		910 Hz	
	error	total	error	total	error	total
4I4O Filtered-X LMS	33.1	0.5	31.8	3.3	20.9	1.5

**Table 6-10. Sound pressure level at microphones in Cessna experimental fuselage for Filtered-X LMS algorithm (error mic. locations are shaded)**

Microphone #	710 Hz	
	before control	$\Delta$ SPL (dB) with control
1	81.2	0.1
2	65.2	-5.6
3	86	34.2
4	71.3	-1.8
5	67.3	3.1
6	85.6	32.2
7	70.1	-11.6
8	78.9	-25.3
9	79.5	38.1
10	78.6	5.6
11	77.3	-1.1
12	77.7	0.2
13	84.6	0
14	73.7	3.3
15	63.7	-5.2
16	76.3	14.9

### 6.3.2. TAG LMS and biologically inspired hierarchical (BIO) algorithms

The TAG LMS and biologically inspired hierarchical (BIO) algorithms were applied to the Cessna experimental aircraft fuselage to evaluate control performance applied to a realistic double panel system. In this section, the controllers used four error sensors and eight control actuators. The one exception is the biologically inspired hierarchical (BIO) control algorithm using the master actuator only where one control actuator was used. A comparison of the performance for the control algorithms is presented in Table 6-11. In this Table, the reduction in

averaged sound pressure level (SPL, dB) at the error microphones and at all the microphones (referred to as total) is displayed. Note that the 4I1O TAG LMS algorithm would be the same as the “master” algorithm in the preceding BIO algorithm discussions. Since it has been shown that the acoustical response of the fuselage structural-acoustic system is dominated by acoustical resonances (Gibbs, et al. 1995), the results in this section are presented for only the acoustical resonance at 710 Hz.

At the acoustical resonance, the best reduction in the error signals (13.7 dB) was obtained by the 4I8O BIO phase variation algorithm. In general, the reduction at the error microphone using the BIO algorithms was greater than 12 dB. Compared to the 4I1O TAG LMS controller, significant increases in control performance were obtained with additional control actuators. Comparing the total performance, the additional control actuators did not increase the spillover in the structural-acoustic system significantly except for the BIO adaptive phase (AP) method. One possible explanation is that the adaptive phase method relies on modal restructuring to achieve effective control where an acoustical resonance of the fuselage can most effectively be controlled by modal reduction. This is consistent with the good performance of the BIO phase variation (PV) adaptive magnitude (AM) method.

**Table 6-11. Reduction in interior noise levels (dB) in Cessna experimental fuselage for various BIO control methodologies (710 Hz)**

Controller	error	global
4I1O TAG LMS	2.39	-0.4
4I8O TAG LMS	12.7	3.5
4I8O BIO PV	13.7	1.4
4I8O BIO AM	13.0	2.9
4I8O BIO AP	13.0	-0.5

### 6.3.3. Summary

Active structural acoustic control of double panel systems has been investigated on a realistic structure, the Cessna experimental aircraft fuselage. An active trim panel was used to control the interior noise field at a fuselage structural resonance, a fuselage interior acoustical resonance and an off resonance frequency. The results show that good local control (control at the error microphones) can be achieved at all three tested frequencies. However, global control (control at adjacent microphones) was not achieved due to high modal density of the fuselage structural vibration and the fuselage interior acoustic field.

The BIO hierarchical control system was also investigated on the Cessna experimental aircraft fuselage. All of the BIO control algorithms performed comparable to the TAG LMS algorithm at an acoustical resonance of the Cessna experimental aircraft fuselage. Again, good local control was achieved at the error microphones, while global control was not achieved.

The above results show the potential for active structural acoustic control of double panel system in realistic structures. To achieve global control, it is evident that either the modal density of the fuselage structure and/or the interior acoustic field must be lower. This can be accomplished by increasing the stiffness of the structure and/or lowering the excitation frequency. The other solution is to implement a very large number of sensors and actuators. As mentioned in Section 1.2, this presents problems with the computational time and memory requirements and raises the controller collinearity issue and it is in this situation that the BIO controller shows much potential.

## **7. Conclusions**

The intent of this investigation is to show the general trends and principles of active structural acoustic control when applied to double panel systems and determine the advantages and limitations of this approach. This includes the application of novel hierarchical control approaches which sought to reduce the controller complexity and collinearity issues for large order controllers. This research was initiated by an interest in controlling the interior noise field generated by an advanced turboprop engine through the aircraft fuselage and the interior trim into the interior acoustic field.

The primary system studied was a double panel model consisting of two rectangular, uniform, flat plates separated by a sealed air cavity. This double panel system model approximated the behavior of an aircraft fuselage and interior trim. The disturbance was an oblique acoustic plane wave that is assumed to be steady state, single frequency and sinusoidal. This disturbance is an approximation of the primary tone of the exterior acoustic field generated by an advanced turboprop engine. The double panel system vibration radiated energy into an acoustic free field which approximated a highly damped interior acoustic space of the fuselage. Control inputs were provided by piezoelectric transducers that were mounted directly on the double panel system

incident or radiating plates. Error sensors were microphones placed in the acoustic free field. The cost function was defined as an approximation of the total radiated sound power into an acoustic free field surrounding the radiating plate.

Specifically, the objectives of this investigation were: First, to study the application of active structural acoustic control to sound transmission through double panel systems. This was done by developing a model for investigating active control with structural control inputs and an acoustic cost function of double panel systems. Although most of the component structural and acoustic models were available, the double panel system excitation from the radiating panel was derived and then the structural and acoustic models were combined. Once completed, the influence of double panel system parameters on control performance was studied. Double panel system parameters were perturbed and results were presented for the radiating plate stiffness, the application of PZT actuators to the incident or radiating plates, the oblique angle of incident plane wave, and air cavity mass and stiffness.

Next, the biologically inspired (BIO) hierarchical controller was applied to the double panel system. The influence of the number of control actuators and the master actuator number on the various local rules was studied including computational effort and stability aspects of the BIO and Filtered-X LMS controllers.

The investigation used theoretical models to provide analytical results. The analytical results were then verified experimentally. Experiments were mostly performed in the Transmission Loss Test Facility at Virginia Tech on the primary simple structures. Additional limited experiments

were done on the Cessna experimental aircraft fuselage also at Virginia Tech.

From the analytical investigation of active structural acoustic control (ASAC) applied to double panel systems, the best control performance was exhibited by a double panel system excited by a normal plane wave and controlled by PZT control actuators mounted on a sandwich board radiating plate. The sandwich board radiating plate double panel system exhibits a decreased coupling between the incident and radiating plates and a lower modal density which results in increased uncontrolled and controlled transmission loss. A sandwich board radiating plate was also seen to decrease the control effort required due to better impedance matching between the PZT and the radiating plate. Taking the control effort into account, piezoelectric (PZT) control actuators should be mounted on the radiating plate of a double panel system where they can directly affect the structural acoustic coupling.. A double panel system excited by a normal incident wave exhibits better control performance than one excited by an oblique incident wave due to more uniform forcing function which results in a double panel system with a low number of excited modes. As expected, better control is achieved with more control actuators since a more distributed forcing function can be attained. However, for on-resonance excitation, the increased number of actuators often decreases the performance due to collinearity of the actuators which results in spillover. Doubling the air cavity mass has little effect on control performance, however uncontrolled TL is reduced at higher frequencies ( $>400$  Hz). Doubling the air cavity stiffness increases the coupling between the incident and radiating plates resulting in decreased uncontrolled TL and slightly better control performance for PZT's mounted on the incident plate.

The analytical investigation of the biologically inspired hierarchical (BIO) control algorithm

indicated that significant performance increases over a one output channel controller were attained for all of the BIO methods. One advantage of the hierarchical control structure was the ability to avoid the collinearity issue when the degrees of freedom excited in the system was less than the number of control channels. In this instance, the hierarchical structure exhibited less spillover than a fully adaptive LQOCT controller. With the addition of more control actuators, BIO controller performance generally increased except in cases where collinearity became an issue. The choice of the master actuator on BIO control performance was seen to have little effect.

The computational effort of the various control algorithms was presented. For a high number of input and output channels (40I32O) the BIO control algorithm number of floating point operations for one update was approximately half of the Filtered-X LMS algorithm. However, for lower order systems (~5I4O), computational effort is approximately the same. Stability of the BIO control algorithms was predicted and indicates that the maximum convergence parameter for a stable system decreases with an increasing number of control actuators.

Experimental results performed in the transmission loss test facility showed the same trends predicted by the analytical ASAC and BIO results, although the amount of control for the experimental results was significantly lower due to discrepancies in the analytical model and the physical system. These discrepancies include the incident acoustic field, the double panel system boundary conditions, the structural flanking path of the transmission loss test facility, and excitation of a structure by piezoelectric actuators.



All of the control algorithms were applied to the Cessna experimental aircraft fuselage to gauge the performance on a realistic double panel system structure. For these experiments, the frequency range was high (500-1000 Hz) and therefore the acoustical wavelengths were relatively short (0.7 to 0.3 meters). At these high frequencies, the Filtered-X LMS controller was able to reduce the error signals by greater than 20 dB however the total reduction of the fuselage interior acoustic field measured at 12 microphone locations was poor (~3 dB). The main detrimental effect was the amount of spillover at certain microphone locations. The BIO control algorithms exhibited good reduction of 12 dB at the error microphones for an fuselage interior acoustical resonance.

In general, the potential for active structural acoustic control of double panel systems has been shown an effective means of reducing the associated radiated noise field. The structural and acoustic models were experimentally verified and provide a means for investigating various double panel system properties and control algorithms. This investigation has developed models and shown trends that are directly applicable to the interior noise problem in modern aircraft. The potential of reducing the interior noise using active structural acoustic control has been clearly demonstrated. The potential of the BIO hierarchical control algorithms for reducing the control system complexity has been shown with performance approaching a multiple input, multiple output controller of the same order. The ability of the hierarchical structure to handle actuator collinearity was also shown to be extremely important.

## **8. Recommendations**

For future investigations, the following recommendations are made.

It has been shown that the control of the radiating plate of a double panel system is more effective considering the control effort required. This directly indicates that the interior trim of an aircraft should be the controlled structure rather than the fuselage structure. It was also shown that control of the interior trim of the Cessna experimental aircraft fuselage will tend to impart local control at frequencies above 500 Hz. Therefore, it is recommended the amount of reduction in the local and global interior acoustic field is evaluated when controlling the interior trim at frequencies below 500 Hz.

It is evident that the BIO control approach has significant advantages in computational complexity for high order control systems. Also, the ability of the hierarchical structure to handle actuator collinearity was shown to be extremely important. Therefore, it is recommended that the biologically inspired hierarchical (BIO) control approach should further be studied to improve its performance relative to the Filtered-X LMS algorithm. This includes convergence speed and overall control performance.

## References

- Boucher, C.C., S.J. Elliot, and P.A. Nelson, "The Convergence Behavior of a Multichannel Active Noise Control System," Proceedings of the Institute of Acoustics, vol. 12, Part I, pp. 719-727, 1990.
- Bullmore, A. J., P.A. Nelson, S.J. Elliot, "Active Minimization of Acoustic Potential Energy in Harmonically Excited Cylindrical Enclosed Sound Fields," AIAA Paper 86-1958, 1986.
- Carneal, J.P. and C.R. Fuller, "A Biologically Inspired Controller for Sound and Vibration Applications," Presented at the 35th Structures, Structural Dynamics and Materials Conference Adaptive Structures Forum, 1994. (AIAA Paper 94-1785).
- Carneal, J. P. and C. R. Fuller, "A Biologically Inspired Controller," *Journal of the Acoustical Society of America*, **98** (1), July 1995a, pp. 386-396.
- Carneal, J. P. and C. R. Fuller, "A Biologically Inspired Controller for Sound Applications," *AIAA Journal*, Vol. 33, No. 5, May 1995b, pp. 794-797.
- Carneal, J. P., and C. R. Fuller, "Active Structural Acoustic Control of Noise Transmission through Double Panel Systems," *AIAA Journal*, Vol. 33, No. 4, April 1995c, pp. 618-623.
- Clark, R.L., and C.R. Fuller, "Control of Sound Radiation with Adaptive Structures," *Journal of Intelligent Material Systems and Structures*, Vol. 2, pp.431-452, July 1991.
- Clark, R.L., C. R. Fuller and A. L. Wicks, "Characterization of Multiple Piezoelectric Actuators for Structural Excitation," *Journal of the Acoustical Society of America*, 90(1), pp. 346-357, 1991.
- Clark, R.L. "Advanced Sensing Techniques for Active Structural Acoustic Control," Ph.D. Dissertation, VPI & SU, 1992.

- Dimitriadis, E.K. and C.R. Fuller, "Investigation on Active Control of Sound Radiation from a Panel Using Piezoelectric Actuators," *AIAA Journal*, 29(11), pp. 1771-1777, 1991. (also AIAA Paper 89-1062).
- Elliot, S.J., I.M. Strothers, and P.A. Nelson, "A Multiple Error LMS Algorithm and Its Application to the Active Control of Sound and Vibration," *IEEE Transaction on Acoustic Speech and Signal Processing*, Vol. ASSP-35, No. 10, pp. 1423-1434, 1987.
- Fuller, C.R. and J.D. Jones, "Experiments on Reduction of Propeller Induced Interior Noise by Active Control of Cylinder Vibration," *Journal of Sound and Vibration*, Vol. 112, No. 2, pp. 389-395, 1987.
- Fuller, C.R., 1989. "Active Control of Sound Transmission/Radiation from Elastic Plates by Vibration Inputs: I Analysis," *Journal of Sound and Vibration*, pp. 1-13.
- Fuller, C.R., C.H. Hansen and S.D. Snyder, 1989. "Active Control of Structurally Radiated Noise using Piezoceramic Actuators," *Inter-Noise 89*, pp. 509-511.
- Fuller, C. R., S.D. Snyder, C.H. Hansen, and R.J. Silcox, "Active Control of Interior Noise in Model Aircraft Fuselages using Piezoceramic Actuators," Presented at the 13th Aeroacoustics Conference, 1990. (AIAA Paper 90-3922).
- Fuller, C.R. and J.P. Carneal, "A Biologically Inspired Control Approach for Distributed Elastic Systems," *Journal of the Acoustical Society of America*, **93** (6), pp. 3511-3513, 1993.
- Gibbs, G.P. and C.R. Fuller, "Excitation of Thin Beams Using Asymmetric Piezoelectric Actuators," *Journal of the Acoustical Society of America*, **92** (6), pp. 3221-3227, 1992.
- Gibbs, G.P., B. Mahnken, and C.R. Fuller, "System Identification and Preliminary Active Control of the Interior Acoustic Field of a Cessna Citation III Fuselage," VAL Technical Report No. VAL-9401, Vibration and Acoustics Laboratories, VPI&SU, Blacksburg, VA,

August, 1994.

Grosveld, F.W., and K.P. Sheperd, "Active Sound Attenuation Across a Double Wall Structure,"

AIAA 29th Aerospace Sciences Meeting, Jan. 7-10, Reno, Nevada.

Hansen, C.H., S.D. Snyder, and C.R. Fuller, "Noise Reduction of a Vibrating Square Panel by

Use of Active Sound Sources and Active Vibration Sources," Proceedings of Noise and Vibration 89, Singapore, pp. E50-E57, 1989.

Hexcel Corporation, "The Basics on Bonded Sandwich Construction," Hexcel Technical

Bulletin TSB 124, Fall 1986.

Kinsler, L.E., A.R. Frey, A.B. Coppens, and J.V. Saunders, "Fundamentals of Acoustics," John

Wiley & Sons, Inc., New York, NY, 1982.

Landau, B.R., "Essential Human Anatomy and Physiology," Scott, Foresman and Company,

Glenview, Illinois, pp. 191-192, 1976.

Lefebvre, S., "Active Control of Interior Noise Using Piezoelectric Actuators in a Large-Scale

Composite Fuselage Model," VPI&SU Thesis, 1991.

Leissa, A., "Vibrations of Plates," Acoustical Society of America, 1993.

Mahnken, B., "Active Structural Acoustic Control of Aircraft Interior Flow Noise via the Use of

Active Trim Panels", VPI&SU Thesis, 1995.

Maidanik, G., 1962, "Response of Ribbed Panels to Reverberant Acoustic Fields," JASA, 34(6),

pp. 809-826.

McCray, T. W., "Construction and Characterization of Removable and Reusable Piezoelectric

Actuators," VPI&SU Thesis, 1994.

Meirovitch, L. and M. A. Norris, "Vibration Control," Proceedings of Inter-Noise 84, Noise

Control Foundation, Poughkeepsie, NY, pp. 477-482, 1984.

- Mixson, J.S., and C.A. Powell, "Review of Recent Research on Interior Noise of Propeller Aircraft," AIAA/NASA 9th Aeroacoustics Conference, Williamsburg, VA Oct 15-17, 1984, AIAA-84-2349.
- Nelson, P.A., and S.J. Elliot, "Active Control of Sound," Academic Press Inc., San Diego, CA, 1992.
- Pierce, A.D., "Acoustics: An Introduction to its Physical Principles and Applications," McGraw Hill, New York, 1981.
- Roussos, L.A., "Noise Transmission Loss of a Rectangular Plate in an Infinite Baffle," NASA Technical Paper 2398, 1985.
- Silcox, R.J., S. Lefebvre, V.L. Metcalf, T.B. Beyer, and C.R. Fuller, "Evaluation of Piezoceramic Actuators for Control of Aircraft Interior Noise," Presented at the 14th Aeroacoustics Conference, 1992. (DGLR/AIAA Paper 92-02-091).
- Simpson, M.A., T.M. Luong, C.R. Fuller, and J.D. Jones, "Full-Scale Demonstration Tests of Cabin Noise Reduction Using Active Vibration Control," *Journal of Aircraft*, Vol. 28, No. 3, pp. 208-215, March 1991.
- Singh, M.G., "Dynamical Hierarchical Control," North-Holland, 1980.
- Thomas, D.R., P.A. Nelson, and S.J. Elliot, "Experiments on the Active Control of the Transmission of Sound through a Clamped Rectangular Plate," *Journal of Sound and Vibration*, Vol. 139, No. 2, pp. 351-355, 1990.
- Thomas, D.R., P.A. Nelson, S.J. Elliot, "An Experimental Investigation into the Active Control of Sound Transmission through Stiff Light Composite Panels," *Inter-noise 91*, 271-274.
- Thomas, D.R., P.A. Nelson, S.J. Elliot, "Experiments on the Active Control of the Transmission of Sound through a Clamped Rectangular Plate," *JSV* (1990) 139(2), 351-355

Thomas, D.R., "The Active Control of the Transmission of Sound," Ph.D. Dissertation, University of Southampton, England, March 1992.

Wallace, C.E., 1972, "Radiation resistance of a rectangular panel," JASA, 51(3), pp.946-952.

Webster's Dictionary, College Edition, Delair Publishing Co. New York, New York, 1981.

Widrow, B. and S. Stearns, "Adaptive Signal Processing," Prentice-Hall, 1985.

Zhou, Ning, "Active Control of Sound Transmission through Plates in a Reverberant Environment," VPI&SU Thesis, 1992.

## Appendix A. Reverberant chamber characteristics

A brief introduction to the characteristics of a reverberation chamber and the specific characteristics of the chamber used in the experimental investigation of this dissertation are presented. The total pressure measured at a point in the reverberant environment can be approximated as the sum of the direct sound field radiated by the source and the effective pressure of the reverberant field, given by:

$$P^2 = \rho_o c \Pi \left( \frac{1}{4\pi r^2} + \frac{4}{A} \right) \quad (\text{A-1})$$

where  $\rho_o c$  is the impedance of air,  $\Pi$  is the acoustic output of the source in watts,  $r$  is the radial distance from the source, and  $A$  is the total sound absorption of the room (Kinsler, et al., 1982).

An important parameter in the choice of placing the source to achieve plane wave excitation of the incident plate of the double panel system is the radius of reverberation, defined as the radius where the direct field and the reverberant field contribute equally to the total pressure. Points located very close to the source,  $4\pi r^2 \ll (A/4)$ , are dominated by the direct field, whereas points located very far from the source,  $4\pi r^2 \gg (A/4)$ , are dominated by the reverberant field. By setting the contribution of the direct field equal to the reverberant field, the radius of reverberation can be found to be:

$$R_o = \sqrt{\frac{A}{16\pi}} \quad (\text{A-2})$$

Substituting the definition of reverberation time,  $T=0.161V/A$ , where  $V$  is the volume of the reverberation chamber reduces equation (6) to:



$$R_o \approx 0.1 \sqrt{\frac{V}{T\pi}} \quad (\text{A-3})$$

A summary of characteristics of the reverberation chambers used in the experimental investigation (see Section 4.1.1) at 500 Hz is shown in Table A-1.

**Table A-1. Reverberant chamber characteristics**

Parameters	Source chamber	Receiving chamber
volume (m <sup>3</sup> )	47.76	49.67
reverb. time @ 500 Hz (s)	6.11	7.63
reverb. radius (m)	0.16	0.14
Schroeder cutoff frequency (Hz)	588	648

An important consideration in performing the measurement of acoustic power level in a reverberant environment is the Schroeder cutoff frequency, defined as the frequency above which the sound field is theoretically diffuse, where the average energy density is the same throughout the volume of the enclosure and all directions of propagation are equally probable (Kinsler, et al., 1982). Below this frequency, standing wave patterns can exist in the room. The Schroeder cutoff frequency is defined as (Pierce, 1981):

$$f_s = 2000 \sqrt{\frac{T}{V}} \quad (\text{A-4})$$

The Schroeder cutoff frequencies of both the source and receiving chambers are presented in Table A-1. Since the excitation frequencies are below the cutoff frequency of the receiving chamber (648 Hz), an average of sound pressure across the chamber must be used to provide a reasonable estimate of the total transmitted power.

## **Appendix B. Incident pressure field**

Verification was needed to prove that the incident pressure field approximated the three different types of acoustic excitation studied in this dissertation. Three different types of acoustic excitation were provided by a Klipsch Forte II speaker placed at the prescribed locations in the source chamber at an excitation frequency of 361 Hz. For the plane wave excitation, the speaker was placed parallel to the incident plate at a distance of 0.260 m from the center and the acoustical transmission path from the speaker to the incident plate was surrounded by acoustic foam. This distance was on the order of the radius of reverberation at 361 Hz of the source chamber, shown in Table A-1, and should provide the intended excitation. Oblique plane wave excitation was provided by placing the speaker 45 degrees from the normal of the incident plate at a distance of 0.260 m and the acoustical transmission path from the speaker to the incident plate was surrounded by acoustic foam. For reverberant excitation, the speaker was placed in the far corner of the source chamber. At this speaker location, the distance from the speaker to the incident plate was much greater than the radius of reverberation. The incident pressure field magnitude and phase were determined by the auto correlation and cross correlation, respectively, of two microphones placed directly in front of the incident plate. The first microphone was positioned in the center of the plate, while the second was placed at eight locations defining the corners and mid-section of the sides. Incident field magnitude was measured by a calibrated microphone at the indicated location, while phase was determined by the time delay from the second microphone relative to the first. Data for this preliminary experiment was taken and processed with a Bruel and Kjaer Type 2032 dual channel signal analyzer.

Measurements of plane wave, oblique plane wave and reverberant excitation are presented in

Figure B-1. Note that the phase measurements are displayed in parentheses. As can be seen, plane wave excitation exhibits a uniform pressure field with little variation in phase. The oblique plane wave excitation displays a relatively uniform pressure and phase field, with negative phase on the side of the panel closest to the excitation, and positive phase on the farther side. Note there is also some variation in magnitude due to spherical spreading. Reverberant excitation exhibits randomly distributed pressure magnitude and phase, as expected. Therefore, the experimental configuration reasonably approximates those used in the analyses.

94.2 (0)	94.9 (0)	95.4 (0)
97.5 (-5)	96.3 (0)	95.9 (5)
95.4 (-16)	97.6 (0)	96.0 (0)

a) Plane Wave, 0.270 m from plate, 362 Hz

101.7 (-17)	100.5 (0)	92.7 (122)
103.2 (-32)	101.8 (0)	95.9 (77)
104.2 (-20)	100.5 (-2)	91.0 (93)

b) Oblique Plane Wave (45 deg. angle), 0.270 m from plate, 362 Hz

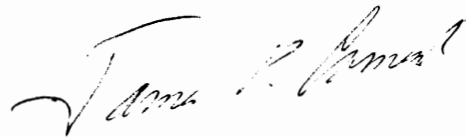
94.2 (0)	95.8 (0)	99.1 (-27)
98.9 (10)	100.8 (0)	98.5 (-27)
99.5 (0)	101.9 (-15)	98.8 (-25)

c) Reverberant Wave, In Far Corner of Source Chamber, 362 Hz

**Figure B-1. Incident wave magnitude (dB) and phase (degrees) measured at incident panel.**

## Vita

The author, James P. Carneal was born in Richmond, Virginia on September 23, 1965 and was raised in the quaint town of Ashland. He graduated from Patrick Henry High School in May, 1983. After graduating with a Bachelor of Science in Mechanical Engineering from Virginia Tech, he entered graduate school in the same department. After completion of his masters, a year hiatus from the wonderful mountains of Blacksburg was taken as he worked at Garrett Gas Turbine in Phoenix, Arizona. Fortunately, Garrett was in serious financial trouble and they provided the author with a lot of incentive to return to pursue his Ph.D., which was always his intent. After completion of his Ph.D. he will marry the woman he loves and they will live in the mountains or at the beach and have a wonderful life together. Professionally, James will complete the post-doc he is currently working on and future possibilities will probably include going into academia and/or starting a bicycle frame, components, and accessories manufacturing company.

A handwritten signature in black ink, reading "James P. Carneal". The signature is written in a cursive style with a large initial "J" and a long, sweeping underline.

James P. Carneal